Relation between ionized gas kinematics and Lyman-alpha observables in galaxies

Masterarbeit von
Anna Lena Schaible

12. Oktober 2023

Betreuer: Dr. Edmund Christian Herenz[1, 2]
Erster Prüfer: Prof. Dr. Jörg Main[3]
Zweiter Prüfer: Prof. Dr. Thomas Speck[4]

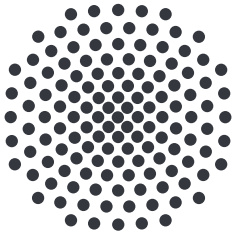

Institut für Theoretische Physik I
Universität Stuttgart
Pfaffenwaldring 57, 70550 Stuttgart

[1]Leiden Observatory, Leiden University, Niels Bohrweg 2, 2333 CA Leiden, The Netherlands
[2]European Southern Observatory, Av. Alonso de Cordova 3107, 763 0355 Vitacura, Santiago, Chile
[3]Institut für Theoretische Physik I, Universität Stuttgart, 70550 Stuttgart, Germany
[4]Institut für Theoretische Physik IV, Universität Stuttgart, Heisenbergstr. 3, 70569 Stuttgart, Germany

Contents

Abstract

Light from objects far away changes in wavelength due to cosmological redshift ($\lambda_{\rm obs} = \lambda_{\rm lab}\,[1+z]$). In the early universe, galaxies can be detected via their Lyman α emission, which is redshifted in the optical wavelength range (Lyα, $\lambda_{\rm Ly\alpha} = 1215.7\,$Å, 2p to 1s transition of hydrogen). However, not all galaxies in the early universe show Lyα emission. The reasons for this are only partly understood. Neutral hydrogen has a high absorption cross-section for Lyα photons. In galaxies, this leads to a spatial and spectral random walk of the Lyα photons in the interstellar-medium (ISM), which increases the absorption probability by interstellar dust of the Lyα photons and is a main reason that not all galaxies show Lyα emission. The random walk of the photons leads to a diffusion spatially and spectrally, which makes it harder to detect the Lyα radiation. The study of spatially resolved observations with samples of galaxies with and without Lyα emission can give important insights in the prevailing ISM conditions for promoting Lyα escape. Such studies can be performed well on a sample of nearby galaxies, which resemble galaxies from the early universe. For nearby galaxies multi-wavelength observations can be obtained, which allow a detailed study of the ISM conditions influencing the Lyα escape.

This thesis uses integral field spectroscopic data obtained from the Potsdam Multi Aperture Spectrophotometer at the Calar Alto 3.5 m telescope to investigate the kinematics of ionized gas in 42 nearby galaxies with young stellar populations and active star formation. We use the Balmer α line (Hα, $\lambda_{\rm H\alpha} = 6562.8$ Å, 3 to 2 transition) as a tracer for the intrinsic Lyα radiation field in the galaxies. Additionally, we use photometric observations from the Hubble Space Telescope for the Lyman α Reference Sample (LARS) and Extended Lyman α Reference Sample (eLARS) galaxies to obtain the Lyα observables.

Turbulent kinematics may shift emitting and absorbing material out of resonance, increasing the likelihood of Lyα escaping from galaxies. To test this hypothesis, we perform a global analysis of the kinematic properties of the LARS and eLARS sample, along with their Lyα observables. We derive velocity fields and velocity dispersion maps from the Hα observations, and then we focus on the relation between integrated kinematic quantities and the Lyα observables (luminosity, equivalent width and escape fraction). Prior to the analysis, we apply a newly

introduced gradient method to correct our data for point spread function smearing. Our results from Kendall tau statistic tests between ionized gas kinematics and Lyα observables support the hypothesis that galaxies dominated by turbulent kinematics, rather than ordered motions, favor the escape of Lyα.

Furthermore, we apply a multivariate linear regression method on the Lyα observables luminosity, equivalent width and escape fraction to asses the importance of the integrated kinematic parameters. Again, we find that intrinsic velocity dispersion is an important parameter in affecting the emergence of Lyα emission.

We therefore suggest that dispersion dominated ionized gas kinematics may be a necessary, but not a sufficient condition for facilitating Lyα escape. We find indications that there exist favorable conditions for Lyα escape in low-mass galaxies with dispersion dominated kinematics.

Zusammenfassung

Das Licht von weit entfernten Objekten ändert aufgrund des kosmologischen Rotverschiebungseffekts ($\lambda_{\mathrm{obs}} = \lambda_{\mathrm{lab}}\,[1+z]$) seine Wellenlänge. Im frühen Universum können Galaxien über ihre in den optischen Wellenlängenbereich verschobene Lyman-α-Emission (lyα, $\lambda_{\mathrm{Ly}\alpha} = 1216\,\text{Å}$, Übergang von 2p zu 1s bei Wasserstoff) gefunden werden. Allerdings zeigen nicht alle Galaxien im frühen Universum Lyα-Emission. Die Gründe dafür sind nur teilweise verstanden. Neutrales Wasserstoffgas hat einen hohen Wirkungsquerschnitt für die Lyα-Emission. In Galaxien führt dies zu einem räumlichen und spektralen random walk der Lyα-Photonen im interstellaren Medium (ISM), was die Absorptionswahrscheinlichkeit durch interstellaren Staub der Lyα-Photonen erhöht und ein Hauptgrund dafür ist, dass nicht alle Galaxien Lyα-Emission zeigen. Der random walk der Photonen führt zu einer räumlichen und spektralen Diffusion, die es erschwert, die Lyα-Strahlung zu detektieren. Die Untersuchung räumlich aufgelöster Beobachtungen an Stichproben von Galaxien mit und ohne Lyα-Emission kann wichtige Einblicke in die vorherrschenden ISM-Bedingungen geben, die das Entkommen von Lyα Photonen begünstigen. Solche Studien können gut an einer Stichprobe von nahegelegenen Galaxien durchgeführt werden, die Galaxien aus dem frühen Universum ähneln. Für nahegelegene Galaxien können Multiwellenlängenbeobachtungen durchgeführt werden, die eine detaillierte Untersuchung der ISM-Bedingungen ermöglichen, die das Entkommen von Lyα Strahlung begünstigen.

Diese Arbeit verwendet integralspektroskopische Daten, die mit dem Potsdam Multi Aperture Spectrophotometer am Calar-Alto 3.5-m-Teleskop beobachtet wurden, um die Kinematik des ionisierten Gases in 42 nahegelegenen Galaxien mit jungen stellaren Populationen und aktiver Sternentstehung zu untersuchen. Wir verwenden die Balmer-α-Linie (Hα, $\lambda = 6562,8\,\text{Å}$, Übergang von 3 zu 2) als Tracer für das intrinsische Lyα-Strahlungsfeld in den Galaxien. Darüber hinaus verwenden wir photometrische Beobachtungen vom Hubble Space Telescope für die Lyman-α-Referenzstichprobe (LARS) und erweiterte Lyman-α-Referenzstichprobe (eLARS) von Galaxien, um die Lyα Größen zu erhalten.

Turbulente Kinematik könnte emittierendes und absorbierendes Material aus der Resonanz verschieben und die Wahrscheinlichkeit erhöhen, dass Lyα Photonen aus Galaxien entkommen. Um diese Hypothese zu überprüfen, führen wir eine

globale Analyse der kinematischen Eigenschaften der LARS- und eLARS-Galaxien durch. Wir leiten Geschwindigkeitsfelder und Geschwindigkeitsdispersionskarten aus den Hα Beobachtungen her und untersuchen dann auf die Beziehungen zwischen integrierten kinematischen Größen und den Lyα Größen (Leuchtkraft, Äquivalentbreite und escape fraction). Vor der Analyse wenden wir eine neu eingeführte Gradientenmethode an, um unsere Daten auf Verwischung durch die Punktverbreiterungsfunktion zu korrigieren. Unsere Ergebnisse aus Kendall-Tau-Statistiktests zwischen ionisierten Gaskinematiken und Lyα Größen unterstützen die Hypothese, dass Galaxien, die von turbulenter Kinematik dominiert werden anstelle von geordneten Bewegungen, das Entkommen von Lyα begünstigen.

Darüber hinaus wenden wir eine multivariate lineare Regressionsmethode auf die Lyα Größen Leuchtkraft, Äquivalentbreite und escape fraction an, um die Bedeutung der integrierten kinematischen Parameter zu bewerten. Erneut finden wir, dass die intrinsische Geschwindigkeitsdispersion ein wichtiger Parameter ist, der sich auf das die Lyα-Emission auswirkt.

Unsere Analyse zeigt, dass dispersionsdominierte Kinematiken das Entkommen von Lyα Photonen aus Galaxien begünstigen. Dispersionsdominierte ionisierte Gaskinematiken sind eine notwendige, aber keine ausreichende Bedingung für das begünstigte Entkommen von Lyα Photonen aus Galaxien.

1 Introduction

1.1 Motivation

Due to the expansion of the universe, light from more distant objects gets more redshifted and we observe wavelengths of

$$\lambda_{\text{obs}} = [1 + z]\lambda_{\text{restframe}} \tag{1.1}$$

dependent on the redshift z of our observed object. The ΛCDM cosmology model with $H_0 = 70$ kms^{-1}Mp^{-1}, $\Omega_m = 0.3$ and $\Omega_\Lambda = 0.7$ is an interpretation of this observational effect. For very distant objects, Lyα gets shifted in the optical and gets accessible via optical ground-based telescopes. So, Lyα opens a window into the distant universe.

Lyα ($\lambda = 1215.67$ Å) is the strongest recombination line emitted from ionized gas surrounding star-forming regions and hot stars, corresponding to the 2p to 1s transition in hydrogen. Lyα photons are emitted during recombinations of protons and electrons after the hydrogen atoms were photo-ionized by energetic radiation from short-lived massive stars. Lyα is also, at least intrinsically, the brightest line in the spectrum. 5% - 10% of the bolometric luminosity of a star-forming galaxies will be emitted in Lyα photons (Partridge and Peebles 1967, Blaizot et al. 2023). At higher redshifts, the line shifts into the optical range and therefore, Lyα is the line to detect very faint objects in the high-z Universe. Lyα has a large cross section and therefore it is a tracer of neutral hydrogen between the distant objects and the observer, which allows to study the ionization state of the intergalactic medium (IGM). Also, Lyα is a resonant line. A photon with an energy close to the 1s to 2p transition can excite the electron of an neutral hydrogen atom form the 1s state to a higher excitation level, e.g. 2p. Afterwards the electron deexcides by emitting a Lyα photon. Therefore, the Lyα photons scatter many times in the ISM and circum galactic medium (CGM) until they can escape and reach an observer or until they are destroyed by dust grains in the interstellar medium (ISM). Emitted Lyα photons undergo a random walk in space and frequency during the scattering until they reach an observer (Blaizot et al. 2023). The optical depth describes how much light gets absorbed on the way from the object to the observer. Low neutral

hydrogen (HI) column densities, which corresponds to low optical depths help Lyα photons to escape from galaxies.

Dust and gas in the ISM along the line of sight interact with the light and cause absorption and scattering. The extinction curve quantifies, how much light at different wavelengths is absorbed and scattered by the ISM between source and observer. By analyzing the shape of the curve, details about the size, composition, and distribution of dust grains along the line of sight can be interfered. Shorter wavelengths are affected stronger by extinction. To characterize this reddening, we use the nebular extinction or color excess $E(B-V)$

$$E(B-V)_n = (B-V)_{\text{observed}} - (B-V)_{\text{intrinsic}} \tag{1.2}$$

between the observed magnitude[1] in the blue band B and in the visual band V and calibrate the difference. Higher $E(B-V)_n$ indicates higher extinction.

Depending on the nebular extinction, we can determine which fraction of produced Lyα photons escapes a galaxy, if Lyα would not be resonant. This would be the case if Lyα photons would escape directly along the sight line towards the observer, facing only extinction by the amount of dust in front of the emitting photon. Figure 1.1 shows this for the extended Lyman α Reference Sample (eLARS) and reveals an anti-correlation between the nebular extinction and escape fraction (see also Section 1.2.4). Thus, indeed, dust will extinguish Lyα. A fraction of Lyα photons emitted by galaxies is absorbed by dust in the interstellar medium (ISM) (Dijkstra 2019). Different works derived different ISM extinction curves, which are presented as lines in Figure 1.1. The extinction law formulated by Cardelli, Clayton, and Mathis (CCM, Cardelli, Clayton, and Mathis 1989) assumes a simple dust screen model for nebular emission lines, without considering resonant scattering effects. This extinction law follows the general trend of the anti-correlation between the Lyα escape fraction and color excess. When we assume a clumpy ISM instead of an isotropic ISM, we can derive different relations for nebular extinction and escape fraction. Curves from clumpy dust models with different numbers of clumps along the line of sight are shown in dotted gray in Figure 1.1. None of these curves can trace the data points very good. The reason is that those extinction curves assume static gas and do not include that the Lyα radiative transfer is a resonant scattering process.

However, before looking in detail on the Lyα radiative transfer, which causes the problem between theoretic expectations and observations in Figure 1.1, we will first have a look at the different observables and quantities, we can derive from the observations in Section 1.2 and Section 1.3.

[1] Astronomic magnitudes measure the brightness of an object in the wavelength range of a certain filter.

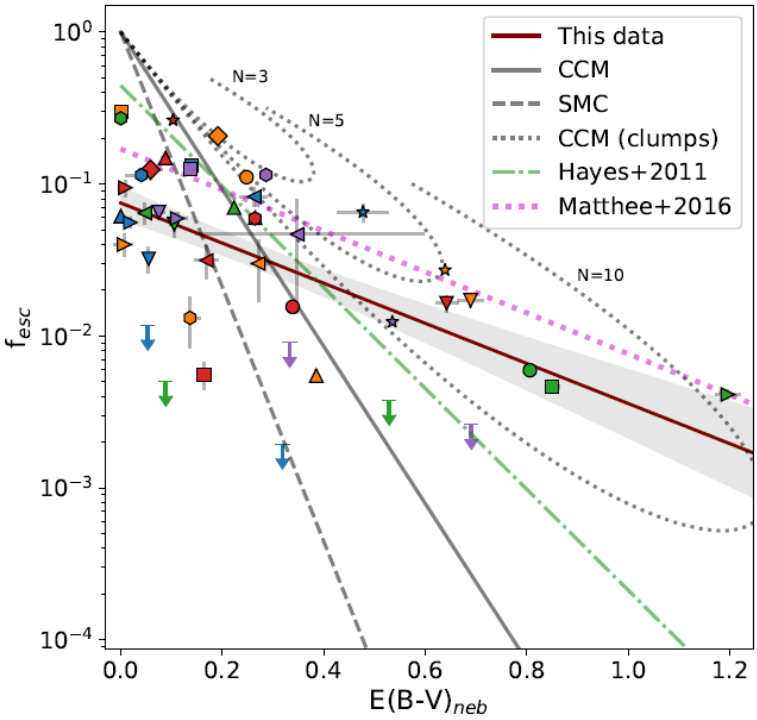

Figure 1.1: Global escape fraction versus nebular extinction for the extended Lyman α reference sample with predictions for different ISM extinction curves (gray lines). The dotted gray lines are predictions from clumpy dust models with different numbers of clumps along the line of sight (Melinder et al. 2023).

1.2 Observational methods of global Lyα observables

In this section first we want to introduce the principle of integral field spectroscopy (IFS) methods in Section 1.2.1. Then we introduce the observational parameters Lyα luminosity (Section 1.2.2) and Lyα equivalent width (Section 1.2.3). These observed parameters can be translated into meaningful physical parameters. Therefore, here we introduce the parameter Lyα escape fraction (Section 1.2.4).

1.2.1 Integral field spectroscopy

Photons carry a lot of the information that we can gain from observed galaxies. We can use imaging to study an object to get a spatial resolved image for a certain wavelength range, which is determined by the filter used for the observation. On the other hand, we can use spectroscopy, where we get a spectrum of our object.

Combining both observational methods we end up with integral field spectroscopy

(IFS). IFS provides detailed spatial and spectral information. IFS gives us an image of a galaxy, where each pixel contains the full spectrum in this area and is therefore called spaxel. We end up with two spatial dimensions and one spectral dimension. There are different types of IFS instruments. Fiber-based IFS instruments use an array of optical fibers to collect light from different regions of an object and then route it to a spectrograph for analysis. Each fiber corresponds to a specific spatial element, and the collected light is dispersed into its spectrum for analysis. Slicer-based IFS instruments use an array of image slicers to partition the incoming light from an object into multiple slices. These slices are then rearranged spatially and sent through the spectrograph for spectral analysis (Bacon and Monnet 2017). For our analysis of the ionized gas kinematics we work with data from PMAS at Calar Alto. PMAS is a IFS with a fiber-coupled lens array (Roth et al. 2005).

1.2.2 Total luminosities of Lyα, Hα and Hβ

For the here studied low-z galaxies, Lyα line observations require data from space based observations since ground-based telescopes cannot detect it, because the Lyα line is in the UV and the atmosphere absorbs most of the UV light. For our analysis we directly use the Lyα luminosity and we use the Hα and Hβ luminosities for calculating the Lyα escape fraction.

We observe flux, which has to be converted into luminosity. Flux measures the total amount of energy received by the detector and is traditionally measured in units of $\mathrm{erg\,cm^{-2}s^{-1}}$ in astronomy[2]. The flux density specifies the energy which is received in a particular wavelength and is measured in units of $\mathrm{erg\,s^{-1}cm^{-2}\AA^{-1}}$. The flux depends on the luminosity and the distance of the object. The luminosity is the total amount of energy emitted by the object per time and is measured in units of $\mathrm{erg\,s^{-1}}$. It measures the intrinsic brightness and is distance independent.

For the LARS and eLARS sample, Melinder et al. (2023) derives the flux maps. Spectral Energy Distribution (SED) fitting (Melinder et al. 2023) is used to estimate continuum contribution in the HST passbands. Subtracting the continuum yields the emission line maps. The measured fluxes can then be converted to luminosities by the redshift of the objects. Melinder et al. (2023) ends up with luminosity maps with individual values assigned to each spaxel.

To determine the total luminosity of the recombination lines, Melinder et al. (2023) performs circular photometry on the maps using an aperture that is sufficiently large to encompass the entire detected galaxy.

[2] $1\ \mathrm{erg\,cm^{-2}s^{-1}} = 10^{-3}\ \mathrm{J\,s^{-1}m^{-2}}$

1.2.3 Lyα equivalent width

The Lyα equivalent width $\mathrm{EW}_{\mathrm{Ly}\alpha}$ is defined as the ratio between the Lyα flux and the continuum flux density at the wavelength of Lyα relative to the continuum. This provides a parameter to assess the strength of the Lyα line.

The equivalent width is measured in units of Å and can be calculated using the following formula:

$$\mathrm{EW} = \int_{\lambda_0}^{\lambda_1} \frac{f_{\mathrm{Ly}\alpha}^{\mathrm{line}} - f_{\mathrm{Ly}\alpha}^{\mathrm{cont}}}{f_{\mathrm{Ly}\alpha}^{\mathrm{cont}}} \mathrm{d}\lambda, \tag{1.3}$$

where λ_0 and λ_1 represent the wavelength range of the Lyα line, and $f_{\mathrm{Ly}\alpha}^{\mathrm{line}}$ and $f_{\mathrm{Ly}\alpha}^{\mathrm{cont}}$ denote the flux density of the Lyα line and the continuum, respectively. Traditionally, stellar spectroscopists, but also researchers studying quasar absorption lines, define the EWs of absorption lines as positive and those of emission lines negative. However, in our sub-field it has become consensus to use the reversed sign. Therefore, Lyα absorbers have negative equivalent widths.

When the Lyα line flux $f_{\mathrm{Ly}\alpha}^{\mathrm{line}}$ is much greater than the continuum flux $f_{\mathrm{Ly}\alpha}^{\mathrm{cont}}$, the equivalent width simplifies to the ratio of the Lyα flux and the continuum flux density:

$$\mathrm{EW} \approx \frac{F_{\mathrm{Ly}\alpha}^{\mathrm{line}}}{f_{\mathrm{Ly}\alpha}^{\mathrm{cont}}}, \tag{1.4}$$

as described, e.g. in Kerutt et al. (2022).

To account for redshift effects, the equivalent width is typically corrected by dividing by $(1 + z)$, yielding the rest-frame equivalent width EW^0 (Kerutt et al. 2022). We are interested in the rest-frame equivalent width, because it is independent of the distance of the object, which is a requirement when comparing different galaxies and comparing with models.

Galaxies at high-z are selected via their Lyα EW with narrow band surveys. The narrow bands are designed to avoid bright sky lines and narrowband surveys maximize the sensitivity (J. X. Wang et al. 2004, Rhoads and Malhotra 2001). For example, Malhotra and Rhoads (2002) applies a Lyα EW selection criterium of ≥ 80 Å for their narrow band survey. Stellar models predict a maximum Lyα equivalent width of 240 Å (Malhotra and Rhoads 2002). However, surveys of high-z Lyα emitters find higher Lyα equivalent widths. For example, Figure 3.67 in Ouchi 2019 shows that Lyα EWs are higher than theoretic predictions. 10-30% of Lyman α emitters (LAE) in narrowband-selected samples of LAE studies at $z \sim 2 - 7$ show Lyα EWs with $\gtrsim 200 - 300$ Å (Ouchi 2019).

1.2.4 Lyα escape fraction

As mentioned earlier, Lyα observations provide a window into the high-z universe. However, to interpret the observed Lyα luminosities and equivalent widths, we need to determine the fraction of intrinsic Lyα radiation that escapes from a galaxy. This fraction is known as the Lyα escape fraction and is described in Chapter 4.1 of Hayes (2019).

As shown in the beginning of the introduction, the escape fraction is related to the extinction, showing that dust impacts the Lyα escape fraction. Higher nebular extinction leads to lower Lyα escape fractions, because the probability that the photon is destroyed on its way out of the galaxy is higher. Figure 1.1 illustrates the effect of dust on the escape fraction. The lines in the figure represent different geometric models, uniform dust and clumpy dust with varying amounts of dust clumps along the line of sight (Scarlata et al. 2009).

A possible simple scenario is a dust screen located far away from the radiation source with uniform dust distribution throughout the screen. The dust screen is commonly used to estimate the wavelength dependent extinction due to dust. For a higher optical depth the Lyα/Hα ratio gets smaller. The clumpy dust screen model yields similar ratios for moderate values, but it differs a lot for clumps with large optical depth.

The Lyα escape fraction is defined as:

$$f_{\mathrm{esc}}^{\mathrm{Ly}\alpha} = \frac{L_{\mathrm{Ly}\alpha}^{\mathrm{obs}}}{L_{\mathrm{Ly}\alpha}^{\mathrm{int}}} \approx \frac{L_{\mathrm{Ly}\alpha}^{\mathrm{obs}}}{8.7 \cdot L_{\mathrm{H}\alpha}^{\mathrm{int}}} \tag{1.5}$$

where $L_{\mathrm{Ly}\alpha}^{\mathrm{obs}}$ represents the observed Lyα luminosity and $L_{\mathrm{Ly}\alpha}^{\mathrm{int}}$ denotes the intrinsic Lyα luminosity. Estimating the intrinsic Lyα luminosity requires the use of other indicators, such as the UV continuum or the Hα line. Hα, being a non-resonant line and less affected by dust compared to Lyα, serves as a useful tracer of the intrinsic Lyα emission. Additionally, the UV continuum provides insights into the radiation field surrounding young, hot, massive stars.

To calculate the nebular extinction using the dust screen model, the following equation is used:

$$f_{\mathrm{esc}}^{\mathrm{H}\alpha,\mathrm{screen}} = 10^{-0.4k(\mathrm{H}\alpha)E(B-V)_n} \tag{1.6}$$

where $k(\mathrm{H}\alpha)$ is the extinction coefficient for the Hα wavelength, which represents how much the intensity of the Hα line ($L_{\mathrm{H}\alpha}^{\mathrm{obs}} = f_{\mathrm{esc}}^{\mathrm{H}\alpha} \cdot {}^{\mathrm{int}}_{\mathrm{H}\alpha}$) is reduced due to dust extinction along the line of sight (we assume the Cardelli, Clayton, and Mathis 1989 extinction law). Hα is the second strongest line in hydrogen and is less dust affected than Lyα. Hα can be corrected for dust extinction using Hβ, which is

the most reliable method. By assuming temperatures T around 10^4 K and case B recombination (see Section 1.4), the line ratio is Hα/Hβ = 2.86 (Osterbrock and Ferland 2006, Hummer and Storey 1987). The intrinsic Lyα/Hα ratio depends on electron density and temperature, as depicted in Figure 4.2 of Hayes (2019). The ratio typically ranges between 8 and 10 for temperatures ranging from 1000 to 30 000 K, with a plateau around 10^4 K where thermal instabilities in the ISM do not affect the ratio significantly. Assuming an intrinsic Lyα/Hα ratio of 8.7 for case B recombination, the Lyα escape fraction can be calculated using the formula:

$$f_{\mathrm{esc}}^{\mathrm{Ly}\alpha} = \frac{F_{\mathrm{Ly}\alpha}}{8.7 \cdot F_{\mathrm{H}\alpha} \cdot 10^{-0.4k(\mathrm{H}\alpha)E(B-V)_n}} \tag{1.7}$$

as described in Melinder et al. (2023).

To estimate the strength of the star formation episodes in high redshift galaxies we need to unveil their intrinsic Lyα luminosity. However, for this we would need to estimate the Lyα escape fraction as a function of any of the observable parameters, which is challenging. Sobral and Matthee (2019) derived an empirical correlation between the Lyα EW and the Lyα escape fraction for star-forming galaxies up to $z \sim 2.6$. The Lyα equivalent width is sensitive to various properties of the galaxy. Galaxies with higher SFRs tend to have stronger Lyα emission lines, resulting in a higher intrinsic Lyα EW. Young, massive stars are more likely to produce Lyα photons. Therefore, galaxies with a relatively young stellar population or ongoing star formation tend to have higher intrinsic Lyα EWs. Low-metallicity galaxies, which are often found in the early universe, may have higher Lyα EWs because they contain fewer metals that can absorb Lyα photons.

If star-formation would proceed as longlasting episodes, so the SFR would be constantover few hundreds of Myr, statistically most of the observed galaxies would be in the equilibrium/stationary case with intrinsic Lyα EWs $\leq$ 100 Å. This does not seem to be the case. Assuming standard stellar populations synthesis models (with no Pop III stars), Lyα EWs $>$ 150 Å are not compatible with long-lasting star formation episodes. It seems that most of the Lyman α emitting galaxies we know at high redshift are experiencing very young and/or short lived episodes of star formation. Short-lived very massive starbursts could be very efficient in accelerating/cleaning the gas surrounding the massive star clusters and therefore favor the Lyα escape. Sobral and Matthee (2019) revealed a linear relationship between the EW and the Lyα escape fraction. This correlation allows to use the Lyα EWs as a statistical proxy for the Lyα escape fraction. Also, we identified this linear relation in our sample, expressed as

$$f_{\mathrm{esc}}^{\mathrm{Ly}\alpha} = (0.0040 \pm 0.00050)\mathrm{EW}_{\mathrm{Ly}\alpha}^{0} \pm 0.013 \tag{1.8}$$

(Melinder et al. 2023).

1.3 Measuring galaxy parameters

In this section first we want to introduce the stellar mass (Section 1.3.1) and star formation rate (Section 1.3.2) that we use for our analysis. Then we introduce the ionized gas kinematics (Section 1.3.3).

1.3.1 Stellar mass

The determination of stellar mass for galaxies is derived based on the mass-luminosity relation of stars, discovered first by Eddington (1924). Main sequence stars in a similar evolutionary state derive their energy from hydrogen-to-helium conversion and share common characteristics. The mass of a star is directly related to its energy sources, which, in turn, determine its luminosity. Thus, a relationship between mass and luminosity exists (Courteau et al. 2014, Unsöld and Baschek 1981).

We can extend this knowledge to estimate the stellar masses of galaxies through spectrophotometric analysis, where spectroscopy and photometry is combined. We measure the intensity of light across different wavelength for the galaxy. Luminous galaxies may have only moderate masses if they contain numerous young stars with high specific luminosity, which makes this task challenging. The dominance of young stars in the spectral energy distribution can overshadow the contribution of older, colder, and less luminous stars (Weigert, Wendker, and Wisotzki 2012). While it is possible to estimate stellar mass solely from luminosity by assuming a fixed mass-to-light ratio, this approach can be misleading as it overlooks factors such as stellar age and extinction.

In the LARS and eLARS sample, Melinder et al. (2023) derives stellar masses through Spectral Energy Distribution (SED) fitting using Starburst99 models (Leitherer et al. 1999) applied to imaging data from the HST. To perform the SED fitting, Melinder et al. (2023) generates a model spectrum for each spaxel in the galaxy, which is then normalized to a specific stellar mass. From these modeled spectra, Melinder et al. (2023) calculates the observed flux for different filters, typically using two far ultraviolet (FUV) filters and three optical filters.

To account for variations in stellar age and extinction, Melinder et al. (2023) creates numerous spectral models, as different ages and extinctions cause changes in the shape of the continuum spectrum, resulting in varying flux levels at different wavelengths. It is important to note that changing the mass only affects the overall brightness of the spectrum, while the shape of the spectral energy distribution remains unchanged (Melinder et al. 2023).

For the fitting process, Melinder et al. (2023) employs two models: one with

varying age, extinction, and mass, and another with a fixed age (set to a very old age), zero extinction, and varying mass. Through the fitting procedure, Melinder et al. (2023) determines four free parameters: the age and extinction of the young stellar population, as well as the mass of the young population and the mass of the old population. Previously we talked about nebular extinction, where a dust screen is assumed. Stellar extinction assumes that the star are mixed together with the dust.

The output of the SED fitting is presented as a map, displaying the stellar mass for each pixel, representing the combined masses of the young and old stellar populations. To obtain total mass estimates, Melinder et al. (2023) performs circular photometry on the maps, using an aperture large enough to encompass the entire detected galaxy. For our study we use the stellar masses of our galaxies derived by Melinder et al. (2023).

The masses are also derived from the Sloan Digital Sky Survey. Their results differ because they use a different method to derive the masses (Brinchmann et al. 2004). They use a different initial mass function (IMF) and they use the photometry from SDSS, Melinder et al. (2023) uses photometry of significant higher quality and depth based on HST observations.

1.3.2 Star formation rate (SFR)

The SFR represents the amount of gaseous matter converted into stars per time[3]. Since individual young stars are often unresolved, determining the SFR of galaxies relies on integrated light measurements obtained from various observations. These measurements include the ultraviolet (UV) and far-infrared (FIR) emissions, as well as nebular recombination lines, which provide direct information about the young stellar populations. The short lifetimes of very luminous young stars allow for estimates of the SFR. The number of massive stars is directly proportional to the current SFR.

One commonly used estimator for SFR is the luminosity of the Hα emission line, which originates from the HII regions surrounding young, hot stars (e.g. O and B stars). These stars emit Ly continuum photons (for O stars[4] around 5-10 % of the bolometric luminosity and for B stars[5] around 1-5 %) with enough energy to ionize hydrogen in the surrounding ISM. To convert Hα to SFR, an initial mass

[3]In the case of our Milky Way, the observationally derived SFR is approximately 1.65 solar masses per year (Licquia and Newman 2015)

[4]O stars have luminosities of $\geq 30\,000\,L_{\odot}$ and masses of $\geq 16\,M_{\odot}$

[5]B stars have luminosities of $25 - 30\,000\,L_{\odot}$ and masses of $2 - 16\,M_{\odot}$

function (IMF)[6] must be assumed. An IMF describes the distribution of stellar masses at the time of their formation in a population of star. The IMF provides information about the relative distribution of stellar masses in a given population of stars. Additionally, Hα measurements are sensitive to the presence of dust, which can be corrected using the Hβ line (see Equation 1.6).

UV radiation ($\lambda \sim 1500$ Å), on the other hand, is emitted by young, hot stars with masses greater than or equal to 5 $M_\odot$ (1 solar mass $M_\odot = 2 \cdot 10^{30}$ kg). These stars have main-sequence lifetimes of less than 100 million years and predominantly emit UV continuum radiation. Ground-based observations can access galaxies with redshifts ranging from 1 to 5, while space-based observations are necessary for lower-redshift galaxies when using UV-based estimators. Since low-mass stars dominate the total mass of newly formed stars, while UV emission primarily traces massive stars, an initial mass function (IMF) is required to convert UV luminosity to SFR (Kennicutt 1998a).

Recombination lines such as Hα are sensitive to shorter lifetimes of approximately 1 million years, while UV radiation traces longer timescales of up to 100 million years (Kennicutt and Evans 2012). Comparing these different SFR estimators can yield varying results for a single galaxy. Combining multiple diagnostics provides more accurate results, but it can be observationally challenging and resource-intensive (Schneider 2006, Mo, Bosch, and White 2010). At higher redshifts, directly measuring the Hα and Hβ luminosities becomes difficult, and in such cases, stellar-population models are fitted to the spectral energy distribution (SED) (Green, Glazebrook, McGregor, Damjanov, et al. 2014).

For the galaxies in our sample, we use the values from Melinder et al. (2023) that estimate the galaxy wide star-formation rate from the dust extinction corrected Hα luminosity. Melinder et al. (2023) uses the integrated Hα maps produced from the HST imaging data (see Section 1.2.2). Melinder et al. (2023) then applies the following calibrator to calculate the SFR out of the Hα luminosity (Kennicutt 1998b)

$$\mathrm{SFR}[\mathrm{M}_\odot \mathrm{yr}^{-1}] = \frac{L(\mathrm{H}\alpha)}{1.26 \cdot 10^{41}} \, [\mathrm{ergs\ s}^{-1}] \cdot 0.56 = 4.44 \cdot 10^{-42} L(\mathrm{H}\alpha) \, [\mathrm{ergs\ s}^{-1}] \quad (1.9)$$

where $L(H\alpha)$ is the dust corrected Hα luminosity (Law, Steidel, et al. 2007, Law, Belfiore, et al. 2022, Kennicutt 1998a). Because Hα is from a certain type of stars, we have to take a stellar mass distribution into account, for example the Chabrier IMF Chabrier 2003), which introduces the factor 0.56. For our study we use the SFR of our galaxies derived from Hα by Melinder et al. (2023).

[6] Melinder et al. (2023) assumes the Kroupa IMF (Kroupa, Tout, and Gilmore 1993)

1.3.3 Ionized gas kinematics

We discussed that geometric and static models can not fully describe the observed Lyα properties. Therefore, in this thesis we study the ionized gas kinematics traced by the Hα emission line. These photons originate from the regions where also Lyα photons are created. We will study the influence of the ionized gas kinematics on the Lyα observables.

As Lyα photons are resonant and get absorbed and re-emitted by neutral hydrogen and also scatter at dust, the probability to observe a photon decreases with the distance which photons have to overcome to reach an observer. Turbulent ionized gas kinematics may shift enough absorbing and emitting material out of resonance and therefore favor the escape of Lyα photons. After Lyα, the next prominent line in hydrogen is Hα, which falls within the optical range at a wavelength of $\lambda_{\mathrm{H}\alpha} = 6562.8$ Å (Chapter 4.1.3 in Hayes 2019).

Since the radiative transfer of Lyα is influenced by neutral hydrogen along the line of sight, in Section 3.2 we also study the kinematics along this direction, which is also the only observational possible direction. One can quantify the ionized gas kinematics of a galaxy by v_{shear}, which traced the large-scale ordered motions, and σ_0, which provides a measurement of turbulence in the gas.

The non-ordered motions in the gas can be accessed by the observed width of the Hα line. For data with small aperture or spatially resolved data, this width is a convolution of the natural Hα line, thermal effects in the ionized gas, the non-thermal motions in the gas, which can e.g. origin from turbulent motions of the ionized gas and the instrumental component (which is subtracted in squares) caused by the line spead function (LSF; e.g. Jiménez-Vicente et al. 1999). For an integrated spectrum of a galaxy, e.g. as in SDSS, the width of the observed line is also convolved with rotation.

The Hα line has a natural line width, like every spectral line. Energy levels above the ground state have a certain lifetime Δt (in the order of micro-/nanoseconds) and by the quantum mechanic uncertainty principle a state with energy E has a uncertainty in energy by

$$\Delta E \Delta t \sim h. \tag{1.10}$$

Short lived states have large uncertainties in energy. A photon emitted in a transition from a level to the ground state has a range of possible frequencies

$$\Delta\nu \sim \frac{\Delta E}{h} \sim \frac{1}{2\pi\Delta t}, \tag{1.11}$$

which leads to the natural line width of the transition.

The velocity dispersion values we obtain are higher than the expected natural line width (around 3 $\mathrm{km\,s^{-1}}$ (E. C. Herenz et al. 2016), which is normally negligible) and the thermal broadening

$$\Delta\nu\frac{c}{\nu_0} = \sqrt{\frac{2k_BT}{m_\mathrm{H}}} \tag{1.12}$$

of approximately 10 $\mathrm{km\,s^{-1}}$ for typical ionized gas temperatures of 10^4 K (M. R. Varidel, Croom, Lewis, Fisher, et al. 2020, Law, Belfiore, et al. 2022). This suggests that non-thermal motions, such as turbulent motions, dominate the observed broadening of the Hα line. Non-thermal broadening is caused by other processes that are not related to thermal motions. It arises from turbulence, shocks, magnetic fields, gravitational effects or other forms of non-thermal energy sources present in the system. These processes introduce additional velocity fluctuations that contribute to the broadening of the spectral line.

We are interested in the intrinsic velocity dispersion, which traces the random motions of the ionized gas. The mechanisms that create turbulence in the ionized phase are not yet fully unterstood. On the one hand, feedback from star-formation inject turbulence. On the other hand gravitational instabilities also contribute to the observed turbulence. Stellar feedback refers to the influence of stars on their surrounding environments. Stellar processes like stellar winds, supernova explosions, and radiation pressure can inject energy and momentum into the ISM. Stellar feedback can drive turbulence, create shocks, and induce gas motions, resulting in broadening of the Hα line. Observational, the literature finds a relation between velocity dispersion and SFR (Terlevich and Melnick 1981, Green, Glazebrook, McGregor, Abraham, et al. 2010, Law, Belfiore, et al. 2022). High-velocity dispersion indicates highly turbulent ionized ISM. HII regions are located, where the local gas density is high enough to condense and initiate star formation. The star formation then affects the surrounding gas by emitting ionizing photons, which heat the gas and provide radiative feedback, and by mechanical feedback from stellar winds and supernovae, which leads to turbulence in the bright HII-regions (Law, Belfiore, et al. 2022). On the other hand, gravitational instabilities play a crucial role. Thermal pressure, resulting from the temperature of the gas and dust in a cloud, tends to prevent the cloud from collapsing. Gravitational instabilities, however, can overcome this pressure. When a region within the cloud becomes denser than its surroundings, its self-gravity can dominate and lead to collapse which results in star formation, whereas these stars then inject feedback.

Also, gravitational interactions play a crucial role in shaping the structure and dynamics of astrophysical systems, and they can impact the intrinsic velocity dispersion of the Hα line in several ways: The overall gravitational field, can induce

motions and cause line broadening. Interactions between stars, galaxy mergers, galaxy interactions, cluster mergers, tidal interactions, and gravitational potential gradients can also induce motions and turbulence (M. R. Varidel, Croom, Lewis, Fisher, et al. 2020, Law, Steidel, et al. 2007, Yu et al. 2021, Krumholz et al. 2018).

1.4 Lyα radiation

After we introduced the observational accessible quantities and the physical parameters, we will now discuss the theoretical background that can be addressed and studied by these quantities and parameters. In this section we start by looking in detail into the Lyα radiation. In Section 1.2.2 we introduced the Lyα luminosity. Here we will look in detail in the production mechanism of Lyα photons.

Lyα radiation plays a crucial role e.g. in the study of epoch of reionization and the phase transition of the Universe from neutral to ionized. By observing Lyα at different redshifts, the transition from a neutral universe to a ionized universe can be traced, because Lyα is scattered at neutral hydrogen.

Lyα originates from the transition of an electron in a hydrogen atom from the first excited state to the ground state (2p to 1s). Due to the energy difference between these states, a photon with a wavelength of $\lambda_{\mathrm{Ly}\alpha} = 1215.67$ Å is emitted (Chapter 1.2 in Dijkstra 2019, Edmund Christian Herenz 2016).

The probability of a transition from an excited state to a lower state, accompanied by the emission of a photon, is determined by the Einstein coefficients. These coefficients are calculated through overlap integrals and represent the likelihood of the transition occurring. Quantum mechanics provides insights into the selection rules governing permissible transitions. The selection rule states that the difference in the orbital quantum number Δl must be ± 1. This selection rule ensures the conservation of angular momentum during the transition, with the emitted photon carrying an angular momentum of $\hbar$. The excited state typically has a lifetime in the order of nanoseconds. For example, the 2p state has a lifetime of 1.6 nanoseconds (Verolaĭnen and Nikolaich 1982). Higher excited states have a bit longer lifetimes in the hydrogen atom (see Table 1 in Verolaĭnen and Nikolaich 1982). The lifetime τ_i is related to the Einstein coefficient A_{ik} by $\tau_i = 1/A_{ik}$. The recombination process results in the emission of a cascade of photons with characteristic energies. In quantum mechanics, only the ground state 1s is stable, and the electron sequentially decays from one state to another until it reaches the ground state (Chapter 1.2 in Dijkstra 2019).

When the recombination process of hydrogen in the interstellar medium balances with ionization, a state known as photoionization equilibrium is established.

The recombination series are named after spectroscopists, who first observed them, with the lowest five levels known as the n_1 Lyman, n_2 Balmer (H), n_3 Paschen, n_4 Brackett and n_5 Pfund series. The transitions $n_2 - n_1$ are labeld by the Greek letters α, β, γ, δ, ... The Balmer series and the Paschen series is accessible in the optical by ground-based observations. The higher series are observed in the infrared and Lyman is observed in the UV with space-based telescopes.

Among these series, Lyα radiation is particularly significant due to its high intensity and the high probability that a recombination of a proton and electron end up in producing a Lyα photon. When an electron is captured by a proton, the result is an exited hydrogen atom. This excited atom decays via intermediate states into the ground state. We are interested in the probability that a recombination of an electron and proton ends up emitting a Lyα photon

$$P(n, l \rightarrow \mathrm{Ly}\alpha) = \sum_{n',l'} P(n, l \rightarrow n', l') P(n', l' \rightarrow \mathrm{Ly}\alpha). \tag{1.13}$$

This probability for a decay can be calculated by the Einstein coefficients by

$$P(n, l \rightarrow n', l') = \frac{A_{n,l,n',l'}}{\sum_{n'',l''} A_{n,l,n'',l''}}. \tag{1.14}$$

If we now sum over all quantum states, which can produce a Lyα photon during the radiative cascade to the 1s state, and weigh them by the probability that a fresh recombined electron and proton is in this quantum mechanic state, we can calculate the probability that a recombination event results in the production of a Lyα photon. To calculate this probability, two commonly scenarios of the medium, in which the recombination takes place, are used in the context of astrophysic plasmas: Case A describes a recombination that takes place in a for all photons optically thin medium (sum in Equations 1.13 and 1.14 start from $n = 1$ in case A). The optical depth is $\tau = 0$ for the Lyman series. The optical depth represents the measure of how much light is absorbed or scattered as it passes through a medium. It quantifies the degree of opacity of that medium to electromagnetic radiation. Case B recombination assumes a medium that is optically thick for all Lyman series photons ($\tau = \infty$ for Lyman series, sum in Equations 1.13 and 1.14 start from $n = 2$ in case B). The scattering cross-section depends on the photon energy and therefore, higher Lyman series photons are more likely to be scattered. The higher order Lyman photons get re-absorbed, cascade and get re-emitted. Therefore, it becomes more likely that the initial recombination of a proton and electron results in emitting a Lyα photon. For case B recombination, we get a probability of $P(\mathrm{Ly}\alpha) = 0.68$ at $T = 10^4$ K (case A: $P(\mathrm{Ly}\alpha) = 0.41$). Thus, assuming case B, around 2/3 of all recombination processes of an electron and proton produce a Lyα

photon. At gas densities, which we find in most astrophysical plasmas, hydrogen populates the ground state and then case B represents an realistic scenario that the astrophysic gas efficiently re-absorbs higher order Lyman series and ionizing photons (chapter 1.2.3, 1.2.4 and 1.3.2 in Dijkstra 2019, Edmund Christian Herenz 2016).

Lyα radiation is a prominent recombination line with a high contrast to the continuum emission, and its intrinsic intensity is proportional to the SFR of a galaxy. As Lyα radiation is produced around young, hot and massive stars, knowing the IMF allows us to convert the luminosity into an estimate of how many massive stars are present and from that to the SFR. By assuming an IMF and an intrinsic Lyα/Hα ratio of 8.7, the Lyα luminosity can be expressed as $L_{\mathrm{Ly}\alpha}[\mathrm{ergs, s^{-1}}] = 1.10 \times 10^{42} \times \mathrm{SFR}[\mathrm{M_\odot yr^{-1}}]$, because the Ly$\alpha$ emission is directly proportional to the SFR by ignoring the effects of radiative transfer here (see also Section 1.3.2). The more stars being born, the more Lyα photons are produced and the higher is the intrinsic Lyα luminosity. For example, a galaxy at redshift $z = 6$ with an SFR of 5 $\mathrm{M_\odot yr^{-1}}$ would emit Lyα radiation with an observed flux of approximately 10^{-17} erg $\mathrm{s^{-1}}$ $\mathrm{cm^{-2}}$ by assuming ΛCDM cosmology with $H_0 = 70$ $\mathrm{kms^{-1}Mp^{-1}}$, $\Omega_m = 0.3$ and $\Omega_\Lambda = 0.7$. Such emission can be detected by 8-10 m telescopes in a short observation time with a high signal-to-noise ratio (chapter 4.1.1 in Hayes 2019).

However, the resonant nature of the Lyα line poses challenges to its observation, which will be discussed in the following section, when introducing the Lyα radiative transfer.

1.5 Lyα radiative transfer

In the previous section, we discussed the production of Lyα radiation. Now, the photons have to escape the galaxies ISM and then the CGM (and have to travel trough the universe) to be observed by our telescopes. This radiative transfer is not straight forward, as the Lyα transition is a resonant transition in the hydrogen atom. We will discuss in detail this Lyα radiative transfer.

The radiative transfer of Lyα photons leads to a spatial and spectral diffusion of the galaxies intrinsic Lyα radiation field. Explaining the spatial diffusion, photons undergo a random walk through numerous scattering events until they reach regions of low neutral hydrogen column density, allowing them to escape the galaxy. The increased path length of the scattering process makes Lyα photons susceptible to the absorption by dust grains. Frequency diffusion arises from the energy conservation requirement during absorption and re-emission by hydrogen atoms. An atom that

absorbs a Lyα photon must re-emit a Lyα photon with the same frequency in its rest frame. However, due to the motion of the atom relative to an observer, the frequency of the emitted Lyα photon can be shifted (see also Figure 3.1 in Laursen 2010). In terms of the absorption cross-section, this frequency diffusion corresponds to the photon moving into the wings of the Voigt profile[7], where the absorption cross-section is lower. This increases the likelihood of Lyα photons escaping from galaxies (chapter 1.5.4 in Dijkstra 2019, Edmund Christian Herenz 2016). Both processes, the spatial diffusion and the spectral diffusion occur simultaneously.

The resonant nature of the Lyα line poses challenges to its observation. The optical depth is proportional to the inverse square root of temperature ($T^{-1/2}$) and the hydrogen column density (N_{HI}). The hydrogen column density quantifies the amount of hydrogen atoms along the line of sight and indicates how much hydrogen lies in the path of observation. Therefore, the optical depth τ can be calculated by $\tau = N_{\mathrm{HI}} \cdot \sigma$, where σ is the absorption cross section of neutral hydrogen. In the Milky Way (MW), arbitrary sight lines looking from the sun outwards of the MW disk often have hydrogen column densities above 10^{20} cm^{-2}, resulting in optical depths of the order of 10^7. For observing Lyα radiations, such high hydrogen column densities would make it unlikely to observe the Lyα radiation (chapter 4.1 in Hayes 2019).

Figure 12 in Smith et al. (2022) shows the escaping surface brightness for Hα and Lyα for a modeled disc-like galaxy. It shows the physical connection between the different stages in the radiative transfer. Ionizing photons are primarily emitted from highly clustered young stellar regions. Hα photons reveal the internal structure of the production of ionizing radiation, Lyα accounts for resonant scattering and shows a more spatially diffuse image.

Even, if galaxies have a high intrinsic Lyα radiation field, they may not emit Lyα radiation due to increased path length and absorption by dust. Dust grains can reflect and absorb Lyα photons, preventing their escape from the galaxy. This effect can reduce the observed Lyα flux and alter its spectral properties (chapter 4.1 in Hayes 2019).

Overall, understanding the behavior and escape of Lyα radiation is crucial for interpreting observations and unraveling the properties of galaxies at different cosmic epochs. Various models have been developed to describe the radiative transfer of Lyα, such as the shell model proposed by Verhamme et al. (2012) or before that in simpler scenarios with homogeneous slabs. While these models can

[7] The Lyα absorption cross-section of a collection of moving atoms is described by a Voigt profile, which is a convolution of a Lorentzian with a Gaussian. This accounts for natural Lorentz broadening and Doppler broadening caused by random motions of neutral hydrogen atoms in the gas (chapter 1.2.3 and 1.2.4 in Dijkstra 2019, Edmund Christian Herenz 2016).

reproduce the shape of the Lyman α emission line, they fail to explain why certain galaxies exhibit strong Lyman α emission while others do not, as the Lyα radiative transfer is highly sensitive to gas distribution and gas kinematics.

1.6 How to understand the Lyα observations?

We have now an overview on observational methods and a theoretical background in Lyα radiation and Lyα radiative transfer. However, why do we exactly care about hydrogen and its transitions, especially Lyα, so much? And why is studying the Hα kinematics important and interesting in comparison to other observational efforts?

Hydrogen, the most abundant element in our Universe, constitutes 76% of the baryonic mass and contributes to 4.6% of the Universe's energy density (chapter 1.2 in Dijkstra 2019). The evolution of our Universe shows a significant transformation in the intergalactic medium (IGM) from a state of complete neutrality to full ionization, known as the Epoche of Reionization (EoR). During this phase, ionized hydrogen (HII) bubbles formed in overdense regions, separated by the IGM. Over time, as the number of star-forming galaxies within these HII bubbles increased, the size of the ionized regions expanded, eventually leading to their overlap (chapter 1.9 in Dijkstra 2019, Laursen 2010). Lyα from galaxies within a neutral universe will not be observable, Lyα from galaxies in the reionised-ionized universe will be observable. Therefore, we can study the temporal evolution of this phase transition.

However, to study the IGM and the scattering of Lyα, we have to know the Lyα output of the galaxies. To address the question of what makes a galaxy a Lyα emitter, we investigate the role of ionized gas kinematics in the Lyman α radiative transfer. We study the ionized gas kinematics through the Hα line. The Lyα radiation originates from the vicinity of hot O- and B-stars, where these massive, hot and luminous stars ionize the interstellar medium. With Hα we can not trace the scattering medium of the Lyα photons. However we do can trace the regions, where Lyα photons are produced and have through Hα indirectly an access to the intrinsic Lyα radiation field.

We investigate the relationship between kinematic parameters and Lyα observables, exploring whether turbulent ionized gas kinematics can shift absorbing and emitting material out of resonance, thereby facilitating an easier escape of Lyα radiation.

But before looking in detail into the ionized gas kinematics, let us first introduce our galaxy sample in the next section.

1.7 Our sample

LAE candidates are usually selected in ground-based narrowband imaging surveys. Sometimes follow-up spectroscopy is taken to confirm the LAE candidates (Ning et al. 2022, Hu et al. 2010, Rhoads, Hibon, et al. 2012, Rhoads, Xu, et al. 2004, Kashikawa et al. 2006). Nowadays, blind searches for emission line sources in integral field spectrograph (IFS) datacubes can provide a catalog of spectroscopic confirmed Lyα emitters directly (Edmund Christian Herenz et al. 2019).

Our study focuses on the Lyman α Reference Sample (LARS) and extended Lyman α Reference Sample (eLARS). LARS contains 14 galaxies with z between 0.028 and 0.181 (Östlin et al. 2014). The sample was extended with 28 galaxies for eLARS with z between 0.029 and 0.051 (Melinder et al. 2023). In total, we have a sample of 42 galaxies.

The main astrophysical selection criteria for the LARS sample were star formation rate and stellar age. First, it is based on the far-UV (FUV, $\lambda \sim 1500$ Å) luminosity and second is based on the Hα equivalent width. The Hα line fluxes were measured in SDSS apertures. The Hα EW cutoff is at 100 Å. This biases towards galaxies with young stellar population that produce Lyα photons. This ensures that the galaxies are actively star forming and have a significant production of Lyα photons, whether or not the Lyα photons escape. This selection criterium also biases towards high specific star formation rates, which is SFR divided by galaxy mass, favoring irregular and merging systems and not favoring high mass galaxies. For the eLARS sample the Hα EW criterium was lowered to 40 Å. This includes galaxies with lower specific star formation rate and most of these galaxies are fainter in FUV. Compared to the 14 LARS galaxies, in eLARS are more continuously star forming spiral galaxies included. It was tried to cover a range of FUV luminosities going down to $\log\left(L_{\mathrm{FUV}}/L_{\odot}\right) = 9.0$. The FUV luminosities overlap with those of high-z LAEs and Lyman break galaxies, which makes it a valid comparison sample to high-z star forming galaxies (Östlin et al. 2014, Melinder et al. 2023).

With these selection cirteria galaxies from the Sloan Digital Sky Survey (SDSS, DR6 for LARS and DR8 for eLARS) were selected according to their Hα EW. These selected galaxies were matched to the GALEX (DR3) catalog for the FUV fluxes of the galaxies.

Galaxies with an active galactic nucleus (AGN) emit large amounts of energy across the wavelengths from the compact center regions. This luminosity does not origin from stars. AGN galaxies were excluded by rejecting galaxies with Hα line width (FWHM) larger than 300 $\mathrm{km\,s^{-1}}$ and with emission line ratio diagnostics from SDSS spectra ([OIII]/Hβ and [NII]/Hα). This is done to have the focus on systems that are dominated by star formation.

Foreground extinction describes the absorption of photons due to the dust in our Galaxy. The galaxies were required to have Milky Way extinctions of less than 0.03 in the sample (Östlin et al. 2014, Melinder et al. 2023).

The redshift of our sample ranges from 0.026 to 0.236. We have SFRs in Hα between 0.15 and 67.01 $M_{\odot}$/yr, stellar masses between 0.35 and 15.24 $10^{10} M_{\odot}$ and ages between 3.29 and 87.91 Myr. The galaxies have a broad variety of Lyα properties. The Lyα escape fraction ranges up to 0.30. We have Lyα luminosities up to $5.56 \cdot 10^{42}$ erg s^{-1} cm^{-2} and Lyα equivalent width up to 56.66 Å. The sample has a large range in Lyα observables and other galaxy properties and thus is optimal to study Lyα processes (Östlin et al. 2014, Melinder et al. 2023, E. C. Herenz et al. 2016, Runnholm et al. 2020).

The LARS and eLARS sample is the only sample with the necessary ancillary data for performing the study that we perform in this thesis. For all galaxies we have eight-band photometry with the HST (five broad bands and three narrowbands), UV spectroscopy with the Cosmic Origins Spectrograph (COS) on the HST, optical Slogan Digital Sky Survey spectra (SDSS), 21 cm radio observations with the Very Large Array in D and C configuration and IFU data in the optical wavelength range from the Potsdam Multi aperture Spectrophotometer (PMAS) at Calar Alto 3.5 m telescope (Roth et al. 2005). For the first time we present and use the PMAS data of the eLARS galaxies in this thesis.

As we have HST and PMAS data, we want to know which field of view of the HST observations is covered by the PMAS observation. In Appendix A.1 we show images to get an overview of our sample. We show the PMAS location on the HST data for all eLARS galaxies, as well as HST images and PMAS maps.

2 Observations and data reduction

This chapter describes the observations and data reduction for the LARS and eLARS sample and is documented for completeness here. Significant parts of the work presented in this chapter were performed by my supervisor E.C. Herenz and the team.

2.1 Observations

We obtained integral field spectroscopic observations of the 14 LARS and 28 eLARS galaxies with PMAS at the Calar Alto 3.5m telescope (Roth et al. 2005). We used the $16'' \times 16''$ lens array configuration for most of the galaxies, where each of the 256 spectral pixels is $1'' \times 1''$ on sky. A few LARS galaxies, listed in Table 2.1, are observed in the $8'' \times 8''$ lens array configuration. A log of the observations is presented in Table 2.1. The observing conditions were not always optimal, but by visually monitoring the incoming read outs of the PMAS 4k×4k CCD after each exposure, we ensured that the signal-to-noise ratio in the targeted Hα lines would be sufficiently high for our analysis. Within this field of view the bulk of the high surface-brightness Hα emission of the galaxies in the sample could be covered with a single pointing; exceptions are LARS 9 and 13 and eLARS 3, 5, and 27, which required two pointings each. Due to strong ambient temperature fluctuations, the spectrograph was not always optimally focused, especially during the 2016 run lower values of resolving power R are measured (see Sect. 3.3 in E. C. Herenz et al. 2016 for the procedure to measure R). The resolving power is the ability to separate different wavelengths, particularly in the context of resolving closely spaced emission lines. It is controlled by the grating in the spectrograph. We used the backward-blazed R1200 grating, which delivers a nominal resolving power from $R \sim 5000$ to $R \sim 8000$ within the targeted wavelength ranges[1]. Mathematically, it can be expressed as $R = \lambda/\Delta\lambda$ as the ratio of the wavelength λ to the difference in wavelength $\Delta\lambda$ that can be resolved by the instrument. A higher resolving power means that the instrument can distinguish smaller differences in wavelength.

[1] Values taken from the PMAS online grating tables, available at http://www.caha.es/pmas/PMAS_COOKBOOK/TABLES/pmas_gratings.html#4K_1200_1BW

Fortunately, the galaxy's Hα profiles are always resolved significantly, also in the slightly sub-optimal $R \sim 3000$ datasets. The Hα profiles of LARS 09, 13, eLARS 7 and 24 show double component profiles. For example in eLARS 7 the double component in the center part is a result of the current merging of two galaxies. Also the spread in redshift of the original LARS sample required us to use different grating angles to have the Hα line centered on the detector, whereas eLARS is way more spread in redshift.

2.2 Data reduction

We reduced the observational raw data with the `p3d`[2] pipeline (C. Sandin et al. 2010; Christer Sandin et al. 2012). `p3d` covers all basic steps that we need for reducing our data: bias subtraction, flat fielding, cosmic ray removal, tracing and extraction of the spectra, correction of differential atmospheric refraction and co-addition of exposures (E. C. Herenz et al. 2016). The reduction strategy is already detailed in Sect. 3 of E. C. Herenz et al. (2016). The LARS galaxies are flux calibrated and sky subtracted. Different to E. C. Herenz et al. (2016), we can not flux calibrate the data here, since the relevant standard star observations were not taken. Also it does not make much sense to flux calibrate data observed through cloud cover and for our kinematic analysis an absolute flux calibration is not needed. For the same reason we also do not subtract telluric emission from the extracted spectra, except for galaxies where the redshifted Hα line is in close proximity or even overlapping with a sky line (eLARS 2, and eLARS 22 to 28). The data for targets, where open-shutter time was accumulated over multiple exposures, were stacked via simple addition. The resulting data products from the reduction pipeline are a row-stacked representation of the 256 spaxels for each science target exposure in analogue-digital-units. `p3d` also propagates errors through each step of the reduction chain and stores them in a separate row-stacked spectra array. All arrays were then reformatted to 3D cubes using the lookup table that comes with `p3d`. The spectral range of the datacubes covers $\sim 6100\,\text{Å}$ to $7400\,\text{Å}$, and the spectral sampling is $0.46\,\text{Å}$ per wavelength bin.

[2]Version 2.6.4 obtained from `https://p3d.sourceforge.io/`.

Table 2.1: PMAS observations of LARS and eLARS galaxies - overview.

ID	Night	$t_{\rm obs}$ [s]	R	Seeing FWHM [″]	FoV arcsec^2	Clouds
LARS01	12/03/16	2×1800	5306	1.8	16×16	clear
LARS02	12/03/15	2×1800	5205	1.1	16×16	thin
LARS03	12/03/14	3×1800	5362	1.1	16×16	clear
LARS04	12/03/13	3×1800	5883	1.0	16×16	clear
LARS05	12/03/14	3×1800	5886	1.3	8×8	clear
LARS06	12/03/13	2×1800	5865	1.0	16×16	clear
LARS07	12/03/16	3×900	3925	1.3	16×16	thin
LARS08	12/03/15	3×1800	4415	0.9	16×16	thin
LARS09A	12/03/12	3×1800	5561	0.9	16×16	clear
LARS09B	12/03/14	3×1800	4772	0.9	16×16	thin
LARS10	12/03/14	2×1800	5438	1.5	8×8	clear
LARS11	12/03/15	3×1800	4593	1.0	16×16	thin
LARS12	12/03/14	3×1800	6756	0.9	8×8	clear
LARS13A	11/10/02	4×900	7766	1.2	8×8	clear
LARS13B	11/10/02	4×900	7771	1.2	8×8	clear
LARS14	12/03/13	2×1800	7718	0.9	8×8	clear
ELARS01	16/03/31	1800	3890	2.0	16×16	thick
ELARS02	16/04/02	1800	4348	2.2	16×16	clear
ELARS03A	16/04/01	1800	2975	2.2	16×16	clear
ELARS03B	16/04/01	1800	2931	2.2	16×16	clear
ELARS04	16/04/02	900	2727	2.3	16×16	clear
ELARS05A	16/04/01	1800	3580	2.3	16×16	clear
ELARS05B	16/04/01	1800	3395	2.3	16×16	clear
ELARS06	17/03/26	2×1800	6262	2.0	16×16	thin
ELARS07	16/03/30	3×900	3572	0.8	16×16	clear
ELARS08	16/04/02	1800	3997	1.5	16×16	thick
ELARS09	16/04/03	1800	3831	1.3	16×16	clear
ELARS10	16/04/01	1800	3092	2.3	16×16	thin
ELARS11	17/03/22	2×1800	6174	2.2	16×16	clear
ELARS12	17/03/25	2×1800	5400	1.7	16×16	clear
ELARS13	16/03/30	3×900	3591	1.3	16×16	clear
ELARS14	16/03/30	2×1800	3680	1.2	16×16	clear
ELARS15	17/03/25	2×1800	5732	1.4	16×16	clear
ELARS16	16/04/03	2×1800	4398	1.4	16×16	thin
ELARS17	16/04/03	2×900	5494	1.4	16×16	thick
ELARS18	16/04/03	1800	4361	1.2	16×16	thin
ELARS19	16/03/31	2×1800	3843	1.3	16×16	thin
ELARS20	17/03/26	2×1800	6469	1.9	16×16	thin
ELARS21	17/03/24	1800	4475	2.2	16×16	clear
ELARS22	16/04/01	1800	2677	1.7	16×16	clear
ELARS23	16/04/02	1800	2626	1.7	16×16	clear
ELARS24	16/04/02	1800	2951	2.1	16×16	clear
ELARS25	17/03/26	3×1800	6375	2.1	16×16	thin
ELARS26A	17/03/25	2×1800	5019	1.7	16×16	clear
ELARS26B	17/03/25	2×1800	5301	1.8	16×16	clear
ELARS27	17/03/25	2×1800	5528	1.4	16×16	clear
ELARS28	17/03/22	2×1800	5960	1.1	16×16	clear

2.3 Line-of-sight velocity fields and velocity dispersion maps

We use these cuboids from PMAS for our analysis. They contain 256 spectra for each galaxy in the wavelengthrange of the Hα line. As already stated in Section 1.3.3, we use the Hα line as a tracer of the warm ionized gas. From the spectra we extract the line-of-sight velocity $v_{\mathrm{LOS,i}}$ and the $\sigma_{\mathrm{obs,i}}$ to gain 2D maps with 16 to 16 spaxels.

Our spectra are contaminated and we want to remove the telluric- and stellar continuum to end up with only the emission lines from the galaxy. Therefore, we subtract a running median of 151 wavelength bins width from each spaxel. Then we modell the Hα line of each spaxel by simple single Gaussian

$$f_i(\lambda \,|\, A_i, \lambda_{0,i}, \sigma_i) = A_i \cdot \exp\left(- \left[\frac{(\lambda - \lambda_{0,i})}{\sigma_i} \right]^2 \right), \tag{2.1}$$

where A_i, $\lambda_{0,i}$ and σ_i are the best-fit parameter for each spaxel. The observed line-of-sight velocity for each spaxel can then be calculated by

$$v_{\mathrm{LOS,i}} = c \cdot \frac{(\lambda_{0,i} - \bar{\lambda})}{\lambda_{0,i}}, \tag{2.2}$$

where $\bar{\lambda}$ is the average of the fitted $\lambda_{0,i}$ for a galaxy, and c is the spead of light. The line-of-sight velocity dispersion for each spaxel can be calculated by

$$\sigma_{\mathrm{obs,i}} = c \sqrt{\frac{(\sigma_i^2 - \sigma_{\mathrm{LSF,i}}^2)}{\lambda_{0,i}^2}}, \tag{2.3}$$

where the dispersion from the line spread function is

$$\sigma_{\mathrm{LSF,i}} = \frac{\mathrm{FWHM}_{\mathrm{LSF,i}}}{2\sqrt{2 \ln 2}} \tag{2.4}$$

and is connected to the resolving power of each fiber by

$$R_i = \frac{\lambda_{0,i}}{\mathrm{FWHM}_{\mathrm{LSF,i}}}. \tag{2.5}$$

At PMAS, the resolving power R varies for every fiber. A fiber module couples the light from the IFU to the spectrograph. Through to mechanical motions of the telescope and through different curvatures of the individual fibers, we have

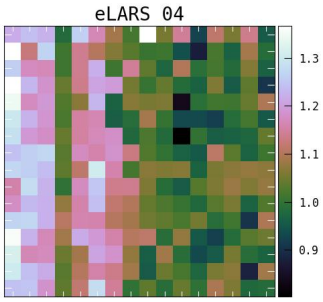

Figure 2.1: Resolving power map in Å for eLARS04.

a varying resolving power in each fiber. To get the R_i of each fiber, we measure $\sigma_{\mathrm{LSF,i}}$ technically. First, we extract the HgNe arc-lamp exposures that flanked each observation. Then, we fit Gaussians to the Ne lines of the lamp, which are on the left and right of the galaxies Hα lines (6717 Å and 6929 Å) for each spaxel. Lastly, we interpolate linearly between these so determined widths to the wavelength $\lambda_{0,i}$ of the galaxies Hα emission. In Table 2.1 we list the averaged resolving power for each galaxy. In Figure 2.1 we show the resolving power map for eLARS04 as an example.

To estimate the uncertainties in σ and v_{LOS}, we employ a Monte Carlo technique. This involves perturbing the spectrum using the noise from the noise cube and fitting the perturbed spectrum with an one-dimensional Gaussian function. The standard deviation, obtained from multiple iterations, characterizes the distribution of the fitting results.

We also define the signal-to-noise ratio for each spaxel by

$$S/N = A\sigma/(\Delta A \Delta\sigma). \tag{2.6}$$

For further analysis, we only use spaxels with $S/N \geq 6$, because they provide us with reliable fits over the overall sample.

As shown by Landman, Roussel-Dupre, and Tanigawa 1982, the statistical uncertainties $\Delta\sigma_0$ and Δv_{los} from least-square fitting of Gaussians to noisy intrinsic Gaussian profiles are expected to be related to S/N. Figure 2.2 illustrates the relationship between $S/N_{\mathrm{H}\alpha}$ and the uncertainties in $\Delta\sigma$ and Δv_{LOS}. Both quantities follow the scaling laws for Gaussian fitting of noisy emission lines, with the uncertainties scaling inversely with the S/N:

$$\Delta v_{\mathrm{LOS}} \sim \Delta\sigma \sim \sqrt{\sigma}(S/N_{\mathrm{H}\alpha})^{-1} \tag{2.7}$$

(Landman, Roussel-Dupre, and Tanigawa 1982, Lenz and Ayres 1992, E. C. Herenz et al. 2016). We test whether these scaling laws hold for our data by linear regression

to the relations $\Delta v_{\rm los} = A_{v_{\rm los}} \times \big(1/2 \times \log_{10}(\sigma_0[\mathrm{km\,s^{-1}}]) - \log_{10}(S/N)\big) + B_{v_{\rm los}}$ and $\Delta\sigma_0 = A_{\sigma_0} \times \big(1/2 \times \log_{10}(\sigma_0[\mathrm{km\,s^{-1}}]) - \log_{10}(S/N)\big) + B_{\sigma_0}$ to the results from all 3473 reliable fits from all eLARS galaxies. The linear regressions result in $A_{\sigma_0} = 1.02$ and $B_{\sigma_0} = 1.00$ and $A_{v_{\rm los}} = 0.99$ and $B_{v_{\rm los}} = 0.99$. Thus they are in near perfect agreement with the expected relations. This scaling relationship is also true for the LARS galaxies (Figure 4 in E. C. Herenz et al. 2016[3]). This also shows that the Gaussian parameterization is adequate for the Hα emission lines of most of the PMAS spaxels throughout the LARS and eLARS sample. For reference, at a minimum S/N of 6, the eLARS galaxies exhibit typical errors of around 10 kms^{-1}.

In a last step, we visually check the adequateness of the Gaussian profiles of each of the 256 fits for each galaxy. For most spaxels the Hα line is traced well by the single Gaussian. We have four exceptions: LARS09, LARS13, eLARS07 and eLARS24. Some spaxels show clear Hα double component profiles, which lead to too high σ_0 values in the fits. Due to this reason, we exclude these four galaxies form all statistical analyses involving the velocity dispersion.

[3] $\Delta\sigma$ needs to be converted to $\Delta v_{\rm FWHM}$ using a factor of 2.355

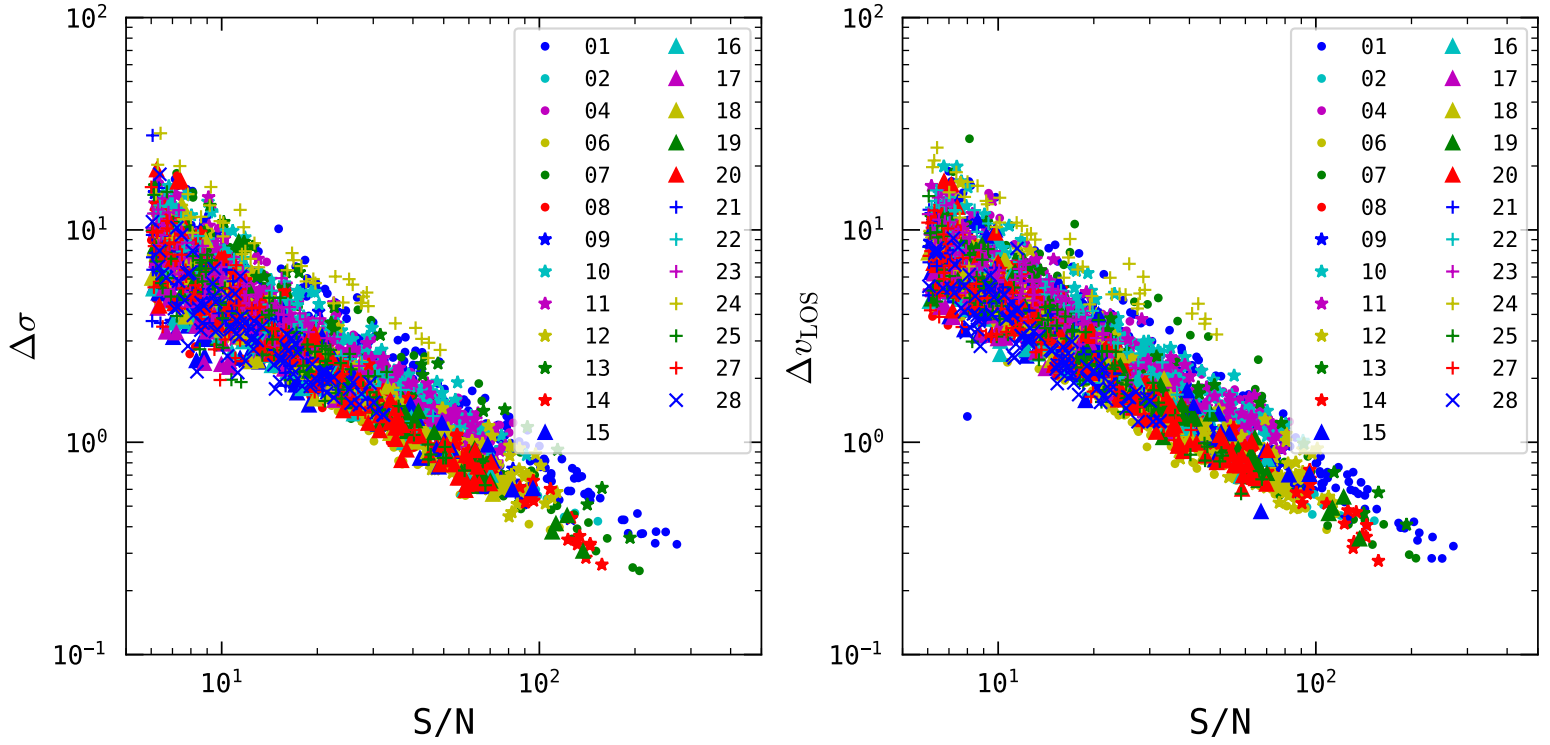

Figure 2.2: Uncertainties of derived velocity dispersions (left) and line-of-sight velocities (right) in $\mathrm{km\,s^{-1}}$ for Gaussian profile fits to the Hα line versus S/N for all eLARS galaxies. Each symbol in the figure represents the uncertainties associated with all spaxels within a particular galaxy, as indicated in the legend.

3 Characterizing the ionized gas velocity fields qualitatively and quantitatively

As already discussed in the introduction, we are interested in how the ionized gas kinematics influence the Lyα observables. We study the kinematics of the ionized gas in the LARS and eLARS samples in a qualitative (Section 3.1) and quantitative manner (Section 3.2), and we relate our kinematics to the Lyα observables (Chapter 4).

3.1 Qualitative categorization of the integrated ionized gas kinematics

We aim to understand which conditions influence the difference among galaxies in Lyα equivalent width, Lyα escape fraction and Lyα luminosity as outlined in the introduction. We may assume that ISM conditions in galaxies with complex velocity fields are favorable for Lyα escape. For example, irregular and merging systems are often characterized by high sSFRs. This can lead to spatially concentrated injection of momentum and energy from stellar feedback processes. Winds and outflows then may lead to a more effective clearing of escape channels for Lyα (and also Lyman continuum) radiation. The combined LARS and eLARS sample allows for a first statistical exploration of such a scenario. First of all, we characterize the velocity fields qualitatively. Subsequently, we investigate, whether Lyα observables from different qualitative kinematic categories show differences or can statistically origin from the same underlying Lyα observable distribution.

We use a classification scheme from the literature to divide the sample into three groups characterized by the appearance of the galaxy's velocity field (Flores et al. 2006, Sect. 3.3 in Glazebrook 2013, E. C. Herenz et al. 2016):

- **Rotating Disks (RD):** The velocity field appears as an a regular symmetric dipolar pattern and has a steep gradient in the center. The optical major

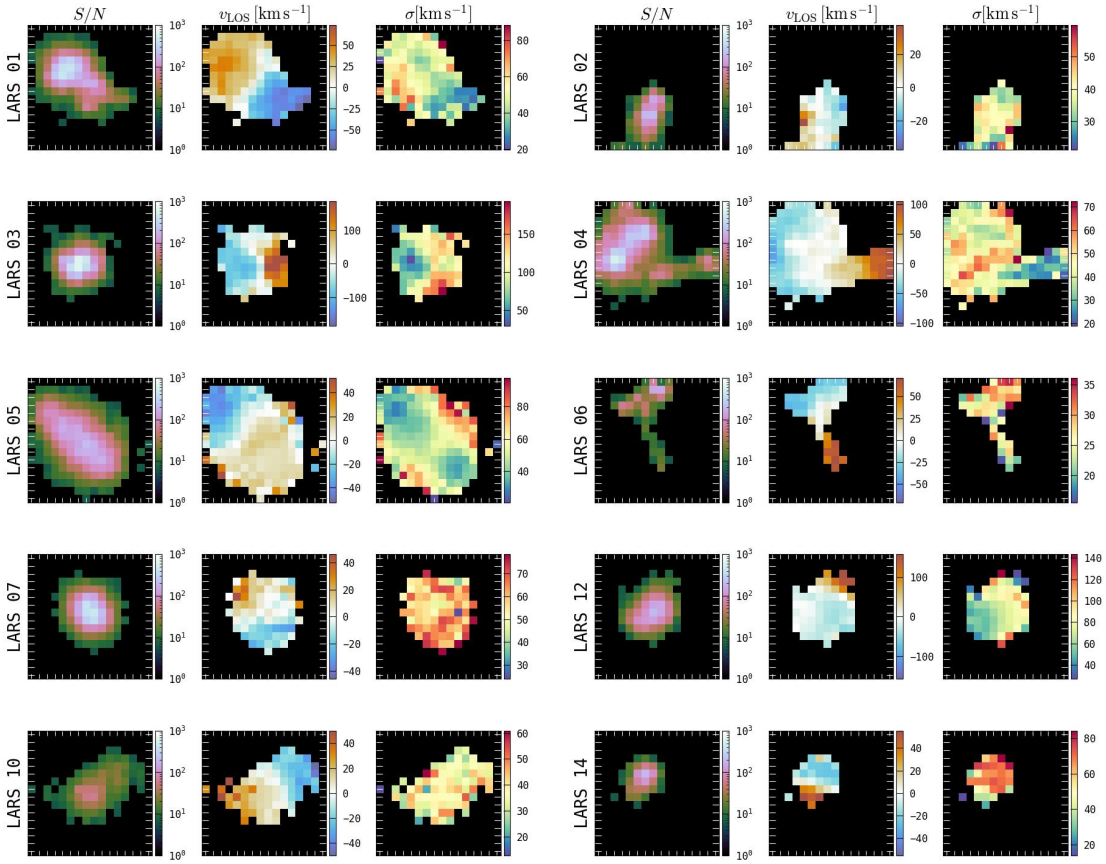

(a) LARS PRs **(b)** LARS CKs

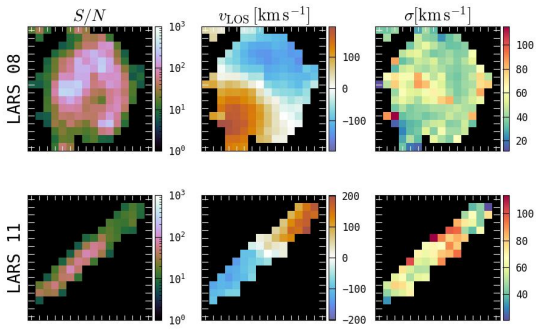

(c) LARS RDs

Figure 3.1: S/N (first column), line of sight velocity (second column) and velocity dispersion (column) for the LARS galaxies, sorted by the visual kinematic class.

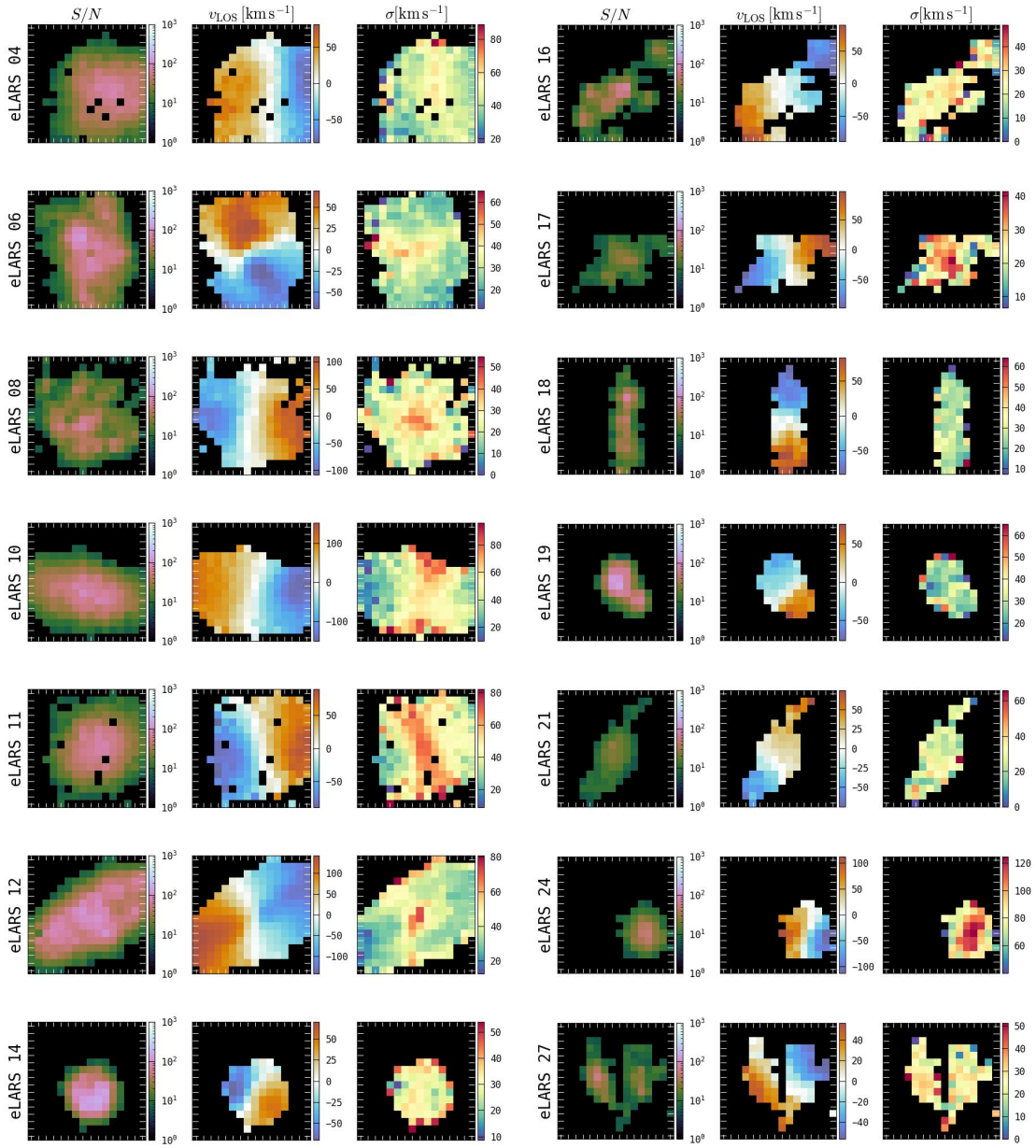

(a) eLARS RDs **(b)** eLARS RDs

Figure 3.1 continued for the eLARS galaxies.

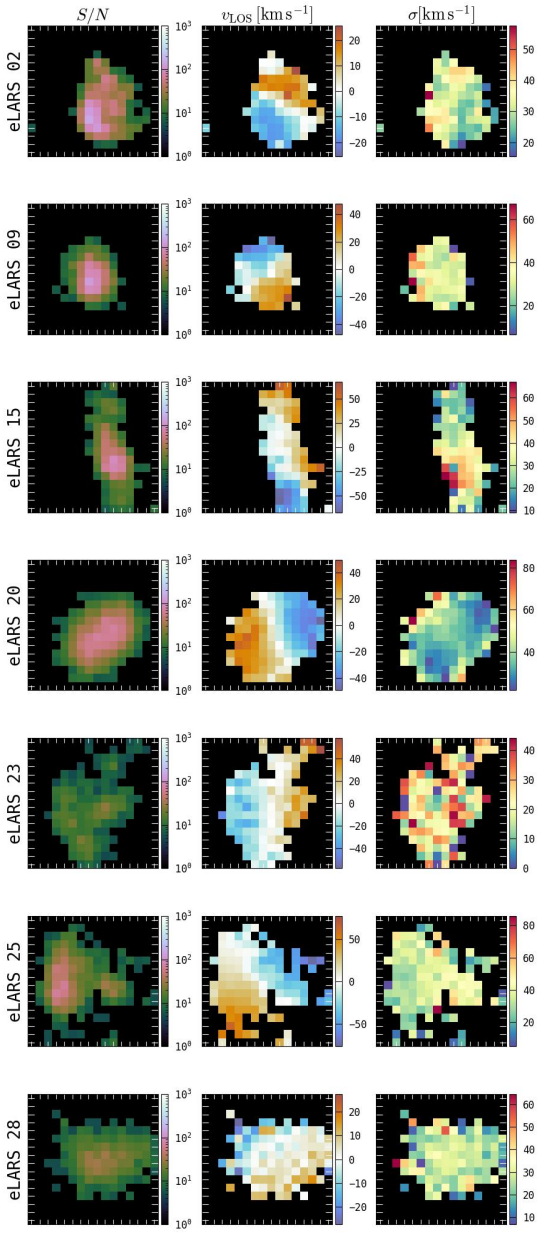

(a) eLARS PRs

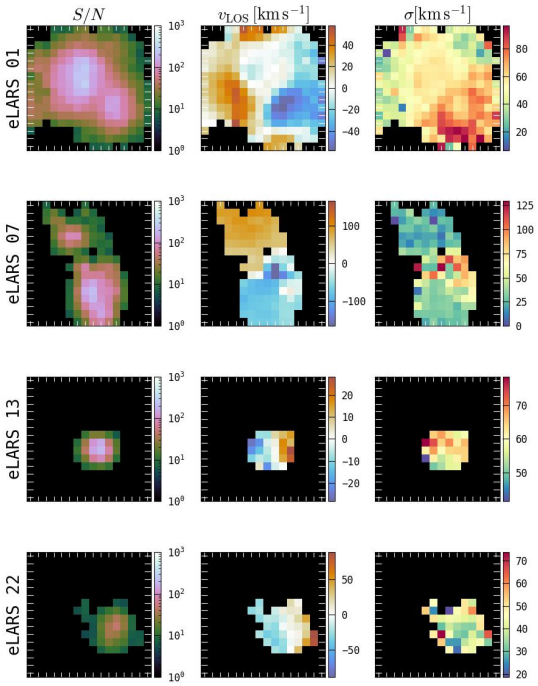

(b) eLARS CKs

Figure 3.1 continued for the eLARS galaxies.

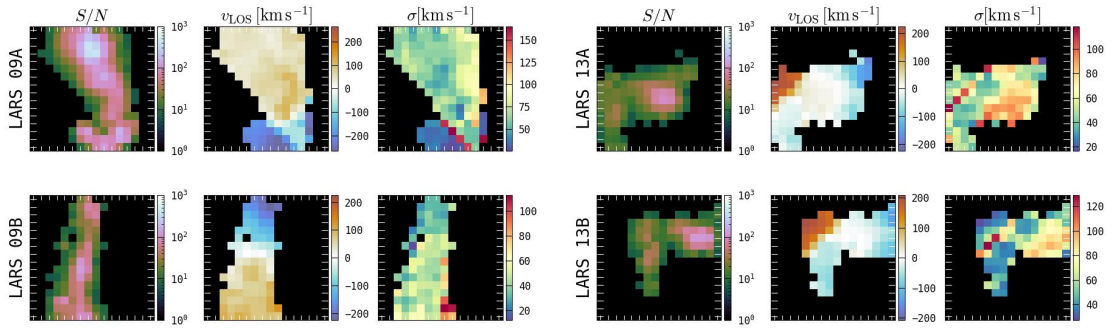

Figure 3.1 continued for the LARS galaxies with two pointings. For LARS09 we use both data cubes, because they have almost no overlap. For LARS13 the two pointings overlap over a large area. We use LARS13A for our analysis, because it has more spaxels than LARS13B and has almost the same field of view as LARS13A.

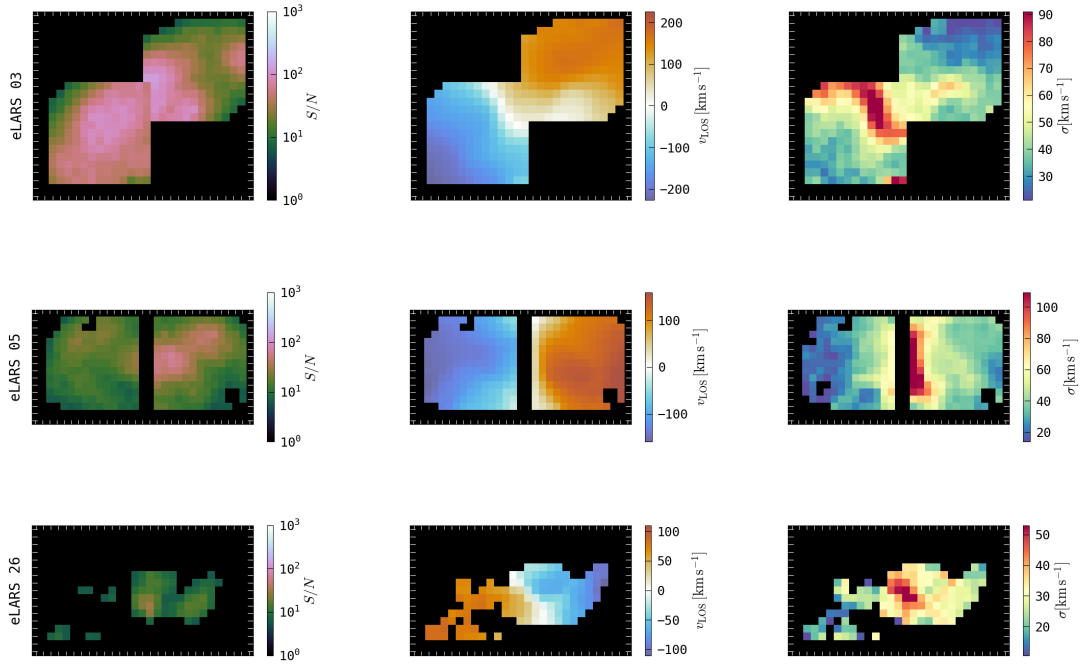

Figure 3.1 continued for eLARS double pointings.

axis is aligned with the rotation axis of the velocity field. The local velocity dispersion map shows a peak near the kinematic center. Gravity leads to an increase of the velocity dispersion in the center for reasons discussed in Section 3.3. This class can be associated with spiral galaxies, which have a flattened, rotating structure with prominent spiral arms.

- **Perturbed Rotators (PR):** The kinematics of a "perturbed rotator" are still characterized by orbital motions and a dipolar velocity field, but the velocity field is not perfectly symmetric and thus appears perturbed compared to a classic disk. Again, the optical major axis is aligned to the rotation axis of the velocity field. A second feature appears in the velocity gradient, which is most of the time very weak. This class traces disk galaxies with minor kinematic disturbance caused by minor mergers or feedback effects. Morphologically this class can be related to galaxies with distorted or assymmetrical features, like tidal tails or interacting galaxies.

- **Complex Kinematics (CK):** The galaxies show chaotic and sometimes multipolar velocity fields with no symmetries and they have irregular morphology in the images. The velocity dispersion maps are also different to a normal rotating disk. This class describes mergers, strong interactions between galaxies, AGN feedback, outflows or non-circular motions in the disk.

Using this classification scheme, five members of our team voted on the kinematic classes for our sample. In Figure 3.1 we present the maps for S/N, line of sight velocity and velocity dispersion for our sample, ordered by the visual kinematic classes. The LARS double pointings are not stitched together, because they were not sampled on the same wavelength grid. The result of the voting on our galaxy sample can be found in Table 3.1. The classification was not straight forward for every galaxy and for some galaxies there were different opinions between the voters. The voting result was not clear for galaxies eLARS13 and eLARS27. eLARS13 consists of a low number of spaxels and has a small spatial extension. The same number of votes were on RD and CK. As it is hard to characterize the velocity field by eye with only a few spaxels, we decided to put eLARS13 in the CK class. For eLARS27 the same number of votes were on RD and PR. We decided to put eLARS27 in the RD class. The datacube has some center spaxels missing and this could be the reason that some voted for PR instead of RD. The kinematic classes of the LARS galaxies are the same as in E. C. Herenz et al. (2016).

Table 3.1: Kinematic class and morphological classification (Galaxy Zoo, Lintott et al. 2011) of the LARS and eLARS galaxies.

ID	Class		Hα double component	flag GZ	GZ votes after debiasing procedure	GZ2
LARS01	PR		0	U	0.198	-
LARS02	CK		0	U	0.243	-
LARS03	PR		0	U	0.148	Sm
LARS04	CK		0	U	0.13	S
LARS05	PR		0	U	0.1	E
LARS06	CK		0	U	0.04	-
LARS07	PR		0	U	0.15	-
LARS08	RD		0	U	0.269	S
LARS09	CK		1	-	-	S
LARS10	PR		0	U	0.412	S
LARS11	RD		0	U	0.664	Sm
LARS12	CK		0	U	0.286	-
LARS13	CK		1	U	0.085	-
LARS14	CK		0	-	-	-
ELARS01	CK		0	U	0.03	Sm
ELARS02	PR		0	S	0.83	S
ELARS03	PR		0	S	0.85	S
ELARS04	RD		0	U	0.08	Sm
ELARS05	RD		0	S	1.0	S
ELARS06	RD		0	S	1.0	S
ELARS07	CK		1	U	0.04	-
ELARS08	RD		0	S	0.97	S
ELARS09	PR		0	U	0.2	S
ELARS10	RD		0	S	1.0	S
ELARS11	RD		0	S	0.83	S
ELARS12	RD		0	S	0.84	S
ELARS13	CK	(RD?)	0	U	0.13	E
ELARS14	RD		0	U	0.1	E
ELARS15	PR		0	S	0.91	S
ELARS16	RD		0	S	0.85	S
ELARS17	RD		0	U	0.8	S
ELARS18	RD		0	U	0.77	-
ELARS19	RD		0	U	0.42	-
ELARS20	PR		0	U	0.52	S
ELARS21	RD		0	S	0.94	-
ELARS22	CK		0	U	0.15	S
ELARS23	PR		0	S	0.97	S
ELARS24	RD		1	U	0.02	E
ELARS25	PR		0	S	0.94	S
ELARS26	RD		0	S	0.88	S
ELARS27	RD	(PR?)	0	S	0.87	S
ELARS28	PR		0	S	0.86	S

For each galaxy the class from the visual kinematic voting is listed and is marked, when the decision is not clear. The flag GZ represents the result from the voting on the GZ project, whether a galaxy is a spiral (S, 0.8 in the voting score is needed for this flag) or undefined (U). The GZ votes determine, whether the galaxy is a spiral, after a debiasing procedure described in Section 3.1 in Lintott et al. (2011). LARS09 and LARS14 have no GZ flag, because they are out of the sample with no redshift for the creation of the catalog. LARS14 is a prototypical Green Pea galaxy. GZ2 states whether a galaxy is elliptical (E), spiral (S) or merging (m) (Willett et al. 2013).

Table 3.2: The total number of galaxies for each kinematic class for the LARS and eLARS sample in comparison.

	RD	PR	CK
LARS	2	5	7
eLARS	16	8	4

In Table 3.1 we also list the morphological classifications from the Galaxy Zoo[1] (GZ) project (Lintott et al. 2011). Here, citizen scientists decided by vote, after being presented with Sloan Digital Sky Survey images[2], whether a galaxy appears to be a spiral or not. We can relate the morphologic spiral class to our rotating disks kinematic class. The GZ votes in Table 3.1 are the votes after the debiasing procedure. All 9 galaxies with CKs, also morphological classified, are U. This matches the expectations that galaxies with complex kinematics are no spirals. For the PRs 6 of 13 galaxies are voted as spirals and for the RDs 10 of 18. For the RDs we expected a higher fraction of spirals. As Galaxy Zoo is based on short ground based images from a 2.5 telescope, the images may not be meaningful for all galaxies and some spirals may be classified as unclear because of the image quality.

In Table 3.1 the last column shows results from the Galaxy Zoo 2 (GZ2) program (Willett et al. 2013), which is an update of galaxy zoo 1 with a fraction of the galaxy zoo 1 galaxies and more detailed morphological analysis. From GZ2, which is again, like GZ1, a citizen science campaign, more than 16 million visual morphological classifications for $>$ 304,000 galaxies in SDSS exist. We compare our visual classification on PMAS data to the GZ2 results. We use the debiased fraction of votes and classify the galaxies as elliptical (votes for smooth) or spiral (votes for features or disks). We also use the debiased fraction of votes, whether a galaxy is in a process of merging. Following Negus et al. (2021), we require a vote fraction of 50%. GZ2 classifies 31 galaxies of our sample. 13 of our RDs are also classified as spirals, two as elliptical and two in a merging process. Ten of our PRs are classified as spirals, one as elliptical and one as merger. For our CKs we have four spirals, one elliptical and one as merger. From our RDs and PRs, 23 of 26 in GZ2 classified galaxies are morphological classified as spirals. However, on the same time all morphological classes are found in all kinematic classes. Interestingly, the morphological class can not conclude on the kinematical class.

Focusing now purely on the kinematics, in Table 3.2 we compare the number of galaxies in each kinematic class for the LARS and eLARS sample. The eLARS

[1] http://zoo1.galaxyzoo.org/
[2] https://classic.sdss.org/gallery/

sample contains 16 RDs out of 28 galaxies and LARS only 2 out of 16. When selecting galaxies for the eLARS catalog the selection criteria was modified by lowering the Hα EW from 100 Å to 40 Å. The higher the Hα EW, the younger are the stellar populations in the galaxies. In reverse lower Hα EWs relate to older ages and this is a reason for more RDs in the eLARS sample. The higher number of RD galaxies in the eLARS sample throws a higher attention on correcting our data for PSF smearing, as the velocity fields show steep gradients in the center parts. However, this correction is also important for the other kinematic classes.

As stated at the beginning of this section, we are interested, whether ISM conditions of different kinematic classes influence the observed Lyα observables. The number of objects in each kinematic class compared to the original LARS sample allow for a statistical exploration regarding possible relations between kinematic classes and Lyα observables.

By looking on the different kinematic classes, we find that the maximum $\mathrm{EW}_{\mathrm{Ly}\alpha}$ (56.7 Å, LARS02), the maximum $f_{\mathrm{esc}}^{\mathrm{Ly}\alpha}$ (0.3, LARS02) and the maximum Lyα/Hα (2.9 , LARS14 and eLARS13) are found in objects classified as CK. The averages of the Lyα observables (excluding measurements that resulted in upper limits) are larger in the CK class ($\langle \mathrm{EW}_{\mathrm{Ly}\alpha} \rangle = 23.15$ Å, $\langle f_{\mathrm{esc}}^{\mathrm{Ly}\alpha} \rangle = 0.102$ and $\langle \mathrm{Ly}\alpha/\mathrm{H}\alpha \rangle = 1.24$) than the averages in the PR class ($\langle \mathrm{EW}_{\mathrm{Ly}\alpha} \rangle = 17.47$ Å, $\langle f_{\mathrm{esc}}^{\mathrm{Ly}\alpha} \rangle = 0.067$ and $\langle \mathrm{Ly}\alpha/\mathrm{H}\alpha \rangle = 0.79$) and the averages in th eRD class ($\langle \mathrm{EW}_{\mathrm{Ly}\alpha} \rangle = 16.36$ Å, $\langle f_{\mathrm{esc}}^{\mathrm{Ly}\alpha} \rangle = 0.057$ and $\langle \mathrm{Ly}\alpha/\mathrm{H}\alpha \rangle = 0.92$). Upper limits in the Lyα observables are found in all three kinematic classes.

We study whether there are differences in the distributions of the Lyα observables $\mathrm{EW}_{\mathrm{Ly}\alpha}$ (Section 1.2.3), $f_{\mathrm{esc}}^{\mathrm{Ly}\alpha}$ (Section 1.2.4) and $L_{\mathrm{Ly}\alpha}/L_{\mathrm{H}\alpha}$ (Section 1.2.2) between the different kinematic classes. We use the Kolmogorov-Smirnov test and compare RDs versus PRs and CKs, RDs versus CKs and RDs and PRs versus CKs. We are interested, if the Lyα variables from both sub-samples originate from the same distribution. Our null-hypothesis H_0 can be formulated as $F(x) \leq G(x)$ for all x, where x is the Lyα observable and $F(x)$ and $G(x)$ are the cumulative distributions for the sub-samples of kinematic classes $\mathcal{A}$ and $\mathcal{B}$. The only alternative hypothesis H_1 states that the sub-samples are drawn from different distributions and that at least for one x $F(x) > G(x)$ (Ivezić et al. 2014, section 4.6). This test can be performed with the single-sided two-sample test. This Kolmogoronov-Smirnov (KS) test is a non-parametric statistical test used to compare two datasets. The test orders the samples in a cumulative way. We then have for each sample a cumulative distribution function (CDF) with jumps of 1/samplesize for each value in the CDF of $\mathrm{EW}_{\mathrm{Ly}\alpha}$, f_{esc} and $L_{\mathrm{Ly}\alpha}/L_{\mathrm{H}\alpha}$. The statistics D_p measures the absolute maximum vertical distance between both CDFs (Wall 1996, Press 1986).

The p_0-value associated with the test statistic indicates the probability of ob-

taining a D_p-value as extreme as the observed one, assuming the null hypothesis is true. The significance level p_0 is calculated by

$$p_0(D_p > D_{p,\text{observed}}) = Q_{\text{KS}}\left(\sqrt{\frac{N_1 N_2}{N_1 + N_2}} D_p\right) \tag{3.1}$$

with N_1 the number of data points in the first and N_2 the number of data points in the second sample and $Q_{\text{KS}}(\lambda) = 2\sum_{j=1}^{\infty}(-1)^{j-1}e^{-2j^2\lambda^2}$[3] the significance of the KS test (Press 1986). In practice we use scipy.stats.kstest[4] to calculate D_p and p_0. If the p-value is above a predetermined significance level (we adopt 0.05), the null hypothesis cannot be rejected. However, if the p-value is below the significance level, it suggests that there is evidence to reject the null hypothesis, indicating that the two samples are likely drawn from different distributions. For the KS-test we exculde galaxies (LARS06, 10, 13, eLARS12, 14 and 16), which are non-detections in Lyα and therefore have upper limits for the Lyα observables.

The problem with the KS-test is that it can only compare two samples, but with our kinematic classification we have three subsamples. Based on our kinematic classification (RD, PR, and CK; see Section 3.1) we create two sub-samples. We divide our three classes in two different subsamples $\mathcal{A}$ and $\mathcal{B}$ and perform the KS-Test for the following combinations:

- RDs in $\mathcal{A}$ and PRs and CKs in $\mathcal{B}$
- RDs in $\mathcal{A}$ and CKs in $\mathcal{B}$
- RDs and PRs in $\mathcal{A}$ and CKs in $\mathcal{B}$

Before looking at the KS-test results, we first look at the distributions of the subsamples $\mathcal{A}$ and $\mathcal{B}$. In Table 3.3 we list the minimum and maximum value, the mean and the median for the $\text{EW}_{\text{Ly}\alpha}$, f_{esc} and $L_{\text{Ly}\alpha}/L_{\text{H}\alpha}$ for the different subsamples $\mathcal{A}$ and $\mathcal{B}$. For RDs versus PRs & CKs, all three Lyα observables have a higher maximal value for PRs and CKs, a higher average and a lower median. The same statement holds for RDs versus CKs and RDs & PRs versus CKs. This indicates that CKs have preferentially higher values in the observed Lyα observables and that complex kinematics may positively influence the escape of Lyα photons.

[3] Monotonic function with the limiting values of $Q_{\text{KS}}(0) = 1$ and $Q_{\text{KS}}(\infty) = 0$.
[4] https://docs.scipy.org/doc/scipy/reference/generated/scipy.stats.kstest.html

Table 3.3: Comparison of Lyα observables between kinematical classes.

Notes: $\mathcal{A}$ = rotating disks (18 galaxies) – $\mathcal{B}$ = perturbed rotators & complex kinematics (24 galaxies)										
	max($\mathcal{A}$)	max($\mathcal{B}$)	min($\mathcal{A}$)	min($\mathcal{B}$)	avg($\mathcal{A}$)	avg($\mathcal{B}$)	med($\mathcal{A}$)	med($\mathcal{B}$)	D_p	p_0
$\mathrm{EW}_{\mathrm{Ly}\alpha}$ [Å]	26.5	56.7	7.88	2.07	16.4	19.9	17.08	12.44	0.381	0.060
$f_{\mathrm{esc}}^{\mathrm{Ly}\alpha}$	0.15	0.30	0.01	0.01	0.06	0.08	0.06	0.05	0.171	0.537
$L_{\mathrm{Ly}\alpha}/L_{\mathrm{H}\alpha}$	1.8	2.9	0.37	0.07	0.92	0.98	0.79	0.54	0.438	0.025
$\mathcal{A}$ = rotating disks (18 galaxies) – $\mathcal{B}$ = complex kinematics (11 galaxies)										
	max($\mathcal{A}$)	max($\mathcal{B}$)	min($\mathcal{A}$)	min($\mathcal{B}$)	avg($\mathcal{A}$)	avg($\mathcal{B}$)	med($\mathcal{A}$)	med($\mathcal{B}$)	D_p	p_0
$\mathrm{EW}_{\mathrm{Ly}\alpha}$ [Å]	42.2	56.7	3.14	2.07	16.9	23.15	16.82	18.11	0.185	0.602
$f_{\mathrm{esc}}^{\mathrm{Ly}\alpha}$	0.15	0.30	0.01	0.01	0.06	0.10	0.06	0.03	0.222	0.487
$L_{\mathrm{Ly}\alpha}/L_{\mathrm{H}\alpha}$	1.8	2.9	0.12	0.07	0.86	1.24	0.68	0.51	0.296	0.284
$\mathcal{A}$ = rotating disks & perturbed rotators (31 galaxies) – $\mathcal{B}$ = complex kinematics (11 galaxies)										
	max($\mathcal{A}$)	max($\mathcal{B}$)	min($\mathcal{A}$)	min($\mathcal{B}$)	avg($\mathcal{A}$)	avg($\mathcal{B}$)	med($\mathcal{A}$)	med($\mathcal{B}$)	D_p	p_0
$\mathrm{EW}_{\mathrm{Ly}\alpha}$ [Å]	26.5	56.7	7.88	2.07	16.4	23.15	17.08	18.11	0.333	0.246
$f_{\mathrm{esc}}^{\mathrm{Ly}\alpha}$	0.15	0.30	0.01	0.01	0.06	0.10	0.06	0.03	0.267	0.398
$L_{\mathrm{Ly}\alpha}/L_{\mathrm{H}\alpha}$	1.8	2.9	0.37	0.07	0.92	1.24	0.79	0.51	0.422	0.107

Notes: avg is the average of the class and med the median of the class. D_p and p_0 provide the test statistic of a single-sided two-sample KS-test. Our null hypothesis is, that the cumulative distribution of the Lyα observables in class $\mathcal{A}$ is always below or equal the cumulative distribution in class $\mathcal{B}$.

Now we test, whether the KS-test also indicates that the complex kinematics differ in the distribution of the Lyα observables. We list the test results D_p and p_0 in Table 3.3. The sample size of each group is quite small and therefore the p_0-values have to be treated with caution. Formally, when adopting a p_0-value of 0.05 to reject the nullhypothesis, only the Lyα/Hα ratio of the CKs and PRs appears to be shifted to have larger values compared to the RDs. The qualitative impression of a galaxies line-of-sight velocity field appears thus unlikely to reflect whether the galaxy is observed as a strong Lyα emitter or not.

The statistic test does not confirm the assumption of the tendency seen in the maximum Lyα values being in complex kinematics. With our sample we cannot rule out our null hypothesis that the subsamples of the KS-test are drawn from the same distribution for all three Lyα observables. It would be worth to test the statistics on a larger sample and see, whether we can rule out the null hypothesis. However, we see that there is a huge overlap in the Lyα observables already in the different classes in our sample. A larger sample could also show our current findings that the qualitative impression of the line-of-sight velocity can not fully reflect whether a galaxy is a Lyα emitter or not. Additionally, it is worth to mention that this visual classification can not be done as finely grained for high-z galaxies.

3.2 Calculation of the integrated ionized gas kinematics

As mentioned earlier, the Lyα photons are resonant and get absorbed and re-emitted by hydrogen and also scatter on dust. Turbulent ionized gas kinematics may shift enough absorbing and emitting material out of resonance and therefore favor the escape of Lyα photons. To study the effect of ionized gas kinematics on Lyα photons, we perform a quantitative analysis of the ionized gas kinematics. We expect that galaxies with turbulent kinematics have higher escape fractions. For galaxies with ordered motions we may expect lower escape fractions and lower equivalent widths in Lyα. To test such statements we study, whether we find relations between integrated ionized gas kinematics and Lyα observables.

As introduced in Section 1.3.3, we characterize the ionized gas kinematics by the shear velocity v_{shear}, intrinsic velocity dispersion σ, and the ratio $v_{\mathrm{shear}}/\sigma$ (e.g. Glazebrook 2013, E. C. Herenz et al. 2016, Alexei V. Moiseev, Tikhonov, and Klypin 2015, Bellocchi et al. 2013, Gonçalves et al. 2010). In the following, we describe the calculation of the parameters for our data. We list the calculated parameters and uncertainties in table 3.4.

3.2.1 Shearing velocity v_{shear}

v_{shear} is a measure of the large-scale gas bulk motion along the line of sight and is calculated by

$$v_{\mathrm{shear}} = \frac{1}{2}\left(v_{95} - v_5\right), \tag{3.2}$$

where v_{95} and v_5 are the values of the upper and lower fifth percentile of the velocity field, to be robust against outliers in the velocity field measurements (E. C. Herenz et al. 2016). To estimate the uncertainty, we take the standard deviation of spaxels within the 100-95 and 5-0 percentile intervals. We end up with asymmetric uncertainties.

For the eLARS sample, v_{shear} ranges from 14.7 $\mathrm{km\,s^{-1}}$ (eLARS28) to 181.9 $\mathrm{km\,s^{-1}}$ (eLARS03). We have a mean shearing velocity of 68.6 $\mathrm{km\,s^{-1}}$ (median shear velocity of 58.0 $\mathrm{km\,s^{-1}}$). In LARS v_{shear} ranges from 15.4 $\mathrm{km\,s^{-1}}$ (LARS02) to 168.5 $\mathrm{km\,s^{-1}}$ (LARS13) with a median of 60.3 $\mathrm{km\,s^{-1}}$ and a mean of 82.3 $\mathrm{km\,s^{-1}}$. In column 6 in Table 3.4 we list the calculated values for each LARS and eLARS galaxy.

To contextualize our findings, Green, Glazebrook, McGregor, Damjanov, et al. (2014) studies the Hα kinematics of 67 galaxies of the DYNAMO sample at $z \sim 0.1$. They adopt a simple disc model and fit a rotation curve. They characterize the rotation velocity at a radius of 2.2 r-band exponential disc scalelengths, where the rotation curve of an ideal, self-gravitating, exponential disc would peak. The rotation velocity ranges from 42 $\mathrm{km\,s^{-1}}$ to 395 $\mathrm{km\,s^{-1}}$ with a mean of 169 $\mathrm{km\,s^{-1}}$. These values are higher than our findings. Isobe et al. (2023) studies six local extremely metal-poor galaxies and report rotation velocities between 5 $\mathrm{km\,s^{-1}}$ and 23 $\mathrm{km\,s^{-1}}$, which are lower than the values for our galaxies.

3.2.2 Intrinsic velocity dispersion σ

There are different methods of measuring the intrinsic velocity dispersion in IFS observations. As described in Sections 1.3.3 and 2.3, the Hα profile in each spaxel is fitted with a Gaussian profile and the measured dispersion in each spaxel, σ_i, is corrected for instrumental broadening by subtracting the dispersion of the LSF in quadrature, as shown in Equation (2.3).

In literature, different notations and different definitions can arise confusion regarding the estimates of the intrinsic velocity dispersion. We will follow the notation of Davies et al. (2011). We start estimating the intrinsic velocity dispersion using a uniformly weighted mean of all σ_i's in each galaxy

$$\sigma_{\mathrm{m,\ uniform}} = \sum_i \frac{\sigma_i}{N} \tag{3.3}$$

where σ_i is the local velocity dispersion measured in the individual spaxels and N is the number of considered spaxels.

The weighted σ_{m} is calculated by taking the weighted average of the observed velocity dispersion by

$$\sigma_{\mathrm{m}} = \frac{\sum_i (S/N)_i \sigma_i}{\sum_i (S/N)_i}, \tag{3.4}$$

where S/N_i is the Hα S/N in each spaxel (E. C. Herenz et al. 2016). In Equation (3.3) and Equation (3.4) we only consider spaxels with $S/N > 6$. In literature, the flux-weighted σ_{m} is commonly used for distant and nearby galaxies (E. C. Herenz et al. 2016, Gonçalves et al. 2010, Glazebrook 2013, Green, Glazebrook, McGregor, Damjanov, et al. 2014, Alexei V. Moiseev, Tikhonov, and Klypin 2015).

Throughout our analysis, we use S/N as weights. This differs from the flux weighting scheme that is commonly adopted in the literature, but we verified that there is no significant difference between the weighting schemes for the LARS galaxies (see Appendix A.2). Also, we can not use the flux weighted mean for eLARS, since we have not performed flux calibration (see Section 2.2).

Both estimators for σ in Equation (3.3) and Equation (3.4) are empirical, model independent and are thus useful for systems that exhibit complex velocity fields, where parametric models cannot be applied straight forward. For example there are quite strong requirements regarding S/N and resolution for modeling (Green, Glazebrook, McGregor, Damjanov, et al. 2014, Davies et al. 2011). Of course, modeling is a way, but on-parametric methods can be also very powerful. In the appendix of A. V. Moiseev, Pustilnik, and Kniazev (2010) they use a more complex model to model the complex kinematics of the inner velocity fiels of SBS0335-052E. This example shows the length one has to go through in order to model complex kinematics and even then the question remains, whether the model one has choosen is meaningful.

In table 3.4 we list the calculated values for the LARS and eLRAS galaxies. The estimate of the intrinsic velocity dispersion is not optimal, as it can be affected by point spread function (PSF) smearing. The PSF smearing broadens the Hα line in the region of a strong velocity gradient. A prominent example are RDs, which have a steep velocity gradient in the center of the velocity field and a peak in the velocity dispersion in the center regions. This results also in a rise of the mean intrinsic velocity dispersion of all spaxels. We explain the effect of PSF smearing and how we correct for this effect in Section 3.3.

We calculate the statistical error on the velocity dispersion by propagating the

uncertainties by

$$\Delta\sigma_{\mathrm{m,\ uniform}} = \frac{\sqrt{\sum_i \Delta\sigma_i^2}}{N}, \tag{3.5}$$

and

$$\Delta\sigma_{\mathrm{m}} = \frac{\sqrt{\sum_i \left((S/N)_i \Delta\sigma_i\right)^2}}{\sum_i (S/N)_i}. \tag{3.6}$$

We list the velocity dispersions and uncertainties in Table 3.4. We have a minimum of σ_{m} of 23.06 $\mathrm{km\,s^{-1}}$ (eLARS23) and a maximum of 99.48 $\mathrm{km\,s^{-1}}$ (eLARS24). Our sample has a mean σ_{m} of 43.43 $\mathrm{km\,s^{-1}}$ and a median of 38.04 $\mathrm{km\,s^{-1}}$. We have a minimum of $\sigma_{\mathrm{m,\ uniform}}$ of 23.88 $\mathrm{km\,s^{-1}}$ (eLARS23) and a maximum of 101.11 $\mathrm{km\,s^{-1}}$ (LARS03). Our sample has a mean $\sigma_{\mathrm{m,\ uniform}}$ of 43.22 $\mathrm{km\,s^{-1}}$ and a median of 39.21 $\mathrm{km\,s^{-1}}$. These values are contextualized with the values of other comparison samples in Section 3.8.

3.2.3 $v_{\mathrm{shear}}/\sigma$

The ratio $v_{\mathrm{shear}}/\sigma$ describes, whether the motions of the ionized gas in a galaxy are dominated by ordered (e.g. orbital) motions or turbulent motions. Galaxies with a small ratio are dispersion dominated (Glazebrook 2013).

For calculating the uncertainty, we have the problem that v_{shear} has asymmetric errors. In literature the errors are often added in quadrature, but this has no statistical justification (see Appendix B in Laursen et al. 2019). Laursen et al. (2019) provides a formally justified prescription of how to do the error propagation correctly for addition. We can not directly adopt this prescription for $v_{\mathrm{shear}}/\sigma$. We thus move to log-space that the calculation of the error of a ratio gets an addition of errors. Then we use the Laursen et al. (2019) recipe, and then we transform back. Here we introduce the transformation for the positive and negative error:

$$\Delta_p^{\log(v)} = \log(v + \Delta v) - \log(v) \tag{3.7}$$

$$\Delta_m^{\log(v)} = \log(v) - \log(v - \Delta v) \tag{3.8}$$

To check, we can move out of the logspace:

$$10^{\log(v)+\Delta_p^{\log(v)}} = 10^{\log(v+\Delta v)} = v + \Delta v \tag{3.9}$$

$$10^{\log(v)-\Delta_m^{\log(v)}} = 10^{\log(v-\Delta v)} = v - \Delta v \tag{3.10}$$

Now we have $\log(v)^{+\Delta_p^{\log(v)}}_{-\Delta_m^{\log(v)}}$, but we want to get Δ_p^v and Δ_m^v. Therefore,

$$v + \Delta_p^v = 10^{\log(v)+\Delta_p^{\log(v)}} = v \cdot 10^{\Delta_p^{\log(v)}} \tag{3.11}$$

$$v - \Delta_m^v = 10^{\log(v)-\Delta_m^{\log(v)}} = v \cdot 10^{-\Delta_m^{\log(v)}}, \tag{3.12}$$

which leads to

$$\Delta_p^v = v(10^{\Delta_p^{\log(v)}} - 1) \tag{3.13}$$

$$\Delta_m^v = v(1 - 10^{-\Delta_m^{\log(v)}}). \tag{3.14}$$

In LARS and eLARS $v_{\mathrm{shear}}/\sigma_{\mathrm{m}}$ ranges from 0.34 (eLARS13) up to 3.76 (eLARS03). The mean $v_{\mathrm{shear}}/\sigma_m$ of the sample is 1.77 and the median is 1.55. The Gassendi Hα survey of spirals sample is mainly composed of rotation-dominated galaxies. They shows values of the ratio V_{max}/σ lower than 2 only for very slow rotators, where $V\mathrm{max} < 100\ \mathrm{km\,s^1}$. Most of the values range from 5 to 20 for rotators ranging from 100 to 400 $\mathrm{km\,s^1}$ (Epinat et al. 2010). Barat et al. (2020) studies the kinematics in the SAMI galaxy survey and finds that the kinematics mostly dominated by σ. 1098 out of 1141 galaxies have $V_{\mathrm{rot}}/\sigma < \sqrt{2}$.

Table 3.4: Global kinematic parameters.

ID	$\sigma_{\mathrm{m,\ uniform}}$ [km s^{-1}]	$\Delta\sigma_{\mathrm{m,\ uniform}}$ [km s^{-1}]	σ_{m} [km s^{-1}]	$\Delta\sigma_{\mathrm{m}}$ [km s^{-1}]	v_{shear} [km s^{-1}]	$\Delta v^{+}_{\mathrm{shear}}$ [km s^{-1}]	$\Delta v^{-}_{\mathrm{shear}}$ [km s^{-1}]
LARS01	47.17	0.55	46.69	0.11	52.4	1.6	2.8
LARS02	38.2	0.73	37.91	0.2	15.4	8.0	2.9
LARS03	101.11	1.41	88.94	0.22	130.2	5.4	6.7
LARS04	43.12	0.32	43.6	0.08	68.2	2.9	5.7
LARS05	51.97	0.49	45.63	0.12	30.6	5.8	1.2
LARS06	26.19	0.45	27.17	0.21	50.6	1.9	1.0
LARS07	60.63	0.77	58.31	0.15	26.0	4.9	2.7
LARS08	46.57	0.4	47.06	0.09	148.9	4.4	3.2
LARS09	58.84	0.41	56.45	0.11	159.6	3.0	8.5
LARS10	36.48	0.61	36.55	0.37	32.4	5.5	6.0
LARS11	66.31	0.98	65.3	0.46	149.1	11.2	6.1
LARS12	70.59	0.97	69.98	0.29	81.3	18.7	3.3
LARS13	62.04	0.72	65.48	0.38	168.5	18.7	3.3
LARS14	59.41	1.1	65.19	0.42	38.8	2.3	0.1
ELARS01	56.21	0.34	57.18	0.11	42.96	2.1	2.0
ELARS02	31.25	0.43	32.75	0.17	17.69	2.1	0.3
ELARS03	45.0	0.17	48.33	0.09	181.85	1.1	2.8
ELARS04	43.74	0.4	45.13	0.19	60.71	2.4	1.7
ELARS05	41.78	0.28	46.86	0.21	145.95	1.9	1.3
ELARS06	29.58	0.22	30.66	0.1	61.34	1.2	1.7
ELARS07	40.22	0.45	38.23	0.15	93.09	1.6	19.3
ELARS08	25.5	0.3	26.57	0.18	87.98	1.6	3.3
ELARS09	32.77	0.66	32.03	0.26	31.86	6.2	4.4
ELARS10	47.35	0.42	47.46	0.2	121.62	2.2	2.2
ELARS11	47.21	0.37	50.36	0.19	77.38	1.3	2.1
ELARS12	37.57	0.25	37.69	0.09	126.37	1.7	1.5
ELARS13	61.66	1.27	63.02	0.4	21.69	3.3	2.2
ELARS14	32.0	0.59	29.58	0.14	55.2	1.5	2.5
ELARS15	32.14	0.41	35.48	0.25	50.41	4.5	3.2
ELARS16	23.92	0.41	24.09	0.24	76.89	4.3	1.6
ELARS17	25.17	0.54	27.04	0.42	85.31	1.8	5.0
ELARS18	26.35	0.55	26.02	0.31	74.89	2.2	3.5
ELARS19	28.94	0.58	26.88	0.2	52.04	6.4	1.6
ELARS20	36.9	0.53	34.78	0.21	37.09	1.2	1.8
ELARS21	26.64	0.81	26.45	0.56	50.56	7.1	3.6
ELARS22	40.43	1.33	38.17	0.79	38.59	18.3	3.0
ELARS23	23.88	0.7	23.06	0.57	31.56	6.2	2.7
ELARS24	90.8	1.5	99.48	0.94	94.99	8.2	2.8
ELARS25	34.12	0.47	33.81	0.26	48.92	3.1	5.7
ELARS26	33.2	0.64	35.01	0.54	88.95	0.8	2.3
ELARS27	26.62	0.6	27.08	0.38	48.88	0.7	1.8
ELARS28	25.76	0.47	26.66	0.33	14.69	0.9	2.4

3.3 Correcting σ_{m} and $\sigma_{\mathrm{m,\ uniform}}$ for PSF smearing

When observing a galaxy, the spatial resolution and sampling of the observation instrument is limited, as already mentioned in Section 3.2.2. Spatial resolution refers to the level of detail or the smallest distinguishable features that can be resolved in the observation. The measure that describes the spatial resolution is given by the width (e.g., FWHM) of the point spread function. For ground based observations without adaptive optics this is determined by the atmospheric seeing of the observations (Hickson 2014). Formally, the effect of seeing on the observations is described by a convolution of the intrinsic light profiles with the point spread function. Typical models for point spread function are a simple 2D Gaussian profile or a Moffat profile (Moffat 1969). Spatial sampling refers to the process of discretely measuring or capturing data points in a regularly spaced grid across a 2D space. This means that the observed galaxy is divided into small spatial elements (spaxels) that are the PSF convolved gas motions at different velocities along the line of sight within a single spaxel. This causes the emission line to appear broader than it actually is. This broadening of the Hα line is known as PSF smearing.

When looking at the maps for the velocity dispersion in Figure 3.1, we can observe a peak in the center of RDs. This peak is, beside gravity (see also Section 3.6), a consequence of the PSF smearing artificially increasing the observed velocity dispersion in the central regions (see Section 1.3.3). Galaxies classified as CKs exhibit irregular or non-linear velocity fields, often associated with mergers, interactions, or other dynamical processes. In such galaxies, the PSF smearing effect also complicates the interpretation of the observed velocity dispersion.

E. C. Herenz et al. (2016) did not apply a PSF smearing correction to the LARS sample, so it remained unclear whether the intrinsic velocity dispersions used in their analysis were biased high. We here present a method that objectively masks spaxels deemed to be affected by line broadening due to the PSF smearing effect and apply the method to all LARS and eLARS galaxies. We use the velocity gradient to create a mask. Our method is non-parametric and model independent. We can apply our method to RDs, PRs and CKs.

A gradient refers to the change in intensity or value of a function with respect to spatial coordinates. It represents the rate of change of the function's value in different directions, typically computed as the partial derivatives of the function with respect to the spatial coordinates. In our context, the gradient provides us information about the variation in the velocity field. We calculate the differences to the eight neighbors and get a vector with eight entries, each representing the magnitude and the direction of the velocity shift towards all neighboring spaxels

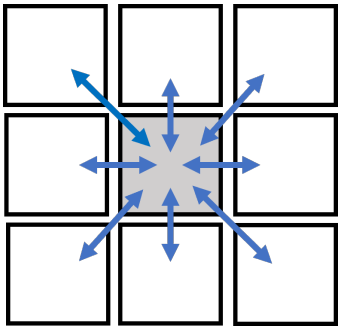

Figure 3.6: To quantify the magnitude of the rate of change in the line of sight velocity field, we calculate the difference to all eight neighbor spaxels, add them in quadrature and pull the root.

(8-connected topology, see Figure 3.6). We square these eight differences and take the square root

$$v_g(x,y) = \sqrt{\sum_{i=(-1,0,1)} \sum_{j=(-1,0,1)} [v(x-i, y-j) - v(x,y)]^2}, \tag{3.15}$$

which represents the amplitude. By this we obtain a map that tries to quantify the magnitude of velocity change expected within a spaxel. Squaring the differences emphasizes the steepness or sharpness of the intensity transition. Regions with rapid and prominent changes in the observed line of sight velocity field will have larger squared differences, indicating a higher rate of change. Our gradient maps calculated by Equation 3.15 are shown in Figure 3.7 for our sample (spaxels from yellow to red will be masked).

We define a binary mask,

$$m(x,y) = \begin{cases} 1 & \Leftrightarrow v_g(x,y) \leq v_{g,\mathrm{thresh}} \\ 0 & \Leftrightarrow v_g(x,y) > v_{g,\mathrm{thresh}} \end{cases}, \tag{3.16}$$

to calculate masked versions of the mean (Equation 3.3),

$$\sigma_{\mathrm{m,\ uniform,\ corr}} = \frac{1}{\sum_{x,y} m(x,y)} \sum_{x,y} m(x,y) \cdot \sigma_{x,y}\ , \tag{3.17}$$

and the weighted mean (Equation 3.4),

$$\sigma_{\mathrm{m,corr}} = \frac{1}{\sum_{x,y} m(x,y) \cdot w_{x,y}} \sum_{x,y} m(x,y) \cdot w_{x,y} \cdot \sigma_{x,y}\ , \tag{3.18}$$

respectively.

We visually inspect the gradient maps and determine a value of the gradient, which captures all regions with a steep gradient and at the same time does not mask out to many spaxels. We conclude to set the masking value of the gradient to 70 $\mathrm{km\,s^{-1}}$ (spaxels that are yellow to red in the color scheme of Figure 3.7). We mask for the calculation of the velocity dispersion of all spaxels with a gradient larger than 70 $\mathrm{km\,s^{-1}}$. In table 3.5 we list the velocity dispersion values calculated with our gradient masking method and also how many spaxels are affected by our method.

For eLARS 24 we have with 22 $\mathrm{km\,s^{-1}}$ the highest change in velocity dispersion. This galaxy is extended only on a few spaxels and over the half of the spaxles are masked with $v_g(x, y)$, which explains the huge difference. eLARS03, eLARS05 and eLARS07 also have a difference larger than 5 $\mathrm{kms^{-1}}$ for the weighted velocity dispersion. In the center of these galaxies, many spaxels have high values and they are masked, so the number of masked spaxels is very high in theses galaxies. In the center region, eLARS07 shows a very high velocity dispersion per spaxel and also shows a Hα double component profile. For eLARS07 our method masks the spaxels with Hα double components.

Mainly RDs and CKs are affected (13 of 18 RDs, 6 of 13 PRs and 8 of 11 CKs) by our gradient method. RDs show a steep velocity gradient in the center and CKs display steep velocity gradients in different locations. For steep velocity gradients, the PSF smearing gets larger, which implies that the gradient method affects galaxies where a correction is mostly desired.

Most intrinsic velocity dispersions $\sigma_{\mathrm{m,\ uniform}}$ of individual galaxies differ in a few $\mathrm{kms^{-1}}$. The maximal change in velocity dispersion is 12.8 $\mathrm{km\,s^{-1}}$ and the minimum affection 0.1 $\mathrm{km\,s^{-1}}$ (galaxies not masked by our method excluded). The mean is 2.8 $\mathrm{km\,s^{-1}}$ and the median change in velocity dispersion 1.0 $\mathrm{km\,s^{-1}}$. As expected, the masking lowers the value of σ, because spaxels which contain high local velocity dispersion values are masked out.

We are not the first in attempting to correct low-spatial resolution IFS kinematic maps for the PSF smearing effect (e.g. Davies et al. 2011). The downward correction of the intrinsic velocity dispersion compared to the uncorrected intrinsic velocity dispersion is also reported in M. R. Varidel, Croom, Lewis, Fisher, et al. (2020). Other studies correct by own empiric methods (e.g. M. Varidel et al. 2016, Zhou et al. 2017) or use disk fitting models (e.g. Green, Glazebrook, McGregor, Damjanov, et al. 2014). The DYNAMO study by Green, Glazebrook, McGregor, Damjanov, et al. (2014) corrects their data also for beam smearing by using a disk fitting model. They have a median correction of 3.6 $\mathrm{kms^{-1}}$. This is in the same order of magnitude as our method corrects for PSF smearing. Our method takes

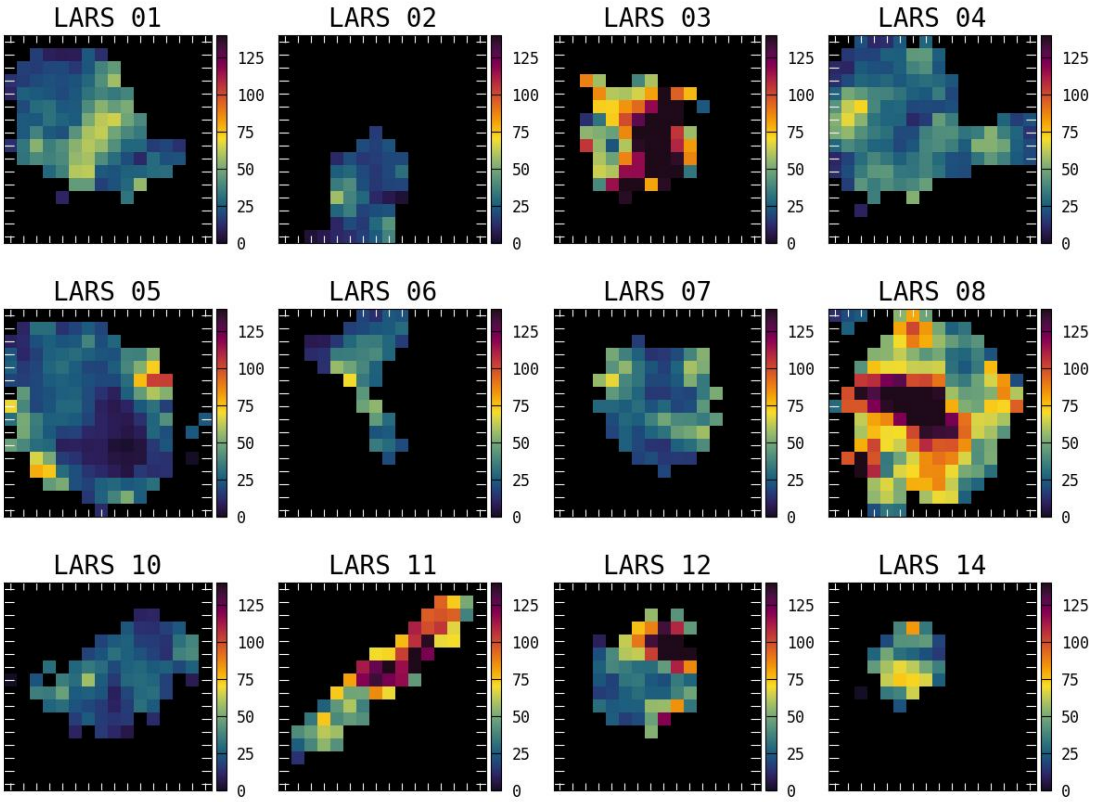

Figure 3.7: Gradient maps for the LARS sample with a single pointing in units of $\mathrm{km\,s^{-1}}$.

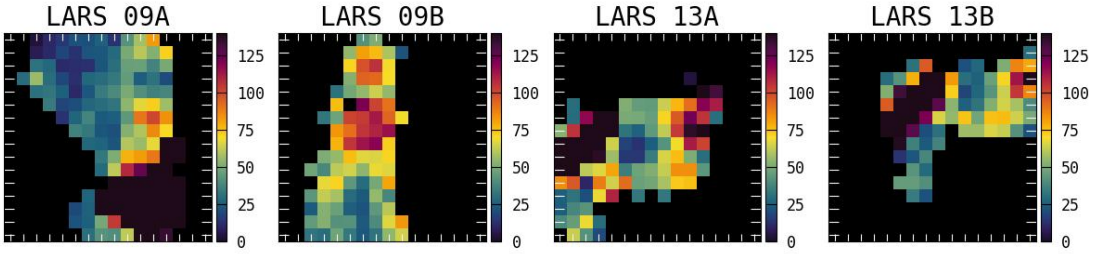

Figure 3.7 continued for LARS double pointings.

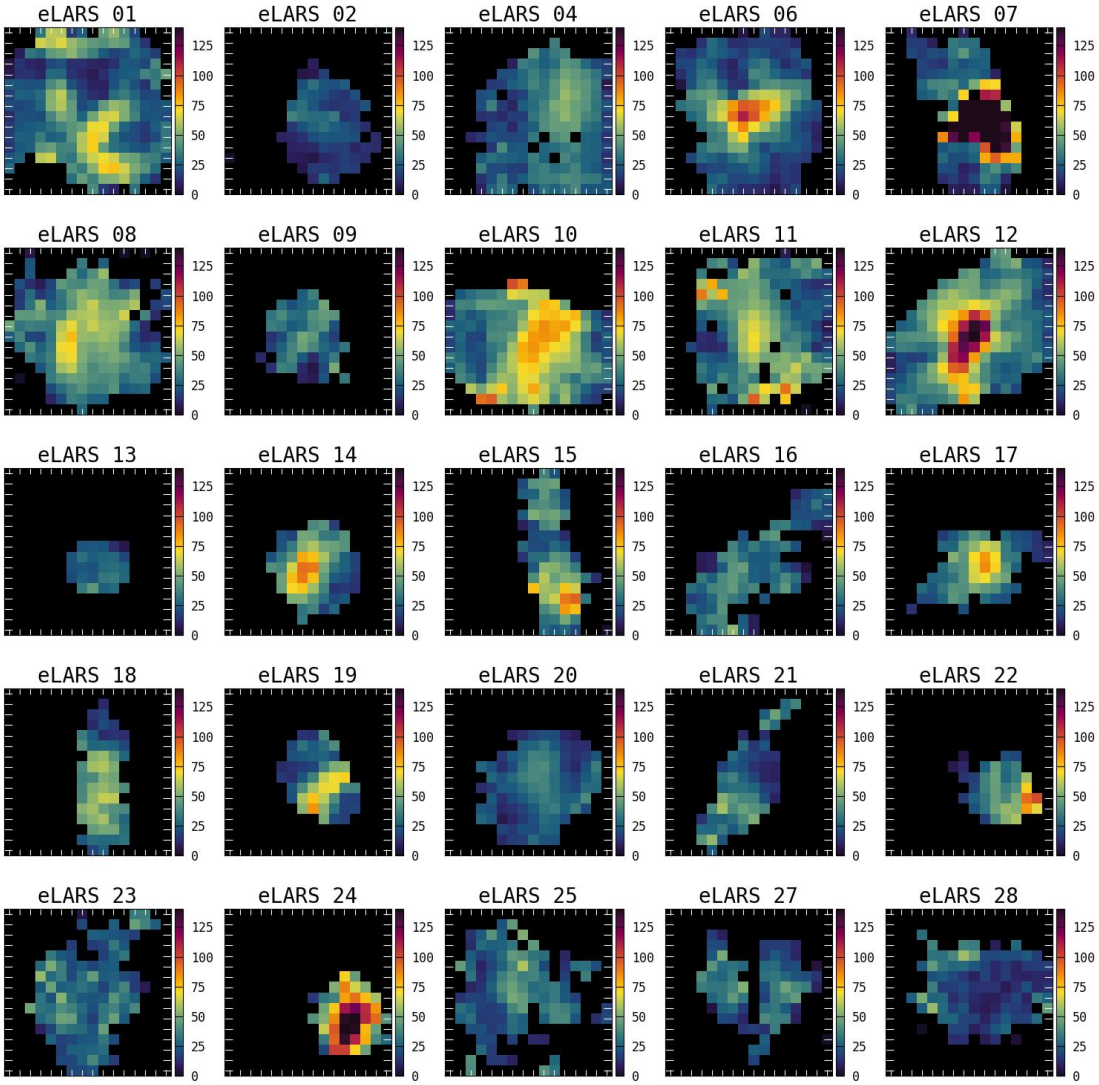

Figure 3.7 continued for eLARS single pointings.

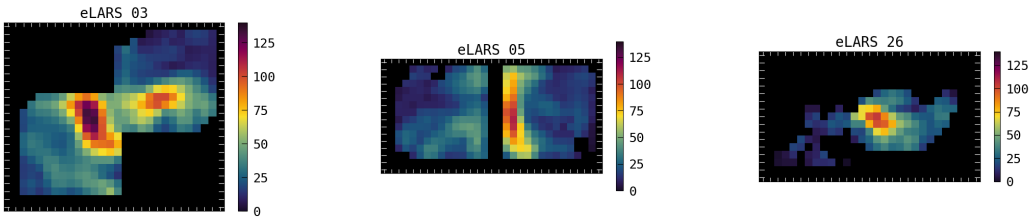

Figure 3.7 continued for eLARS double pointings.

the neighbor spaxels and the edge spaxels into account and slightly differs from the gradient method used for the SAMI sample (Zhou et al. 2017, M. Varidel et al. 2016). We are setting all nan values to 0 for the gradient calculation. The nan values occur for spaxels with S/N smaller than 6, as already described in Section 2.3. Therefore, we do not loose edge spaxels compared to the other method in Zhou et al. (2017) and M. Varidel et al. (2016). Compared to our method, they calculate the gradient out of the four neighbor spaxels and do not consider the edge spaxels. They apply different selection criteria to correct for PSF smearing. Yu et al. (2021) also applied a PSF smearing correction for their data. They extract the velocity dispersion along the major axis and only use spaxels with radii where the rotation curve is already flat. In Sections 3.4 and 3.5 we will apply both methods to our sample and in Section 3.7 we compare the different methods.

Table 3.5: Velocity dispersion corrected for PSF smearing by our gradient method.

ID	spaxels masked	spaxels used	$\sigma_{\mathrm{m,\ uniform,\ corr}}$ [km s^{-1}]	$\Delta\sigma_{\mathrm{m,\ uniform,\ corr}}$ [km s^{-1}]	$\sigma_{\mathrm{m,\ corr}}$ [km s^{-1}]	$\Delta\sigma_{\mathrm{m,\ corr}}$ [km s^{-1}]
LARS01	0	106	47.2	0.6	46.7	0.1
LARS02	0	45	38.2	0.7	37.9	0.2
LARS03	47	69	77.4	2.9	54.0	0.5
LARS04	1	134	43.0	0.3	43.5	0.1
LARS05	6	155	51.2	0.5	45.4	0.1
LARS06	0	43	26.2	0.5	27.2	0.2
LARS07	0	74	60.6	0.8	58.3	0.2
LARS08	71	160	41.2	0.4	40.2	0.1
LARS09	76	232	56.1	0.4	55.6	0.1
LARS10	0	76	36.5	0.6	36.6	0.4
LARS11	28	55	60.9	1.4	58.2	0.6
LARS12	16	59	64.8	1.1	66.3	0.3
LARS13	43	100	61.0	0.9	65.4	0.4
LARS14	3	30	59.0	1.2	65.5	0.4
ELARS01	4	213	55.6	0.3	56.8	0.1
ELARS02	0	74	31.3	0.4	32.8	0.2
ELARS03	41	321	40.7	0.2	42.1	0.1
ELARS04	0	161	43.7	0.4	45.1	0.2
ELARS05	21	321	37.7	0.3	39.4	0.2
ELARS06	12	179	28.7	0.2	29.0	0.1
ELARS07	34	109	30.6	0.5	29.2	0.2
ELARS08	2	159	25.4	0.3	26.4	0.2
ELARS09	0	54	32.8	0.7	32.0	0.3
ELARS10	26	161	43.7	0.4	43.4	0.2
ELARS11	7	164	46.7	0.4	50.2	0.2
ELARS12	27	185	35.4	0.3	33.5	0.1
ELARS13	0	27	61.7	1.3	63.0	0.4
ELARS14	9	62	31.9	0.7	28.4	0.2
ELARS15	6	74	31.1	0.4	34.9	0.3
ELARS16	0	87	23.9	0.4	24.1	0.2
ELARS17	3	65	24.7	0.6	26.2	0.5
ELARS18	0	58	26.4	0.6	26.0	0.3
ELARS19	3	50	28.2	0.6	26.6	0.2
ELARS20	0	101	36.9	0.5	34.8	0.2
ELARS21	0	61	26.6	0.8	26.5	0.6
ELARS22	9	41	39.5	1.3	37.7	0.8
ELARS23	17	103	23.9	0.7	23.1	0.6
ELARS24	26	45	78.0	2.9	77.3	2.5
ELARS25	15	113	34.1	0.5	33.8	0.3
ELARS26	10	124	30.9	0.7	32.1	0.6
ELARS27	0	75	26.6	0.6	27.1	0.4
ELARS28	13	102	25.8	0.5	26.7	0.3

3.4 Correcting for PSF smearing as in M. Varidel et al. (2016)

M. Varidel et al. (2016) introduces a velocity gradient

$$v_g(x,y) = \sqrt{[v(x+1,y) - v(x-1,y)]^2 + [v(x,y+1) - v(x,y-1)]^2} \tag{3.19}$$

by considering the four next neighbor spaxels. Then they introduce an empirical model, which states that the velocity dispersion for each individual spaxel can be fitted by a 2D linear model

$$\sigma_i[F(\mathrm{H}\alpha_i), v_{g,i}] = m_{\mathrm{H}\alpha} \log_{10}[F(\mathrm{H}\alpha_i)] + m_{v_g} v_{g,i} + c \tag{3.20}$$

by assuming that the velocity dispersion in each spaxel is a dependent variable of the Hα flux in each spaxel $F(\mathrm{H}\alpha_i)$ and of the velocity gradient in each spaxel $v_{g,i}$. The fitting parameters of this 2D linear model are $m_{\mathrm{H}\alpha}$, m_{v_g} and c. This model captures two features: they address higher velocity dispersion through feedback processes, because the parametric maps of the velocity dispersion and the Hα flux, which is related to the local star-formation rate, correlate. The second thing they capture is the PSF smearing through the velocity gradient. However, in their empirical model they do not take into account gravitational instabilities, which also leads to higher velocity dispersions. For our sample we use the S/N in Hα for the fitting process. In Figure 3.9 we display the observed velocity dispersion, the fitted velocity dispersion and the residual for our galaxies. After determining the best fit values $m_{\mathrm{H}\alpha}$, m_{v_g}, and c for each spaxel, they set $m_{v_g} = 0$, to obtain a corrected $\sigma_{i,\mathrm{corr}}$ and calculate with

$$\sigma_{i,\mathrm{corr}}[F(\mathrm{H}\alpha_i), v_{g,i}] = m_{\mathrm{H}\alpha} \log_{10}[F(\mathrm{H}\alpha_i)] + c \tag{3.21}$$

the velocity dispersion in each spaxel. Now we have the for PSF corrected velocity dispersion maps and then we can calculate the velocity dispersion $\sigma_{\mathrm{m,\ uniform,\ Varidel}}$ and $\sigma_{\mathrm{m,\ Varidel}}$ with Equation (3.3) and (3.4)[5].

M. Varidel et al. (2016) underestimate by this empirical model the intrinsic velocity dispersion and one reason was already stated, when introducing Equation (3.20). They do not consider that the velocity dispersion depends on a gravitational part, which increases the velocity dispersion in the central parts (see also Section 3.6). In galaxies, the gravitational forces play a significant role in shaping the velocity distribution of stars and gas. In the central regions, where the gravitational potential

[5]LARS09 and LARS13 are not calculated with the M. Varidel et al. (2016) method, as they contain two observations that were not sampled on the same wavelength grid.

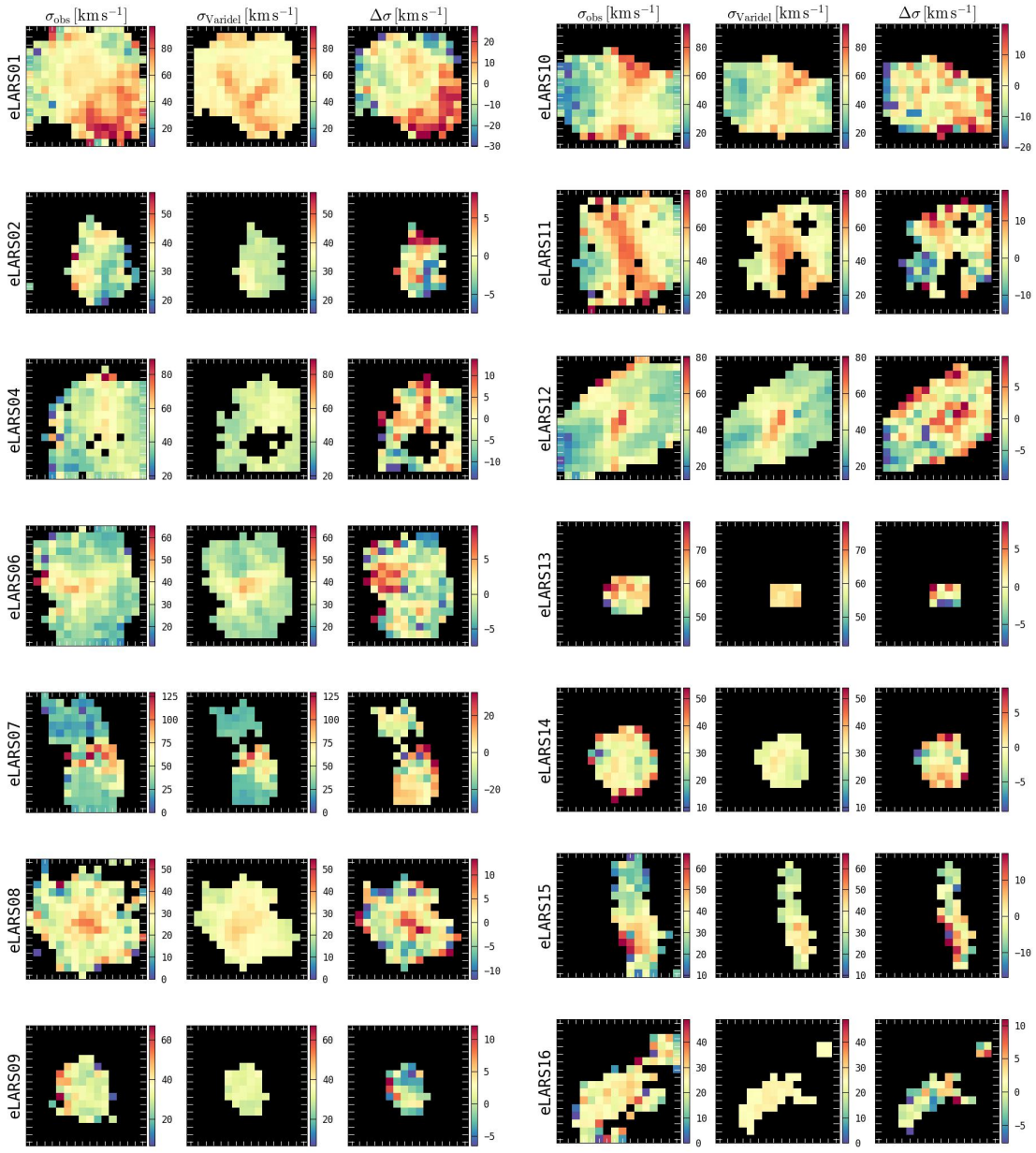

Figure 3.9: The observed velocity dispersion (left), the M. Varidel et al. (2016)-fitted velocity dispersion (middle) and the residual (right) for our sample. The color bar stretch is the same in the left and centre panel, but different in the right hand panels.

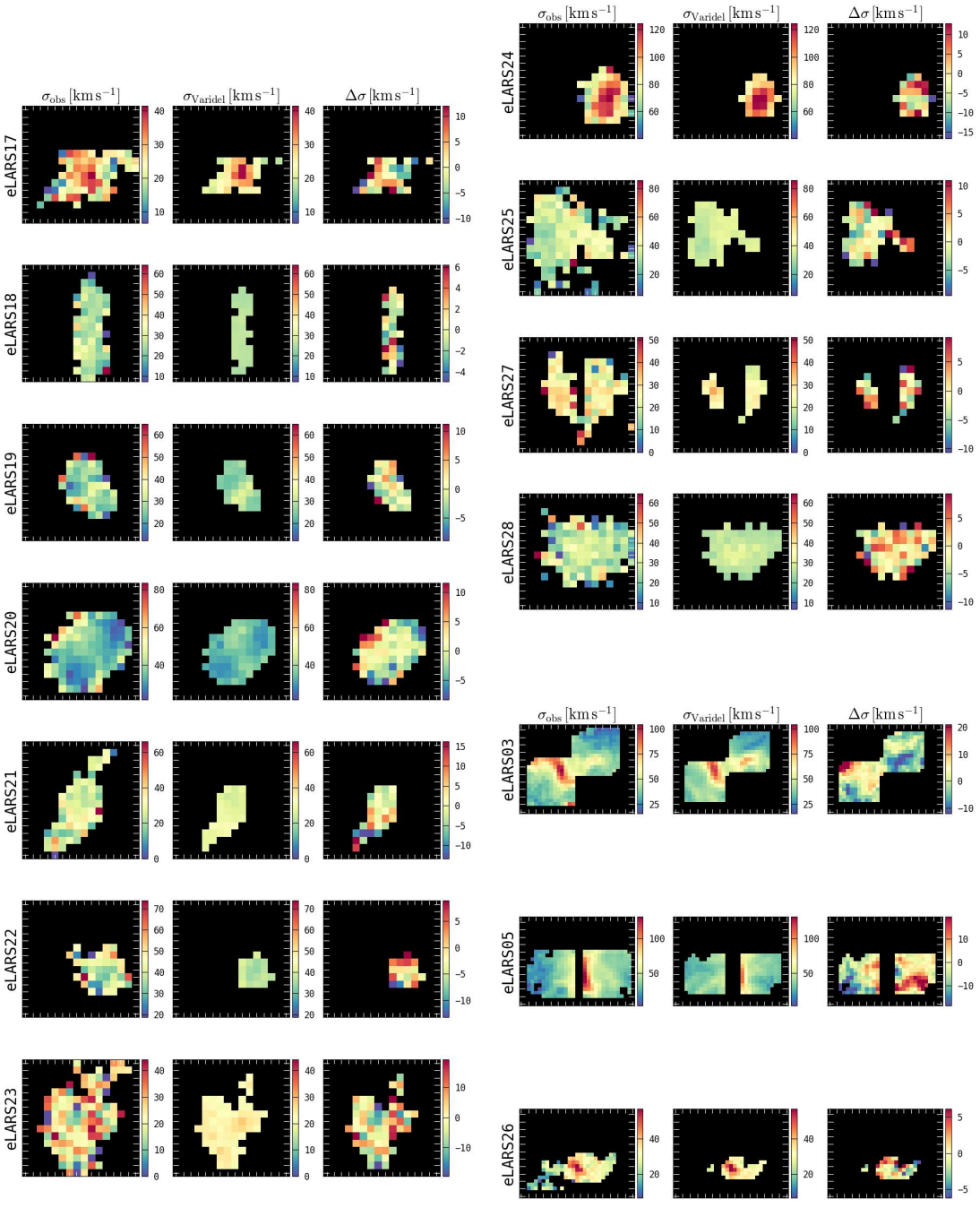

Figure 3.9 continued.

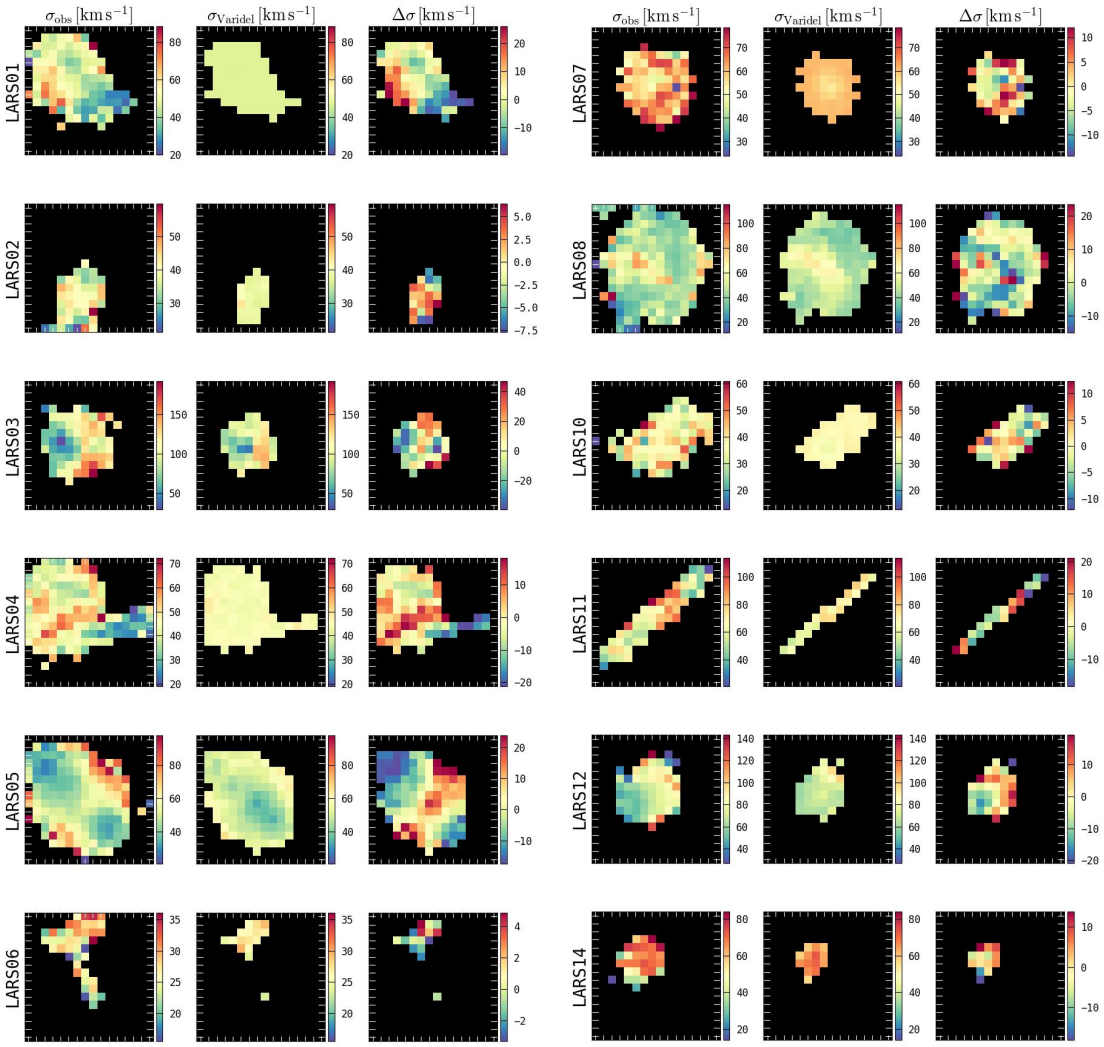

Figure 3.9 continued.

is often stronger due to the concentration of mass, the gravitational component of the velocity dispersion has to be higher. This is because the gravitational attraction between stars and gas leads to increased random motions and a higher overall velocity dispersion. Moreover, in their calculation they loose the edge spaxels, which is problematic for galaxies with a low number of spaxels with S/N larger than 6. In Table 3.6 we present the calculated velocity dispersion values for the M. Varidel et al. (2016) empiric model on our LARS and eLARS galaxies. The uniform weighted mean ranges from 1.5 $\mathrm{km\,s^{-1}}$ (LARS06) to 29.7 $\mathrm{km\,s^{-1}}$ (eLARS01) with a mean of 7.4 $\mathrm{km\,s^{-1}}$, significantly lower than our empiric method (see Section 3.2 and 3.3). The weighted mean ranges from 12.5 $\mathrm{km\,s^{-1}}$ (eLARS27) to 54.7 $\mathrm{km\,s^{-1}}$ (eLARS24) with a mean of 27.2 $\mathrm{km\,s^{-1}}$.

Table 3.6: Velocity dispersions for our sample derived with the method introduced in M. Varidel et al. (2016).

ID	$\sigma_{\mathrm{m,\ uniform,\ Varidel}}$ [km s^{-1}]	$\Delta\sigma_{\mathrm{m,\ uniform,\ Varidel}}$ [km s^{-1}]	$\sigma_{\mathrm{m,\ Varidel}}$ [km s^{-1}]	$\Delta\sigma_{\mathrm{m,\ Varidel}}$ [km s^{-1}]
LARS01	13.0	0.6	44.0	0.1
LARS02	3.1	0.7	30.9	0.2
LARS03	9.8	1.4	45.5	0.2
LARS04	14.4	0.3	36.7	0.1
LARS05	19.2	0.5	38.0	0.1
LARS06	1.5	0.5	15.2	0.2
LARS07	10.8	0.8	53.9	0.2
LARS08	13.7	0.4	28.3	0.1
LARS10	6.2	0.6	28.2	0.4
LARS11	4.4	1.0	30.6	0.5
LARS12	7.9	1.0	54.5	0.3
LARS14	3.2	1.1	50.3	0.4
ELARS01	29.7	0.3	45.1	0.1
ELARS02	5.5	0.4	27.6	0.2
ELARS03	8.8	0.2	20.5	0.1
ELARS04	13.8	0.4	25.4	0.2
ELARS05	9.7	0.3	18.4	0.2
ELARS06	12.0	0.2	20.4	0.1
ELARS07	4.9	0.5	16.3	0.2
ELARS08	8.0	0.3	16.5	0.2
ELARS09	3.2	0.7	22.7	0.3
ELARS10	8.4	0.4	14.5	0.2
ELARS11	12.0	0.4	23.7	0.2
ELARS12	12.1	0.3	19.6	0.1
ELARS13	2.6	1.3	47.1	0.4
ELARS14	3.5	0.6	21.1	0.1
ELARS15	3.7	0.4	20.7	0.3
ELARS16	3.3	0.4	14.3	0.2
ELARS17	1.7	0.5	8.8	0.4
ELARS18	2.7	0.6	17.0	0.3
ELARS19	2.6	0.6	19.3	0.2
ELARS20	6.7	0.5	21.9	0.2
ELARS21	2.8	0.8	15.2	0.6
ELARS22	2.8	1.3	28.6	0.8
ELARS23	5.5	0.7	18.0	0.6
ELARS24	6.6	1.5	54.7	0.9
ELARS25	6.6	0.5	23.6	0.3
ELARS26	2.6	0.6	19.9	0.5
ELARS27	2.2	0.6	12.5	0.4
ELARS28	5.9	0.5	20.6	0.3

3.5 Correcting for PSF smearing as in Yu et al. (2021)

Wisnioski et al. (2015) introduced another PSF correction method and uses it on the initial dataset of the KMOS^{3D} survey. KMOS^{3D} survey measures the Hα kinematics of high-z galaxies. Yu et al. (2021) applies this method to low-z galaxies. Following Yu et al. (2021) we test this method on our sample. Yu et al. (2021) measures the velocity dispersion along the major kinematic axis. We estimate the major kinematic axis by `pafit fit_kinematic_pa`[6] (see Appendix C in Krajnovic et al. (2006)). We show the derived axis on the velocity maps and velocity dispersion maps in Figure 3.12 in the first two columns. Along this derived axis, we extract the spaxles and their observed line of sight velocity and velocity dispersion, which are in a distance of maximal $\pm 1''$ to the major kinematic axis. This is shown in Figure 3.12 in the last two columns.

We determine a radius by eye for each galaxy, where the rotation curve along the line of sight flattens (blue vertical line in the figures). We can now distinguish the along the kinematic major axis extracted spaxels into larger and smaller radius than the determined radius. We then calculate the PSF smearing corrected velocity dispersion, σ_{Yu}, by averaging the spaxels with radius larger than the determined radius (red data points in the figures). We apply the method to our RDs and we list the values of σ_{Yu} in Table 3.9.

[6] https://pypi.org/project/pafit/

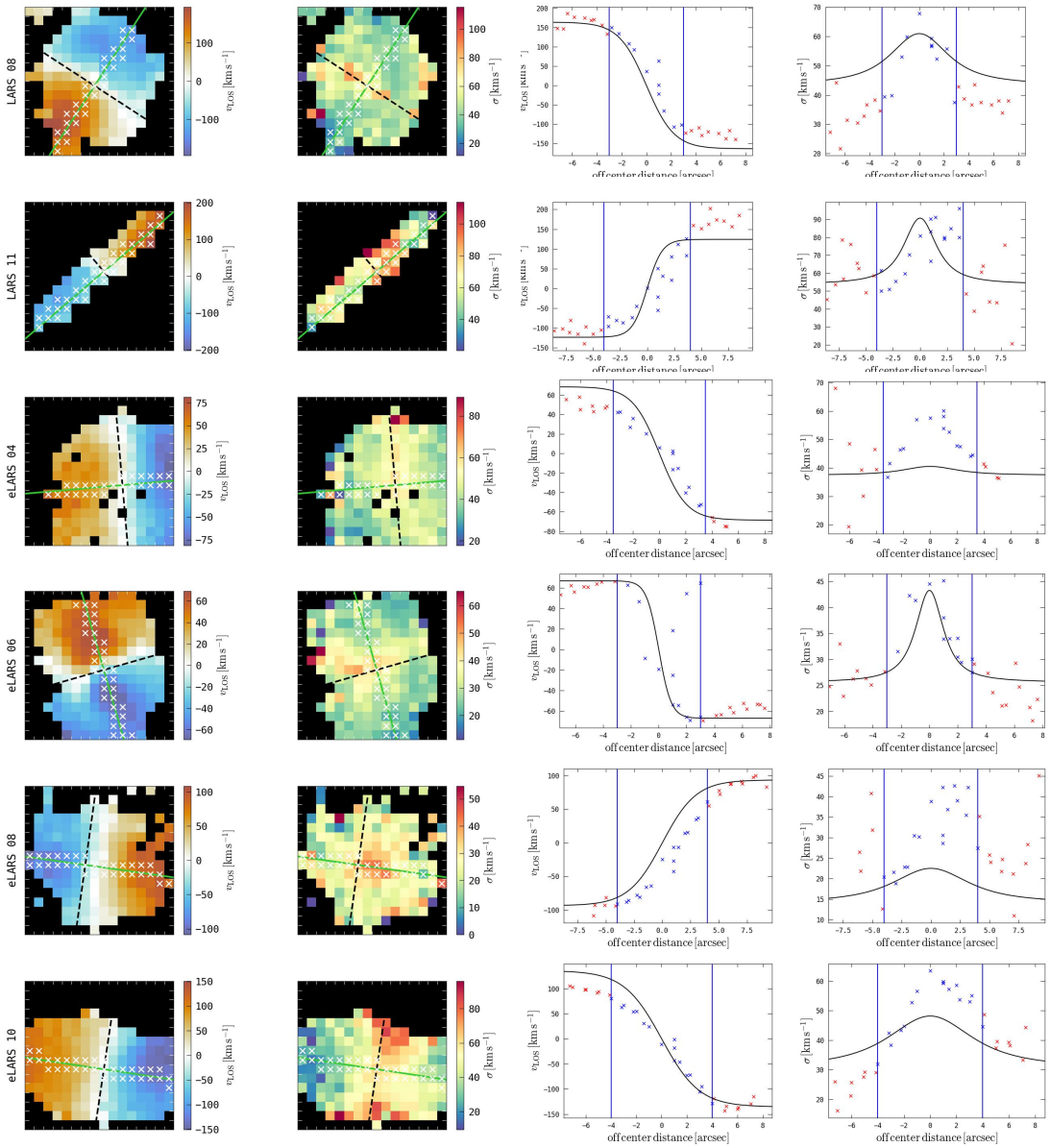

Figure 3.12: Velocity dispersion σ_{Yu} with the Yu et al. (2021) method. First column: line of sight velocity, in green the estimated major kinematic axis, in black the estimated minor kinematic axis. Second column: line of sight velocity dispersion overplotted with the kinematic axis. Third column: along the major kinematic axis extracted line of sight rotation curve, in black the rotation curve modeled with galpak, blue vertical line: estimated radius, where the rotation curve flattens. Fourth column: Velocity dispersion along the major kinematic axis, black: the galpak modeled velocity dispersion (see Section 3.6).

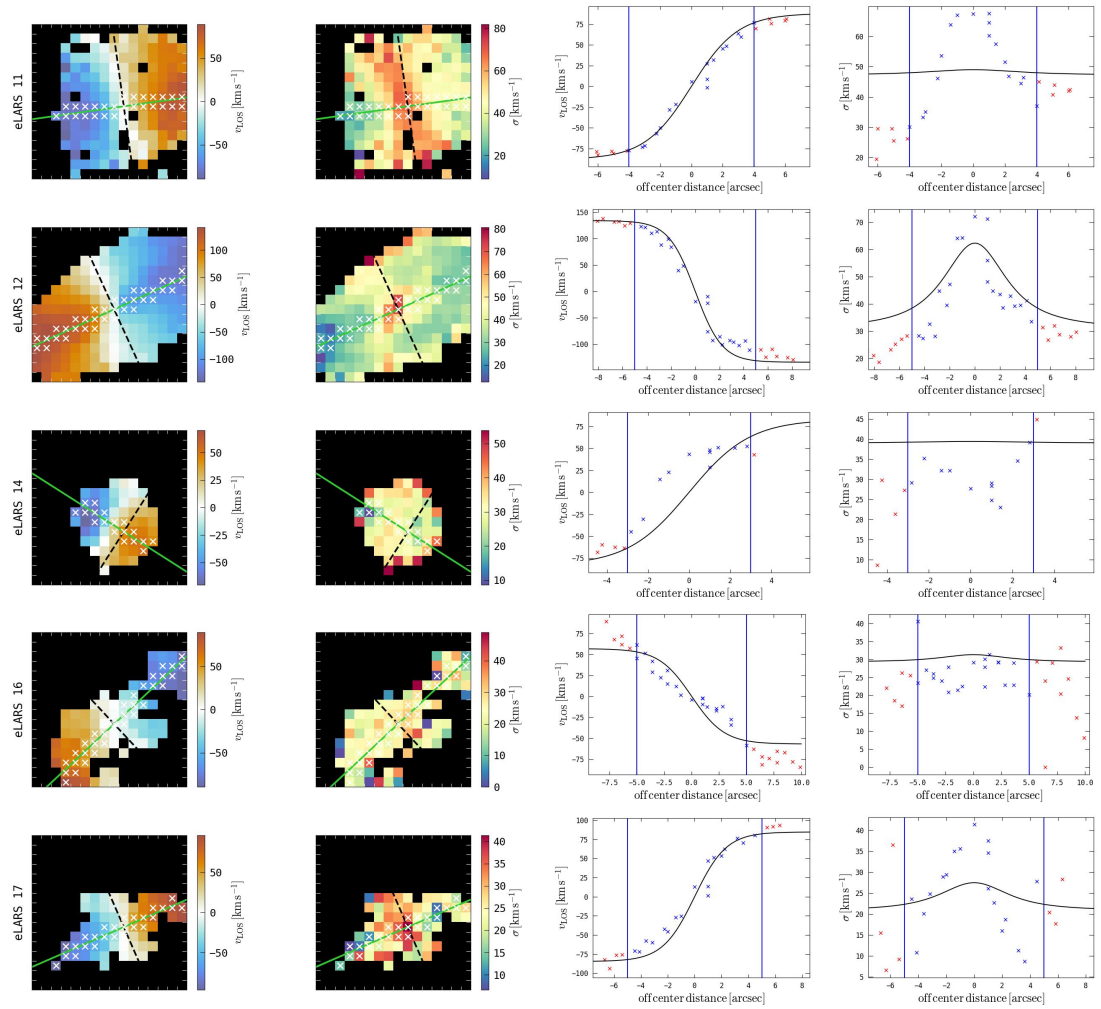

Figure 3.12 continued.

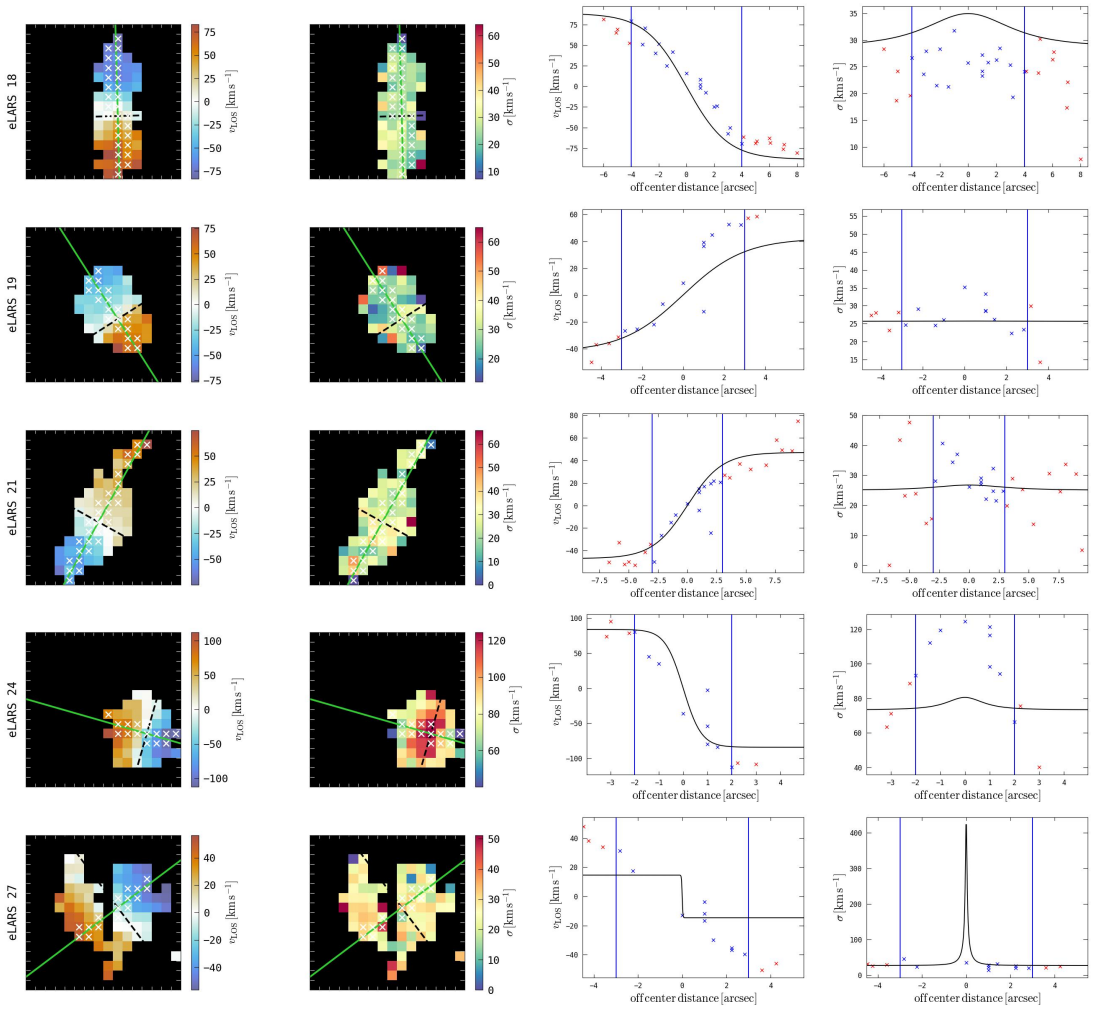

Figure 3.12 continued.

3.6 Modeling with GalPaK3D

We have introduced four different empiric approaches to obtain kinematic parameters of a galaxy. Now we want to introduce a completely different approach: a disk model. We model our RDs with the software GalPaK3D (Bouché et al. 2015). GalPaK3D uses a full 3D parametric disk model that is fitted on the 3D data cube. To model our RDs, we subtract a running median in spectral direction (width of the median is 150 spectral pixels) to remove the stellar continuum and cut out the PMAS data cube and the variance cube in the wavelength range of the Hα line.

The model employs Markov Chain Monte Carlo (MCMC) techniques to explore the high-dimensional parameter space and find the best-fit model that matches the observed data. MCMC uses a Markov Chain, which is a sequence of parameter values, where each value is only dependent on the previous one and moves by taking random steps in the parameter space, guided by a proposal distribution. For each proposed parameter value, an acceptance step is performed. The likelihood of the data given the proposed parameter value and the likelihood given the current parameter value are compared. If the new value improves the fit to the data, it is accepted with a higher probability. Otherwise, it may still be accepted with some probability to allow exploration of the parameter space. The Markov Chain continues to move through the parameter space, generating a sequence of parameter values. After the so-called burn-in phase, the chain tends to converge to the true posterior distribution, which represents the best-fit model that matches the observed data. In Figure A.43 of the appendix we show the characteristic 'burn-in' phase and the convergence phase for the GalPaK3D MCMC on a specific galaxy.

GalPaK3D uses a Sersic profile to describe the surface brightness distribution of the galaxies

$$I(r) = I_e \exp\left(-b_n \left[(r/R_e)^{1/n} - 1\right]\right), \tag{3.22}$$

with the Sersic index, which determines the shape of the profile, with R_e the effective radius, with b_n such that R_e is equivalent to the half-light radius $R_{1/2}$ and I_e the surface brightness at the effective radius R_e. For simplicity, we fix $n = 1$, which gives an exponential profile with $b_{1.0}1.68$ (Bouché et al. 2015, Graham and Driver 2005). $n = 0.5$ would give a Gaussian profile and $n = 4$ a De-Vaucouleurs profile. Higher value of n results in a more centrally concentrated profile, while lower values of n correspond to more extended profiles. GalPaK3D was mainly used to model high-z galaxies and therefore the light profile is a bit simplistic for most of our star-forming disks. It is not perfect for our galaxies, because some show several different bright regions, but it works quite well, as demonstrated below. Blobby3D (M. R. Varidel, Croom, Lewis, Brewer, et al. 2019) is an alternative

for a code that provides a more versatile light distribution, but at the price of computational complexity.

We want to model the kinematics of the whole disk and therefore, we need to assume a functional form for the galaxy rotation curve. The main assumptions in disk models are circular orbits and therefore simplify the description of the kinematics as a radial function. We do not see the circular orbits, we see a projection of them. Different models for the rotation curve exist, like an arctan profile ($v(r) = V_{\rm max}\frac{2}{\pi}\arctan(r/R_t)$, Puech et al. 2008) or an inverted exponential profile ($v(r) = V_{\rm max}[1 - \exp(r/R_t)]$, Feng and Gallo 2011). For the velocity we assume a rotating disk and use a tanh profile, as the rotation curves of rotating disks show a steady rise to a peak velocity (Andersen and Bershady 2013):

$$v(r) = V_{\rm max}\tanh\left(\frac{r}{R_t}\right) \tag{3.23}$$

with $V_{\rm max}$ as the maximum circular velocity, R_t the turnover radius and r the radius in the galaxy plane. Physically the rotation curve rises in the center part of a galaxy and in the outer regions the rotation curve levels off and flattens. The tanh provides a smooth transition between the central rising part and the outer flatted part.

For the LSF and PSF we assume Gaussians. The Gaussians are caracterized by their FWHM. For the spectral LSF we take for the FWHM the ratio of the peak position of the Hα line and the resolving power. For the spatial PSF we take the seeing from Table 2.1 for the FWHM.

In the GalPaK3D model the total line of sight velocity dispersion $\sigma_{\rm GalPaK3D}$, which is the intrinsic velocity dispersion of the model (comparable to the velocity dispersion introduced in Section 3.2), consists of three terms added in quadrature:

- **Local isotropic velocity dispersion $\sigma_{\rm GalPaK,grav}$**: This term is driven by the self-gravity of the disk and is for compact thick or large thin disks

$$\sigma_{\rm Galpak,grav}(r)/h_z = v(r)/r, \tag{3.24}$$

  where $v(r)$ is the radial velocity profile and h_z is the disk thickness, which is fixed in GalPaK3D to 0.15 half-light radius $R_{1/2}$.

- **Mixing term $\sigma_{\rm GalPaK,mix}$**: This mixing arises due to the three-dimensional nature of the rotating disk and the projection of its velocity field onto the two-dimensional plane of the sky. When we observe such a system, the line of sight velocities from different spatial locations along the line-of-sight axis get mixed together. This is important especially for thick disks with large h_z.

- **Intrinsic dispersion** $\sigma_{\mathbf{GalPaK,const}}$: This turbulence term is isotropic and spatially constant and dominates the other two terms.

We give GalPaK3D our data cuboid and our variance cuboid and set the random scale parameter for the MCMC, the number of iterations and the seeing of the observations and the model returns us the modeled data cube, maps and parameters. The model compares the data directly with a parametric model mapped in x, y, λ coordinates. The model applies a spectral LSF and a spatial PSF to generate a 3D convolution kernel depending on the observing instrument conditions. It returns the model parameters, the intrinsic modeled data cube and the modeled observed data cube, which is a convolution of the intrinsic data cube with the kernel.

The output from GalPaK for the velocity dispersion is the intrinsic dispersion and we will use this to compare our different empiric methods. We list the output parameters for our RD from GalPaK in Table 3.7.

In Figure 3.15 we compare the model and our data for the 16 RDs that we modelled in our sample. We find that the model resembles the measured data very well except at some border spaxels, where sometimes the modeled galaxy is not extended enough. For most of the galaxies the simple parametric model results in line of sight velocity maps that capture qualitatively the large scale kinematics of the Hα emitting gas. However the residuals do not appear to be spatially randomly distributed noise. They show kinematical features that are not captured by GalPaK. The differences are significantly smaller that the overall shearing velocity (see $\Delta_{v,\mathrm{GP}}$ in Table 3.8). The velocity dispersion shows also some times kinematical features that are not captured by GalPak (eg. eLARS10 or eLARS11), however, for most of the galaxies the residual maps appear to be randomly distributed noise. We get an absolute mean $|\Delta_{\sigma,\mathrm{GP}}| \lesssim 5\,\mathrm{km\,s^{-1}}$ for most of the sample, which is satisfactory. The model tend to have slightly higher dispersions. The standard deviation of the residual maps is typically around $10\,\mathrm{km\,s^{-1}}$. GalPaK was made to model spatially unresolved high-z disk galaxies. We model with GalPaK low-z galaxies, which are spatially resolved. So it is not surprising that individual sub-structures are not captured by GalPaK. However, the overall congruence of the velocity and velocity dispersion maps of model and data is satisfactory. The good congruence between data and model can also be seen as affirmation for us visually classifying these systems as disks. Isobe et al. (2023) models low-z low-metallicity star-forming galaxies and present also a satisfactory agreement between model and data.

Overall, we can conclude this section that GalPaK delivers valuable results for the RDs. We will thus use $\sigma_{\mathrm{GalPaK,const}}$ values as our ground truth. Given the above analysis of the residual maps, we consider a method as successful in recovering the truth, if it is on average within $10\,\mathrm{km\,s^{-1}}$ of the dispersion values from the model.

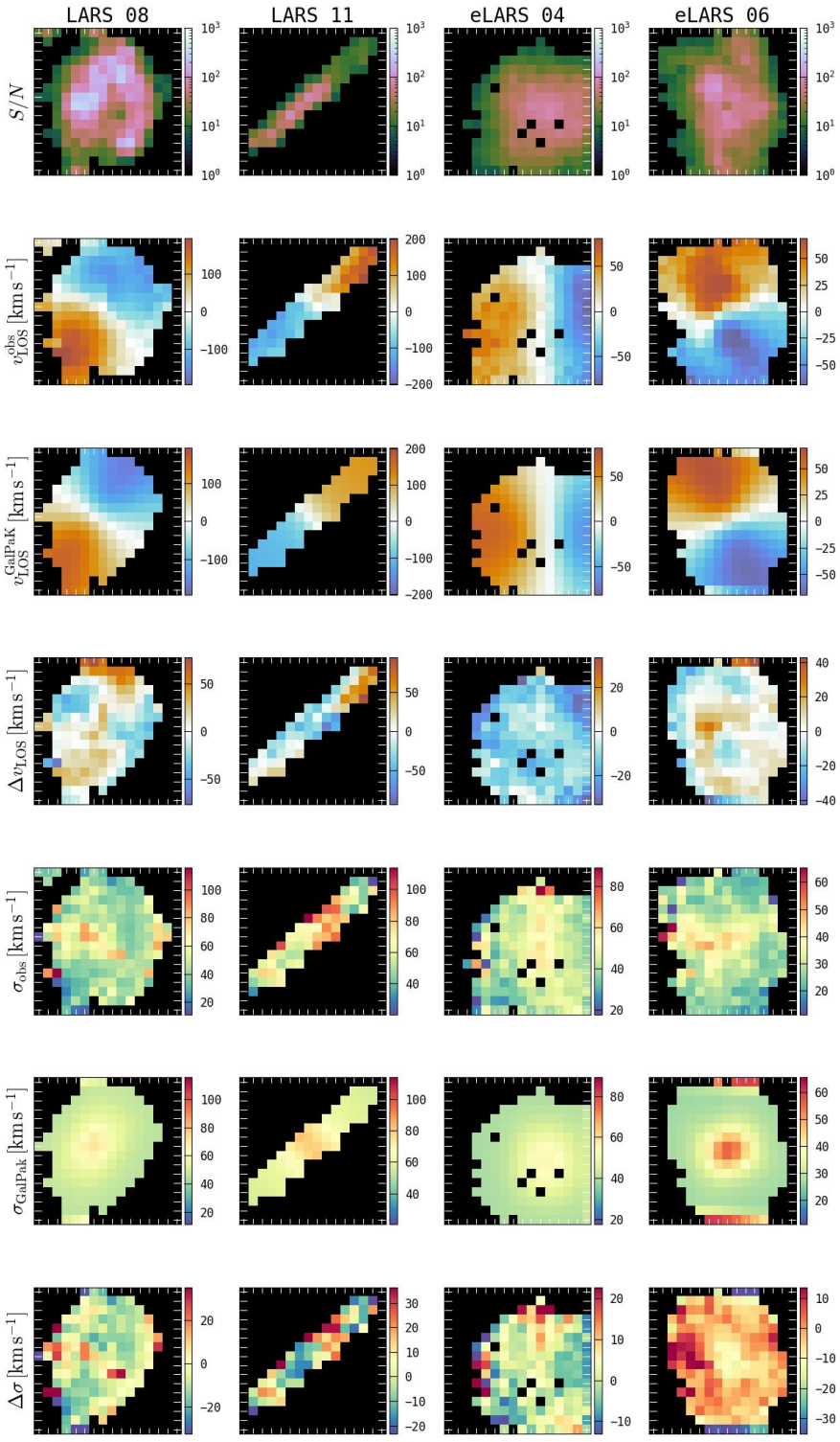

Figure 3.15: Comparison of PMS data and GalPaK model, from top to bottom: PMAS S/N in Hα, observed line of sight velocity measured from the Hα line, GalPaK modeled line of sight velocity, residual map for the velocity, observed velocity dispersion map measured on the Hα line, GalPaK modeled velocity dispersion and residual map for the velocity dispersion. Except for the S/N, all maps are in units of km s^{-1}.

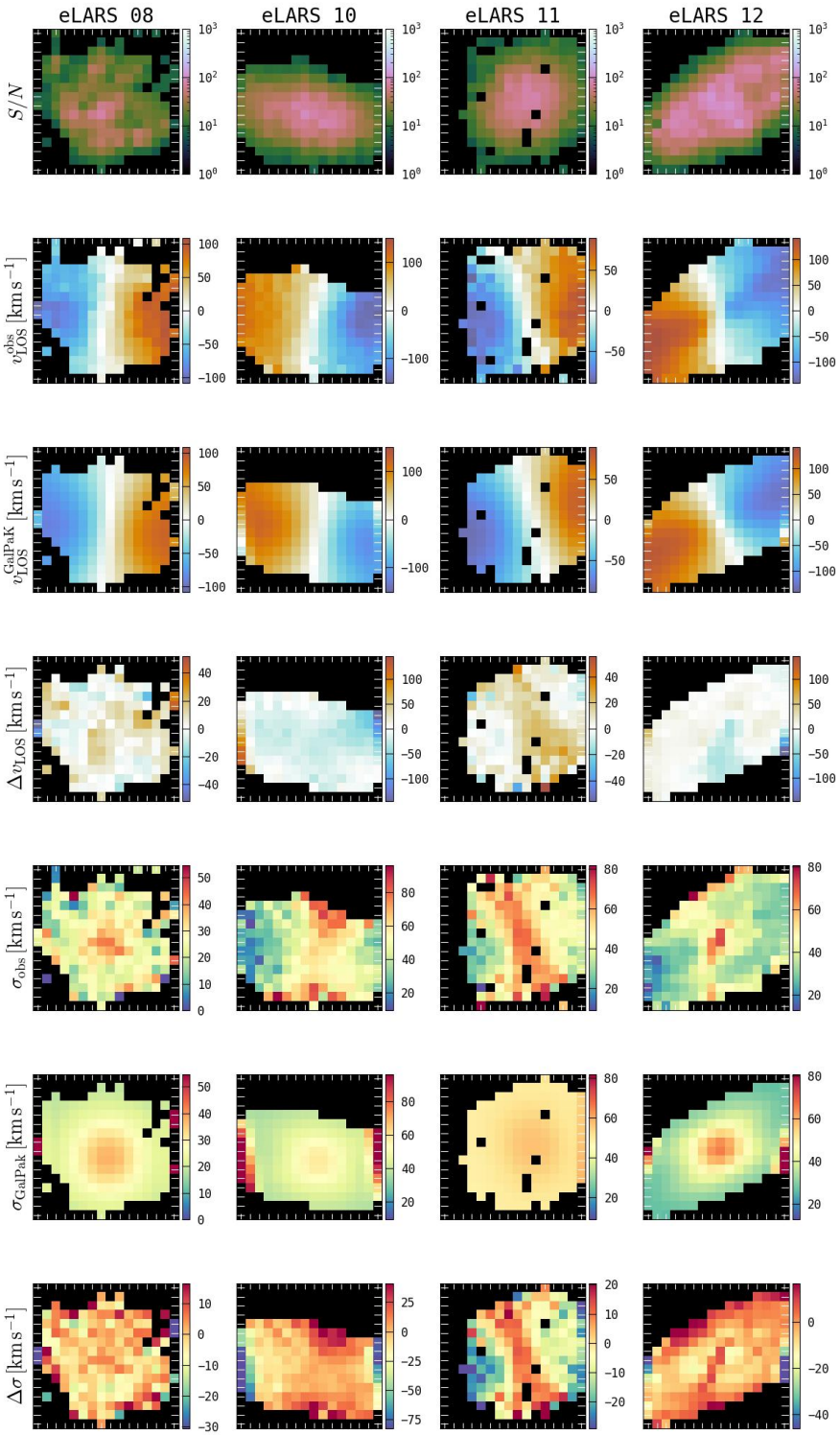

Figure 3.15 continued.

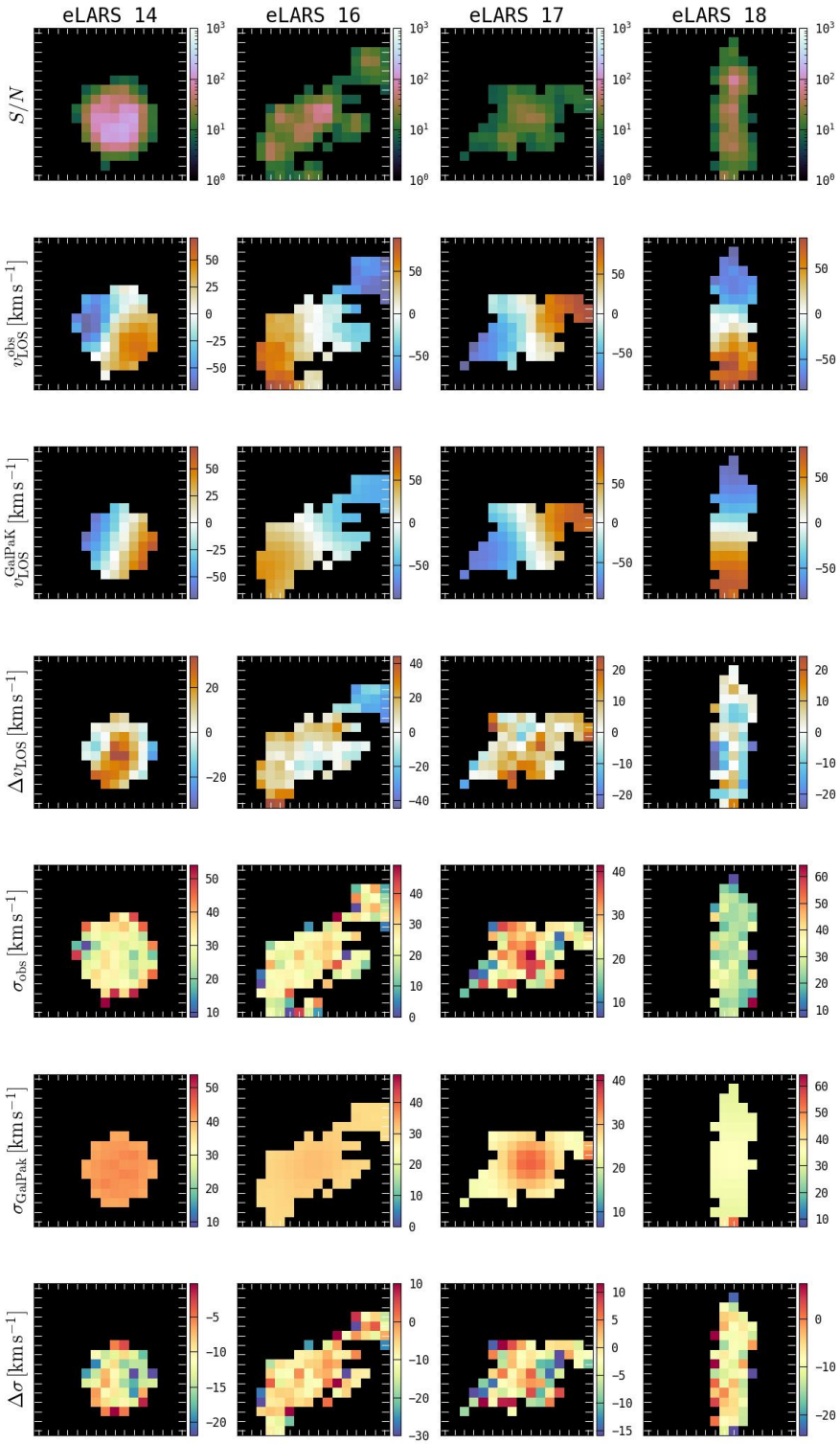

Figure 3.15 continued.

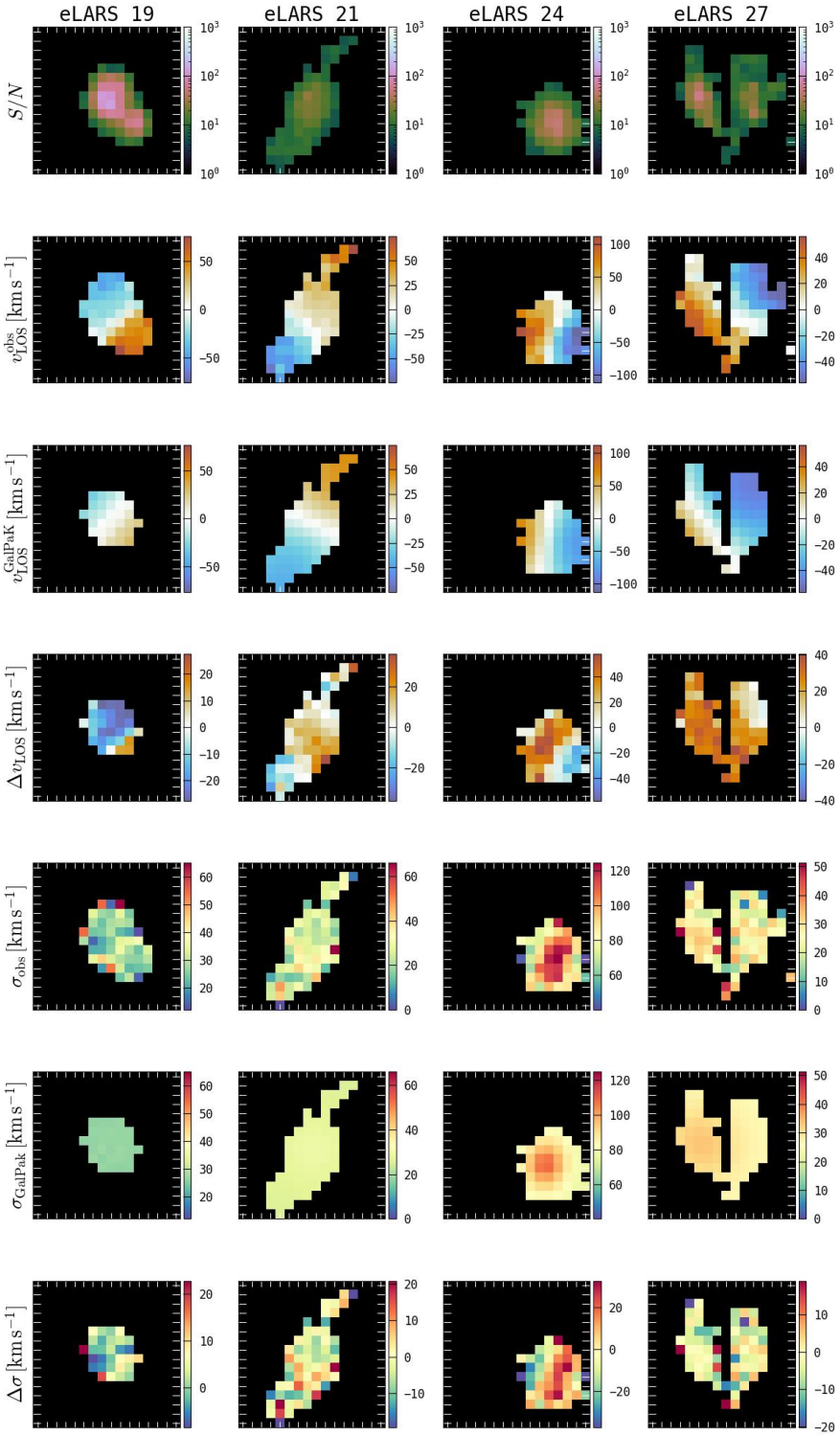

Figure 3.15 continued.

Table 3.7: Random scale parameter and number of iterations for the MCMC and GalPaK output values for all modeled RDs of our sample.

ID	random scale	max iteration	$R_{1/2}$ [pix]	$\Delta R_{1/2}$ [pix]	$R_{\rm t}$ [pix]	$\Delta R_{\rm t}$ [pix]	$V_{\rm max}$ [km s^{-1}]	$\Delta V_{\rm max}$ [km s^{-1}]	$\sigma_{\rm GalPaK,const}$ [km s^{-1}]	$\Delta\sigma_{\rm GalPaK,const}$ [km s^{-1}]
LARS08	0.08	20000	3.89	0.01	2.23	0.01	210.32	0.38	43.28	0.15
LARS11	0.08	40000	5.42	0.03	1.38	0.04	124.17	0.82	53.64	0.6
ELARS04	0.08	20000	3.09	0.01	2.05	0.03	162.79	1.52	37.43	0.31
ELARS06	0.02	80000	3.1	0.01	0.89	0.01	99.61	0.43	25.52	0.15
ELARS08	0.08	40000	3.77	0.02	3.0	0.01	167.02	2.23	13.95	0.62
ELARS10	0.08	20000	5.49	0.02	2.99	0.01	147.39	0.36	30.41	0.34
ELARS11	0.02	80000	2.95	0.01	2.99	0.01	169.22	2.22	47.25	0.23
ELARS12	0.08	20000	5.97	0.02	2.21	0.01	147.39	0.36	30.41	0.34
ELARS14	0.08	20000	1.34	0.0	2.99	0.03	204.53	2.02	38.96	0.12
ELARS16	0.02	40000	3.89	0.04	3.0	0.0	61.85	0.73	29.27	0.38
ELARS17	0.08	80000	3.37	0.08	2.37	0.1	110.75	2.12	20.75	0.79
ELARS18	0.02	80000	4.55	0.04	2.98	0.02	88.95	0.64	28.46	0.39
ELARS19	0.08	20000	1.04	0.01	2.99	0.01	67.05	1.08	25.62	0.21
ELARS21	0.08	20000	4.05	0.08	2.98	0.03	50.69	1.07	24.97	0.67
ELARS24	0.08	60000	1.99	0.01	0.75	0.03	259.57	3.3	73.28	0.67
ELARS27	0.8	20000	5.99	0.02	0.03	0.01	47.32	0.83	26.67	0.61

3.7 Comparing methods to calculate the velocity dispersion

In the previous sections, we had a look at different empiric methods and a disk model to calculate the intrinsic velocity dispersion for our sample. Now we have four different empiric methods to calculate the observed intrinsic velocity dispersion and seven different non-parametric values σ_{m}, $\sigma_{\mathrm{m,\ uniform}}$, $\sigma_{\mathrm{m,\ corr}}$, $\sigma_{\mathrm{m,\ uniform,\ corr}}$, $\sigma_{\mathrm{m,\ Varidel}}$, $\sigma_{\mathrm{m,\ uniform,\ Varidel}}$, σ_{Yu}. Additionally, we have the modeled value by GalPaK3D. All velocity dispersion values are listed in Table 3.9 for the RDs, as we modeled only these galaxies with GalPaK3D. Now, we are interested, which of our different empiric values resembles the true intrinsic velocity dispersion best. Therefore, we consider GalPaK3D to be the ground truth. In Table 3.10 we list the differences between the empiric velocity dispersion values and GalPaK3D. To test, which empiric estimate is best, we calculate the parameter $\mathcal{P}$, which is an analogous to the standard deviation. It was introduced by Davies et al. (2011) for this purpose, and it is calculated via

$$\mathcal{P} = \mathcal{S}\left[\frac{1}{n}\sum_{j=1}^{n}\left(\sigma_j^{\mathrm{empiric}} - \sigma_j^{\mathrm{GalPaK}}\right)^2\right]^{1/2} \tag{3.25}$$

with

$$\mathcal{S} = \frac{\langle \sigma_j^{\mathrm{empiric}} - \sigma_j^{\mathrm{GalPaK}} \rangle}{\left|\langle \sigma_j^{\mathrm{empiric}} - \sigma_j^{\mathrm{GalPaK}} \rangle\right|} \tag{3.26}$$

as sign, which indicates whether the empiric value is, on average, more or less than the GalPaK3D value; n the number of galaxies.

We list $\mathcal{P}$ for the different methods in the last row in Table 3.10 and in the legend of Figure 3.15. eLARS24 is a RD, but shows Hα double components and is not considered in our analysis. If $|\mathcal{P}|$ is smaller than 10 $\mathrm{km\,s^{-1}}$, we consider the method useful, based on our findings in the previous section. Our comparison shows that M. Varidel et al. (2016) largely underestimates the velocity dispersion. Their method seems to over correct the actual bias. The Yu et al. (2021) method works nice for most of the galaxies, which results in $\mathcal{P} < -10\,\mathrm{km\,s^{-1}}$, but the method fails for four galaxies.

We find an acceptable positive bias for the weighted and unweighted mean, but the bias slightly decreases by 1 $\mathrm{km\,s^{-1}}$, when we use our masking scheme. Based on this analysis, we adopt $\sigma_{\mathrm{m,uniform,corr}}$ as our observational estimate of the intrinsic velocity dispersion and we use $\sigma_{\mathrm{m,uniform,corr}}$ for our further analysis. We note that we have also performed the analysis in Chapter 4 with the other measures for which

Table 3.8: Summarizing statistics of the residual maps $v_{\rm obs} - v_{\rm GalPaK}$ and $\sigma_v - \sigma_{\rm GalPaK,const}$ shown in Figure 3.15. Here, $\Delta_{v,\rm GP}$ is the mean of the absolute deviation over all spaxels, $\Delta_{v,\rm GP} = \langle |v_{{\rm obs},i} - v_{{\rm GalPaK},i}| \rangle$, and $\mathrm{std}_{v,\rm GP}$ is the associated standard deviation. Moreover, $\Delta_{\sigma,\rm GP} = \langle \sigma_{{\rm obs},i} - \sigma_{{\rm GalPaK,const},i} \rangle$, and $\mathrm{std}_{\sigma,\rm GP}$ is the associated standard deviation.

ID	$\Delta_{v,\rm GP}$ [km s^{-1}]	$\Delta_{\sigma,\rm GP}$ [km s^{-1}]	$\mathrm{std}_{v,\rm GP}$ [km s^{-1}]	$\mathrm{std}_{\sigma,\rm GP}$ [km s^{-1}]
L08	20.5	-5.4	15.3	14.9
L11	30.0	2.1	21.0	16.8
E04	13.2	0.6	7.1	8.8
E06	8.8	-3.5	7.5	10.4
E08	7.9	-1.1	7.9	10.7
E10	22.3	-5.0	23.0	28.5
E11	10.8	-5.0	8.9	12.8
E12	11.9	-2.8	15.5	12.0
E14	13.2	-11.6	9.4	5.7
E16	13.7	-7.5	9.8	8.4
E17	8.4	-2.5	5.9	7.2
E18	7.4	-8.3	6.1	6.6
E19	17.2	2.3	7.6	7.7
E21	10.7	-0.9	7.8	9.9
E27	22.6	-2.6	10.1	8.3

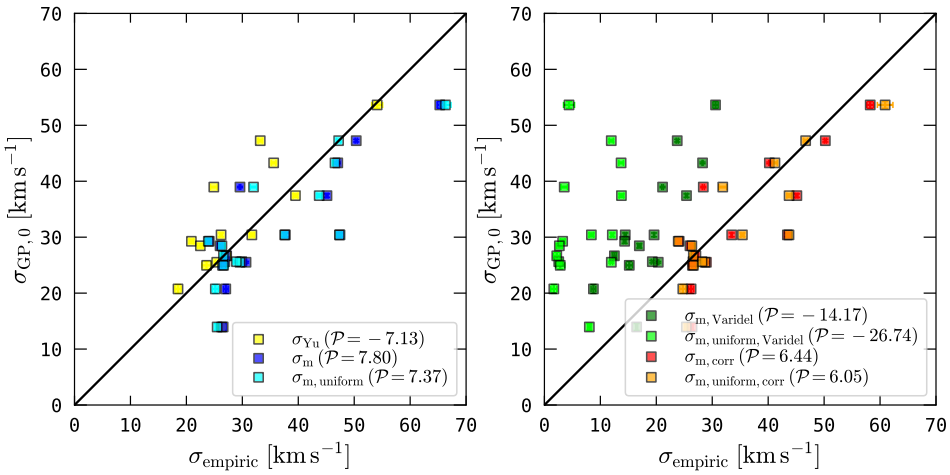

Figure 3.16: Comparison between velocity dispersions calculated with the empirical methods and the velocity dispersion from the GalPak^{3D} modelling. For each method the $\mathcal{P}$ measure from Equation 3.25 is given in the legend.

$\mathcal{P} < 10\,\mathrm{km\,s^{-1}}$, and we find they do not affect the quantitative and qualitative results of our analysis.

Davies et al. (2011) also compare different methods to calculate the intrinsic velocity dispersion using the same parameter $\mathcal{P}$. They also report that the mean weighted dispersion estimators that are biased towards brighter regions, are more affected by PSF smearing, which is in agreement with our findings.

Our simple mean and our simple weighted mean are not so biased in our data. We may assume that our galaxies are too close to be significant affected by PSF smearing. This does not hold for observations at high-z, e.g. for the KMOS^{3D} survey and further work has also to be investigated in high-z galaxies.

Table 3.9: Different empiric and modeled velocity dispersion values with uncertainties for all RDs of the LARS and eLARS sample.

ID	$\sigma_{\mathrm{m,\ uniform}}$ $[\mathrm{km\,s^{-1}}]$	σ_{m} $[\mathrm{km\,s^{-1}}]$	$\sigma_{\mathrm{m,\ uniform,\ corr}}$ $[\mathrm{km\,s^{-1}}]$	$\sigma_{\mathrm{m,\ corr}}$ $[\mathrm{km\,s^{-1}}]$	$\sigma_{\mathrm{m,\ uniform,\ Varidel}}$ $[\mathrm{km\,s^{-1}}]$	$\sigma_{\mathrm{m,\ Varidel}}$ $[\mathrm{km\,s^{-1}}]$	$\sigma_{\mathrm{GalPaK,\ const}}$ $[\mathrm{km\,s^{-1}}]$	σ_{Yu} $[\mathrm{km\,s^{-1}}]$
LARS08	46.6 ± 0.4	47.1 ± 0.1	41.2 ± 0.4	40.2 ± 0.1	13.7 ± 0.4	28.3 ± 0.1	43.3 ± 0.2	38.0
LARS11	66.3 ± 1.0	65.3 ± 0.5	60.9 ± 1.4	58.2 ± 0.6	4.4 ± 1.0	30.6 ± 0.5	53.6 ± 0.6	20.5
ELARS04	43.7 ± 0.4	45.1 ± 0.2	43.7 ± 0.4	45.1 ± 0.2	13.8 ± 0.4	25.4 ± 0.2	37.4 ± 0.3	36.4
ELARS06	29.6 ± 0.2	30.7 ± 0.1	28.7 ± 0.2	29.0 ± 0.1	12.0 ± 0.2	20.4 ± 0.1	25.5 ± 0.2	34.0
ELARS08	25.5 ± 0.3	26.6 ± 0.2	25.4 ± 0.3	26.4 ± 0.2	8.0 ± 0.3	16.5 ± 0.2	13.9 ± 0.6	15.3
ELARS10	47.4 ± 0.4	47.5 ± 0.2	43.7 ± 0.4	43.4 ± 0.2	8.4 ± 0.4	14.5 ± 0.2	30.4 ± 0.3	25.9
ELARS11	47.2 ± 0.4	50.4 ± 0.2	46.7 ± 0.4	50.2 ± 0.2	12.0 ± 0.4	23.7 ± 0.2	47.3 ± 0.2	42.4
ELARS12	37.6 ± 0.2	37.7 ± 0.1	35.4 ± 0.3	33.5 ± 0.1	12.1 ± 0.3	19.6 ± 0.1	30.4 ± 0.3	29.8
ELARS14	32.0 ± 0.6	29.6 ± 0.1	31.9 ± 0.7	28.4 ± 0.2	3.5 ± 0.6	21.1 ± 0.1	39.0 ± 0.1	25.0
ELARS16	23.9 ± 0.4	24.1 ± 0.2	23.9 ± 0.4	24.1 ± 0.2	3.3 ± 0.4	14.3 ± 0.2	29.3 ± 0.4	8.2
ELARS17	25.2 ± 0.5	27.0 ± 0.4	24.7 ± 0.6	26.2 ± 0.5	1.7 ± 0.5	8.8 ± 0.4	20.8 ± 0.8	17.8
ELARS18	26.4 ± 0.6	26.0 ± 0.3	26.4 ± 0.6	26.0 ± 0.3	2.7 ± 0.6	17.0 ± 0.3	28.5 ± 0.4	7.7
ELARS19	28.9 ± 0.6	26.9 ± 0.2	28.2 ± 0.6	26.6 ± 0.2	2.6 ± 0.6	19.3 ± 0.2	25.6 ± 0.2	27.4
ELARS21	26.6 ± 0.8	26.5 ± 0.6	26.6 ± 0.8	26.5 ± 0.6	2.8 ± 0.8	15.2 ± 0.6	25.0 ± 0.7	30.4
ELARS24	90.8 ± 1.5	99.5 ± 0.9	78.0 ± 2.9	77.3 ± 2.5	6.6 ± 1.5	54.7 ± 0.9	73.3 ± 0.7	81.4
ELARS27	26.6 ± 0.6	27.1 ± 0.4	26.6 ± 0.6	27.1 ± 0.4	2.2 ± 0.6	12.5 ± 0.4	26.7 ± 0.6	24.6

Table 3.10: Difference (in $\mathrm{km\,s^{-1}}$) between velocity dispersions calculated with the empirical methods and the intrinsic velocity dispersion $\sigma_{\mathrm{GP},0}$ of the GalPak^{3D} models. The last row shows $\mathcal{P}$ according to Equation 3.25.

ID	$\sigma_{\mathrm{m,\ Varidel}} - \sigma_{\mathrm{GalPaK,const}}$	$\sigma_{\mathrm{m,\ uniform,\ Varidel}} - \sigma_{\mathrm{GalPaK,const}}$	$\sigma_{\mathrm{Yu}} - \sigma_{\mathrm{GalPaK,const}}$	$\sigma_{\mathrm{m}} - \sigma_{\mathrm{GalPaK,const}}$	$\sigma_{\mathrm{m,\ uniform}} - \sigma_{\mathrm{GalPaK,const}}$	$\sigma_{\mathrm{m,\ corr}} - \sigma_{\mathrm{GalPaK,const}}$	$\sigma_{\mathrm{m,\ uniform,\ corr}} - \sigma_{\mathrm{GalPaK,const}}$
L08	-15.0	-29.6	-5.3	3.8	3.3	-3.1	-2.1
L11	-23.1	-49.2	-33.1	11.7	12.7	4.6	7.3
E04	-12.0	-23.7	-1.0	7.7	6.3	7.7	6.3
E06	-5.2	-13.6	8.5	5.1	4.1	3.4	3.2
E08	2.5	-5.9	1.4	12.6	11.6	12.4	11.4
E10	-16.0	-22.0	-4.5	17.1	16.9	13.0	13.3
E11	-23.5	-35.3	-4.9	3.1	-0.0	3.0	-0.5
E12	-10.8	-18.3	-0.6	7.3	7.2	3.1	5.0
E14	-17.8	-35.4	-14.0	-9.4	-7.0	-10.6	-7.1
E16	-14.9	-26.0	-21.1	-5.2	-5.3	-5.2	-5.3
E17	-12.0	-19.1	-2.9	6.3	4.4	5.5	4.0
E18	-11.5	-25.8	-20.8	-2.4	-2.1	-2.4	-2.1
E19	-6.3	-23.1	1.8	1.3	3.3	0.9	2.6
E21	-9.8	-22.1	5.4	1.5	1.7	1.5	1.7
E27	-14.2	-24.5	-2.1	0.4	-0.1	0.4	-0.1
$\mathcal{P}$	-14.2	-26.7	-12.5	7.8	7.3	6.4	6.1

3.8 Our velocity dispersion compared to other studies

We contextualize our results by comparing them to the literature.

For our sample the observed intrinsic velocity dispersion $\sigma_{\mathrm{m,\ uniform,\ corr}}$ ranges from 23.9 $\mathrm{km\,s^{-1}}$ to 78.0 $\mathrm{km\,s^{-1}}$. We have a mean $\sigma_{\mathrm{m,\ uniform,\ corr}}$ of 41.1 $\mathrm{km\,s^{-1}}$ (median $\sigma_{\mathrm{m,\ uniform,\ corr}}$ at 37.3 $\mathrm{km\,s^{-1}}$).

The DYNAMO sample contains 67 star-forming galaxies with $z \sim 0.1$. From their analysis they report a mean velocity dispersion of around 50 $\mathrm{km\,s^{-1}}$ (Green, Glazebrook, McGregor, Damjanov, et al. 2014), slightly higher than our result. The MaNGA survey studying 4517 star-forming galaxies at $z \sim 0.02$, reports Hα velocity dispersions around 15-30 $\mathrm{km\,s^{-1}}$ (Law, Belfiore, et al. 2022), slightly lower than our result. Oliva-Altamirano et al. (2018) studies 7 turbulent, clumpy disc galaxies from the DYNAMO sample around $0.07 \leq z \leq 0.2$. They report high gas velocity dispersion around 40-80 $\mathrm{km\,s^{-1}}$. Isobe et al. (2023) studies 6 local extremely metal-poor galaxies in the EMPRESS sample and report velocity dispersions of 17-31 $\mathrm{km\,s^{-1}}$. The SAMI sample contains 383 star-forming galaxies at $z \lesssim 0.1$ (M. R. Varidel, Croom, Lewis, Fisher, et al. 2020). They report a median velocity dispersion of 18.8 $\mathrm{km\,s^{-1}}$, which is lower than previously reported for studies of gas kinematics and lower than our finding. Yu et al. (2021) studies 7 galaxies from the xCOLD GASS survey at $z \sim 0.04$ and finds velocity dispersions between 19.4 $\mathrm{km\,s^{-1}}$ and 36.1 $\mathrm{km\,s^{-1}}$.

Comparing our findings to other kinematic studies, we find studies reporting higher values and studies reporting lower values. The velocity dispersion relates through SFR and the difference in ranges in the literature are caused by different SFR ranges that however, appear to overlap with our range. With comparing our kinematic parameters to other observation campaigns aiming the study of kinematics, we show that our sample is not biased to the high- or low- end of velocity measurements for typical star-forming galaxies. This is important, as we want to state general results between galaxy kinematics and Lyα observables later and therefore, we want to use a galaxy sample which shows a similar behavior to other kinematic samples.

4 Relation between Hα kinematics and Lyα observables

Lyα emitters (LAEs) at high-z are predominantly found among low-mass galaxies ($M < 10^{10}\mathrm{M}_{\odot}$) above the star-forming main sequence (SFR $\sim 10\mathrm{M}_{\odot\,\mathrm{yr}^{-1}}$) (e.g. Rhoads, Malhotra, et al. 2014, Oyarzún et al. 2017, Kusakabe et al. 2018, Pucha et al. 2022). Looking from a kinematic perspective, studies find for example that SFR is tightly correlated with the intrinsic velocity dispersion (e.g. Green, Glazebrook, McGregor, Damjanov, et al. 2014, Law, Belfiore, et al. 2022). Before we study correlations between kinematic parameters and Lyα observables, we investigate in the correlations between kinematic parameters and galaxy parameters in Section 4.1. Afterwards we investigate in the correlations between kinematic parameters and Lyα observables (Section 4.2). Based on the results for the 14 galaxies of the LARS sample (E. C. Herenz et al. 2016), we expect that that strong LAEs exhibit higher velocity dispersions in objects with small rotation velocities.

In Chapter 3 we have derived the kinematic properties v_{shear}, σ_0^{obs} and $v_{\mathrm{shear}}/\sigma_0^{\mathrm{obs}}$ for LARS and eLARS. For σ_0^{obs} we adopt $\sigma_{\mathrm{m,\,uniform,\,corr}}$. In Section 1.2, we showed how Lyα luminosity, Lyα equivalent width and Lyα escape fraction are derived. In Section 1.3, we showed how stellar mass and star-formation rate are derived. For the galaxy properties stellar mass M, $\mathrm{SFR}_{\mathrm{H}\alpha}$, equivalent with $\mathrm{EW}_{\mathrm{Ly}\alpha}$, escape fraction $f_{\mathrm{esc}}^{\mathrm{Ly}\alpha}$ and luminosity $L_{\mathrm{Ly}\alpha}/L_{\mathrm{H}\alpha}$ we use the quantities from Melinder et al. (2023) and they are listed in Table 4.1. Some galaxies (LARS06, LARS10, LARS13, eLARS12, eLARS14 and eLARS16) are non-detections in Lyα and have therefore upper limits for the Lyα observables.

We are interested in how the kinematic galaxy properties correlate with Lyα observables and galaxy properties. Therefore, we use a statistical tests to test for correlations. We apply the Kendall rank-correlation test, which is a non-parametric test that is commonly used in literature (Kendall 1990).

Table 4.1: Lyα luminosity, Hα luminosity, Lyα equivalent width and Lyα escape fraction from Melinder et al. (2023). Positive errors are superscript and negative errors are subscript

ID	$L_{\mathrm{Ly}\alpha}$ $10^{41}\,\mathrm{erg\,s^{-1}\,cm^{-2}}$	$L_{\mathrm{H}\alpha}$ $10^{41}\,\mathrm{erg\,s^{-1}\,cm^{-2}}$	$\mathrm{EW}_{\mathrm{Ly}\alpha}$ Å	f_{esc}
LARS01	$8.345^{0.087}_{0.089}$	$5.126^{0.010}_{0.014}$	$42.195^{0.397}_{0.468}$	0.134 ± 0.002
LARS02	$4.154^{0.093}_{0.116}$	$1.590^{0.011}_{0.012}$	$56.661^{1.304}_{1.946}$	0.299 ± 0.010
LARS03	$1.917^{0.076}_{0.095}$	$6.091^{0.025}_{0.021}$	$34.164^{1.348}_{1.848}$	0.005 ± 0.000
LARS04	$0.276^{0.062}_{0.058}$	$3.831^{0.009}_{0.011}$	$2.065^{0.467}_{0.435}$	0.006 ± 0.001
LARS05	$6.516^{0.107}_{0.107}$	$4.254^{0.018}_{0.013}$	$24.935^{0.471}_{0.467}$	0.126 ± 0.002
LARS06	≤ 0.089	$0.648^{0.007}_{0.006}$	≤ 2.374	≤ 0.012
LARS07	$6.661^{0.132}_{0.144}$	$3.789^{0.016}_{0.015}$	$38.801^{0.935}_{1.000}$	0.111 ± 0.002
LARS08	$4.017^{0.267}_{0.193}$	$11.072^{0.345}_{0.124}$	$17.345^{1.302}_{0.915}$	0.006 ± 0.000
LARS09	$5.810^{0.294}_{0.272}$	$18.962^{0.035}_{0.027}$	$9.827^{0.477}_{0.474}$	0.016 ± 0.001
LARS10	≤ 0.235	$2.005^{0.012}_{0.022}$	≤ 2.100	≤ 0.003
LARS11	$17.899^{1.304}_{0.973}$	$9.929^{0.112}_{0.079}$	$20.515^{0.976}_{0.710}$	0.065 ± 0.009
LARS12	$15.396^{0.896}_{0.758}$	$13.904^{0.144}_{0.092}$	$18.108^{1.045}_{1.041}$	0.027 ± 0.001
LARS13	≤ 2.989	$20.978^{0.084}_{0.074}$	≤ 1.774	≤ 0.004
LARS14	$55.602^{1.914}_{1.982}$	$18.908^{0.239}_{0.238}$	$48.955^{2.281}_{2.102}$	0.263 ± 00.010
eLARS01	$5.169^{0.063}_{0.063}$	$13.134^{0.016}_{0.017}$	$21.156^{0.288}_{0.297}$	0.012 ± 0.000
eLARS02	$3.311^{0.116}_{0.082}$	$6.188^{0.036}_{0.035}$	$12.444^{0.450}_{0.327}$	0.061 ± 0.002
eLARS03	$1.227^{0.145}_{0.119}$	$10.127^{0.032}_{0.025}$	$4.414^{0.535}_{0.428}$	0.005 ± 0.001
eLARS04	$4.419^{0.121}_{0.107}$	$4.223^{0.015}_{0.017}$	$17.078^{0.511}_{0.449}$	0.070 ± 0.002
eLARS05	$5.881^{0.217}_{0.180}$	$3.679^{0.023}_{0.018}$	$26.523^{1.006}_{0.890}$	0.148 ± 0.006
eLARS06	$1.297^{0.142}_{0.096}$	$1.312^{0.018}_{0.025}$	$12.610^{1.402}_{0.956}$	0.060 ± 0.005
eLARS07	$0.811^{0.129}_{0.159}$	$2.537^{0.028}_{0.032}$	$7.062^{1.137}_{1.383}$	0.032 ± 0.006
eLARS08	$1.375^{0.116}_{0.113}$	$1.740^{0.019}_{0.016}$	$16.738^{1.413}_{1.446}$	0.017 ± 0.002
eLARS09	$0.461^{0.079}_{0.083}$	$0.756^{0.015}_{0.012}$	$5.648^{0.978}_{1.029}$	0.054 ± 0.010
eLARS10	$0.929^{0.121}_{0.104}$	$1.379^{0.016}_{0.017}$	$16.738^{1.413}_{1.446}$	0.016 ± 0.002
eLARS11	$0.621^{0.070}_{0.062}$	$0.911^{0.013}_{0.011}$	$8.913^{1.046}_{0.916}$	0.065 ± 0.007
eLARS12	≤ 0.082	$2.311^{0.019}_{0.015}$	≤ 1.272	≤ 0.002
eLARS13	$2.532^{0.092}_{0.087}$	$0.886^{0.006}_{0.007}$	$37.700^{1.627}_{1.384}$	0.207 ± 0.008
eLARS14	≤ 0.066	$1.080^{0.009}_{0.011}$	≤ 1.270	≤ 0.005
eLARS15	$0.807^{0.116}_{0.104}$	$0.646^{0.020}_{0.018}$	$19.969^{3.002}_{2.643}$	0.12 ± 0.018
eLARS16	≤ 0.063	$0.345^{0.009}_{0.012}$	≤ 2.377	≤ 0.009
eLARS17	$0.774^{0.117}_{0.097}$	$0.571^{0.018}_{0.015}$	$19.403^{3.108}_{2.470}$	0.082 ± 0.012
eLARS18	$0.173^{0.059}_{0.075}$	$0.344^{0.012}_{0.012}$	$7.877^{2.730}_{3.330}$	0.030 ± 0.012
eLARS19	$0.270^{0.053}_{0.043}$	$0.430^{0.008}_{0.009}$	$9.996^{2.028}_{1.559}$	0.064 ± 0.010
eLARS20	$0.215^{0.049}_{0.052}$	$0.522^{0.009}_{0.006}$	$7.867^{1.844}_{1.964}$	0.031 ± 0.008
eLARS21	$0.111^{0.042}_{0.039}$	$0.118^{0.010}_{0.008}$	$8.961^{3.473}_{3.117}$	0.047 ± 0.033
eLARS22	$1.854^{0.139}_{0.152}$	$3.644^{0.054}_{0.055}$	$6.808^{0.530}_{0.562}$	0.056 ± 0.005
eLARS23	$1.493^{0.214}_{0.241}$	$4.222^{0.081}_{0.073}$	$6.507^{0.958}_{1.073}$	0.040 ± 0.007
eLARS24	$4.472^{0.180}_{0.184}$	$6.929^{0.064}_{0.071}$	$22.283^{0.982}_{0.927}$	0.004 ± 0.000
eLARS25	$1.643^{0.183}_{0.203}$	$1.954^{0.040}_{0.060}$	$9.564^{1.098}_{1.173}$	0.094 ± 0.012
eLARS26	$2.233^{0.176}_{0.171}$	$3.305^{0.048}_{0.053}$	$21.547^{1.689}_{1.829}$	0.059 ± 0.005
eLARS27	$2.051^{0.159}_{0.156}$	$1.865^{0.038}_{0.045}$	$18.832^{1.638}_{1.491}$	0.115 ± 0.011
eLARS28	$0.370^{0.150}_{0.133}$	$2.326^{0.041}_{0.048}$	$3.138^{1.285}_{1.128}$	0.013 ± 0.005

We have $N = 38$ pairs (we exclude the four galaxies with double components in Hα) of measurement (x_i, y_i), where x_i is the kinematic parameter ($v_{\rm shear}$, $\sigma_0^{\rm obs}$, $v_{\rm shear}/\sigma_0^{\rm obs}$) and y_i the Lyα observable (EW$_{\rm Ly\alpha}$, $f_{\rm esc}$, $L_{\rm Ly\alpha}/L_{\rm H\alpha}$). The general idea of rank-correlation tests is, to replace the value of each x_i and y_i by the value of its rank among all the others x_i and y_i in the sample, i.e. the highest value of x_i and y_i gets rank N, the value below the rank $N-1$, and so on, and the lowest value gets rank 1. The parameter pairs are mapped into a space where any non-monotonic correlation will become a linear correlation (Press 1986).

Kendall τ looks for monotonic correlations and ranges from -1 (perfect anti-correlation) to 1 (perfect correlation). Kendall compares the pairs (x_i, y_i) and (x_j, y_j). The Kendall's tau can then be estimated by

$$\tau = \binom{N}{2}^{-1} \sum_{1 \le i \le j \le N} a_{ij} b_{ij}, \tag{4.1}$$

where N is the number of data pairs, and $a_{ij} = 1$ if $x_i < x_j$ and $a_{ij} = -1$ if $x_i > x_j$. $b_{ij} = 1$ if $y_i < y_j$ and $b_{ij} = -1$ if $y_i > y_j$. Therefore, $a_{ij}b_{ij} = 1$ if $(x_i - x_j)(y_i - y_j) > 0$, which is called a concordant pair and $a_{ij}b_{ij} = -1$ if $(x_i - x_j)(y_i - y_j) < 0$, which is called a discordant pair (Hsieh 2010). We can have the situation that we have ties ($x_i = x_j$ or $y_i = y_j$). Therefore, we have to make modifications. One possible way is to set $a_{ij} = 0$ if $x_i = x_j$ ($b_{ij} = 0$ if $y_i = y_j$), which is called unconditional tau (Hsieh 2010). Since we have upper limits in our Lyα observables, we have to take into account these censored data in the Kendall tau test. The main idea here is to replace the censored data by a proper imputation. Following Melinder et al. (2023), we use the censored Kendall tau test to check for correlations and anti-correlations(Akritas, Murphy, and Lavalley 1995, as implemented as R package CENKEN[1]).

τ has a variance of

$$\mathrm{Var}(\tau) = \frac{4N + 10}{9N(N-1)} \overset{N=38}{=} 0.0128 \tag{4.2}$$

(Press 1986). The Kendall rank-correlation test can be converted to a p_0 value, which is a measurement if the statistical significance of the correlation between the two variables. The p_0 value represents the probability of obtaining a correlation as extreme as the one observed in the sample, under the hypothesis that there is no true correlation in the population. The two-sided p_0 value in the Kendall τ rank correlation test is used to test the null hypothesis that there is no correlation

[1] https://www.rdocumentation.org/packages/NADA/versions/1.6-1.1/topics/cenken

between the variables. It considers both positive and negative correlations. The significance level p_0 can be calculated by

$$p_0 = 1 - \mathrm{ERFC}\left(\frac{\left|\frac{\tau}{\sqrt{\mathrm{Var}(\tau)}}\right|}{1.4142136}\right), \tag{4.3}$$

with ERFC being the error function

$$\mathrm{ERFC}(x) = 1 - \mathrm{ERF}(x) = \frac{2}{\sqrt{\pi}} \int_x^\infty e^{-t^2} \mathrm{d}t \tag{4.4}$$

(Press 1986). If the p_0 value is less than our significance level of 0.05, the test states that there is enough evidence to reject the null hypothesis and concludes that there is a statistical significant correlation between the variables.

One deficiency of the correlation coefficient is that it does not take the error bars of the measurements. However, given the large dynamic range of our sample and the comparatively small error bars, we assume this to be a non-issue.

4.1 Relation between integrated kinematic parameters and galaxy parameters

Our main aim is to explore the relations between the Lyα observables and kinematics in our sample. As stated in the beginning of this chapter, understanding relations between galaxy kinematics and galaxy parameters (M and SFR) appears thus fundamental for correctly interpreting those relations. Therefore, we now study the relation between our integrated kinematic parameters and the stellar mass and the SFR.

In Table 4.2 we provide the τ- and p_0-values of the Kendall rank-correlation test. We adopt a strict cut-off of 0.05 for the p-value. Strict p-value cutoffs can be discussed, a more nuanced discussion of the lowest p-values could perhaps be more valuable. However, first we start with adopting a 0.05 cutoff and investigate in correlations we find with 0.05 or lower. We find a correlation between M and v_{shear}, SFR and v_{shear} and SFR and σ_0^{obs}. We show these correlations graphically in Figure 4.1. Some relations also show apparently randomly distributed behavior.

We find a correlation between SFR and velocity dispersion ($\tau = 0.448$, $p_0 = 7 \cdot 10^{-5}$ for σ_0^{obs} vs. SFR). This correlation was already reported in E. C. Herenz et al. (2016) for the LARS sample. In fact, it has long been known that such a correlation exists (Terlevich and Melnick 1981).

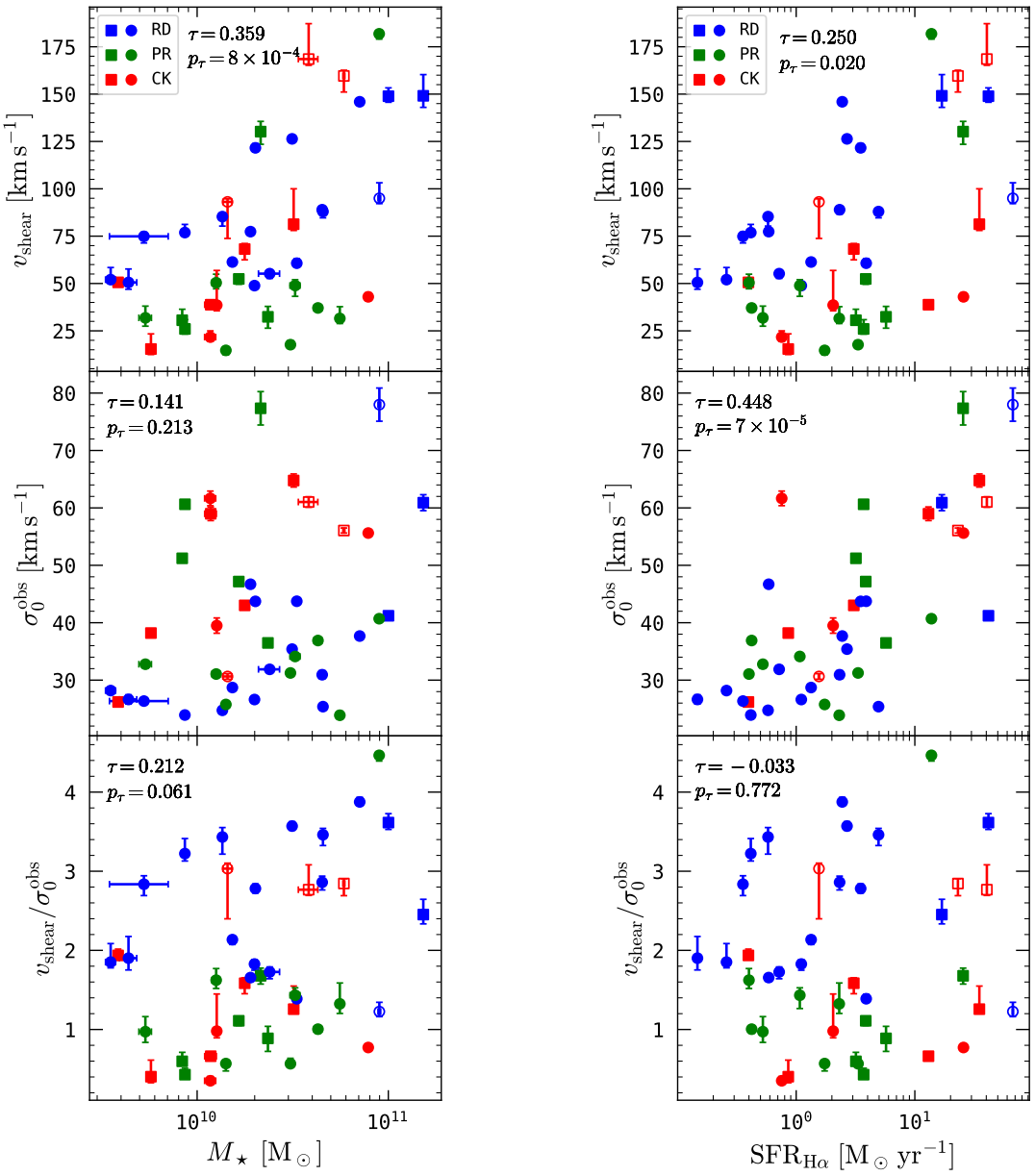

Figure 4.1: Global Hα kinematic parameters $v_{\rm shear}$ (top), $\sigma_0^{\rm obs}$ (middle) and $v_{\rm shear}/\sigma_0^{\rm obs}$ (bottom) in comparison to stellar mass (left) and SFR (right) for our sample. Squares represent the LARS galaxies, the circles the eLARS galaxies and non-filled symbols Hα double components. Blue symbols are RDs, whereas green symbols are PRs and red symbols are CKs.

Table 4.2: Kendall τ correlation coefficient and likelihood p_0 for rejecting the null hypothesis for stellar mass and SFR with kinematic parameters.

	τ	p_0
$\mathbf{M} - v_{\mathbf{shear}}$	0.359	$8 \cdot 10^{-4}$
$M - \sigma_0^{\mathrm{obs}}$	0.141	0.213
$M - v_{\mathrm{shear}}/\sigma_0^{\mathrm{obs}}$	0.212	0.061
$\mathbf{SFR} - v_{\mathbf{shear}}$	0.250	0.020
$\mathbf{SFR} - \sigma_0^{\mathbf{obs}}$	0.448	$7 \cdot 10^{-5}$
$\mathrm{SFR} - v_{\mathrm{shear}}/\sigma_0^{\mathrm{obs}}$	-0.033	0.772

Law, Belfiore, et al. (2022) report in the MaNGA survey of 4517 star-forming galaxies at $z \sim 0.02$ also a well-defined correlation between the velocity dispersion and the SFR. Alexei V. Moiseev, Tikhonov, and Klypin (2015) study 59 nearby dwarf galaxies and observe the same trend between velocity dispersion and SFR. Yu et al. (2021), Übler et al. (2019) and Krumholz et al. (2018) also report the SFR-σ relation. As already discussed in Section 1.3.3, high-velocity dispersions indicate highly turbulent ionized ISM. According to the work by Krumholz et al. (2018), the physical root of this relation is actually, that a highly turbulent ISM effectively forms stars. Additionally, SFR feeds a lot of energy back into the ISM, which increases the gas turbulences. Both effects together contribute to the observed correlation.

The fundamental relation between v_{max} and stellar mass is expected, as the total potential of the galaxy and thereby also the stellar mass is traced by the kinematics. Our shearing velocity v_{shear} is not inclination corrected, despite this we are still having the correlation for v_{shear} and stellar mass in our sample ($\tau = 0.359$, $p_0 = 8 \cdot 10^{-4}$ for v_{shear} vs. M). v_{shear} is a line-of-sight proxy for v_{max} in rotating or perturbed rotators and traces the gas rotation in these system. For the mergers or systems with complex kinematics it traces indeed the observerd large scale shearing. The same relation was already reported for the LARS sample by E. C. Herenz et al. (2016). Gonçalves et al. (2010) study 19 Lyman-break analogs at $z \sim 0.2$ and also reports a trend between shearing velocity and stellar mass.

The so called 'main sequence of star-formation' for galaxies or 'main sequence of galaxies' is given by a fundamental relation between the galaxy's SFR and the galaxy's stellar mass, which have been revealed with observations of large samples. The relation between SFR and stellar mass may be explained with the self-regulating nature of star formation, because of the interplay between gas accretion, star formation and feedback driven outflows (Matthee and Schaye 2019).

Table 4.3: Kendall τ correlation coefficient and likelihood p_0 for rejecting the null hypothesis for Lyα observables with kinematic parameters.

	τ	p_0
$\mathrm{EW}_{\mathrm{Ly}\alpha} - v_{\mathrm{shear}}$	-0.046	0.672
$\mathbf{EW_{Ly\alpha}} - \sigma_0^{\mathbf{obs}}$	0.337	$3 \cdot 10^{-3}$
$\mathrm{EW}_{\mathrm{Ly}\alpha} - v_{\mathrm{shear}}/\sigma_0^{\mathrm{obs}}$	-0.149	0.191
$f_{\mathbf{esc}}^{\mathbf{Ly}\alpha} - v_{\mathbf{shear}}$	-0.300	0.005
$f_{\mathrm{esc}}^{\mathrm{Ly}\alpha} - \sigma_0^{\mathrm{obs}}$	0.156	0.170
$f_{\mathbf{esc}}^{\mathbf{Ly}\alpha} - v_{\mathbf{shear}}/\sigma_0^{\mathbf{obs}}$	-0.256	0.024
$L_{\mathrm{Ly}\alpha}/L_{\mathrm{H}\alpha} - v_{\mathrm{shear}}$	-0.174	0.106
$L_{\mathbf{Ly}\alpha}/L_{\mathbf{H}\alpha} - \sigma_0^{\mathbf{obs}}$	0.238	0.037
$L_{\mathrm{Ly}\alpha}/L_{\mathrm{H}\alpha} - v_{\mathrm{shear}}/\sigma_0^{\mathrm{obs}}$	-0.186	0.102

In view of the SFR-v_{shear} ($\tau = 0.250$, $p_0 = 0.020$ for v_{shear} vs. SFR) correlation and the mass-v_{shear} correlation ($\tau = 0.359$, $p_0 = 8 \cdot 10^{-4}$ for v_{shear} vs. M), we see the kinematic imprint of the galaxy main sequence in our sample.

v_{shear} correlates with M, while σ_0^{obs} does not correlate with M. Therefore, we may expect to find a correlation between $v_{\mathrm{shear}}/\sigma_0^{\mathrm{obs}}$ and stellar mass as in E. C. Herenz et al. (2016). This would imply that dispersion dominated systems are more likely low-mass systems. However, if we use a strict cut-off, we do not find such correlation in our analysis ($\tau = 0.212$, $p_0 = 0.061$ for $v_{\mathrm{shear}}/\sigma_0^{\mathrm{obs}}$ vs. M). But with a small sample size strict cutoffs are not the best idea. If we discuss this in a more nuanced way, we do find a correlation between $v_{\mathrm{shear}}/\sigma_0^{\mathrm{obs}}$ and M.

We tested different methods for correcting the PSF smearing. Some perform better and some worse. In Appendix A.3, we show that using $\sigma_0^{\mathrm{obs}} = \sigma_{\mathrm{m,\ uniform,\ corr}}$ instead of using not PSF corrected velocity dispersions or S/N weighted velocity dispersions does not influence the found correlations. The different methods have no influence on our current analysis of the here studies correlations. We may assume that our galaxies are too close to be significant affected by PSF smearing.

4.2 Relation between integrated kinematic parameters and global Lyα observables

In Figure 4.2 we plot relations between the kinematic parameters and Lyα observables (Table 4.1) and also list for each relation the Kendall τ correlation coefficient τ and the likelihood p_0 that the observables are uncorrelated in Table 4.3. In Figure

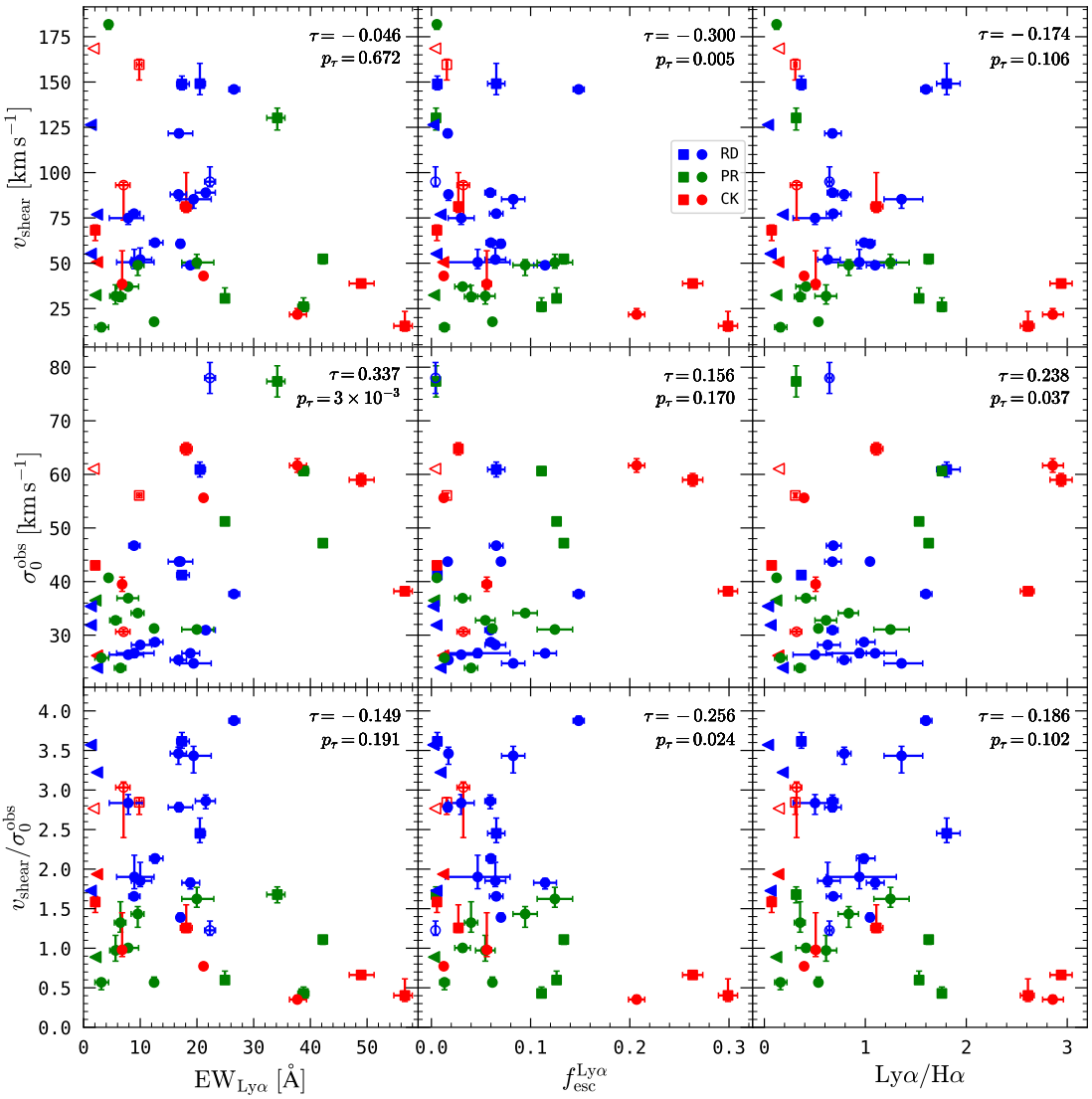

Figure 4.2: Relations between global Lyα properties (EW$_{Ly\alpha}$, Lyα/Hα and $f_{esc}^{Ly\alpha}$) and global kinematic parameters σ_0^{obs}, v_{shear} and v_{shear}/σ_0^{obs} for our sample. Squares represent the LARS galaxies, the circles the eLARS galaxies, triangles the upper limits and non-filled symbols Hα double components. Blue symbols are RDs, whereas green symbols are PRs and red symbols are CKs.

4.2 we find that some parameters anti-/correlate and other only show scatter.

We observe a correlation between $\sigma_0^{\rm obs}$ and $\mathrm{EW}_{\mathrm{Ly}\alpha}$ and $\sigma_0^{\rm obs}$ and $L_{\mathrm{Ly}\alpha}/L_{\mathrm{H}\alpha}$. Galaxies with higher velocity dispersions tend to exhibit larger $\mathrm{EW}_{\mathrm{Ly}\alpha}$ ($\tau = 0.337$, $p_0 = 0.003$ for $\sigma_0^{\rm obs}$ vs. $\mathrm{EW}_{\mathrm{Ly}\alpha}$) and higher luminosities ($\tau = 0.238$, $p_0 = 0.037$ for $\sigma_0^{\rm obs}$ vs. Lyα/Hα). Galaxies with higher velocity dispersions may have more active star-forming regions, as seen in the $\sigma_0^{\rm obs}$-SFR-correlation. This could be one reason for the found correlations.

Galaxies with a high $v_{\rm shear}$ have preferentially lower $f_{\rm esc}^{\mathrm{Ly}\alpha}$ ($\tau = -0.300$, $p_0 = 0.005$ for $v_{\rm shear}$ vs. $f_{\rm esc}^{\mathrm{Ly}\alpha}$). According to the M-$v_{\rm shear}$ relation, galaxies with high Lyα escape fractions are more likely found in systems with low mass. $v_{\rm shear}$ can be corrected for inclination for RDs and then reflects the rotational motion of the galaxy, while $f_{\rm esc}^{\mathrm{Ly}\alpha}$ quantifies the fraction of Lyα photons that manage to escape from the galaxy's ISM without being scattered or absorbed. In Section 4.3, we study the effect of the inclination on the Lyα observables.

We find that higher $f_{\rm esc}^{\mathrm{Ly}\alpha}$ are more commonly observed in dispersion-dominated systems characterized by small $v_{\rm shear}/\sigma_0^{\rm obs}$ values ($\tau = -0.256$, $p_0 = 0.024$ for $v_{\rm shear}/\sigma_0^{\rm obs}$ vs. $f_{\rm esc}^{\mathrm{Ly}\alpha}$). These systems exhibit a significant contribution from the dispersion motion of gas, indicating a turbulent state of the ionized hot gas. The increased turbulence in the ISM may facilitate the escape of Lyα photons by reducing the likelihood of scattering or absorption.

As mentioned in Section 1.2.4 an empiric linear relation between $f_{\rm esc}$ and $\mathrm{EW}_{\mathrm{Ly}\alpha}$ is reported. In this respect it appears interesting that we have a $v_{\rm shear}$ vs. $f_{\rm esc}$ anti-correlation ($\tau = -0.300$, $p_0 = 0.005$ for $v_{\rm shear}$ vs. $f_{\rm esc}$), but we can not rule out a random scatter for $v_{\rm shear}$ and $\mathrm{EW}_{\mathrm{Ly}\alpha}$ ($\tau = -0.046$, $p_0 = 0.672$ for $v_{\rm shear}$ and $\mathrm{EW}_{\mathrm{Ly}\alpha}$). The similar situation occurs for the velocity dispersion. We find a correlation between $\sigma_0^{\rm obs}$ and $\mathrm{EW}_{\mathrm{Ly}\alpha}$ ($\tau = 0.337$, $p_0 = 0.003$ for $\sigma_0^{\rm obs}$ vs. $\mathrm{EW}_{\mathrm{Ly}\alpha}$), but we can not rule out a random scatter for $\sigma_0^{\rm obs}$ and $f_{\rm esc}$ ($\tau = 0.156$, $p_0 = 0.170$). This result my be driven by the scatter in the $\mathrm{EW}_{\mathrm{Ly}\alpha}$ versus $f_{\rm esc}$ relation.

These various correlations and anti-correlations between ionized gas kinematics and Lyα observables in the LARS and eLARS samples demonstrate a potentially important role of dispersion-dominated kinematics in influencing the escape of Lyα photons from galaxies. In Chapter 5, we try to assess the importance by using step-wise regression in the framework of a multi-variate regression.

4.3 Inclination dependence on Lyα observables

We observe the velocity of the ionized gas along the line of sight and have the parameter $v_{\rm shear}$. However, models and theoretical work assuming rotating disks

use the parameter $V_{\rm max}$, which is the maximal velocity of the rotation curve. We have to relate $v_{\rm shear}$ and $V_{\rm max}$ by inclination correction to be able to compare both parameters. However, in this section, we will not look on the velocities and we will focus on the inclination. We want to study how the Lyα observables depend on the inclination. We use the ratio of the minor semi-axis b of the observed ellipse in the I-band and the major semi-axis a to calculate the inclination by

$$\cos^2(i_{\text{I-band}}) = \frac{(b/a) - \alpha^2}{1 - \alpha^2}. \tag{4.5}$$

following Holmberg (1958), where α is the ratio between disk scale height and scale length (W. Wang et al. 2018). For local galaxies α is found in the range of 0.1 to 0.3 (W. Wang et al. 2018, Padilla and Strauss 2008, Unterborn and Ryden 2008 and Rodríguez and Padilla 2013). For our study, we assume the simple case that our galaxies are thin disks and that the inclination can be calculated by

$$\cos(i_{\text{I-band}}) = \frac{b}{a}. \tag{4.6}$$

We have the inclination calculated through I-band observations and we have the output from the GalPaK3D modeling. We list the inclination values for the individual galaxies in Table 4.4.

Radiative transfer simulations of single galaxies find strong viewing angle dependence of $\text{EW}_{\text{Ly}\alpha}$ and $f_{\text{esc}}^{\text{Ly}\alpha}$ (Behrens and Braun 2014, Verhamme et al. 2012 and Smith et al. 2022). The highest $\text{EW}_{\text{Ly}\alpha}$ and $f_{\text{esc}}^{\text{Ly}\alpha}$ values are found, when the simulated galaxies are seen face-on. From the findings of the simulations it could be plausible that high-z samples selected on Lyα emission might be biased towards face-on systems.

We show the inclination dependence of the Lyα observables in our sample in Figure 4.3. It can be seen, that the Lyα observables do not depend on kinematic inclination. Also no trend is observed when we consider the photometric axis ratios as a proxy for the inclination. Here it needs to be kept in mind, that the concept of inclination can not be applied to CK systems. Nevertheless, our analysis does not support the idea that stronger Lyα emitter are preferentially found in face-on disks, even when considering only the disks in the sample. This result indicates, that the inclination dependence found in models of single galaxies may not be generalized for a sample of galaxies.

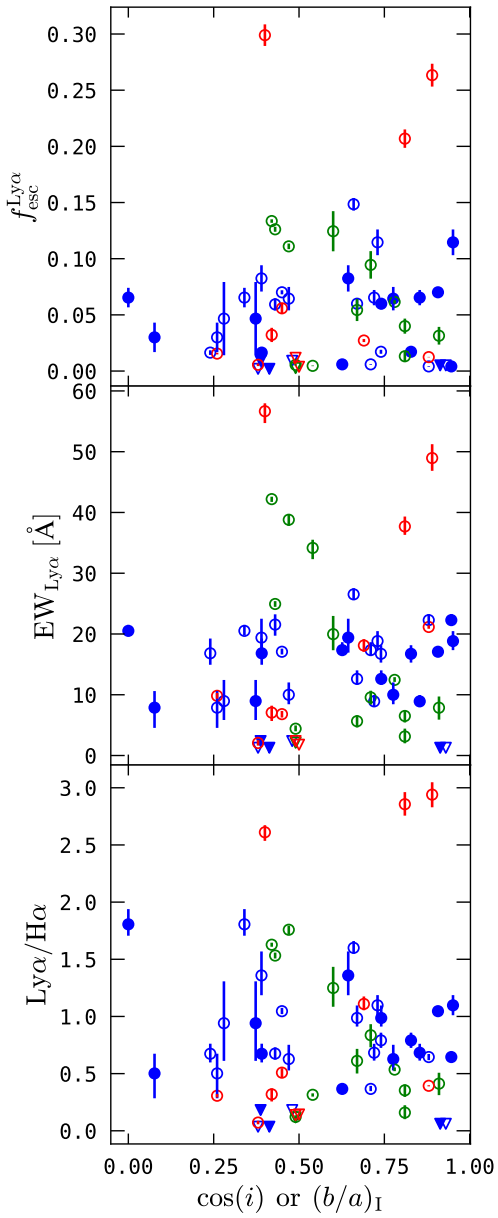

Figure 4.3: Galaxy inclination vs. Lyα observables. Filled blue circles are based on the kinematical inclination $i_{\rm GalPaK}$, from the disk modelling of the RDs with GalPak3D (triangles are galaxies with upper limits in the Lyα observables). Open circles are based on photometric inclinations (blue: RD; green: PR; red: CK) according to $\cos(i_{\rm I\text{-}band}) = \frac{b}{a}$ where $\frac{b}{a}$ is the I-band axis ratio. Perfect disks viewed face-on are thus on the right-hand side of the plot, whereas edge-on disks are on the left-hand side.

Table 4.4: Inclination estimated by GalPaK and photometric inclination by the I-band (Rasekh et al. 2022).

ID	i_{GalPaK} [°]	$\Delta i_{\mathrm{GalPaK}}$ [°]	$b/a_{\mathrm{I\text{-}band}}$	$i_{\mathrm{I\text{-}band}}$ [°]
LARS01			0.42	65.2
LARS02			0.4	66.4
LARS03			0.54	57.3
LARS04			0.38	67.7
LARS05			0.43	64.5
LARS06			0.49	60.7
LARS07			0.47	62.0
LARS08	51.2	0.1	0.71	44.8
LARS09			0.26	74.9
LARS10			0.49	60.7
LARS11	90.0	0.2	0.34	70.1
LARS12			0.69	46.4
LARS13			0.5	60.0
LARS14			0.89	27.1
ELARS01			0.88	28.4
ELARS02			0.78	38.7
ELARS03			0.49	60.7
ELARS04	24.9	0.2	0.45	63.3
ELARS05			0.66	48.7
ELARS06	42.2	0.2	0.67	47.9
ELARS07			0.42	65.2
ELARS08	34.1	0.5	0.74	42.3
ELARS09			0.67	47.9
ELARS10	67.0	0.1	0.24	76.1
ELARS11	31.4	0.5	0.72	43.9
ELARS12	65.6	0.1	0.38	67.7
ELARS13			0.81	35.9
ELARS14	24.0	0.1	0.93	21.6
ELARS15			0.6	53.1
ELARS16	67.2	0.3	0.48	61.3
ELARS17	49.9	1.2	0.39	67.0
ELARS18	85.6	0.3	0.26	74.9
ELARS19	39.1	0.1	0.47	62.0
ELARS20			0.91	24.5
ELARS21	68.1	0.5	0.28	73.7
ELARS22			0.45	63.3
ELARS23			0.81	35.9
ELARS24	18.9	0.2	0.88	28.4
ELARS25			0.71	44.8
ELARS26			0.43	64.5
ELARS27	18.0	0.6	0.73	43.1
ELARS28			0.81	35.9

5 Predicting Lyα observables by using multivariate linear regression

Understanding the production and escape from Lyα photons from galaxies is a long-standing question in astrophysics. In the Epoch of Reionization the Universe transformed from being neutral to being ionized. This transition is traced by the scattering process of Lyα photons. If there would be a possibility to predict the Lyα luminosities of galaxies, it would open a new possibility to explore the Epoche of Reionization. If we know the Lyα output of an galaxy, we can study the medium around the galaxy, which changed from neutral to ionized.

Runnholm et al. (2020) applies a multivariate regression method to obtain a relation between the galaxy properties and emitted Lyα. The derived predictions of the Lyα luminosity are in accuracy with the observations (to have a metric of success, we later introduce the R^2 in Equation 5.4), but they appear to fail when being applied to a different sample. Theory tells us that gas kinematics are an important ingredient for observations of Lyα. The results shown shown in Section 4.2 clearly support this. The main point for the following analysis is, that it is an experiment to assess the importance of the integrated kinematic parameters on the Lyα output quantitatively.

We start with predicting the Lyα luminosity to compare our findings to the results in Runnholm et al. (2020). In Runnholm et al. (2020) predicting f_{esc} and $\mathrm{EW}_{\mathrm{Ly}\alpha}$ did not produce as good results as predicting $L_{\mathrm{Ly}\alpha}$. As showed by correlations in Section 4.2, we assume that kinematics influence f_{esc} and $\mathrm{EW}_{\mathrm{Ly}\alpha}$ and therefore we study, how important the kinematic parameters are for predicting these observables. With including the kinematics, we are especially interested in the predictions of escape fraction and equivalent width. We assume that the ionized gas kinematics may not have an impact on the production of Lyα photons. However, ionized gas kinematics may influence the radiative transfer and therefore should be relevant for predicting the equivalent width or escape fraction.

For the prediction we use a technique known as multivariate linear regression. We assume that our prediction quantity ($L_{\mathrm{Ly}\alpha}$, f_{esc}, $\mathrm{EW}_{\mathrm{Ly}\alpha}$) depend on galaxy

properties in a linear way. We then fit our linear model

$$\log_{10}(L_{\mathrm{Ly}\alpha}[\mathrm{ergs\,s^{-1}}]) - 40 = \sum_i c_i \cdot v_i \tag{5.1}$$

$$\log_{10}(\mathrm{EW}_{\mathrm{Ly}\alpha}[\mathrm{Å}]) = \sum_i c_i \cdot v_i \tag{5.2}$$

$$f_{\mathrm{esc}} = \sum_i c_i \cdot v_i \tag{5.3}$$

on our data. Here i indexes each galaxy. v_i are the variables, which are used to predict the observable and c_i are the fitting coefficients we get out of the multivariate linear regression. With the determined coefficients c_i we have now a prediction model and can predict the coresponding Lyα observable for any galaxy where all v_i known for this galaxy.

Our sample contains 42 galaxies. We remove all galaxies with upper limits in the Lyα observables, which are LARS06, LARS10, LARS13, eLARS12, eLARS14 and eLARS16. Additionally, LARS13 and eLARS12 are Lyα absorbers and because of the negative values not suited for calculation in logarithmic space. Also, we remove LARS09, eLARS07 and eLARS24, because they show Hα double components. We have 33 galaxies for our multivariate regression method.

In multivariate regression, cross-validation is a resampling technique used to assess the performance and generalization ability of the regression model. It divides the dataset into multiple subsets, using some of them for training the model, and the remaining ones for testing its performance. This process is repeated multiple times, with different subsets used for training and testing in each iteration, allowing for a comprehensive evaluation of the model's predictive accuracy and robustness. As we have only a low number of galaxies we do not cross validate.

As we have a large number of variables, we must be careful to not overfit. Overfitting is the situation where the regression model performs very well on the training data but poorly on new, unseen data. This occurs when the model is too complex or flexible, capturing not only the underlying patterns in the data but also noise and random fluctuations. We have to be very careful as we have a low number of galaxies and a high number of input variables. This was already for Runnholm et al. (2020) a problem that had to be faced.

We make predictions out of an set of direct variables and out of an set of physical variables. We divide our variables in these two sets, because observational and theoretical studies should be comparable to our results and observations and theoretic work have access to different variables. The direct variables can be used by comparing to observational studies, the physical variables to theoretical work.

Our observational variables are U band magnitude, B band magnitude, I band magnitude, FUV, UV size, luminosities in Hα, Hβ, [OIII] λ5007, [OII] λ3727+λ3729 and [NII] λ6584, v_{95}, w_{90} and $F_{\rm cov}$. Our physical variables are stellar mass M, UV size, E_{B-V}, O32 ratio, O/H ratio, SFR, v_{95}, w_{90} and $F_{\rm cov}$. We use the values listed in Runnholm et al. (2020), except the $L_{\rm Ly\alpha}$, FUV, Hα, M, E_{B-V} and SFR. There we use the values listed in Melinder et al. (2023). We include the ionized gas kinematics by the parameters $\sigma_{\rm m,\ uniform,\ corr}$ and $v_{\rm shear}$ to both variable sets. We provide here a short description of the variables that are used (more details can be found in Runnholm et al. (2020)):

- FUV, U, B, I [erg s^{-1} Å^{-1}]: absolute magnitudes in FUV (filter F140LP with pivot of 1539.7 Å and width of 258.6 Å or F150LP with pivot of 1612.5 Å and width of 209.6 Å), U (filter F336W with pivot of 3354.5 Å and width of 511.6 Å or F390W with pivot of 3923.7 Å and width of 894 Å), B (filter F438W with pivot of 4326.2 Å and width of 614.7 Å), I (filter F775W with pivot of 7651.4 Å and width of 1179.1 Å, F850LP with pivot of 9176.1 Å and width of 1192.5 Å or F814W with pivot of 8039.1 Å and width of 1565.2 Å) measured in a circular aperture in the HST data(expressed as luminosity densities), (for FUV use values listed in Melinder et al. (2023), for U, B, I use values listed in Runnholm et al. (2020))

- UV size [kpc]: Size of the galaxy measured in the FUV. The F140LP HST filter is used and a single-component 2D Sérsic profile is fit to the galaxy (values listed in Runnholm et al. (2020))

- Hα, Hβ, [OIII] λ5007, [OII] λ3727+λ3729 and [NII] λ6584 line luminosities [erg s^{-1}]: For Hα using HST observations. Hβ, [OIII], [OII] and [NII] are measured in the SDSS spectrum. The SDSS fiber is smaller than the HST apertures. Therefore, we scale the emission lines using the Hα fluxes according $F = \frac{H_{\alpha\,\rm HST}}{H_{\alpha\,\rm SDSS}} F_{\rm SDSS}$ (for Hα and Hβ values listed in Melinder et al. (2023), for [OIII], [OII] and [NII] values listed in Runnholm et al. (2020))

- v_{95} [km s^{-1}]: Outflow velocity of the neutral gas measured by the low-ionization absorption lines (SiII λ1190, SiII λ1193, SiII λ1260, SiII λ1304, OI λ1302, and CII λ1334) in the COS spectroscopy. v_{95} is the velocity with 95 % of the absorbed line flux redward of it (values listed in Runnholm et al. (2020))

- w_{90} [km s^{-1}]: Width of the averaged low-ionization lines. It is the velocity width from 5 % to 95 % of the integrated absorption (values listed in Runnholm et al. (2020))

- F_{cov}: Maximum velocity-binned covering fraction (values listed in Runnholm et al. (2020))
- M [$\mathrm{M}_\odot$]: Stellar mass derived from SED fitting (values listed in Melinder et al. (2023))
- E_{B-V} [mag]: Dust extinction derived from Hα and Hβ (values listed in Melinder et al. (2023))
- O32 ratio: [OIII] λ5007 / [OII] λ3727+λ3729 as measuring the degree of ionization (values listed in Runnholm et al. (2020))
- 12 + log(O/H): Nebular oxygen abundance (values listed in Runnholm et al. (2020))
- SFR [$\mathrm{M}_\odot$ yr^{-1}]: Star formation rate derived from Hα (values listed in Melinder et al. (2023))

Following Runnholm et al. (2020), we choose a least-squares multiple linear regression method[1], which is implemented in the Python package Scikit-Learn.

It is very important to have the variables in the same order of magnitude to avoid biases and numerical issues. Runnholm et al. (2020) moves into logarithmic space and subtracts a constant to have all variables in roughly the same order unity. We follow Runnholm et al. (2020) and move in the logarithmic space and subtract constants to get the variables in roughly the same order unity.

To quantify the performance of our prediction model, we use the R^2 coefficient of determination

$$R^2 = 1 - \frac{\sum_i (y_i - f_i)^2}{\sum_i (y_i - \overline{y})^2}, \tag{5.4}$$

which describes the fraction of the variance in the predicted data. Here y_i are the measured data points, f_i the points predicted by the model and $\overline{y}$ the mean of the data points. $R^2 = 1$ would be a perfect explanatory model, lower values have less explanatory power (James et al. 2013, Runnholm et al. 2020).

Additionally to the multivariate regression, we use a ranking method, which orders the variables in sence of importance. To rank the variables in order of importance, we use forward and backward selection. The forward selection fits a relation between the Lyα observable and each individual variable and calculates the R^2 score. The variable with the highest R^2 score is ranked as the most important variable. Then a relation between the Lyα observable and the most important

[1] https://scikit-learn.org/stable/modules/generated/sklearn.linear_model.LinearRegression.html

variable and one other variable is fit and the second important variable is determined by the highest R^2 score. This procedure is continued until all variables are ranked in an order of importance. The backward selection works the other way around. A relation to all variables is fit and only one variable is excluded each time. The set of variables with the highest R^2 score is chosen and the excluded variable is the least important variable. This procedure is continued by excluding the least important variable and a second variable and calculate again the R^2 score for all possible configurations (James et al. 2013, Runnholm et al. 2020).

We stated the goodness of the model by the R^2 score. If we now include our kinematic parameters in the observational data set, we compare the R^2 of both predictions to conclude which model has a better predicting power. To be comparable, we need the same number of observational variables for the predictions. As $\sigma_{\mathrm{m,\ uniform,\ corr}}$ is derived from the Hα line, for the model with kinematic parameters included, we exchange the Hα luminosity by $\sigma_{\mathrm{m,\ uniform,\ corr}}$. And as v_{shear} correlates with M, we need to replace a variable that traces the stellar mass. There is an fundamental relation between the stellar mass and luminosity for galaxies. The stellar mass is dominated by older stars and therefore, we choose to replace the I band magnitude for v_{shear}. For the physical variable set, as $\sigma_{\mathrm{m,\ uniform,\ corr}}$ correlates with SFR, for the model with kinematics included, we exchange the SFR by $\sigma_{\mathrm{m,\ uniform,\ corr}}$. And as v_{shear} correlates with M, we replace M by v_{shear} (see Section 4.1).

First, we present the results of the multivariate linear regression for prediction the Lyα luminosity. Then we show the results for predicting the equivalent width and escape fraction. After presenting the results, we close this chapter with a section discussing the results of the experiment.

5.1 Predicting the Lyα luminosity

5.1.1 Observational variables

To start the multivariate regression method, we start in reproducing a prediction for the Lyα luminosity as it is done in Runnholm et al. (2020). We start with predicting the luminosity to establish the method and also to test the method with our kinematic parameters. With including the kinematic parameters, we are especially interested in the predictions of escape fraction and equivalent width and we will look more into this in the later sections.

In Table 5.1, we list the observational variables that are used to predict the Lyα luminosity and we list the fitting coefficients (see Equation (5.3)). The linear model

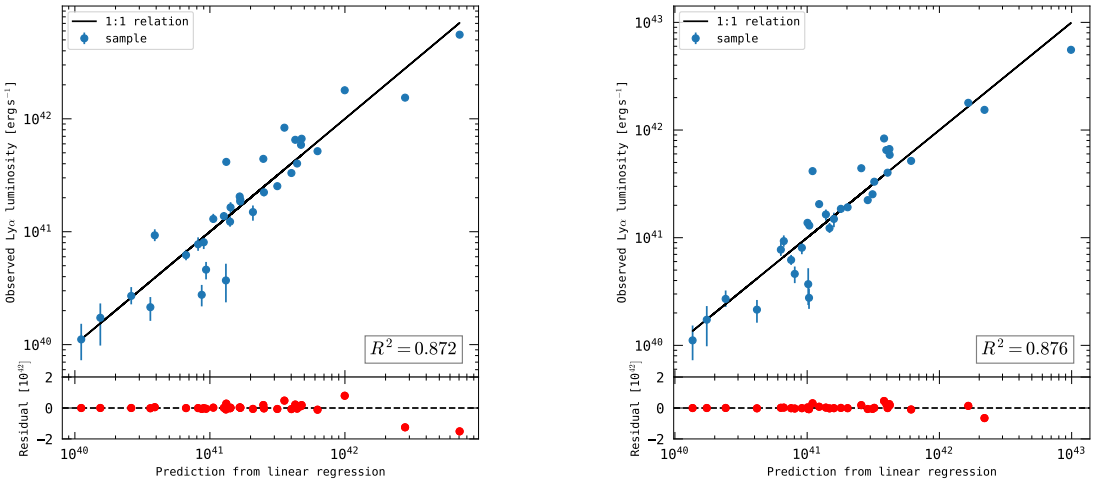

Figure 5.1: Observed Lyα luminosity versus predicted Lyα luminosity from our best-fit relation for the observational variable set without (left) and with (right) kinematic parameters. The line is the 1:1 relation and is expected for a perfect prediction. The bottom panels show the residuals.

has an $R^2 = 0.872$, which leaves only 13 % of the variance of the data unexplained. On the left of Figure 5.1, we show the data versus our Lyα predictions and the residuals.

In Table 5.2, we list the observational variables and kinematic parameters that are used to predict the Lyα luminosity and we list the fitting coefficients. The R^2 score for predictions with kinematic parameters is slightly higher than the predictions with SFR and M ($R^2 = 0.876$). We show the relation between observed and predicted Lyα luminosity on the right of Figure 5.1.

After having a predicting model for the Lyα luminosity out of an observational variable set, we also rank the variables in order of importance. We apply forward and backward selection as described in Section 5. The results and the R^2 scores for each step are listed in Table 5.3 (Table 5.4 with kinematic parameters). Table 5.3 shows the results of forward and backward variable selection on this relation. The forward and backward selection method diverge from each other. We do not find a clear powerful predicting variable in the direct variable set.

5.1.2 Physical variables

To be comparable to theoretic work, we have a physical variable set. Out of these variables, we predict the Lyα luminosity again. We check whether replacing

Table 5.1: Variable and fitting coefficients for the observational variable set for predicting the Lyα luminosity without kinematic parameters.

variable v_i	fitting coefficient c_i
$\log\left(U\,[\mathrm{erg\,s^{-1}\AA^{-1}}]\right) - 40$	-3.605
$\log\left(B\,[\mathrm{erg\,s^{-1}\AA^{-1}}]\right) - 40$	4.527
$\log\left(I\,[\mathrm{erg\,s^{-1}\AA^{-1}}]\right) - 40$	-0.853
$\log\left(L_\mathrm{FUV}\,[\mathrm{erg\,s^{-1}\AA^{-1}}]\right) - 40$	1.305
$\log(L_{\mathrm{H}\alpha}\,[\mathrm{erg\,s^{-1}}]) - 41$	-1.366
$\log(\mathrm{UV\ size\,[kpc]})$	-0.289
$\log(L_{\mathrm{H}\beta}\,[\mathrm{erg\,s^{-1}}]) - 41$	2.608
$\log([\mathrm{OIII}]\,[\mathrm{erg\,s^{-1}}]) - 40$	0.392
$\log([\mathrm{OII}]\,[\mathrm{erg\,s^{-1}}]) - 40$	-2.065
$\log([\mathrm{NII}]\,[\mathrm{erg\,s^{-1}}]) - 40$	0.453
$v_{95}/100$	0.006
$w_{90}/100$	-0.062
F_cov	-0.808

Table 5.2: Variable and fitting coefficients for the observational variable set for predicting the Lyα luminosity with kinematic parameters.

variable v_i	fitting coefficient c_i
$\log\left(U\,[\mathrm{erg\,s^{-1}\AA^{-1}}]\right) - 40$	-3.086
$\log\left(B\,[\mathrm{erg\,s^{-1}\AA^{-1}}]\right) - 40$	3.083
$\log(v_\mathrm{shear}\,[\mathrm{km\,s^{-1}}])$	0.105
$\log\left(L_\mathrm{FUV}\,[\mathrm{erg\,s^{-1}\AA^{-1}}]\right) - 40$	1.353
$\log(\sigma_{\mathrm{m,\ uniform,\ corr}}\,[\mathrm{km\,s^{-1}}])$	0.691
$\log(\mathrm{UV\ size\,}[kpc])$	-0.272
$\log(L_{\mathrm{H}\beta}\,[\mathrm{erg\,s^{-1}}]) - 41$	1.160
$\log([\mathrm{OIII}]\,[\mathrm{erg\,s^{-1}}]) - 40$	0.201
$\log([\mathrm{OII}]\,[\mathrm{erg\,s^{-1}}]) - 40$	-1.400
$\log([\mathrm{NII}]\,[\mathrm{erg\,s^{-1}}]) - 40$	0.003
$v_{95}/100$	0.008
$w_{90}/100$	-0.161
F_cov	-0.680

Table 5.3: Ranking for the observational variable set for predicting the Lyα luminosity without kinematic parameters and with corresponding R^2 scores.

Ranking	Forward Selection	R^2_{forward}	Backward Selection	R^2_{backward}
1	L_{FUV}	0.706	$L_{\text{H}\beta}$	0.872
2	UV size	0.764	F_{cov}	0.872
3	I	0.797	B	0.869
4	F_{cov}	0.818	[OII]	0.865
5	$L_{\text{H}\alpha}$	0.827	L_{FUV}	0.863
6	[OII]	0.839	UV size	0.858
7	$L_{\text{H}\beta}$	0.843	U	0.853
8	U	0.846	w_{90}	0.842
9	B	0.859	[OIII]	0.823
10	w_{90}	0.863	[NII]	0.804
11	[OIII]	0.864	$L_{\text{H}\alpha}$	0.787
12	[NII]	0.872	I	0.745
13	v_{95}	0.872	v_{95}	0.669

Table 5.4: Ranking for the observational variable set for predicting the Lyα luminosity with kinematic parameters and with corresponding R^2 scores.

Ranking	Forward Selection	R^2_{forward}	Backward Selection	R^2_{backward}
1	L_{FUV}	0.706	$L_{\text{H}\beta}$	0.876
2	UV size	0.764	F_{cov}	0.876
3	B	0.789	B	0.875
4	F_{cov}	0.813	[OII]	0.873
5	$\sigma_{\text{m, uniform, corr}}$	0.829	L_{FUV}	0.869
6	U	0.833	UV size	0.860
7	w_{90}	0.839	U	0.853
8	$L_{\text{H}\beta}$	0.846	$\sigma_{\text{m, uniform, corr}}$	0.842
9	[OII]	0.869	w_{90}	0.823
10	[OIII]	0.873	[OIII]	0.804
11	v_{95}	0.875	v_{95}	0.787
12	v_{shear}	0.876	v_{shear}	0.745
13	[NII]	0.876	[NII]	0.669

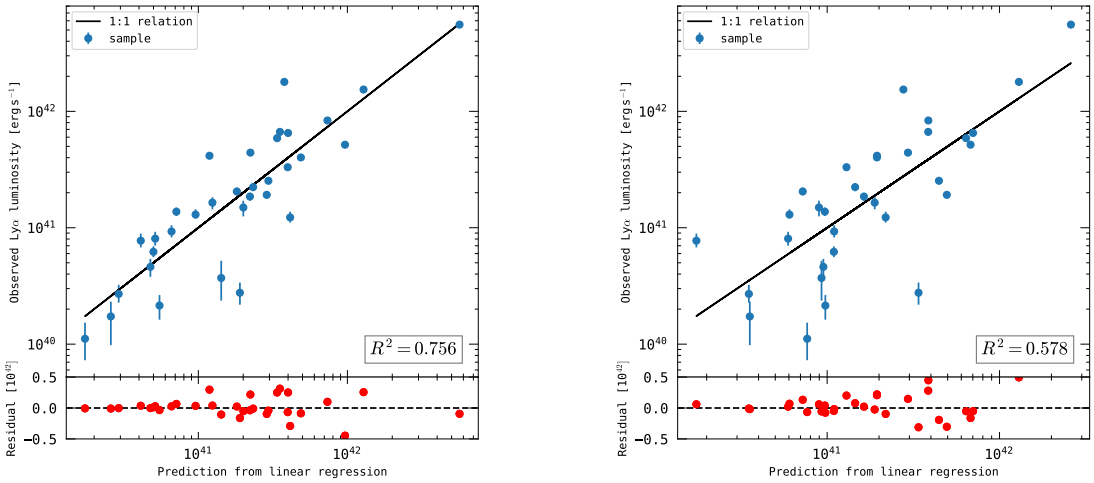

Figure 5.2: Observed Lyα luminosity versus predicted Lyα luminosity from our best-fit relation for the physical variable set without (left) and with (right) kinematic parameters. The line is the 1:1 relation and is expected for a perfect prediction. The bottom panels show the residuals.

the physical parameters by their kinematic counterparts have an influence on the predictive power of the model.

We show the relation between the predictions and observations in Figure 5.2 and list the variables with their fitting parameters in Table 5.5 (Table 5.6 with kinematic parameters included).

Our model has an $R^2 = 0.756$ without kinematic parameters ($R^2 = 0.578$ with kinematic parameters), which leaves 24 % (42 %) of the variance of the data unexplained. Including the kinematic parameters for predicting the Lyα luminosity with a physical variable set gives the model less predictive power.

Table 5.7 and 5.8 show the results of forward and backward variable selection on this relation. Both selection methods agree, which additional supports that the highest ranked variables are most important for Lyα luminosity predictions. From Table 5.7 and Table 5.8 it is clear that a large fraction of the predictive power comes from one variable, in case of the physical set the SFR, E(B-V)$_n$ and F_{cov} and in case with kinematic parameters the $\sigma_{\mathrm{m,\ uniform,\ corr}}$, v_{95} and w_{90}. This can be seen for example at the R^2 scores of the forward selection. The R^2 raises very fast and then stagnates.

Table 5.5: Variable and fitting coefficients for the physical variable set for predicting the Lyα luminosity without kinematic parameters.

variable v_i	fitting coefficient c_i
$\log\big(M\,[M_\odot]\big) - 10$	0.172
$\log(\text{UV size}\,[\text{kpc}])$	-0.183
E(B-V)_n	-1.064
$\log(O32)$	0.057
$12 + \log(O/H) - 7$	-2.775
$\log\big(\text{SFR}_{\text{H}\alpha}\,[M_\odot\,\text{yr}^{-1}]\big)$	0.979
$\log(v_{95}\,[\text{km s}^{-1}]) - 2$	0.072
$\log(w_{90}\,[\text{km s}^{-1}]) - 2$	-0.558
F_cov	-1.123

Table 5.6: Variable and fitting coefficients for the physical variable set for predicting the Lyα luminosity with kinematic parameters.

variable v_i	fitting coefficient c_i
$\log(v_\text{shear}\,[\text{km s}^{-1}])$	-0.081
$\log(\text{UV size}\,[\text{kpc}])$	0.405
E(B-V)_n	-0.172
$\log(O32)$	0.125
$12 + \log(O/H) - 7$	-15.262
$\log(\sigma_\text{m, uniform, corr}\,[\text{km s}^{-1}])$	3.155
$\log(v_{95}\,[\text{km s}^{-1}]) - 2$	2.501
$\log(w_{90}\,[\text{km s}^{-1}]) - 2$	-2.315
F_cov	-0.467

Table 5.7: Ranking for the physical variable set for predicting the Lyα luminosity without kinematic parameters and with corresponding R^2 scores.

Ranking	Forward Selection	R^2_{forward}	Backward Selection	R^2_{backward}
1	$\text{SFR}_{\text{H}\alpha}$	0.489	$\text{SFR}_{\text{H}\alpha}$	0.756
2	E(B-V)_n	0.645	E(B-V)_n	0.756
3	F_{cov}	0.739	F_{cov}	0.756
4	UV size	0.751	UV size	0.755
5	w_{90}	0.754	w_{90}	0.754
6	M	0.755	M	0.751
7	O/H	0.756	O/H	0.739
8	O32	0.756	O32	0.645
9	v_{95}	0.756	v_{95}	0.489

Table 5.8: Ranking for the physical variable set for predicting the Lyα luminosity without kinematic parameters and with corresponding R^2 scores.

Ranking	Forward Selection	R^2_{forward}	Backward Selection	R^2_{backward}
1	$\sigma_{\text{m, uniform, corr}}$	0.376	$\sigma_{\text{m, uniform, corr}}$	0.578
2	v_{95}	0.457	v_{95}	0.577
3	w_{90}	0.489	w_{90}	0.574
4	O/H	0.522	O/H	0.567
5	UV size	0.555	UV size	0.555
6	F_{cov}	0.567	F_{cov}	0.522
7	E(B-V)_n	0.0.574	E(B-V)_n	0.489
8	O32	0.577	O32	0.457
9	v_{shear}	0.578	v_{shear}	0.376

5.2 Predicting the Lyα equivalent width

5.2.1 Observational variables

We use the same variable set for predicting the equivalent width in Lyα as we used for the luminosity, but we exclude the FUV luminosity, as Lyα luminosity and FUV luminosity combine to this quantity (see Section 1.2.3). Again we built up two variable sets - with and without kinematic parameters.

In Table 5.9, we list the observational variables that are used to predict the Lyα equivalent width and we list the fitting coefficients (see Equation (5.3)). The linear model has an $R^2 = 0.571$, which leaves 43 % of the variance of the data unexplained. On the left of Figure 5.3, we show the data versus our Lyα predictions and the residuals.

In Table 5.10, we list the observational variables and kinematic parameters that are used to predict the Lyα equivalent width and we list the fitting coefficients. The predictions with kinematic parameters are a bit better ($R^2 = 0.581$) than the predictions with $L_{\mathrm{H}\alpha}$ and I ($R^2 = 0.571$). We show the relation between observed and predicted Lyα equivalent width on the right of Figure 5.3.

After having a predicting model for the Lyα equivalent width out of an observational variable set, we also rank the variables in order of importance. We apply forward and backward selection as described in Section 5. The results and the R^2 scores for each step are listed in Table 5.11 (Table 5.12 with kinematic parameters). With kinematic parameters, the forward and backward selection method diverge from each other and we can not find a most important variable. Without kinematic parameters, UV size is ranked on the first position both in the forward and backward selection method, the other positions diverge from each other.

5.2.2 Physical variables

For the physical variables we use the same parameter set as for predicting the Lyα luminosity with physical variables. Again we check whether replacing the physical parameters by their kinematic counterparts have an influence on the predictive power of the model.

We show the relation between the predictions and observations in Figure 5.4 and list the variables with their fitting parameters in Table 5.13 (Table 5.14 with kinematic parameters included).

The model has an $R^2 = 0.380$ without kinematic parameters ($R^2 = 0.400$ with kinematic parameters), which leaves 62 % (60 %) of the variance of the data

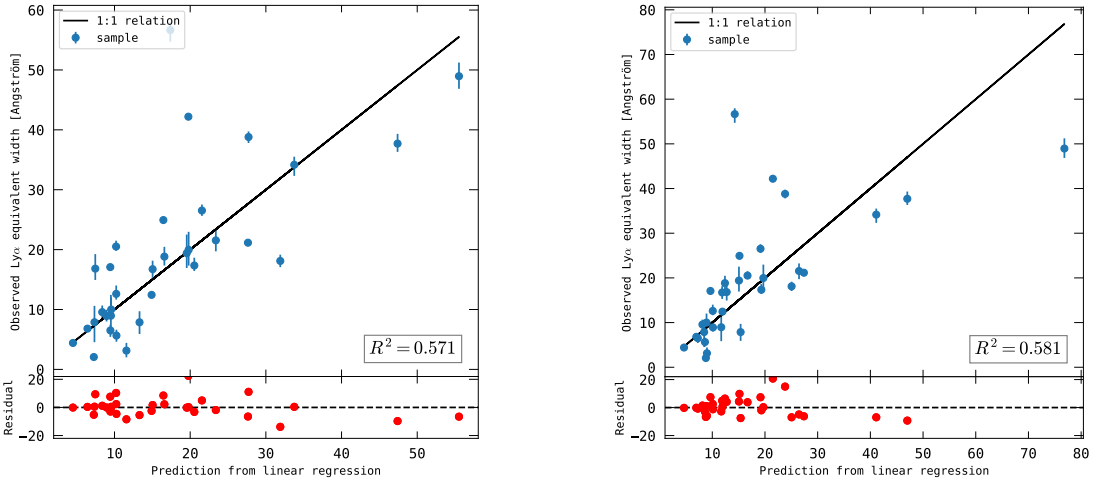

Figure 5.3: Observed Lyα luminosity versus predicted Lyα equivalent width from our best-fit relation for the observational variable set without (left) and with (right) kinematic parameters. The line is the 1:1 relation and is expected for a perfect prediction. The bottom panels show the residuals.

Table 5.9: Variable and fitting coefficients for the observational variable set for predicting the Lyα equivalent width without kinematic parameters.

variable v_i	fitting coefficient c_i
$\log\left(U\,[\mathrm{erg\,s^{-1}\AA^{-1}}]\right) - 40$	-2.894
$\log\left(B\,[\mathrm{erg\,s^{-1}\AA^{-1}}]\right) - 40$	4.016
$\log\left(I\,[\mathrm{erg\,s^{-1}\AA^{-1}}]\right) - 40$	-0.916
$\log(L_{\mathrm{H}\alpha}\,[\mathrm{erg\,s^{-1}}]) - 41$	-1.366
$\log(\mathrm{UV\ size\,[kpc]})$	-0.241
$\log(L_{\mathrm{H}\beta}\,[\mathrm{erg\,s^{-1}}]) - 41$	2.593
$\log([\mathrm{OIII}]\,[\mathrm{erg\,s^{-1}}]) - 40$	0.364
$\log([\mathrm{OII}]\,[\mathrm{erg\,s^{-1}}]) - 40$	-1.903
$\log([\mathrm{NII}]\,[\mathrm{erg\,s^{-1}}]) - 40$	0.465
$v_{95}/100$	-0.009
$w_{90}/100$	-0.043
F_cov	-0.898

Table 5.10: Variable and fitting coefficients for the observational variable set for predicting the Lyα equivalent width with kinematic parameters.

variable v_i	fitting coefficient c_i
$\log\left(U\,[\mathrm{erg\,s^{-1}\AA^{-1}}]\right) - 40$	-2.170
$\log\left(B\,[\mathrm{erg\,s^{-1}\AA^{-1}}]\right) - 40$	2.325
$\log(v_\mathrm{shear}\,[\mathrm{km\,s^{-1}}]) - 41$	0.114
$\log(\sigma_\mathrm{m,\ uniform,\ corr}\,[\mathrm{km\,s^{-1}}])$	0.652
$\log(\mathrm{UV\ size}\,[\mathrm{kpc}])$	-0.222
$\log(L_{\mathrm{H}\beta}\,[\mathrm{erg\,s^{-1}}]) - 41$	1.121
$\log([\mathrm{OIII}]\,[\mathrm{erg\,s^{-1}}]) - 40$	0.176
$\log([\mathrm{OII}]\,[\mathrm{erg\,s^{-1}}]) - 40$	-1.204
$\log([\mathrm{NII}]\,[\mathrm{erg\,s^{-1}}]) - 40$	0.014
$v_{95}/100$	0.067
$w_{90}/100$	-0.140
F_cov	-0.763

Table 5.11: Ranking for the observational variable set for predicting the Lyα equivalent width without kinematic parameters and with corresponding R^2 scores.

Ranking	Forward Selection	R^2_forward	Backward Selection	R^2_backward
1	UV size	0.185	UV size	0.571
2	I	0.327	B	0.571
3	F_cov	0.395	[OII]	0.562
4	B	0.414	$L_{\mathrm{H}\beta}$	0.550
5	$L_{\mathrm{H}\alpha}$	0.423	F_cov	0.541
6	[OII]	0.469	U	0.530
7	U	0.488	w_{90}	0.516
8	$L_{\mathrm{H}\beta}$	0.531	[OIII]	0.466
9	w_{90}	0.542	[NII]	0.417
10	[NII]	0.548	$L_{\mathrm{H}\alpha}$	0.322
11	[OIII]	0.571	I	0.300
12	v_{95}	0.571	v_{95}	0.185

Table 5.12: Ranking for the observational variable set for predicting the Lyα equivalent width with kinematic parameters and with corresponding R^2 scores.

Ranking	Forward Selection	R^2_{forward}	Backward Selection	R^2_{backward}
1	$\sigma_{\text{m, uniform, corr}}$	0.212	UV size	0.574
2	F_{cov}	0.325	B	0.574
3	B	0.368	[OII]	0.572
4	[OII]	0.416	$L_{\text{H}\beta}$	0.564
5	$L_{\text{H}\beta}$	0.476	F_{cov}	0.554
6	U	0.499	U	0.522
7	UV size	0.538	$\sigma_{\text{m, uniform, corr}}$	0.499
8	w_{90}	0.564	w_{90}	0.418
9	[OIII]	0.575	[OIII]	0.366
10	v_{95}	0.578	v_{95}	0.326
11	v_{shear}	0.581	v_{shear}	0.240
12	[NII]	0.581	[NII]	0.060

unexplained. Including the kinematic parameters for predicting the Lyα equivalent width with a physical variable set gives the model a slightly higher descriptive power. However, with the linear model, we do not trace important effects influencing the equivalent width and we cannot explain a large variance of the data.

Table 5.15 and 5.16 show the results of forward and backward variable selection on this relation. Without kinematic parameters, the forward and backward method diverge. Including kinematic parameters, the forward and backward selection method agree in the first two ranking positions with $\sigma_{\text{m, uniform, corr}}$ being first and F_{cov} being second.

5.3 Predicting the Lyα escape fraction

5.3.1 Observational variables

We use the same variable set for predicting the equivalent width in Lyα as we used for the luminosity. Again we built up two variable sets - with and without kinematic parameters.

In Table 5.17, we list the observational variables that are used to predict the Lyα escape fraction and we list the fitting coefficients (see Equation (5.3)). Our model has an $R^2 = 0.643$, which leaves 36 % of the variance of the data unexplained. On the left of Figure 5.5, we show the data versus our Lyα predictions and the

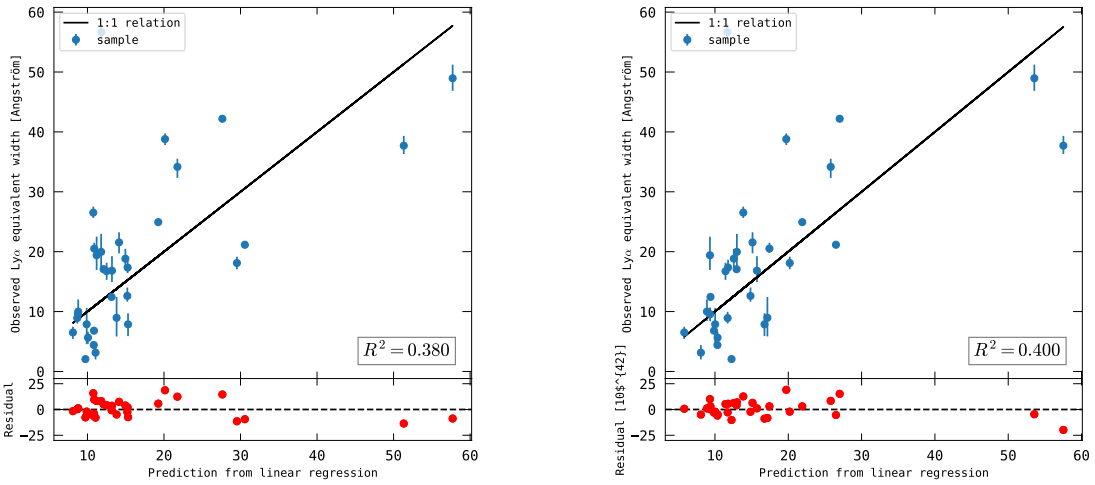

Figure 5.4: Observed Lyα luminosity versus predicted Lyα equivalent width from our best-fit relation for the physical variable set without (left) and with (right) kinematic parameters. The line is the 1:1 relation and is expected for a perfect prediction. The bottom panels show the residuals.

Table 5.13: Variable and fitting coefficients for the physical variable set for predicting the Lyα equivalent width without kinematic parameters.

variable v_i	fitting coefficient c_i
$\log\left(M\,[M_\odot]\right) - 10$	0.063
$\log(\mathrm{UV\ size\,[kpc]})$	-0.264
$\mathrm{E(B\text{-}V)}_n$	0.106
$\log(O32)$	-0.110
$12 + \log(O/H) - 7$	-4.917
$\log\left(\mathrm{SFR}_{\mathrm{H}\alpha}\,[M_\odot\,\mathrm{yr}^{-1}]\right)$	0.196
$\log(v_{95}\,[\mathrm{km\,s^{-1}}]) - 2$	0.152
$\log(w_{90}\,[\mathrm{km\,s^{-1}}]) - 2$	-0.730
F_cov	-0.775

Table 5.14: Variable and fitting coefficients for the physical variable set for predicting the Lyα equivalent width with kinematic parameters.

variable v_i	fitting coefficient c_i
$\log(v_\mathrm{shear}\,[\mathrm{km\,s^{-1}}])$	0.177
$\log(\mathrm{UV\ size}\,[\mathrm{kpc}])$	-0.157
$\mathrm{E(B\text{-}V)}_n$	0.139
$\log(O32)$	-0.128
$12+\log(O/H)-7$	-8.477
$\log(\sigma_\mathrm{m,\ uniform,\ corr}\,[\mathrm{km\,s^{-1}}])$	0.898
$\log(v_{95}\,[\mathrm{km\,s^{-1}}])-2$	0.881
$\log(w_{90}\,[\mathrm{km\,s^{-1}}])-2$	-1.565
F_cov	-0.592

Table 5.15: Ranking for the physical variable set for predicting the Lyα equivalent width without kinematic parameters and with corresponding R^2 scores.

Ranking	Forward Selection	R^2_forward	Backward Selection	R^2_backward
1	UV size	0.185	F_cov	0.380
2	$\mathrm{SFR_{H\alpha}}$	0.254	$\mathrm{SFR_{H\alpha}}$	0.380
3	F_cov	0.344	UV size	0.378
4	w_{90}	0.359	w_{90}	0.377
5	O32	0.371	O32	0.371
6	O/H	0.377	O/H	0.359
7	$\mathrm{E(B\text{-}V)}_n$	0.378	$\mathrm{E(B\text{-}V)}_n$	0.344
8	M	0.380	M	0.259
9	v_{95}	0.380	v_{95}	0.113

Table 5.16: Ranking for the physical variable set for predicting the Lyα equivalent width with kinematic parameters and with corresponding R^2 scores.

Ranking	Forward Selection	R^2_{forward}	Backward Selection	R^2_{backward}
1	$\sigma_{\text{m, uniform, corr}}$	0.212	$\sigma_{\text{m, uniform, corr}}$	0.400
2	F_{cov}	0.325	F_{cov}	0.395
3	E(B-V)$_n$	0.336	w_{90}	0.382
4	UV size	0.345	v_{95}	0.365
5	O32	0.353	v_{shear}	0.347
6	O/H	0.369	UV size	0.341
7	w_{90}	0.378	O/H	0.331
8	v_{95}	0.392	O32	0.325
9	v_{shear}	0.400	E(B-V)$_n$	0.212

residuals.

In Table 5.18, we list the observational variables and kinematic parameters that are used to predict the Lyα escape fraction and we list the fitting coefficients. The predictions with kinematics are a bit better ($R^2 = 0.654$) than the predictions with $L_{\text{H}\alpha}$ and I. We show the relation between observed and predicted Lyα escape fraction with kinematic parameters on the right of Figure 5.5.

After having a predicting model for the Lyα escape fraction out of an observational variable set, we also rank the variables in order of importance. We apply forward and backward selection as described in Section 5. The results and the R^2 scores for each step are listed in Table 5.19 (Table 5.20 with kinematic parameters). Without kinematic parameters, the forward and backward selection method diverge from each other apart from L_{FUV} being ranked on the first position. Including kinematic parameters, forward and backward selection method agree for the first three positions F_{cov}, [OIII] and v_{shear}.

5.3.2 Physical variables

For the physical variables we use the same parameter set as for predicting the Lyα luminosity with physical variables. Again we check whether replacing the physical parameters by their kinematic counterparts have an influence on the predictive power of the model.

We show the relation between the predictions and observations in Figure 5.6 and list the variables with their fitting parameters in Table 5.21 (Table 5.22 with kinematic parameters included).

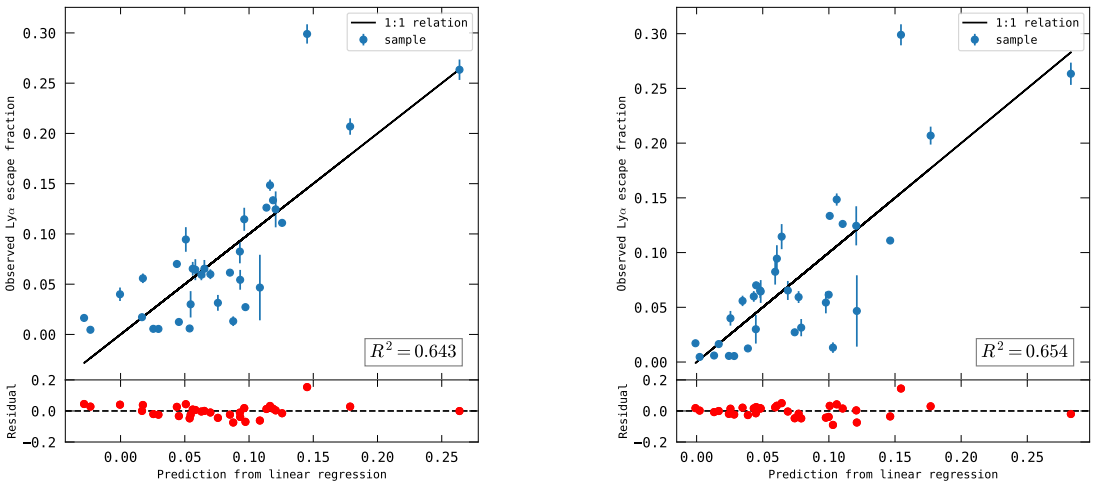

Figure 5.5: Observed Lyα escape fraction versus predicted Lyα escape fraction from our best-fit relation for the observational variable set without (left) and with (right) kinematic parameters. The line is the 1:1 relation and is expected for a perfect prediction. The bottom panels show the residuals.

Table 5.17: Variable and fitting coefficients for the observational variable set for predicting the Lyα escape fraction without kinematic parameters.

variable v_i	fitting coefficient c_i
$\log\left(U\,[\mathrm{erg\,s^{-1}\,\AA^{-1}}]\right) - 40$	-0.821
$\log\left(B\,[\mathrm{erg\,s^{-1}\,\AA^{-1}}]\right) - 40$	0.723
$\log\left(I\,[\mathrm{erg\,s^{-1}\,\AA^{-1}}]\right) - 40$	-0.023
$\log\left(L_\mathrm{FUV}\,[\mathrm{erg\,s^{-1}\,\AA^{-1}}]\right) - 40$	0.227
$\log(L_\mathrm{H\alpha}\,[\mathrm{erg\,s^{-1}}]) - 41$	-0.420
$\log(\mathrm{UV\ size\,[kpc]})$	-0.045
$\log(L_\mathrm{H\beta}\,[\mathrm{erg\,s^{-1}}]) - 41$	0.526
$\log([\mathrm{OIII}]\,[\mathrm{erg\,s^{-1}}]) - 40$	0.097
$\log([\mathrm{OII}]\,[\mathrm{erg\,s^{-1}}]) - 40$	-0.318
$\log([\mathrm{NII}]\,[\mathrm{erg\,s^{-1}}]) - 40$	0.060
$v_{95}/100$	0.042
$w_{90}/100$	-0.058
F_cov	-0.132

Table 5.18: Variable and fitting coefficients for the observational variable set for predicting the Lyα escape fraction with kinematic parameters.

variable v_i	fitting coefficient c_i
$\log\left(U\,[\mathrm{erg\,s^{-1}\,\AA^{-1}}]\right) - 40$	-0.920
$\log\left(B\,[\mathrm{erg\,s^{-1}\,\AA^{-1}}]\right) - 40$	0.790
$\log(v_\mathrm{shear}\,[\mathrm{km\,s^{-1}}])$	-0.076
$\log\left(L_\mathrm{FUV}\,[\mathrm{erg\,s^{-1}\,\AA^{-1}}]\right) - 40$	0.237
$\log(\sigma_\mathrm{m,\,uniform,\,corr}\,[\mathrm{km\,s^{-1}}])$	0.187
$\log(\mathrm{UV\ size\,[kpc]})$	-0.021
$\log(L_{\mathrm{H}\beta}\,[\mathrm{erg\,s^{-1}}]) - 41$	0.109
$\log([\mathrm{OIII}]\,[\mathrm{erg\,s^{-1}}]) - 40$	0.070
$\log([\mathrm{OII}]\,[\mathrm{erg\,s^{-1}}]) - 40$	-0.217
$\log([\mathrm{NII}]\,[\mathrm{erg\,s^{-1}}]) - 40$	-0.022
$v_{95}/100$	0.035
$w_{90}/100$	-0.052
F_cov	-0.178

Table 5.19: Ranking for the observational variable set for predicting the Lyα escape fraction without kinematic parameters and with corresponding R^2 scores.

Ranking	Forward Selection	R^2_forward	Backward Selection	R^2_backward
1	F_cov	0.356	F_cov	0.643
2	[OIII]	0.425	L_FUV	0.643
3	w_{90}	0.452	U	0.633
4	v_{95}	0.477	[NII]	0.610
5	UV size	0.501	B	0.600
6	[OII]	0.505	[OII]	0.555
7	L_FUV	0.524	[OIII]	0.531
8	U	0.530	v_{95}	0.507
9	B	0.599	w_{90}	0.477
10	$L_{\mathrm{H}\beta}$	0.610	UV size	0.475
11	$L_{\mathrm{H}\alpha}$	0.633	$L_{\mathrm{H}\beta}$	0.436
12	[NII]	0.643	I	0.398
13	I	0.643	$L_{\mathrm{H}\alpha}$	0.356

Table 5.20: Ranking for the observational variable set for predicting the Lyα escape fraction with kinematic parameters and with corresponding R^2 scores.

Ranking	Forward Selection	R^2_{forward}	Backward Selection	R^2_{backward}
1	F_{cov}	0.356	F_{cov}	0.654
2	OIII	0.425	OIII	0.652
3	v_{shear}	0.479	v_{shear}	0.647
4	w_{90}	0.489	OII	0.635
5	$\sigma_{\text{m, uniform, corr}}$	0.505	L_{FUV}	0.607
6	v_{95}	0.519	B	0.583
7	OII	0.526	U	0.534
8	L_{FUV}	0.539	$\sigma_{\text{m, uniform, corr}}$	0.500
9	U	0.545	w_{90}	0.500
10	B	0.635	v_{95}	0.482
11	$L_{\text{H}\beta}$	0.647	$L_{\text{H}\beta}$	0.479
12	UV size	0.652	UV size	0.425
13	NII	0.654	NII	0.356

Our model has an $R^2 = 0.574$ without kinematic parameters ($R^2 = 0.610$ with kinematic parameters), which leaves 43 % (39 %) of the variance of the data unexplained. Including the kinematic parameters for predicting the Lyα escape fraction with a physical variable set gives the model a slightly higher descriptive power.

Table 5.23 and 5.24 show the results of forward and backward variable selection on this relation. Without kinematic parameters, F_{cov} and E(B-V)$_n$ are the most important variables for predicting the escape fraction, the other positions diverge between forward and backward method. Including kinematic parameters, the forward and backward selection method agree in the ranking positions. F_{cov} and E(B-V)$_n$ are ranked on the first positions, followed by $\sigma_{\text{m, uniform, corr}}$ being the third most important variable.

5.4 Kinematic parameter importance for predicting Lyα observables

Going through literature, we find many different researches studying many different variables and the relation to the Lyα observables. The studies and also we in Section 4 test statistical for correlations. It is found that "Lyα has been claimed,

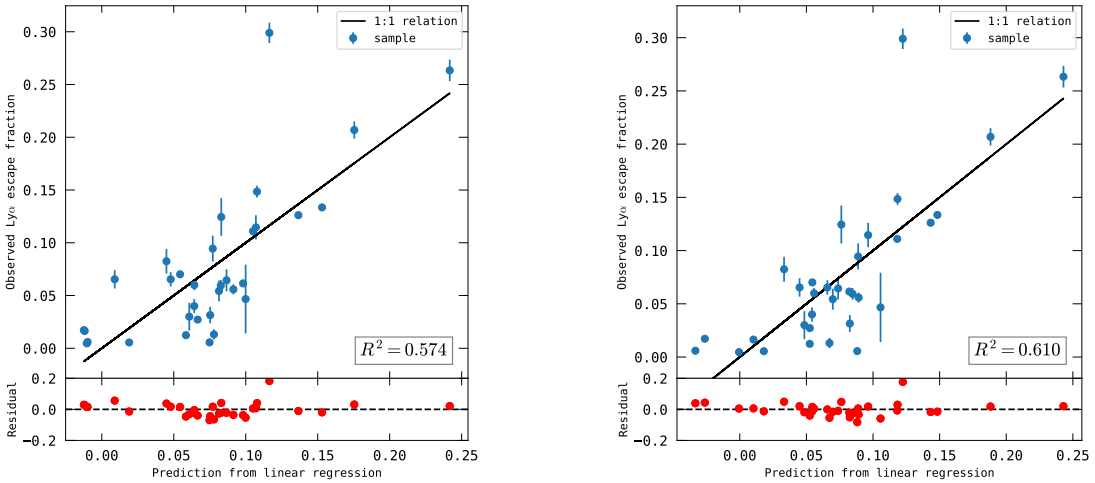

Figure 5.6: Observed Lyα luminosity versus predicted Lyα escape fraction from our best-fit relation for the physical variable set without (left) and with (right) kinematic parameters. The line is the 1:1 relation and is expected for a perfect prediction. The bottom panels show the residuals.

Table 5.21: Variable and fitting coefficients for the physical variable set for predicting the Lyα escape fraction without kinematic parameters.

variable v_i	fitting coefficient c_i
$\log\left(M\,[M_\odot]\right) - 10$	0.007
$\log(\mathrm{UV\ size\,[kpc]})$	-0.023
$\mathrm{E(B\text{-}V)}_n$	-0.123
$\log(O32)$	0.024
$12 + \log(O/H) - 7$	-1.129
$\log\left(\mathrm{SFR}_{\mathrm{H}\alpha}\,[M_\odot\,\mathrm{yr}^{-1}]\right)$	0.021
$\log(v_{95}\,[\mathrm{km\,s^{-1}}]) - 2$	0.085
$\log(w_{90}\,[\mathrm{km\,s^{-1}}]) - 2$	-0.163
F_cov	-0.181

Table 5.22: Variable and fitting coefficients for the physical variable set for predicting the Lyα escape fraction with kinematic parameters.

variable v_i	fitting coefficient c_i
$\log(v_\mathrm{shear}\,[\mathrm{km\,s^{-1}}])$	-0.005
$\log(\mathrm{UV\ size}\,[\mathrm{kpc}])$	0.004
$\mathrm{E(B\text{-}V)}_n$	-0.123
$\log(O32)$	0.014
$12+\log(O/H)-7$	-1.557
$\log(\sigma_\mathrm{m,\ uniform,\ corr}\,[\mathrm{km\,s^{-1}}])$	0.187
$\log(v_{95}\,[\mathrm{km\,s^{-1}}])-2$	0.124
$\log(w_{90}\,[\mathrm{km\,s^{-1}}])-2$	-0.232
F_cov	-0.175

Table 5.23: Ranking for the physical variable set for predicting the Lyα escape fraction without kinematic parameters and with corresponding R^2 scores.

Ranking	Forward Selection	R^2_forward	Backward Selection	R^2_backward
1	F_cov	0.356	F_cov	0.574
2	$\mathrm{E(B\text{-}V)}_n$	0.455	$\mathrm{E(B\text{-}V)}_n$	0.574
3	O32	0.516	UV size	0.569
4	$\mathrm{SFR_{H\alpha}}$	0.541	$\mathrm{SFR_{H\alpha}}$	0.566
5	UV size	0.557	O/H	0.561
6	O/H	0.564	w_{90}	0.548
7	w_{90}	0.569	O32	0.507
8	v_{95}	0.574	v_{95}	0.455
9	M	0.574	M	0.356

Table 5.24: Ranking for the physical variable set for predicting the Lyα escape fraction with kinematic parameters and with corresponding R^2 scores.

Ranking	Forward Selection	R^2_{forward}	Backward Selection	R^2_{backward}
1	F_{cov}	0.356	F_{cov}	0.610
2	E(B-V)$_n$	0.455	E(B-V)$_n$	0.610
3	$\sigma_{\text{m, uniform, corr}}$	0.567	$\sigma_{\text{m, uniform, corr}}$	0.610
4	O/H	0.589	O/H	0.607
5	w_{90}	0.596	w_{90}	0.596
6	v_{95}	0.607	v_{95}	0.589
7	O32	0.609	O32	0.567
8	UV size	0.610	UV size	0.455
9	v_{shear}	0.610	v_{shear}	0.356

probably correctly, to be stronger in younger galaxies, with lower stellar mass, more compact stellar continua, and higher sSFR. These are typically bluer and less dusty, with lower metallicities and higher ionization parameters. They also appear to drive faster outflows, with less rotationally dominated velocity fields, and have lower HI covering fractions and/or column densities" (Dijkstra 2019). This shows that the understanding what makes a galaxy a Lyα emitter and what makes Lyα photons to escape is a very complex question and depends on an interaction of many variables. Looking on the relation of a single quantity with the Lyα variables is not enough.

We tried in this chapter to take many variables and find out, which variables have the most important impact on the Lyα observables. This experiment has the aim to show the potential importance of the global kinematic state of the ionized gas on the Lyα observables. However, it has to be kept in mind that the model is heuristic and is not built up on physical relations.

Du to the fact that we use for the variable sets with and without the kinematic parameters the same number of variables, we are in the position to interpret an increase in the R^2 score after replacing with kinematics that the kinematic counterparts are more important than the photometric counterparts for predicting[2] the Lyα observables under the conditions that the kinematic parameters are ranked high and that the forward and backward selection ranks are consistent.

All predictions with the included ionized kinematics improve the R^2 score, except the physical variable set for predicting $L_{\text{Ly}\alpha}$. This implies that the variable sets with ionized gas kinematic parameters have in the most cases a better predicting

[2]The predictive power is evaluated with the same sample.

power. From our three Lyα observables (Lyα luminosity, $EW_{Ly\alpha}$ and f_{esc}) reaches the luminosity the highest R^2 score. Additional, direct variable sets have more predictive power than physical variable sets. However, the small sample size has an negative impact on the robustness of the results. The slight increase of the R^2 scores, when parameters are replaced with their kinematic counterparts, should thus not be over interpreted.

As mentioned in the beginning of the chapter, we distinguish our variables into the two variable sets that we have an access from the point of view from observations and from a point of view of physical processes. We can argue that we can include our ionized gas kinematics $\sigma_{m,\ uniform,\ corr}$ and v_{shear} in both variable sets. The parameters are directly derived from the Hα line, so we have access to these variables directly from our observations. On the other hand, we calculate the kinematic parameters and can also extract these quantities from models. Therefore, we include the parameters also to our physical variable set.

We state that the multivariate linear model is robust, when forward and backward selection agree. We find three out of twelve robust models in our experiment. All robust rankings are found in physical variable sets. The first robust model is for the prediction of the Lyα luminosity without kinematic parameters. We get a R^2 of 0.756 and the three most important variables are $SFR_{H\alpha}$, $E(B\text{-}V)_n$ and F_{cov}. Regions of ongoing star formation are important for producing ionizing photons and therefore producing Lyα photons. We also recover in our ranking method this importance of SFR for the Lyα luminosity as the SFR is ranked on the first position with a strong positive weight in the fitting parameter. We expect dust to suppress the Lyα emission. This we see also in our ranking method, as $E(B\text{-}V)_n$ being the second most important variable with a negative fitting coefficient. This result is similar to the findings in Runnholm et al. (2020). By including the kinematic parameters and excluding M and SFR, the velocity dispersion is ranked on the first position in both the forward and backward method. The velocity dispersion seems therefore important for predicting the Lyα luminosity. However, the R^2 score is significant lower with 0.578 for the model for the Lyα luminosity with kinematics. Although the velocity dispersion is ranked on the first position, we conclude that kinematics have not an important role in predicting the Lyα luminosity compared to the photometric counterparts. As the Lyα luminosity is in relation with the Lyα production, it appeares intuitive that the velocity dispersion is not directly relate to the Lyα production, whereas the starformation rate is in direct relation with the Lyα production.

The third and final robust linear model is for the escape fraction predicted with the physical variable set with kinematic parameters. The R^2 score increases from 0.574 without kinematic parameters to 0.610 with kinematic parameters. It

appears interesting that we do not get a robust ranking results without kinematic parameters for the escape fraction. With kinematic parameters the ranking is the following: F_{cov} is ranked as the most important variable, followed by E(B-V)$_n$ and $\sigma_{\mathrm{m,\ uniform,\ corr}}$. v_{shear} is ranked on the last position. However, Runnholm et al. (2020) showed with a Monte Carlo simulation that the ranks below the first few positions can fluctuate and should not be interpreted. The first two parameters are also ranked on the first and second position in the physical variable set without kinematic parameters. The escape fraction is a quantity related to the Lyα radiative transfer. Therefore, it is not surprising that the covering fraction and the dust content, which both assumed to influence the Lyα escape along the line of sight, ranked on the first positions. With being ranked on the third position, also the velocity dispersion seems to have an influence on the Lyα radiative transfer.

We may conclude from this statistical experiment, that the kinematic parameters appear as important parameters for regulating the Lyα observables and having influence on the Lyα radiative transfer, but they are certainly not the most important parameters. The finding of kinematic parameters being important on the Lyα observables is in agreement with the correlations found in Section 4.2 and underlines the importance of studying ionized gas kinematics.

Here we study only the ionized gas kinematics. F_{cov}, w_{90} and v_{95} are proxies for the neutral covering, but they are only measured with COS in the brightest regions of the galaxies. Physically, we expect the difference between the covering neutral gas and the kinematics of ionized gas to be of significant importance.

6 Summary and outlook

The Lyα line is an important signature to find high-z galaxies, but the resonant line transfer requires extremely low optical depths for it to actually emerge from galaxies. Turbulent kinematics may shift enough emitting and absorbing material out of resonance and thereby enhance the probability of Lyα escaping. We study spatially resolved the effect of ionized gas kinematics on Lyα observables in the LARS and eLARS sample.

First, we characterize the velocity fields qualitatively and divide our galaxies in three subsets: RDs, PRs and CKs. We have 18 RDs, 13 PRs and 11 CKs in our sample. The minimum, maximum, median and mean indicate that CKs have preverentially higher values in the observed Lyα observables and that complex kinematics may positively influence the escape of Lyα photons. We test this tendency with the Kolomgorov-Smirnov test. The statistic test does not confirm the assumption of the central tendency seen in the maximum, minimum, average and median that complex kinematics favor the Lyα escape from galaxies.

We derive the line of sight kinematic parameters v_{shear} and σ from Hα from PMAS data cuboids. The velocity dispersion has to be corrected for PSF smearing. We introduce a new empiric method to correct for PSF smearing. We built a gradient and mask spaxels in the velocity dispersion map with high gradient values. For our galaxies. We also calculate other empiric approaches. Following M. Varidel et al. (2016), we fit a 2D linear model out of S/N and a gradient on our maps and remove the gradient part. Following Yu et al. (2021), we extract the velocity dispersion along the major kinematic axis in regions, where the rotation curve is flat. We model our RDs with the parametric disk model GalPaK3D (Bouché et al. 2015). Assuming that GalPaK3D resembles the true velocity dispersion value, we compare the performance of the different empiric models. We find that our new introduced gradient method without S/N weighting performs best and we use $\sigma_{\mathrm{m,\ uniform,\ corr}}$ for further analysis.

$\sigma_{\mathrm{m,\ uniform,\ corr}}$ ranges from 23.9 $\mathrm{km\,s^{-1}}$ to 78.0 $\mathrm{km\,s^{-1}}$ with a median of 37.3 $\mathrm{km\,s^{-1}}$. v_{shear} ranges from 14.7 $\mathrm{km\,s^{-1}}$ to 181.9 $\mathrm{km\,s^{-1}}$ with a median of 58.0 $\mathrm{km\,s^{-1}}$. $v_{\mathrm{shear}}/\sigma_{\mathrm{m,\ uniform,\ corr}}$ ranges from 0.4 up to 4.5 with a median of 1.7. The values are in the range of other observation campaigns.

We relate the kinematic parameters to the galaxy parameters SFR and stellar

mass. We apply the Kendall tau correlation test. We find correlations between SFR and v_{shear} and SFR and $\sigma_{\mathrm{m,\ uniform,\ corr}}$. We also find a correlation between stellar mass and v_{shear}. This is in accordance with well known relations in literature.

Further we relate kinematic parameters with the Lyα observables $\mathrm{L_{Ly\alpha}/L_{H\alpha}}$, $\mathrm{EW_{Ly\alpha}}$ and $f_{\mathrm{esc}}^{\mathrm{Ly\alpha}}$. $\mathrm{EW_{Ly\alpha}}$ and $\mathrm{L_{Ly\alpha}/L_{H\alpha}}$ correlate with $\sigma_{\mathrm{m,\ uniform,\ corr}}$. $f_{\mathrm{esc}}^{\mathrm{Ly\alpha}}$ anti-correlates with v_{shear} and $v_{\mathrm{shear}}/\sigma_{\mathrm{m,\ uniform,\ corr}}$, indicating that lower mass galaxies with higher star-formation rates are the stronger Lyα emitters, but from a kinematical perspective.

Finally, we set up a multivariate linear regression model to predict the Lyα observables. We distinguish between an observational and physical variable set to be comparable to theoretic and observational work. Most models have a higher R^2 score, when the kinematic parameters are included, which implies that models with included kinematic parameters have a better predictive power. We apply a forward and backward selection to our variable sets, which ranks the variables in order of importance. We experience that v_{shear} plays an unimportant and $\sigma_{\mathrm{m,\ uniform,\ corr}}$ plays an important role as powerful predictive variable influencing the Lyα observables, espectially in the Lyα radiative transfer.

We find that the integrated ionized gas kinematics influence the escape of Lyα photons. Dispersion dominated kinematics may be a necessary, but not sufficient, condition for facilitating Lyα escape.

In further work, we can study the local relation between the ionized gas kinematics and Lyα observables in the individual galaxies of our sample. Additionally, we plan to apply our gradient masking method on higher redshifted galaxies.

A Appendix

A.1 Overview over our sample

We have data for all 42 LARS and eLARS galaxies from HST and PMAS. We show an overview of the data in Figure A.1 for the eLARS galaxies. The upper left figure shows the I (filter F775W with pivot of 7651.4 Å and width of 1179.1 Å, F850LP with pivot of 9176.1 Å and width of 1192.5 Å or F814W with pivot of 8039.1 Å and width of 1565.2 Å) -, B (filter F438W with pivot of 4326.2 Å and width of 614.7 Å) -, and U (filter F336W with pivot of 3354.5 Å and width of 511.6 Å or F390W with pivot of 3923.7 Å and width of 894 Å) -band images mapped to the RGB channels and the upper right figure shows the composite of Hα in red, Lyα in blue and stellar continuum in the FUV at the wavelength of Lyα in green (Melinder et al. 2023). The middle left figure (middle right figure) shows where the PMAS observation is located within the HST Hα (Lyα) image. All PMAS pointings are a region in the HST observations of the galaxies. The field of view of PMAS is smaller than the field of view of HST. We show with a white square the region of the PMAS observation on the HST Hα and Lyα map. The spatial alignment was done by P. Laursen of the LARS team (`https://www.anisotropela.dk/work/lars/hst2pmas`). The last row shows from left to right the Hα S/N, the Hα line of sight velocity and the Hα velocity dispersion of the PMAS observations. Also, we show an overview of the LARS data where we leave out the middle line with the location of the PMAS pointing on the HST image, which can be found in E. C. Herenz et al. (2016) for the LARS galaxies.

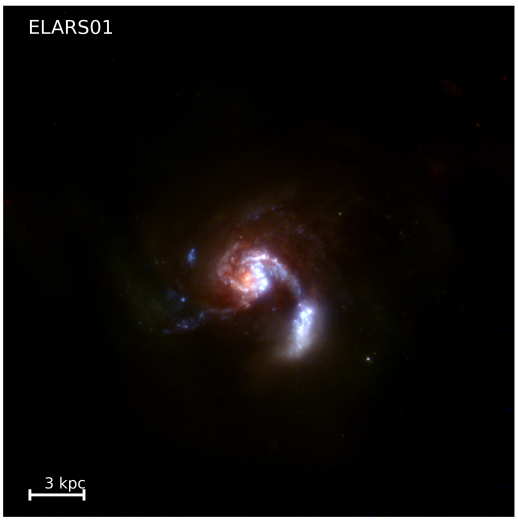

(a) I-, B-, and U-band images mapped to the RGB channels. North is always up and east always on the left.

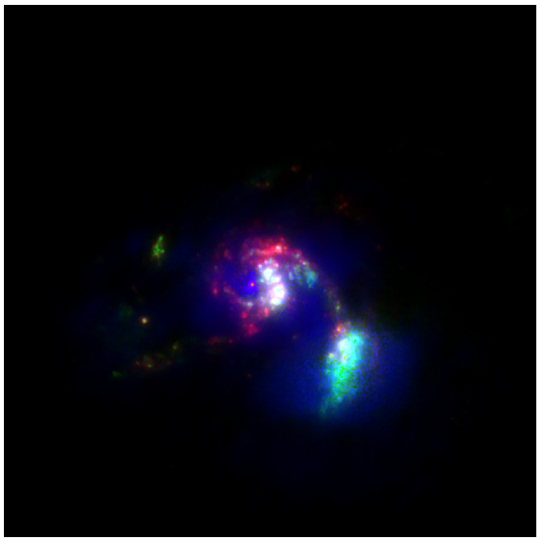

(b) Composite of the Hα (red), Lyα (blue) and stellar continuum in the FUV at the wavelength of Lyα (green).

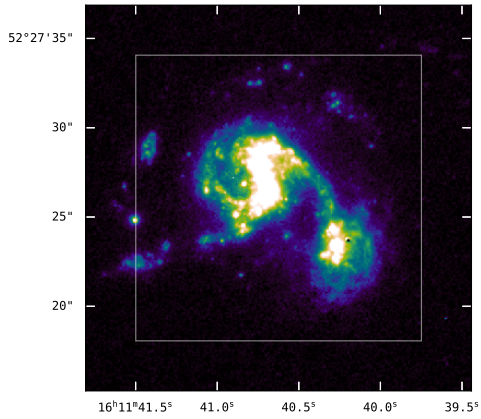

(c) Hα intensity map from HST observation with the rectangular as field of view of the PMAS observation.

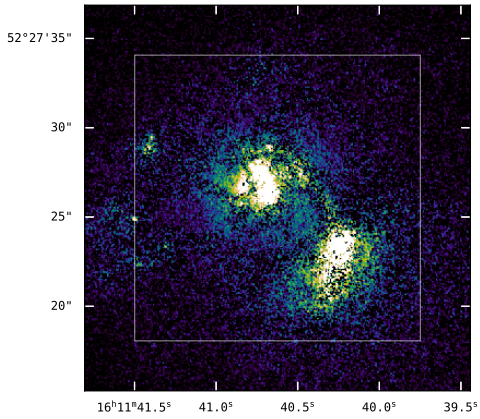

(d) Lyα intensity map from HST observation with the rectangular as field of view of the PMAS observation.

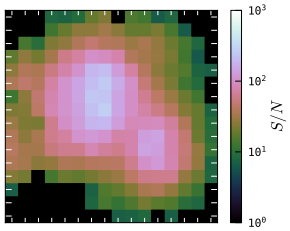

(e) Signal to noise map of the continuum-subtracted Hα signal from the PMAS observation.

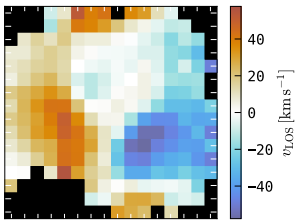

(f) Hα line of sight velocity map from PMAS.

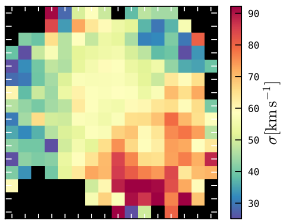

(g) Resolution-corrected Hα velocity dispersion map from PMAS.

Figure A.1: Overview of the HST and PMAS data for the galaxy eLARS01.

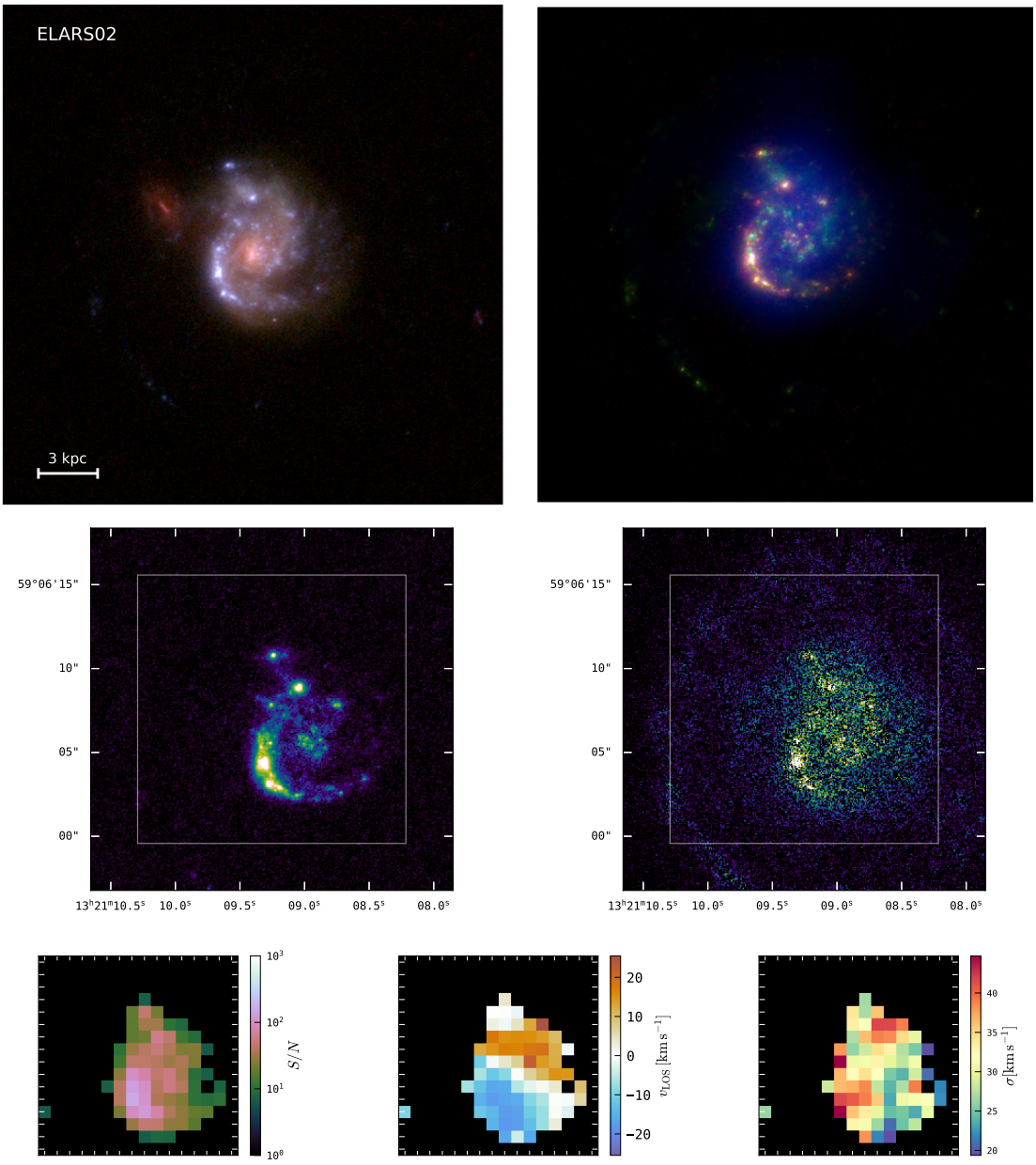

Figure A.1 continued for eLARS02.

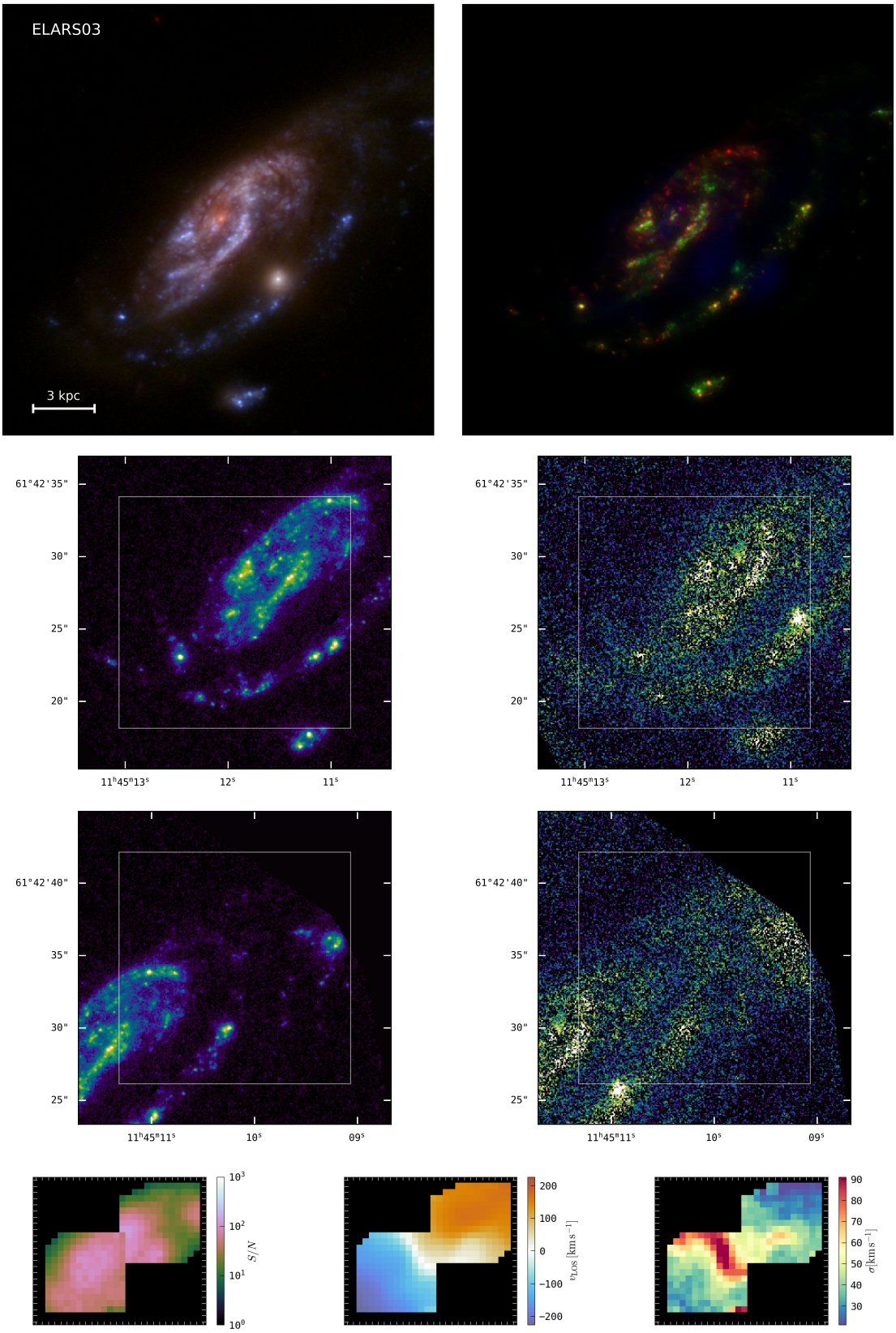

Figure A.1 continued for eLARS03.

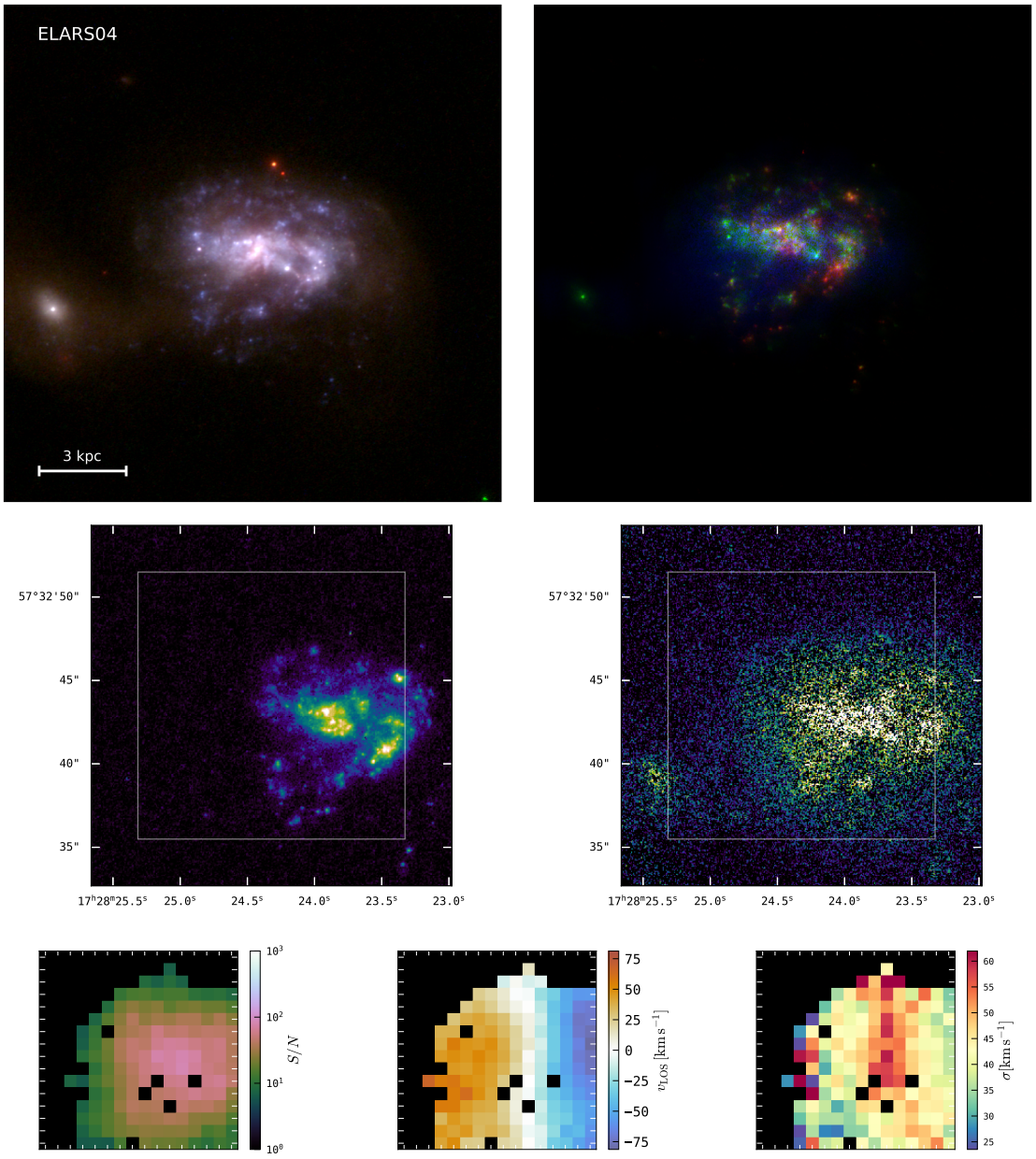

Figure A.1 continued for eLARS04.

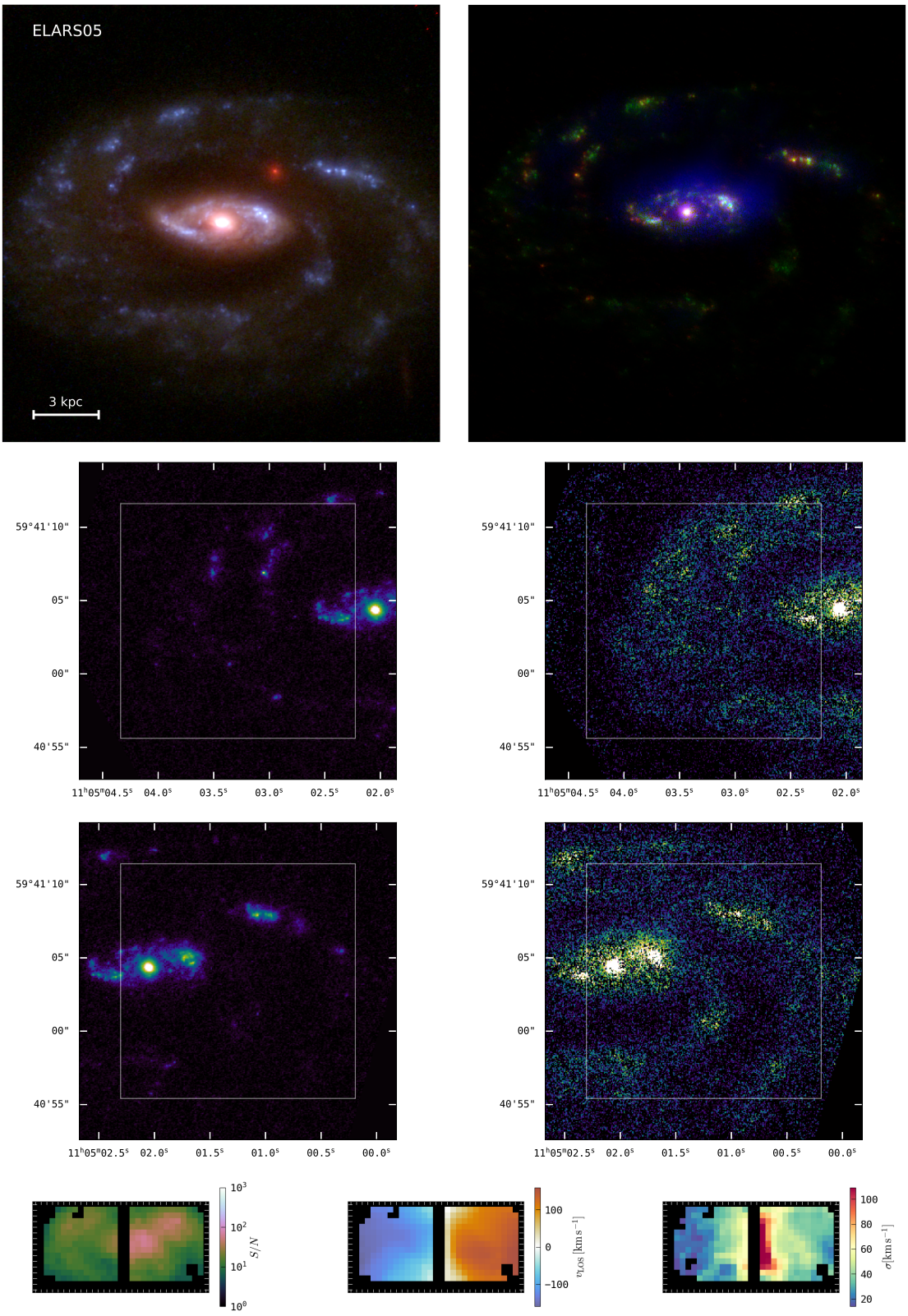

Figure A.1 continued for eLARS05.

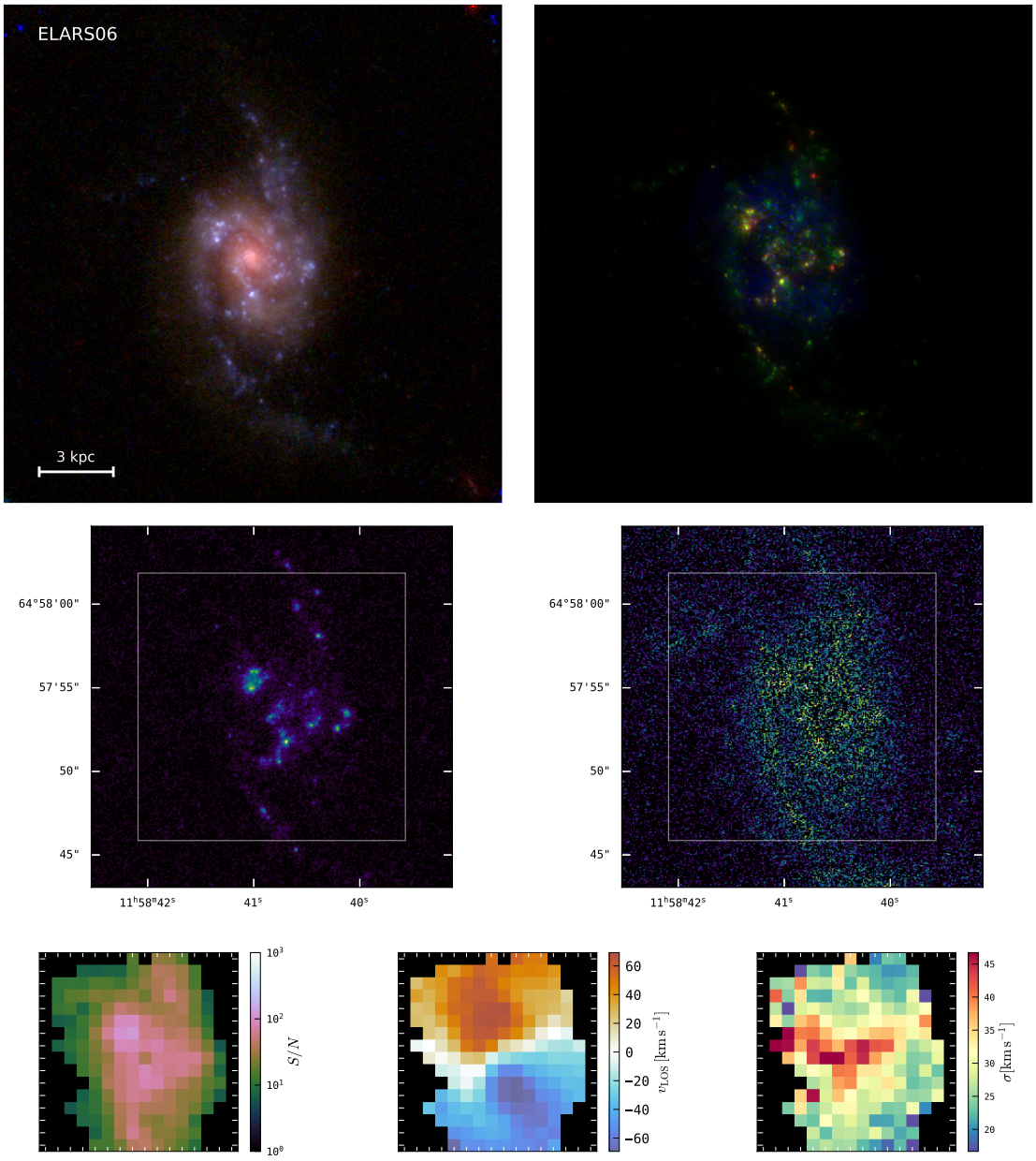

Figure A.1 continued for eLARS06.

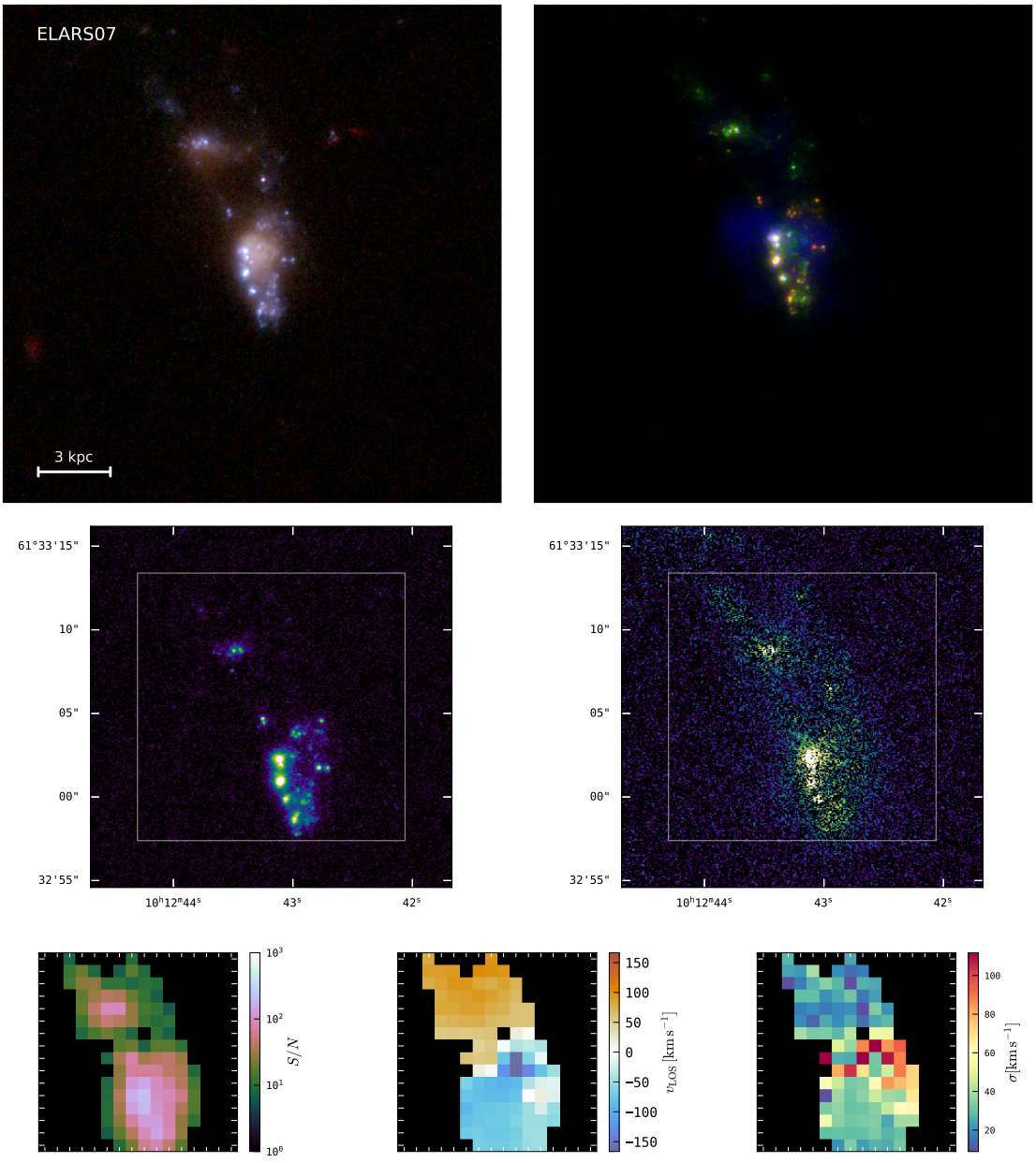

Figure A.1 continued for eLARS07.

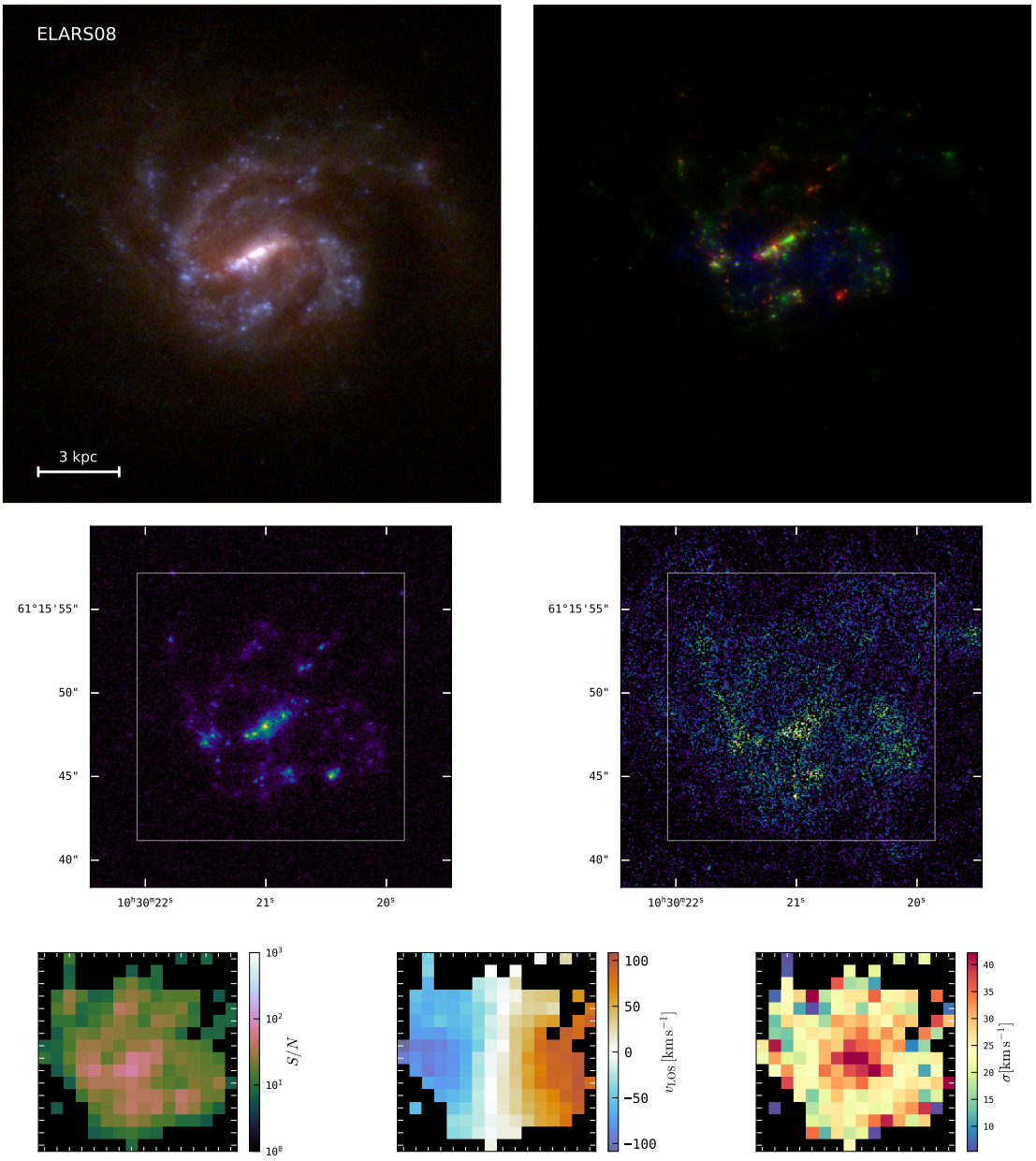

Figure A.1 continued for eLARS08.

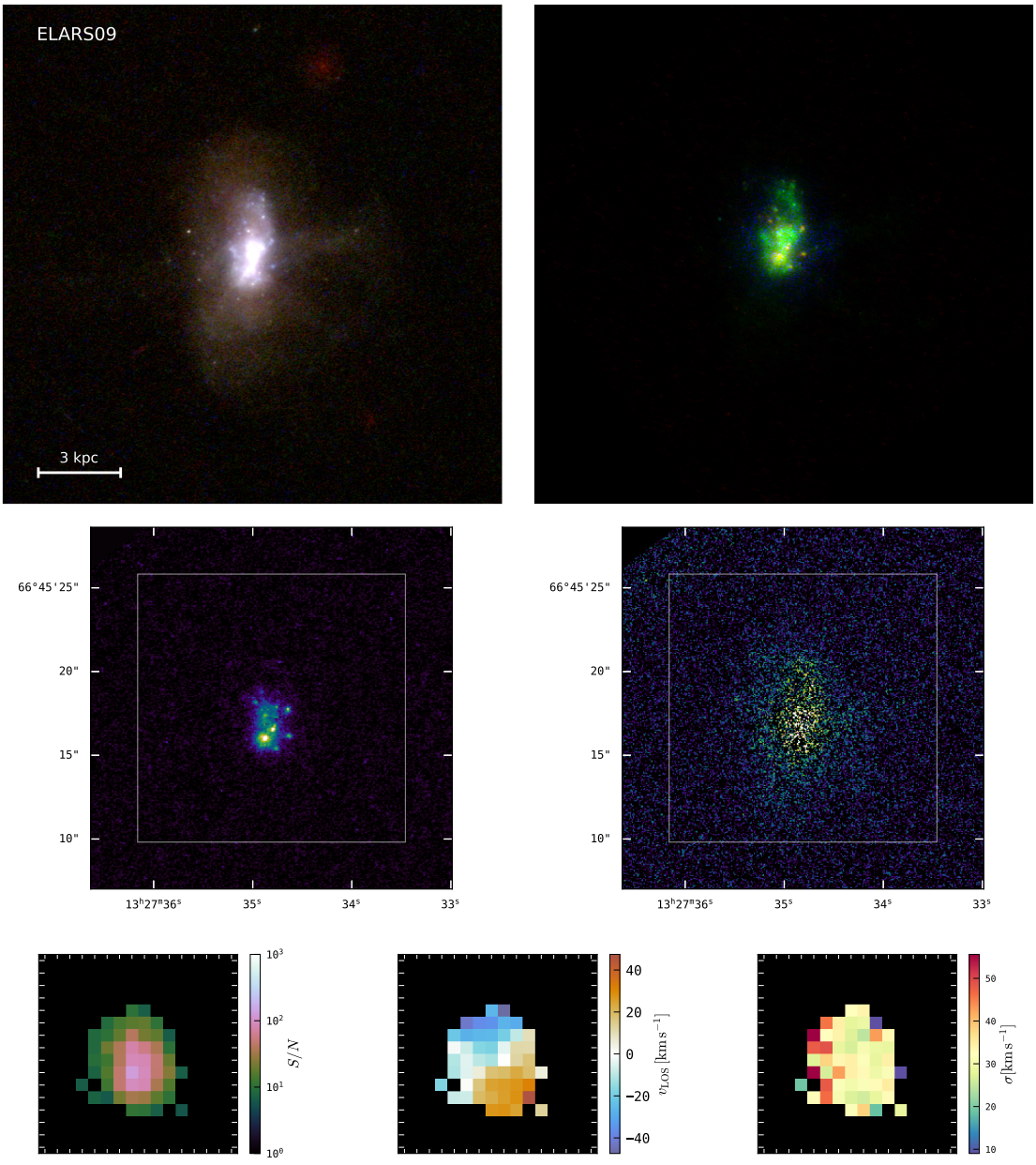

Figure A.1 continued for eLARS09.

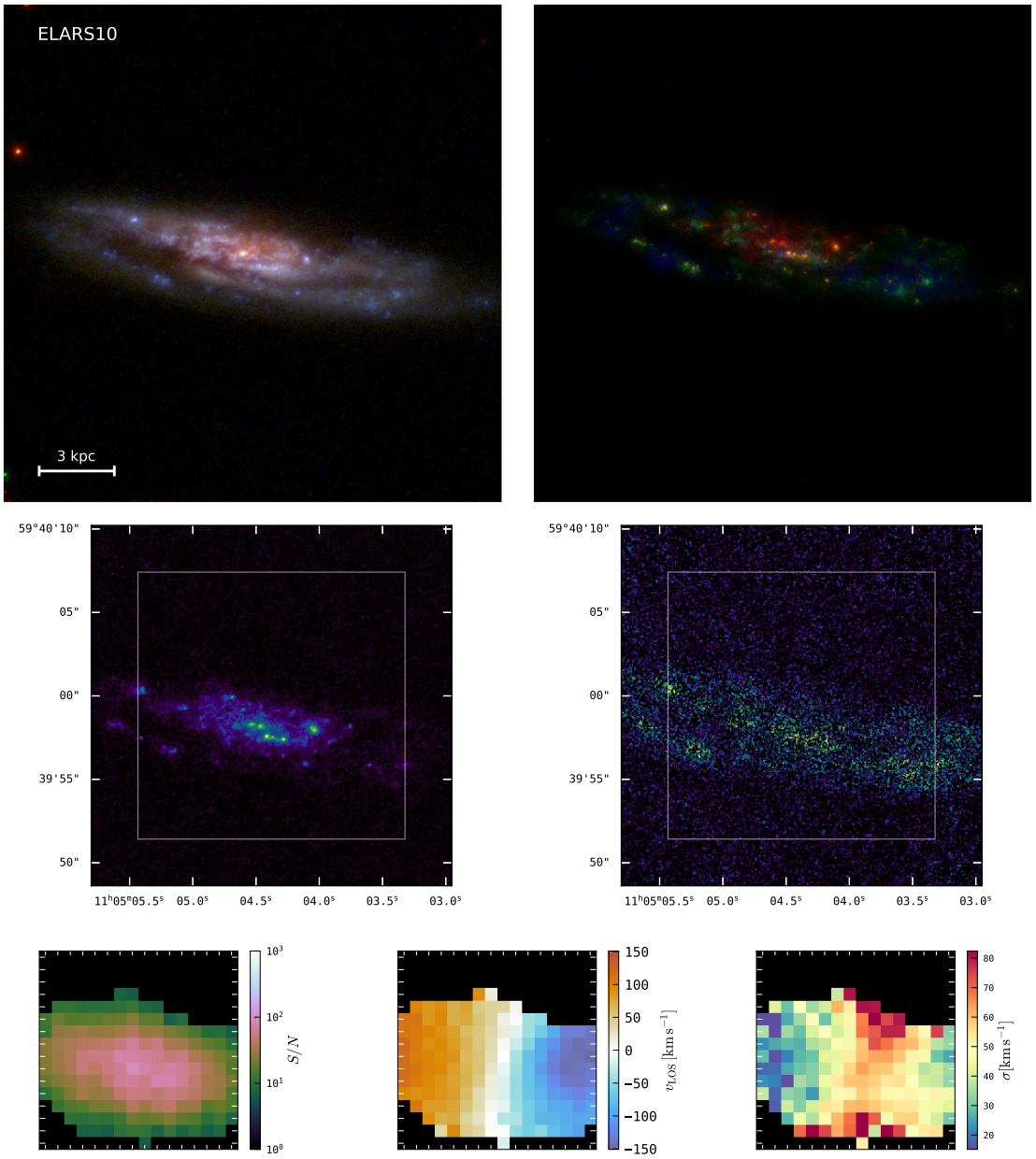

Figure A.1 continued for eLARS10.

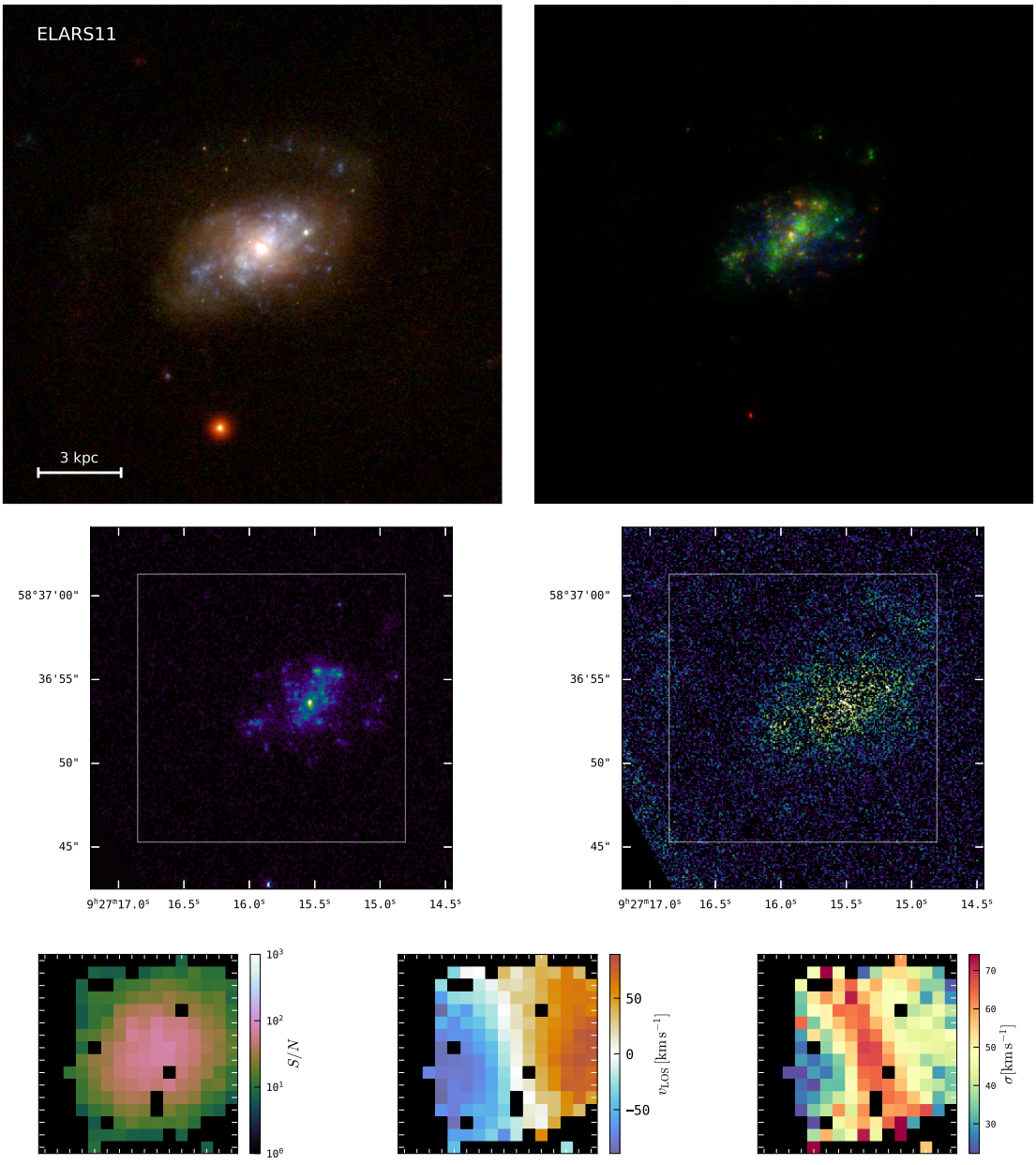

Figure A.1 continued for eLARS11.

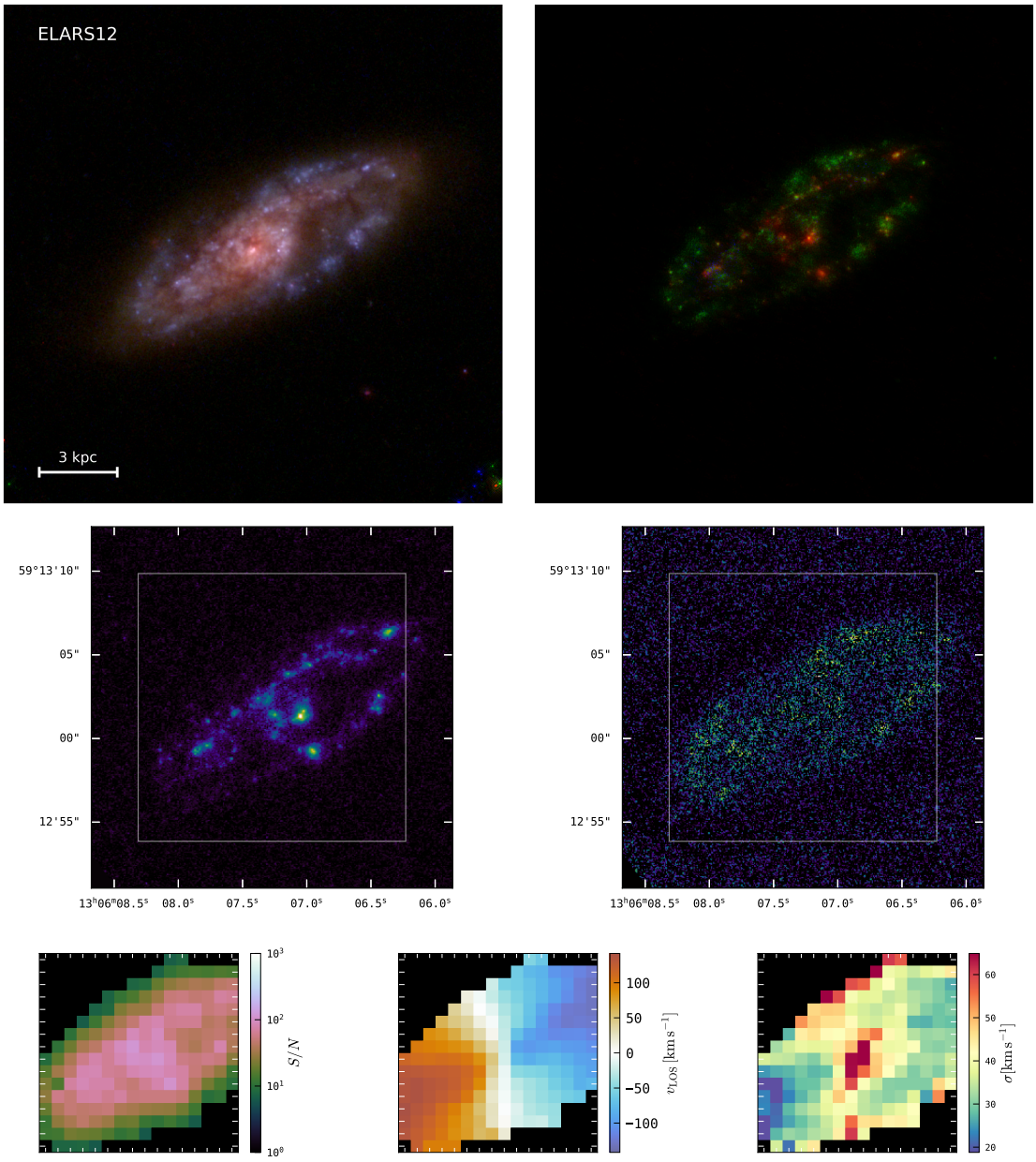

Figure A.1 continued for eLARS12.

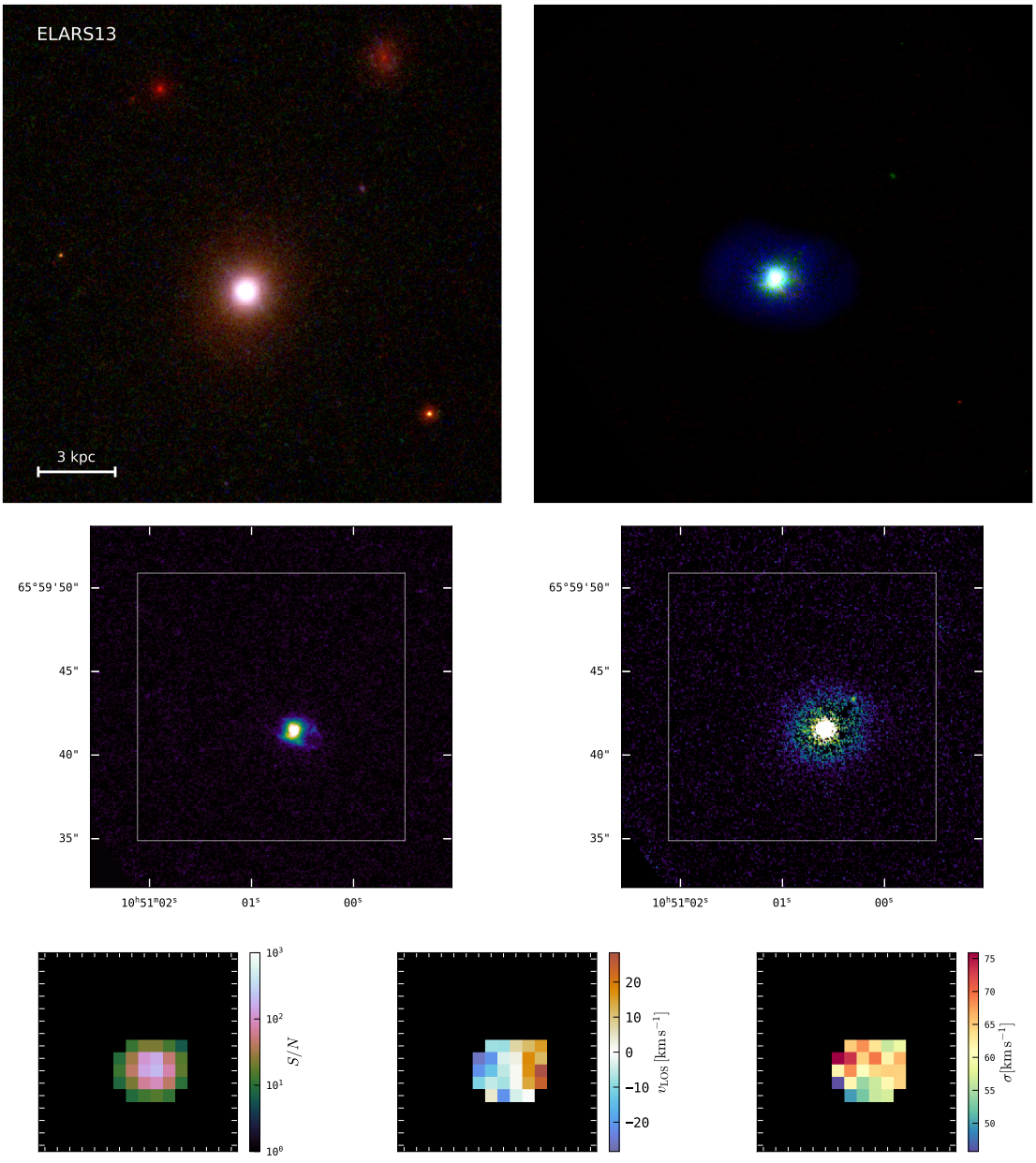

Figure A.1 continued for eLARS13.

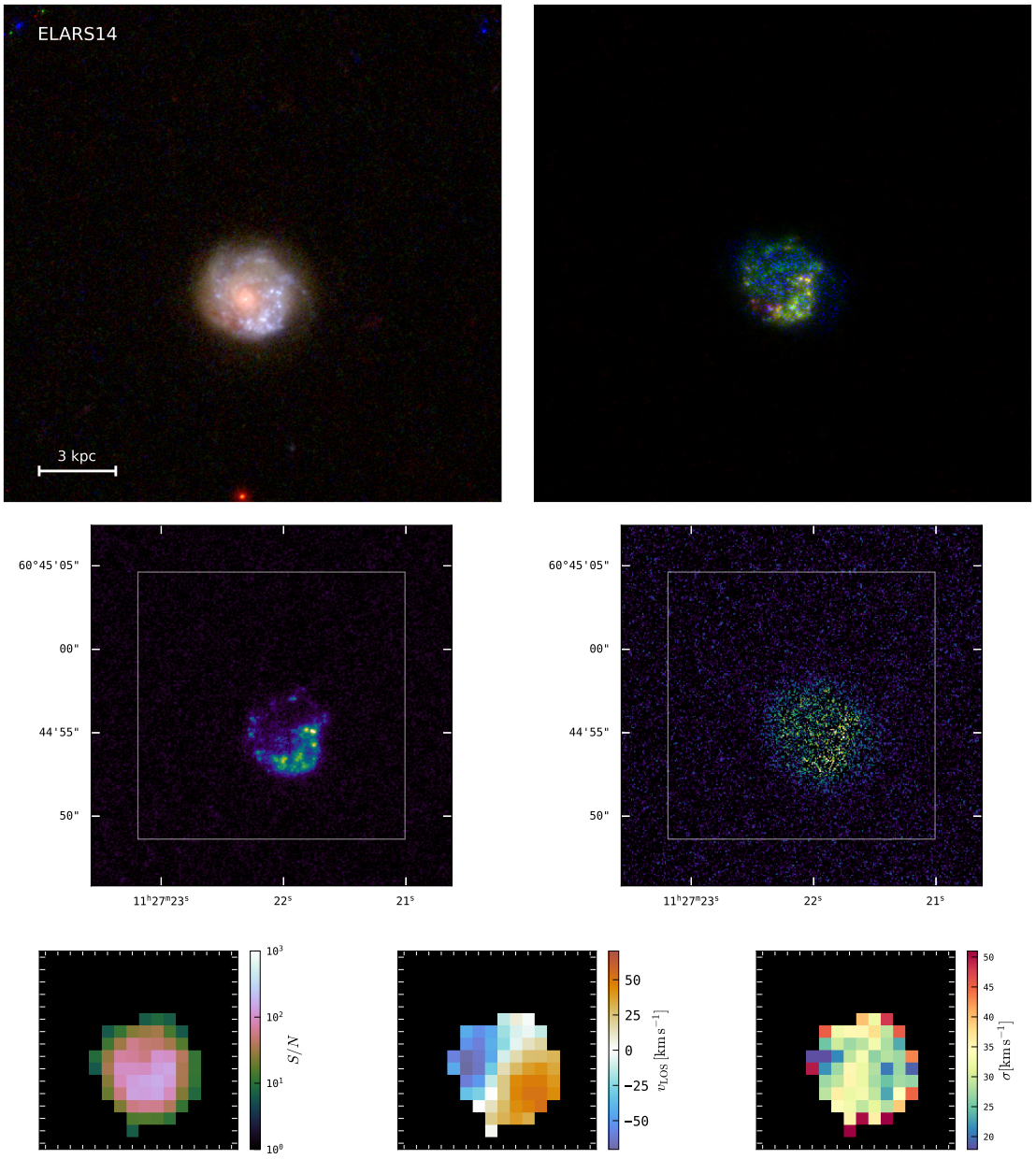

Figure A.1 continued for eLARS14.

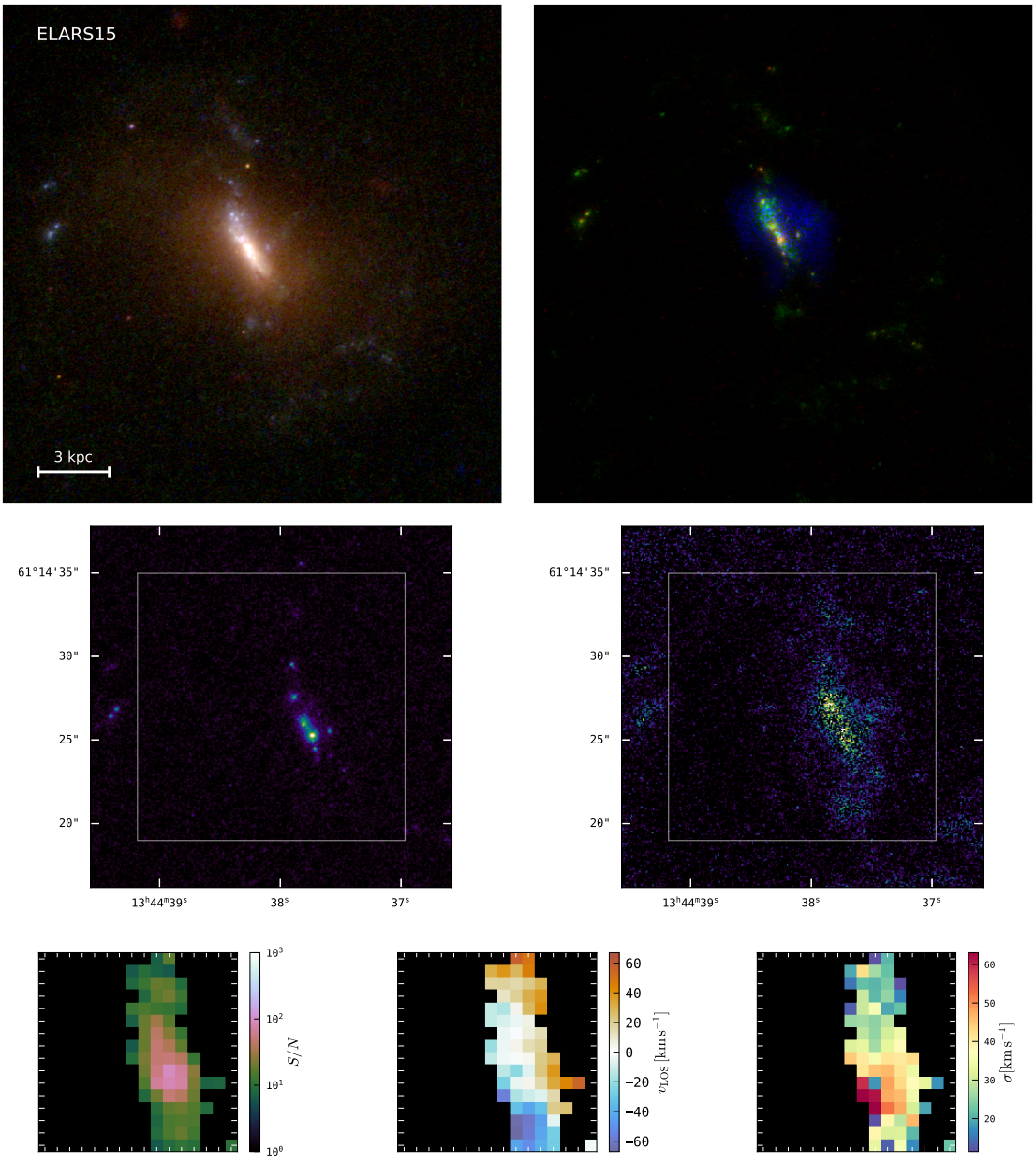

Figure A.1 continued for eLARS15.

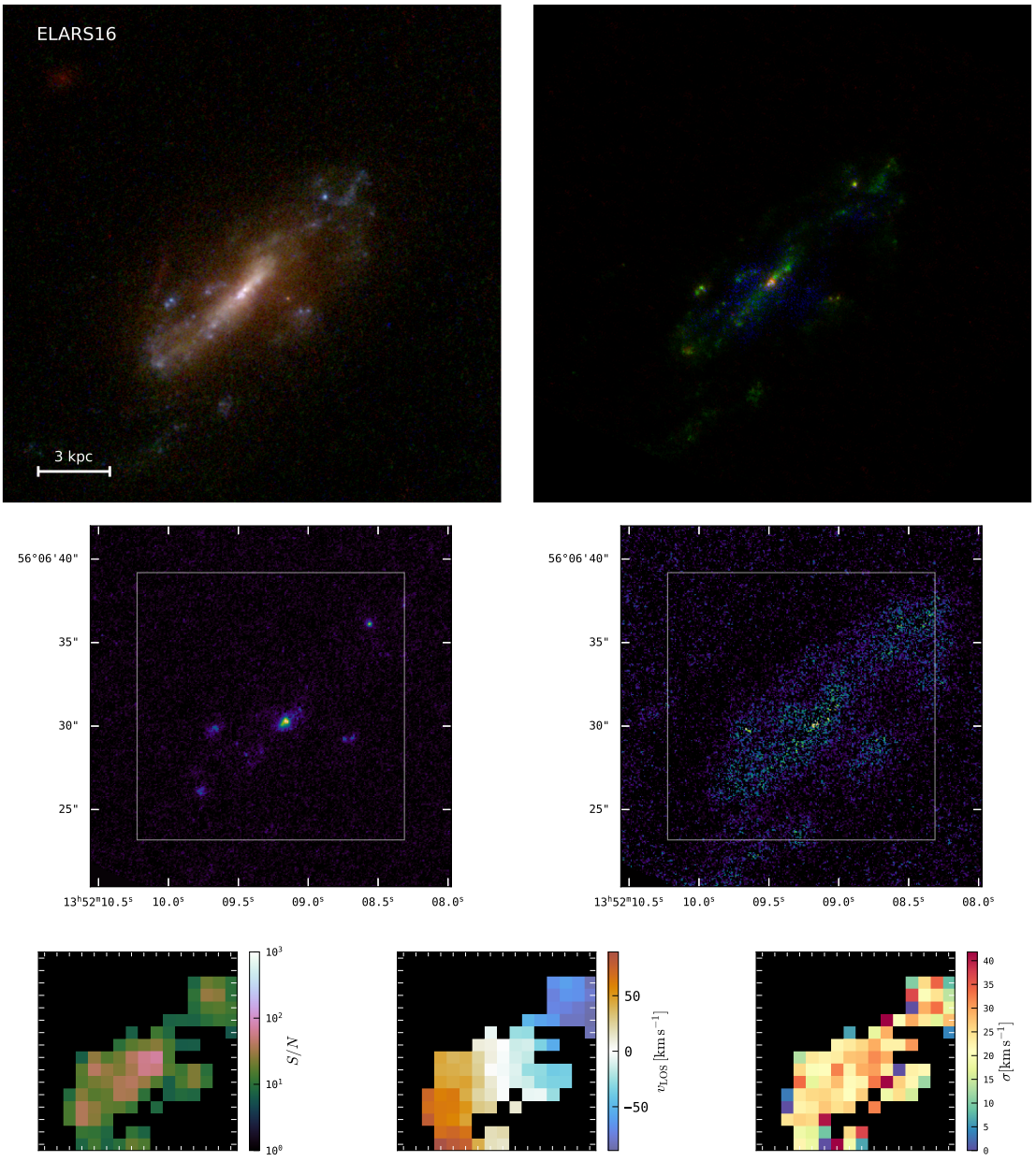

Figure A.1 continued for eLARS16.

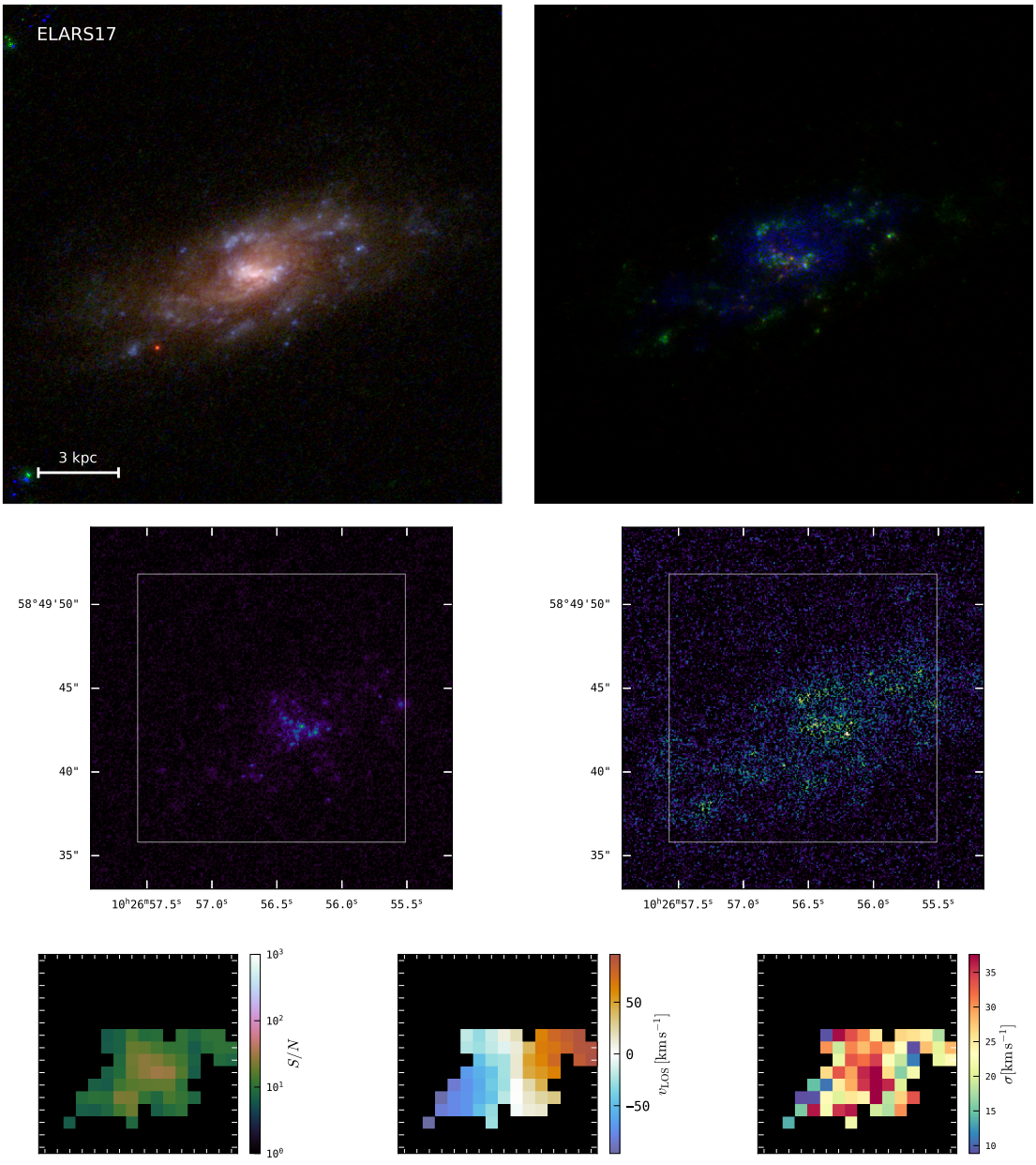

Figure A.1 continued for eLARS17.

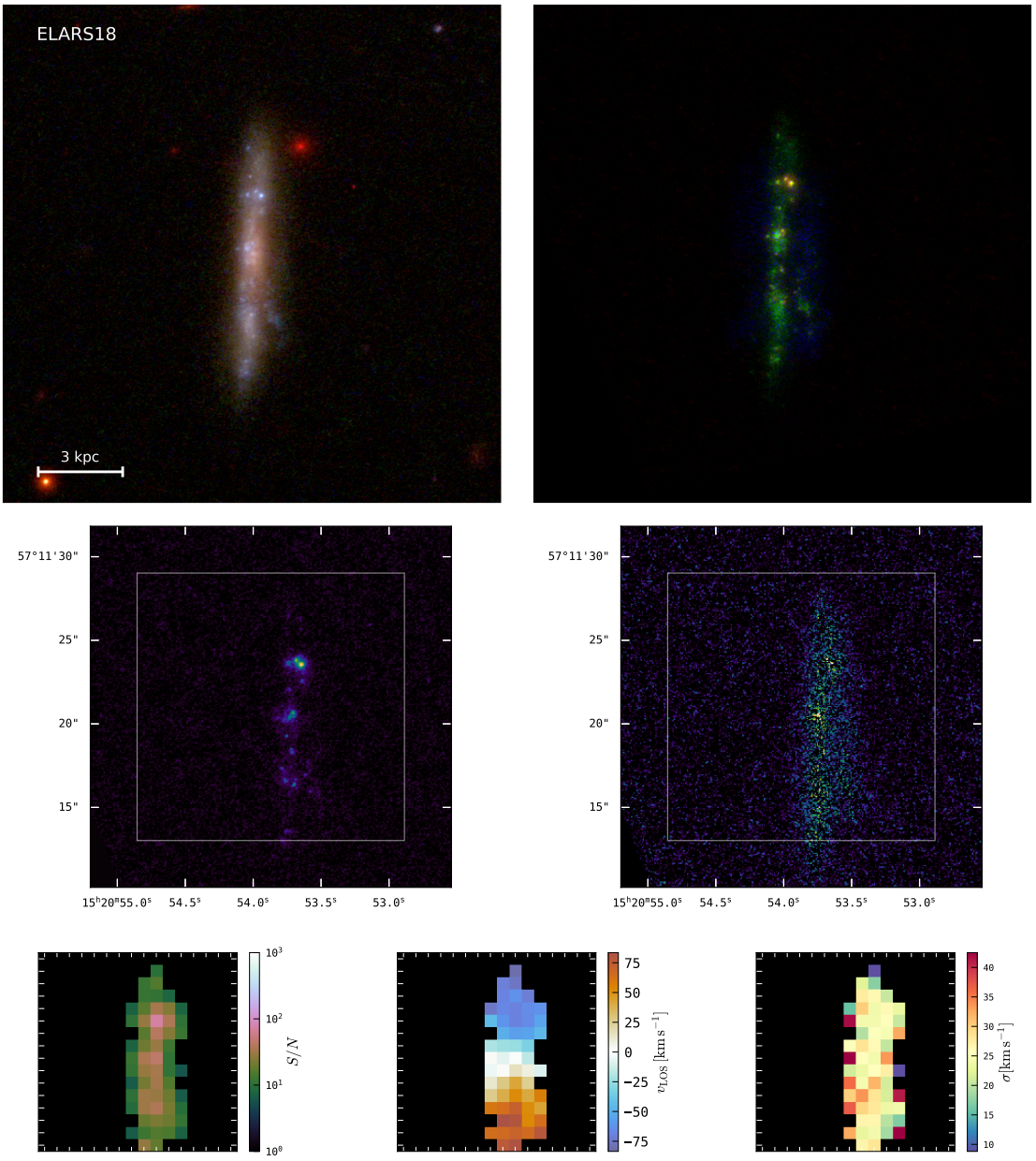

Figure A.1 continued for eLARS18.

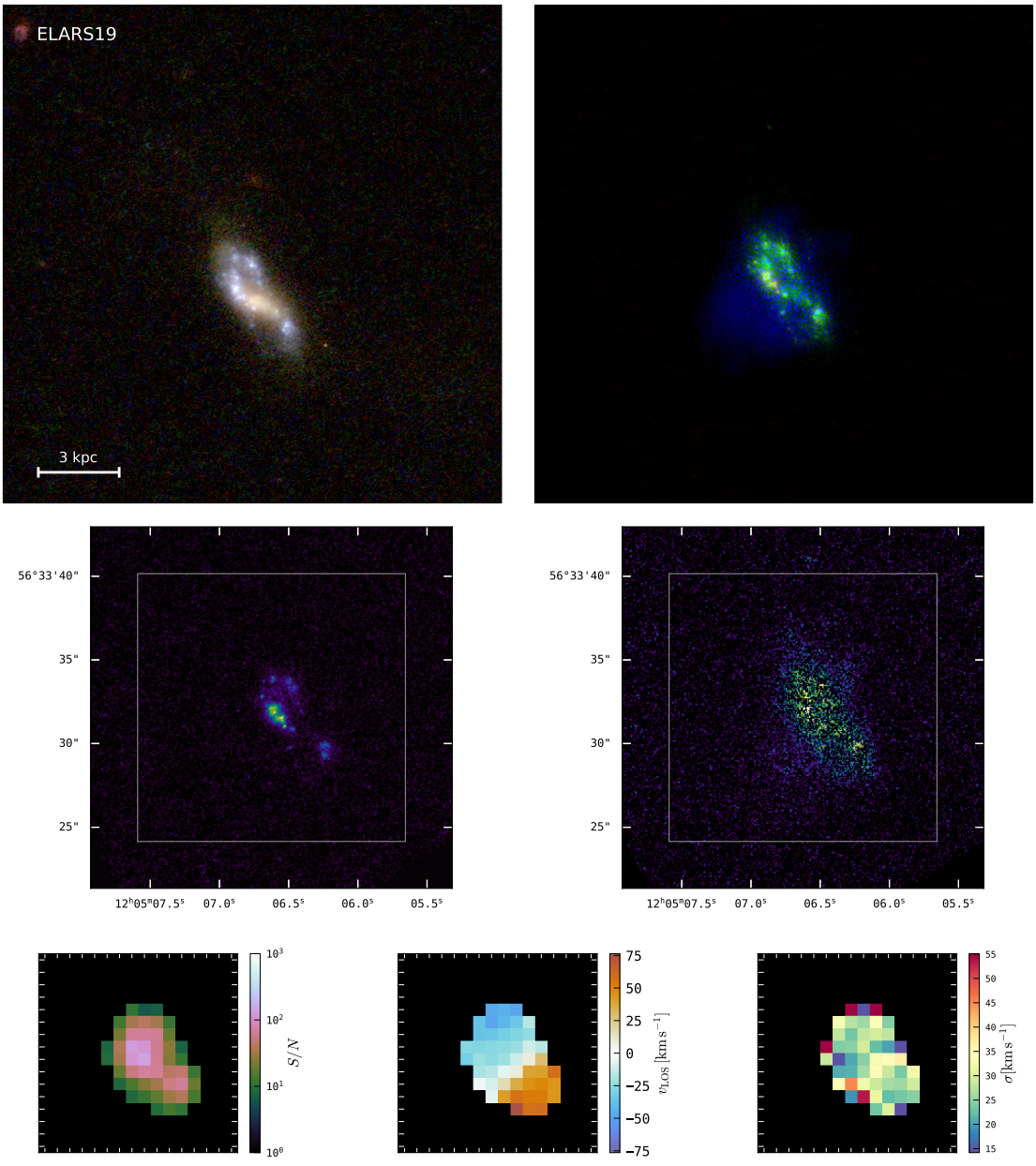

Figure A.1 continued for eLARS19.

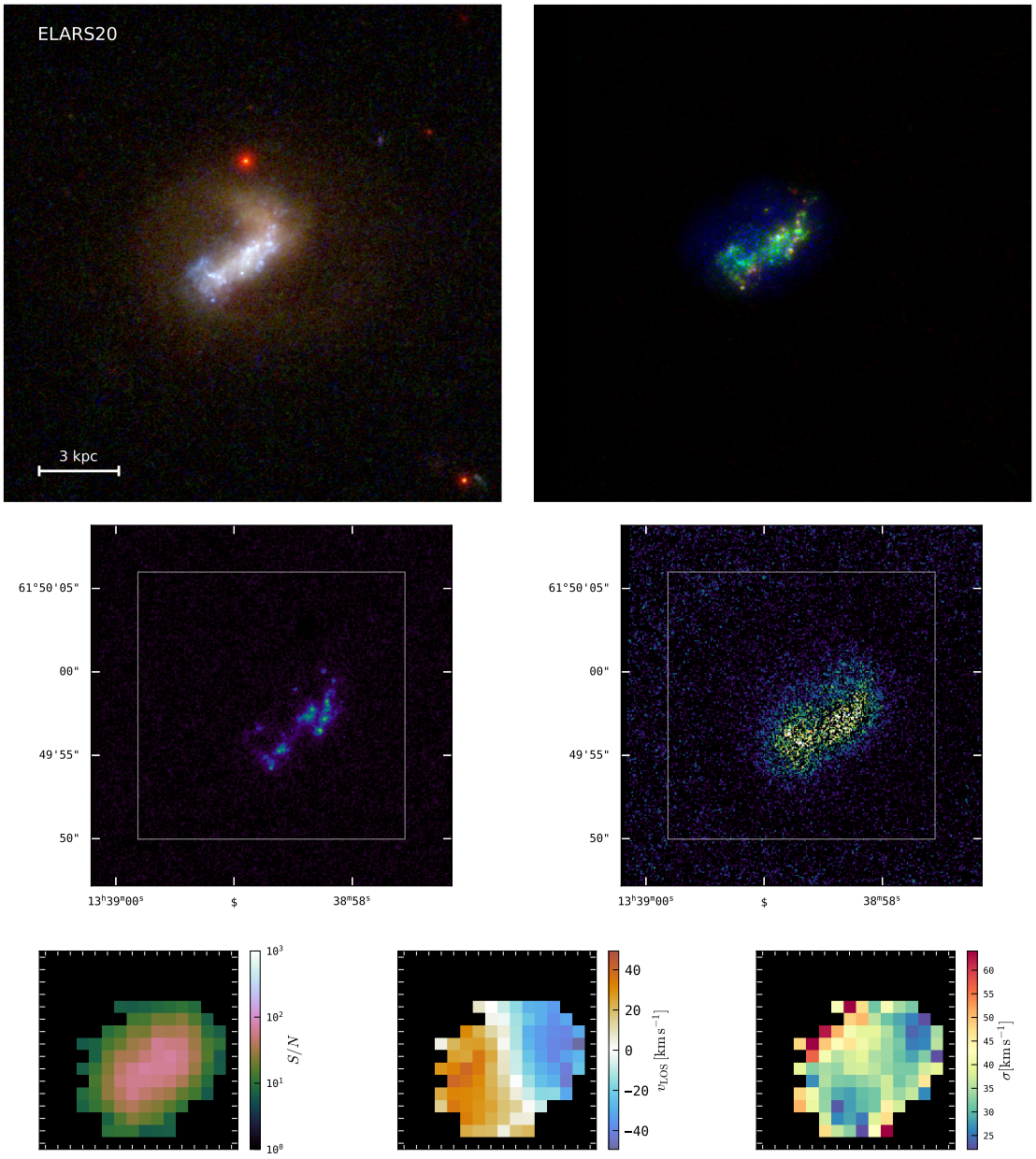

Figure A.1 continued for eLARS20.

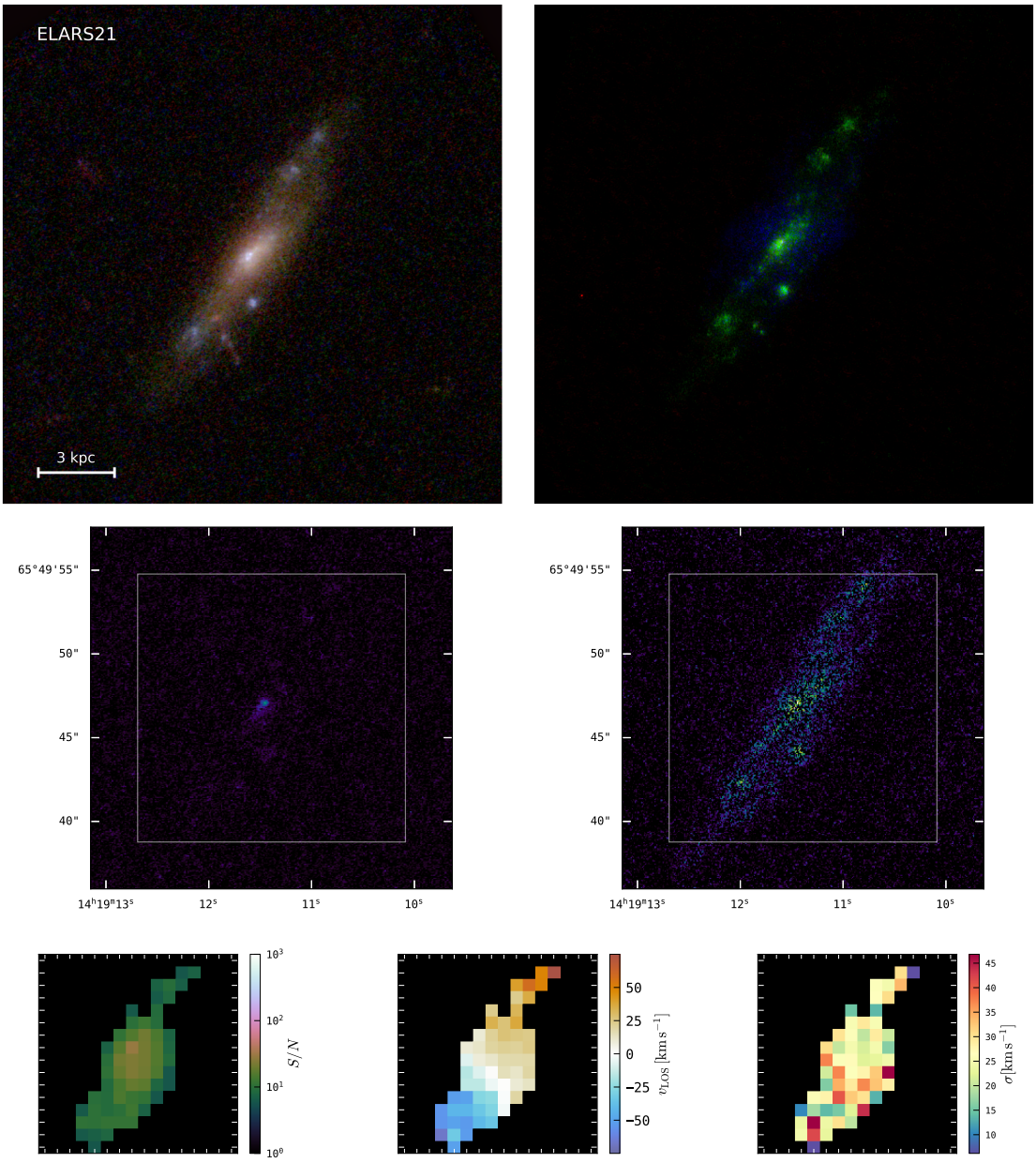

Figure A.1 continued for eLARS21.

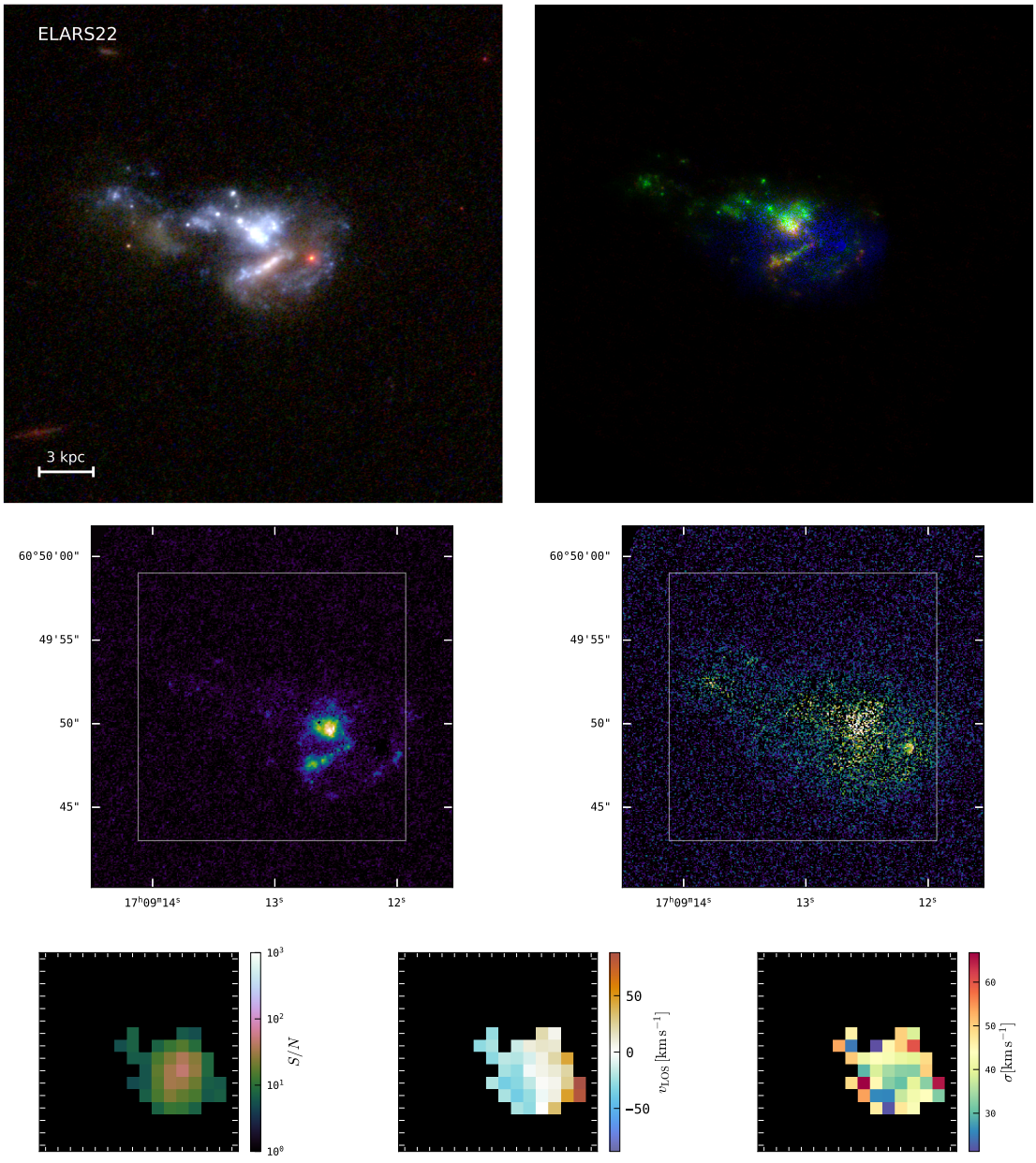

Figure A.1 continued for eLARS22.

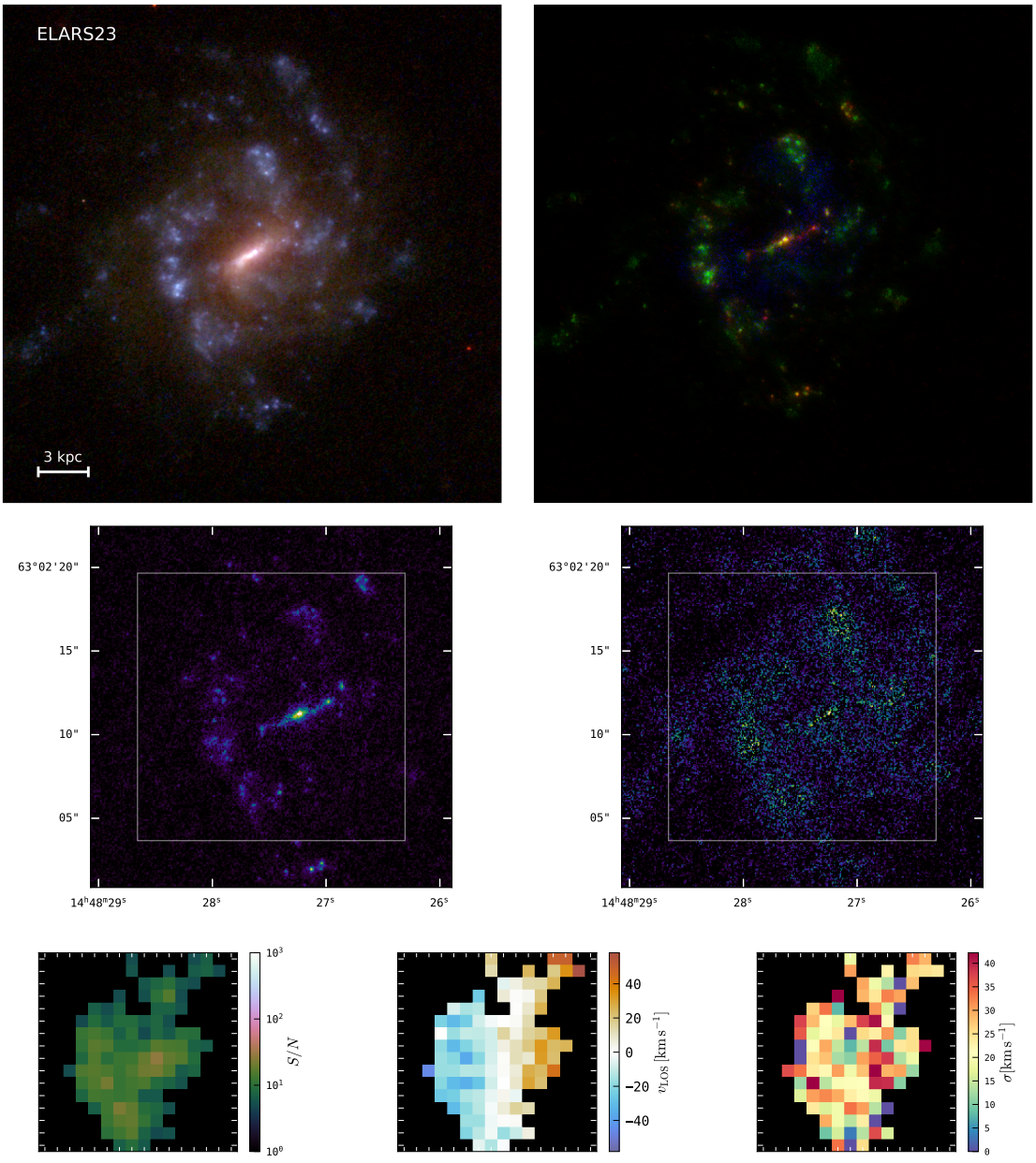

Figure A.1 continued for eLARS23.

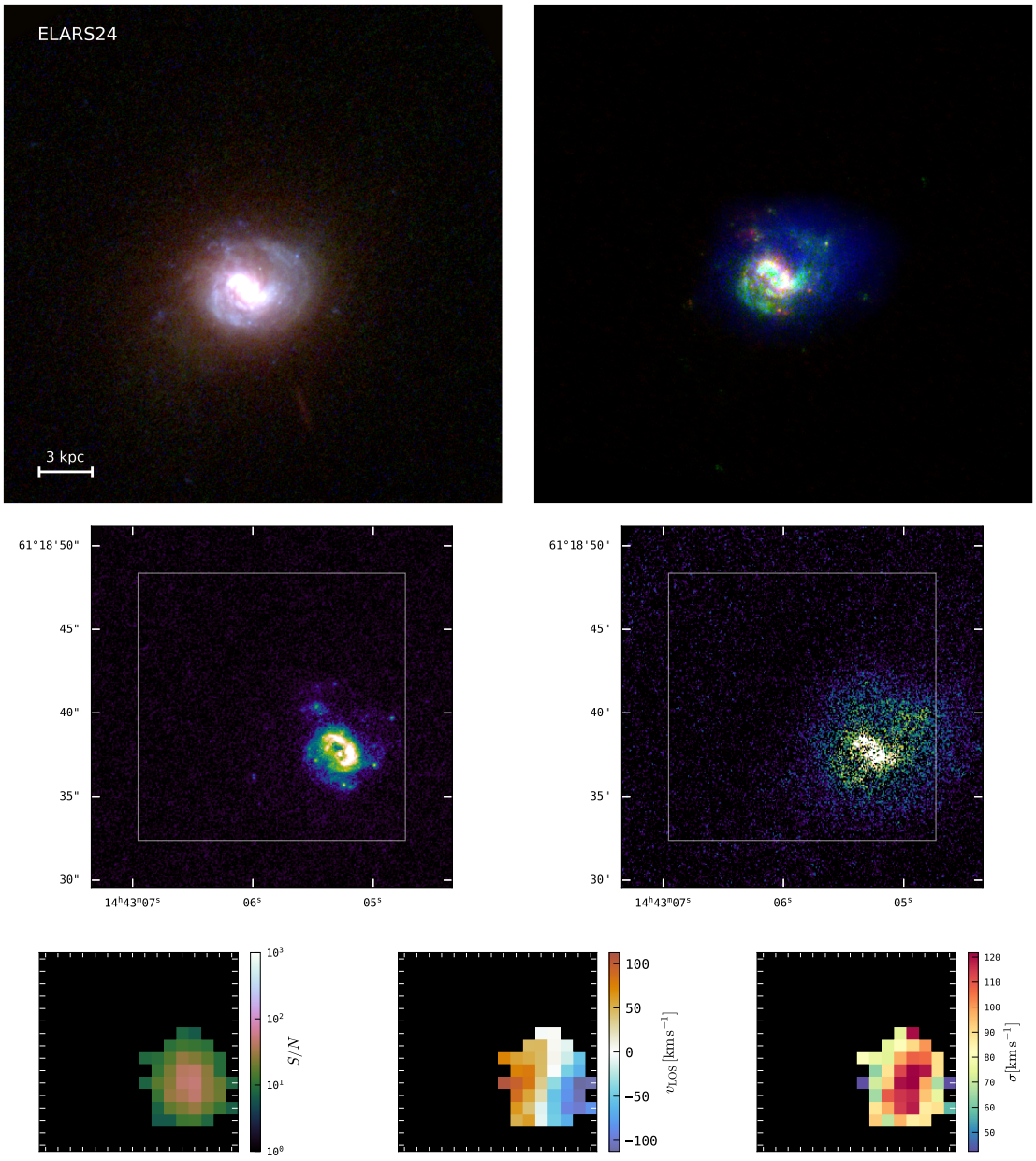

Figure A.1 continued for eLARS24.

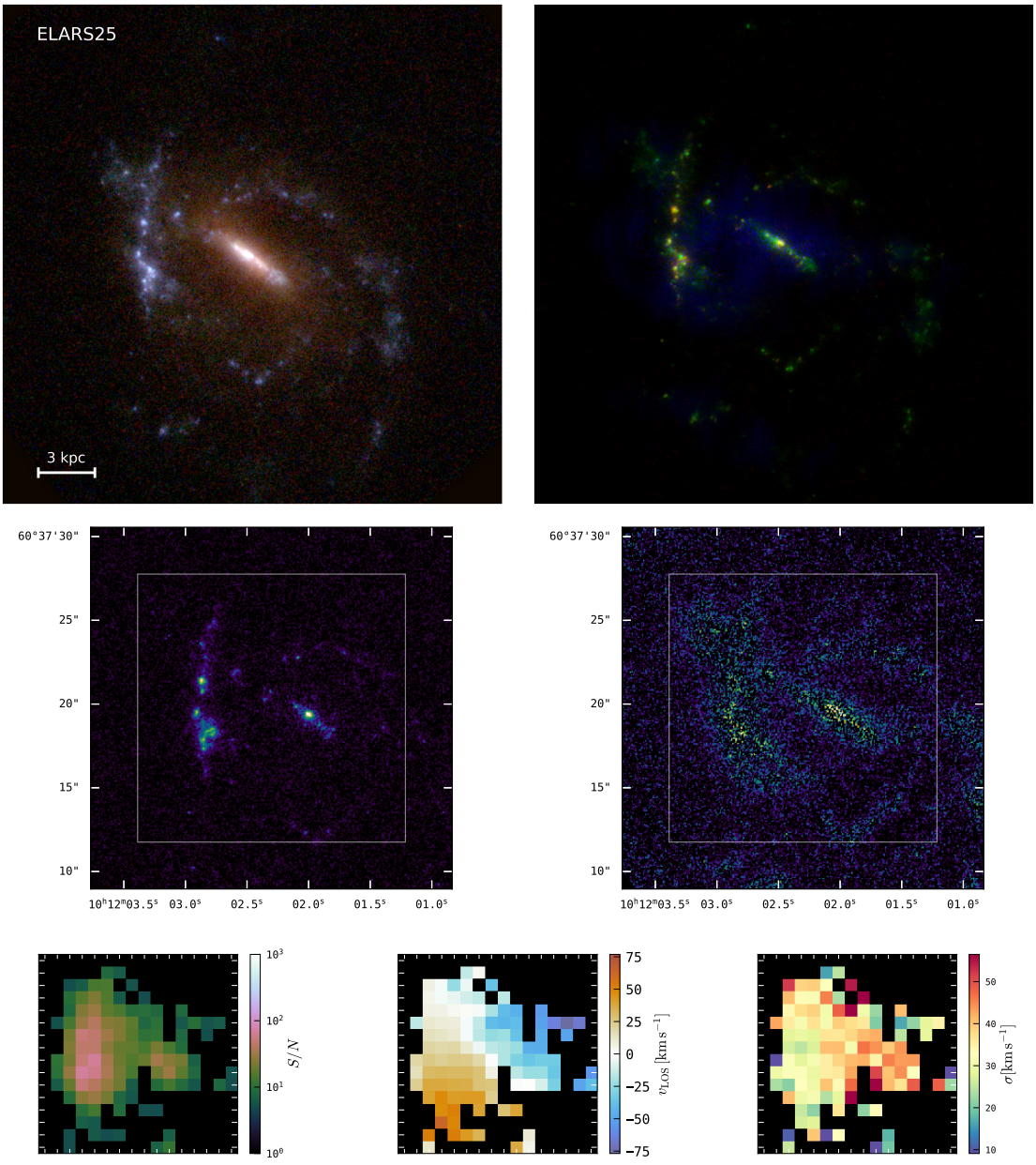

Figure A.1 continued for eLARS25.

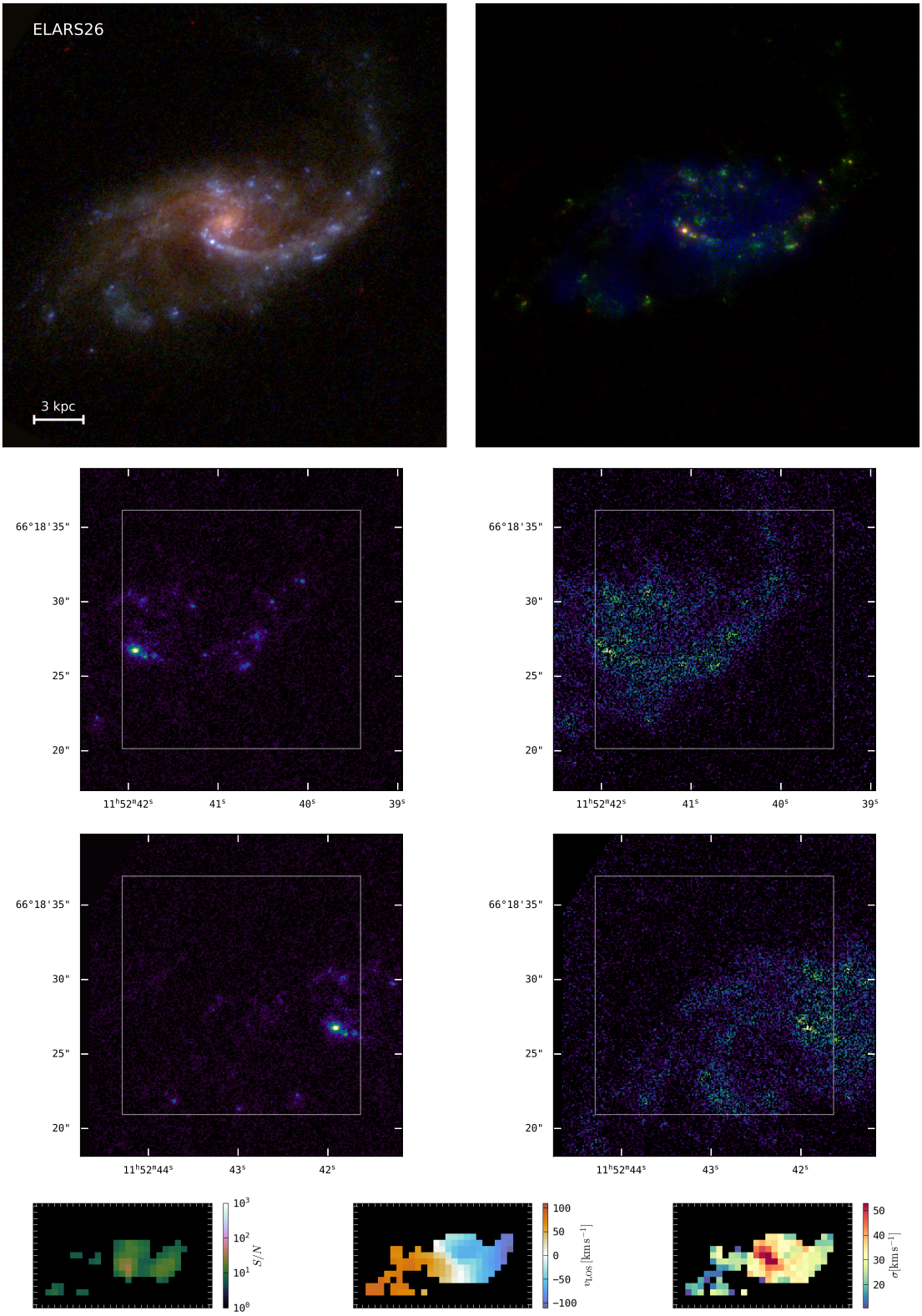

Figure A.1 continued for eLARS26.

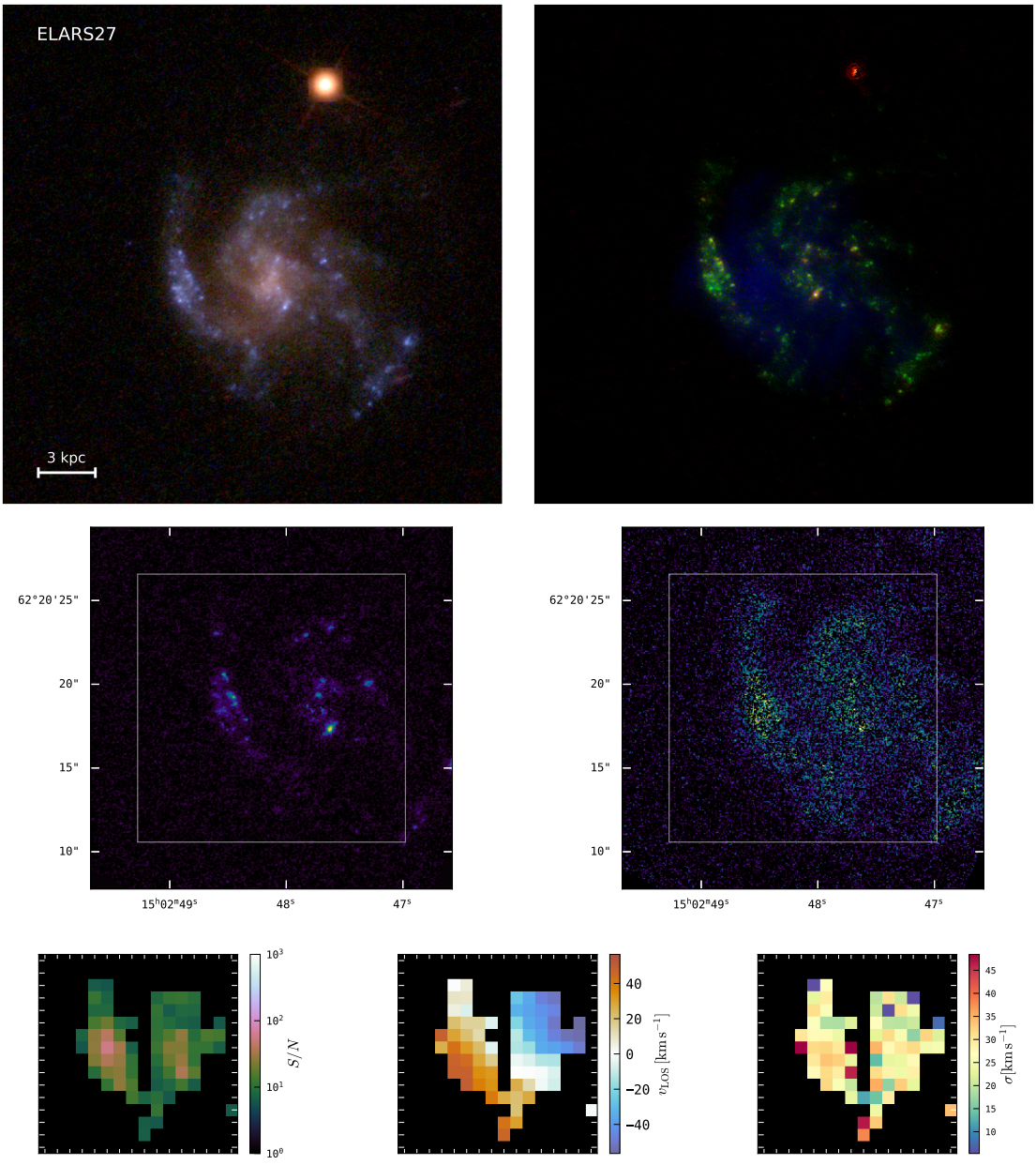

Figure A.1 continued for eLARS27.

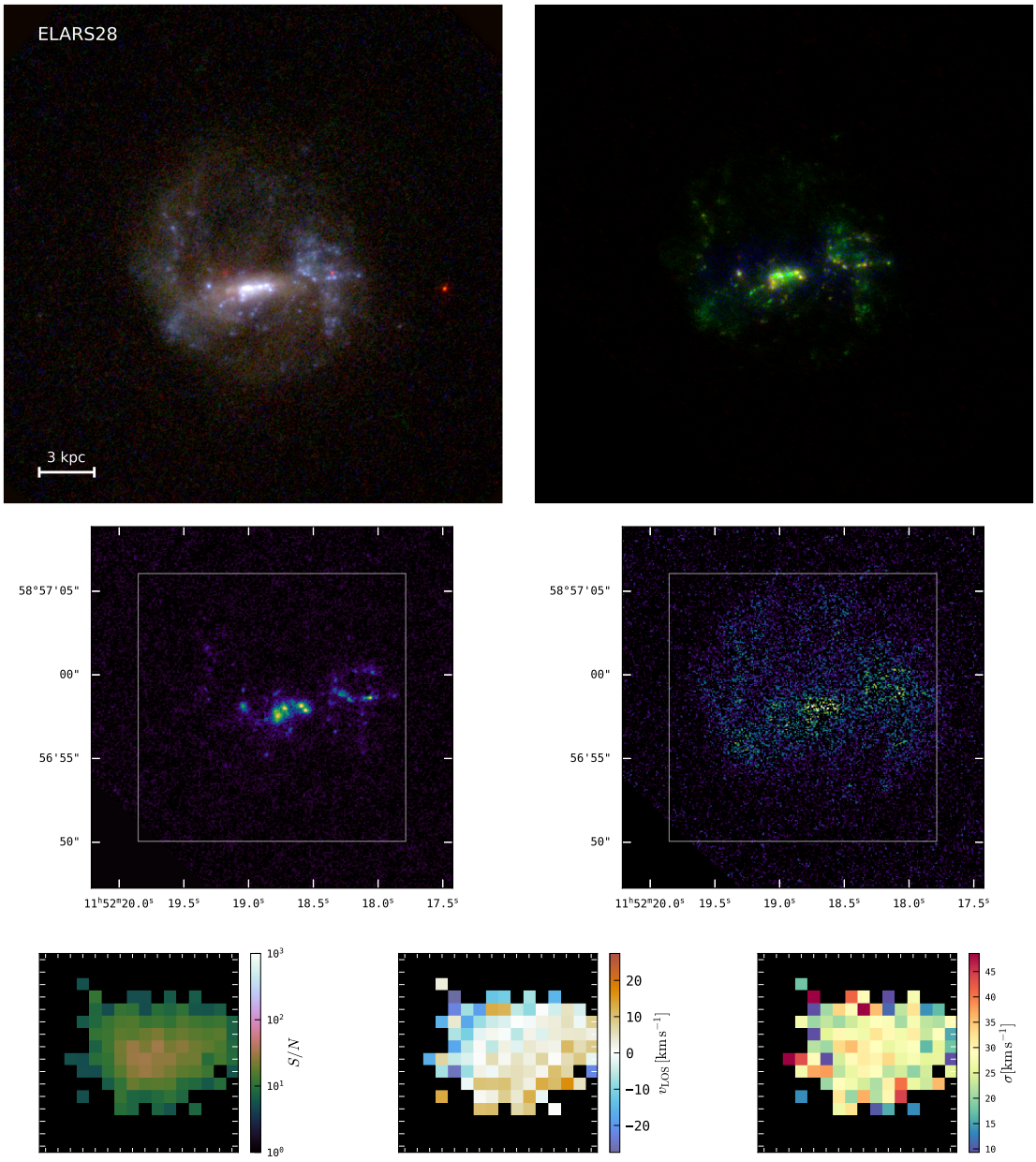

Figure A.1 continued for eLARS28.

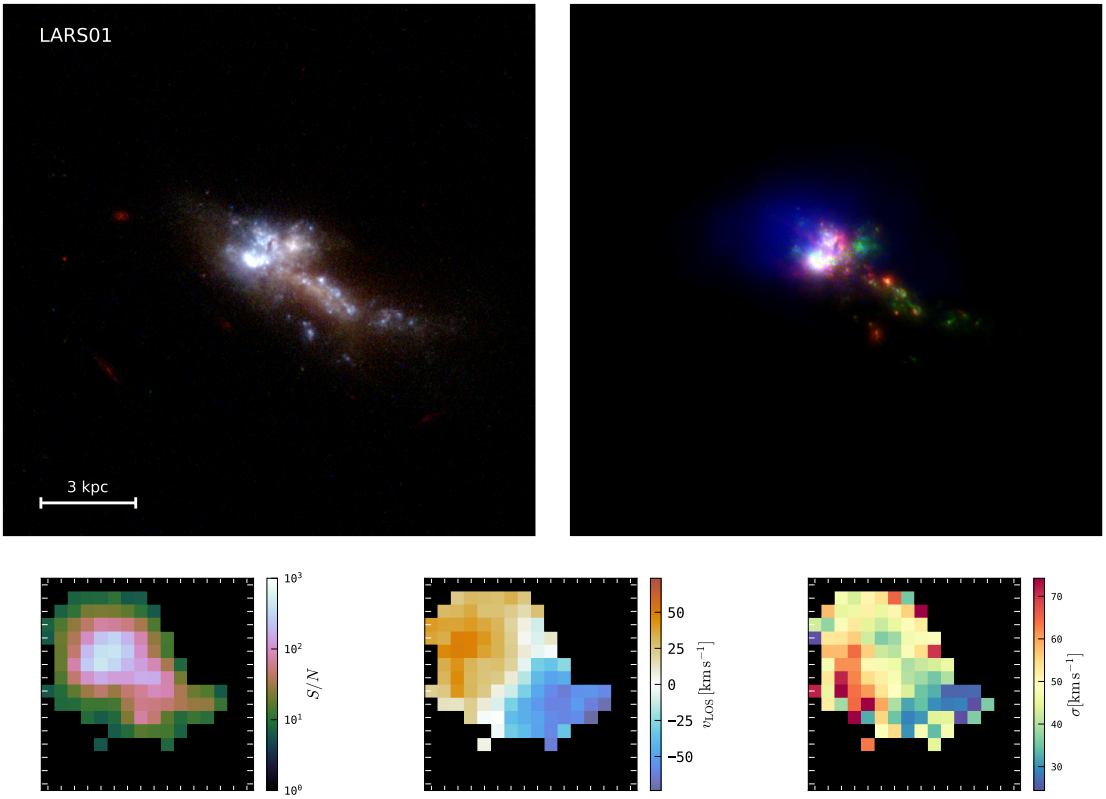

Figure A.1 continued for LARS01.

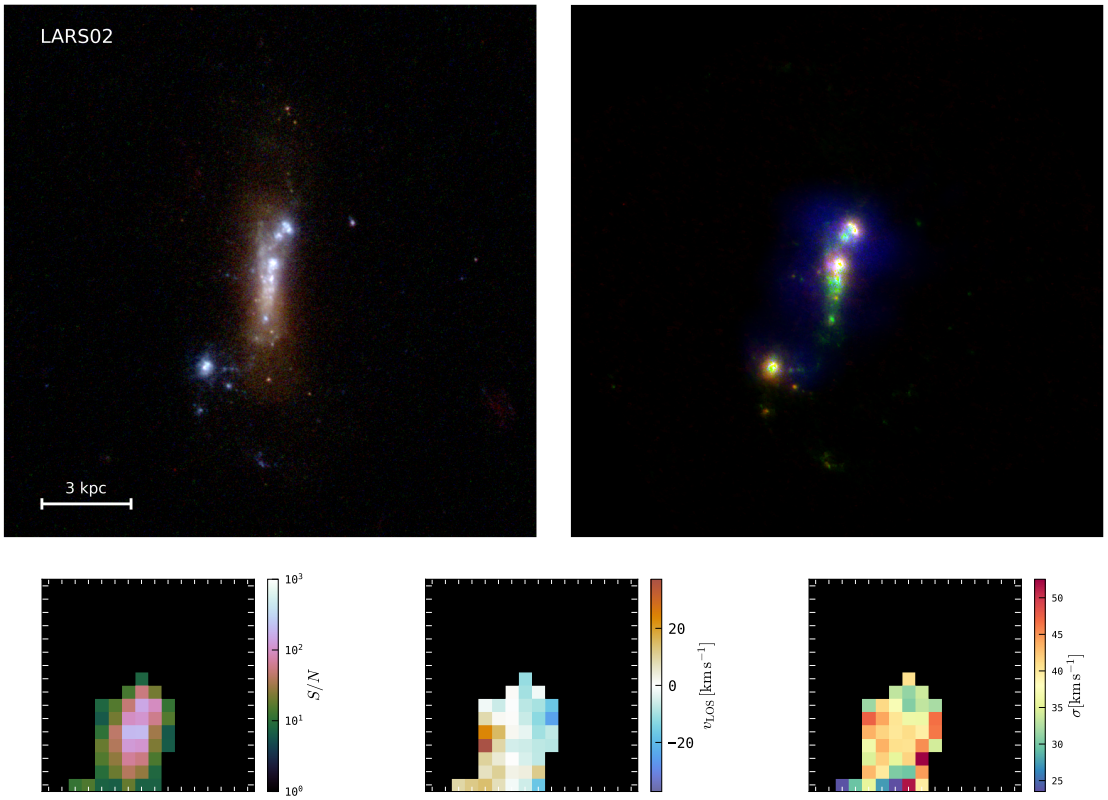

Figure A.1 continued for LARS02.

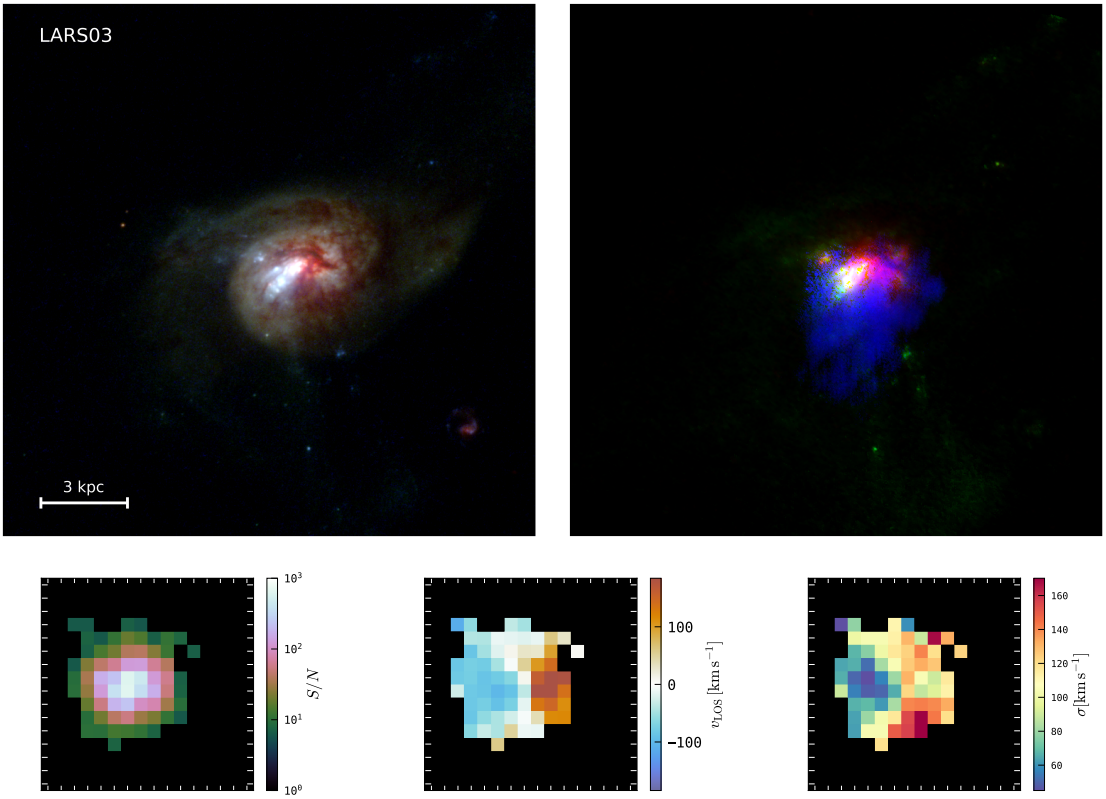

Figure A.1 continued for LARS03.

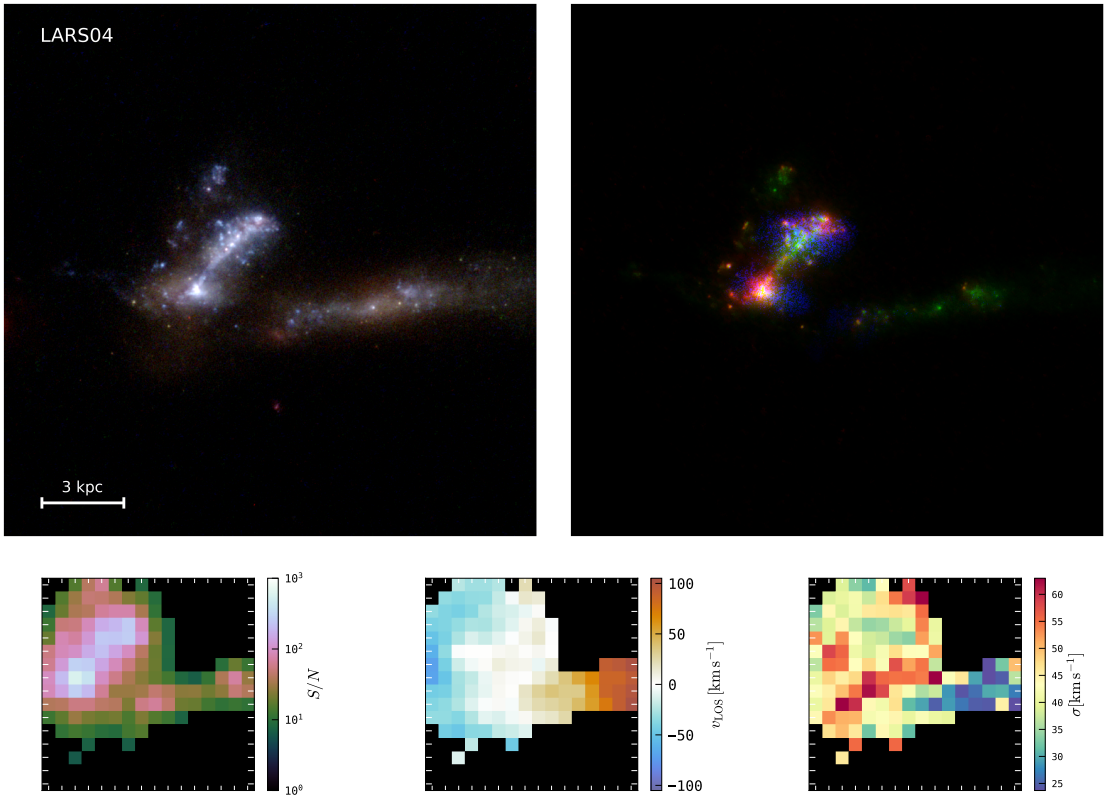

Figure A.1 continued for LARS04.

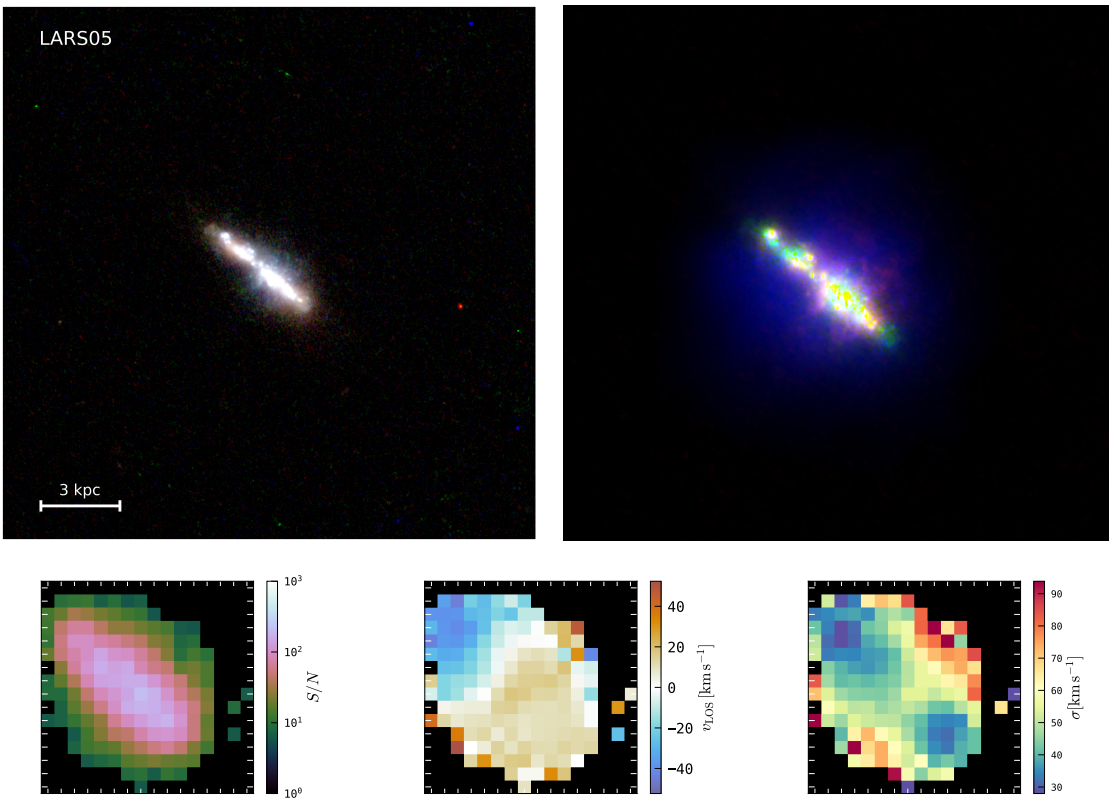

Figure A.1 continued for LARS05.

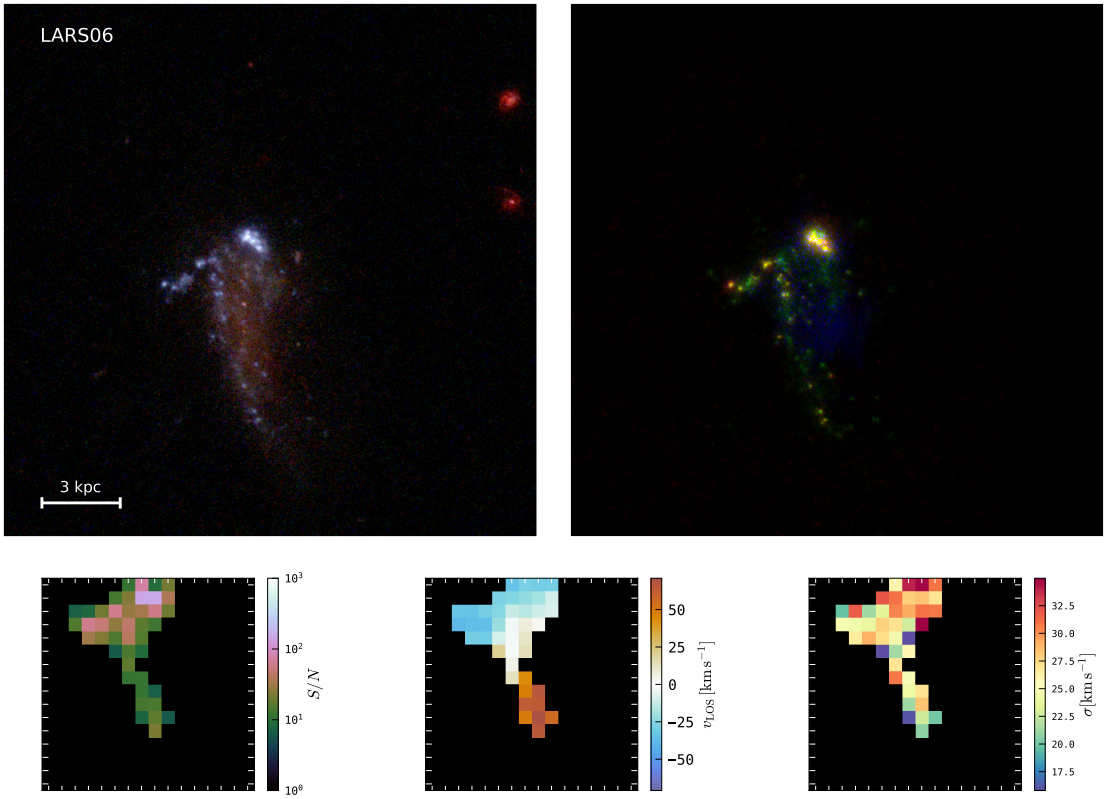

Figure A.1 continued for LARS06.

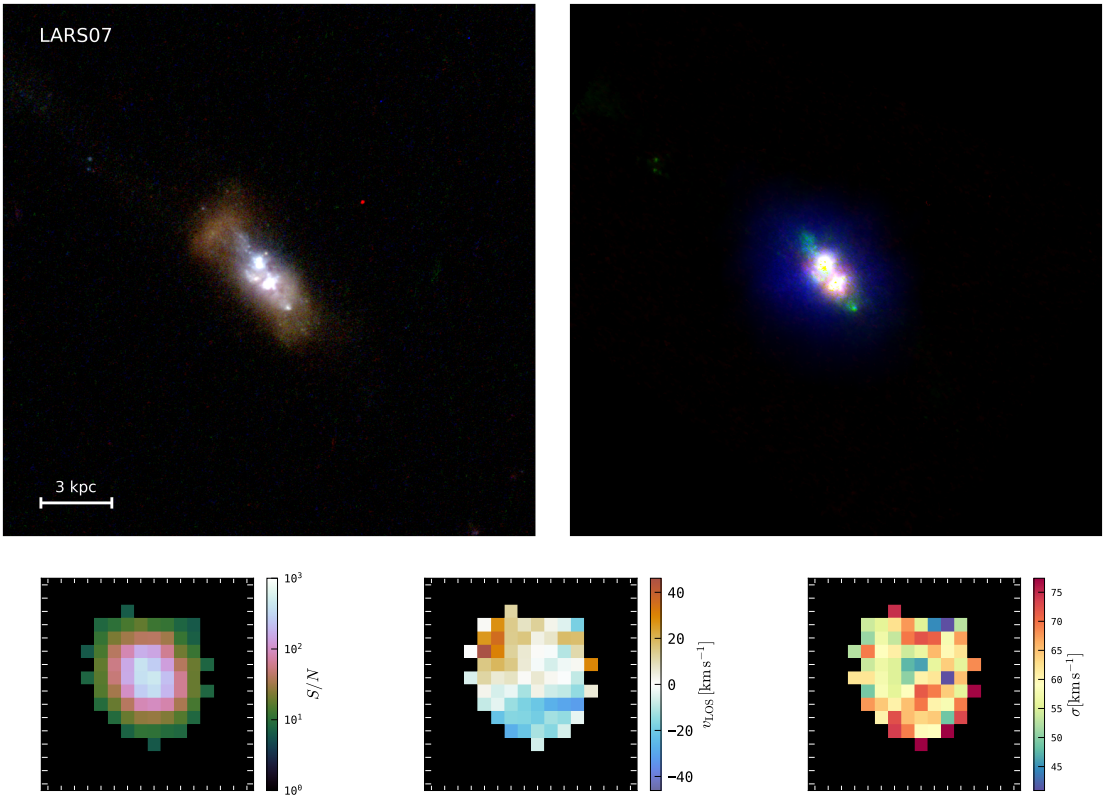

Figure A.1 continued for LARS07.

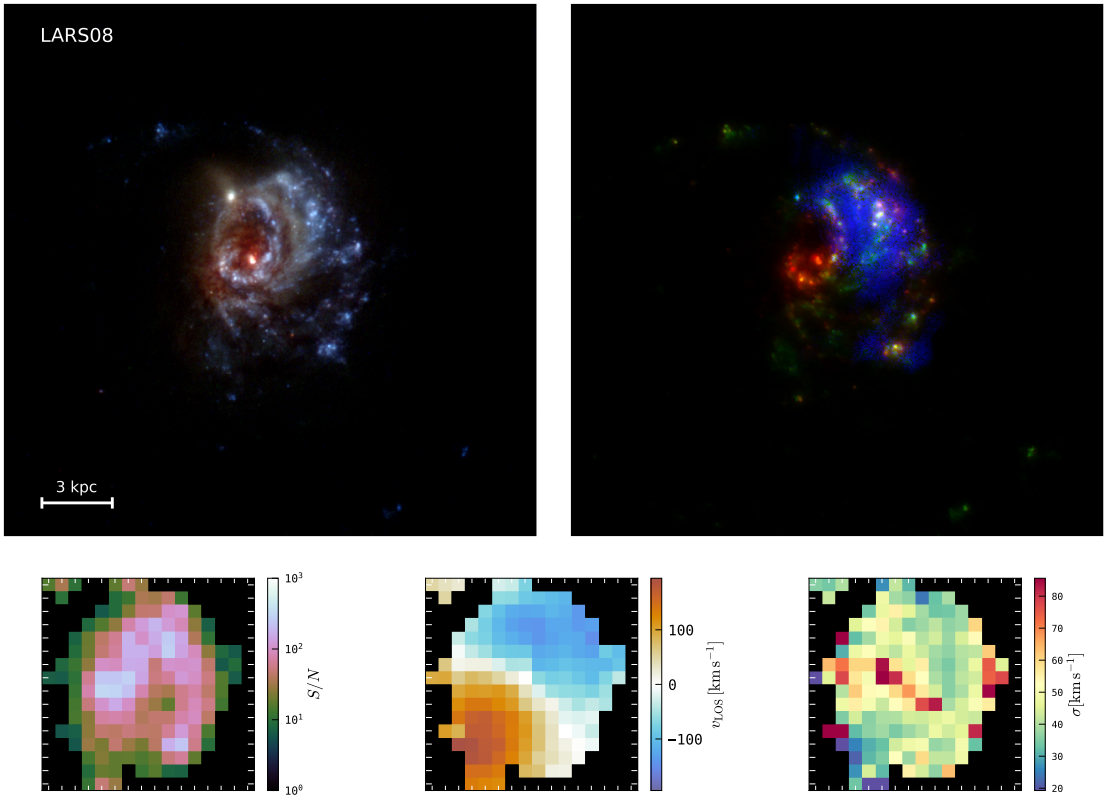

Figure A.1 continued for LARS08.

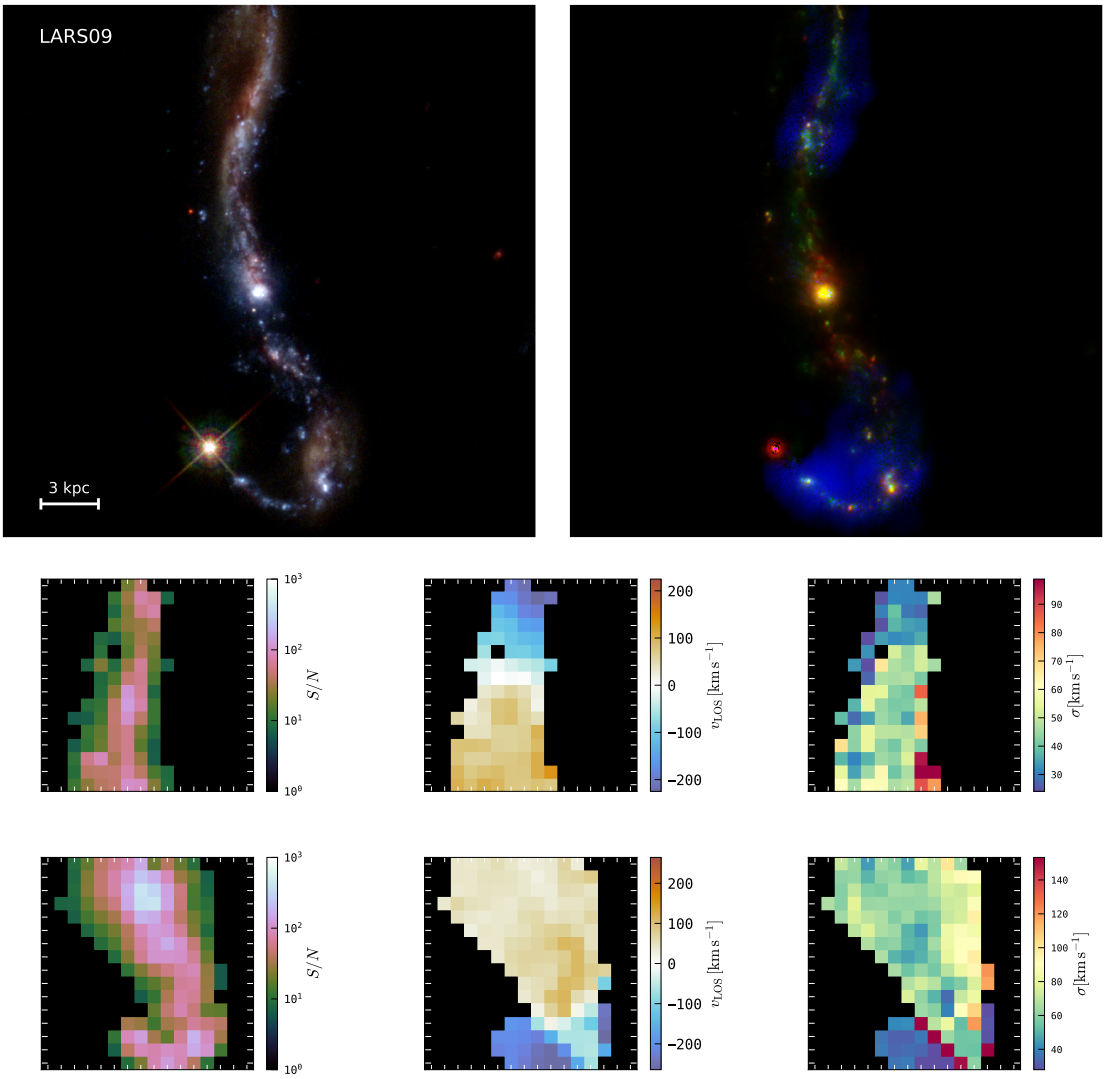

Figure A.1 continued for LARS09.

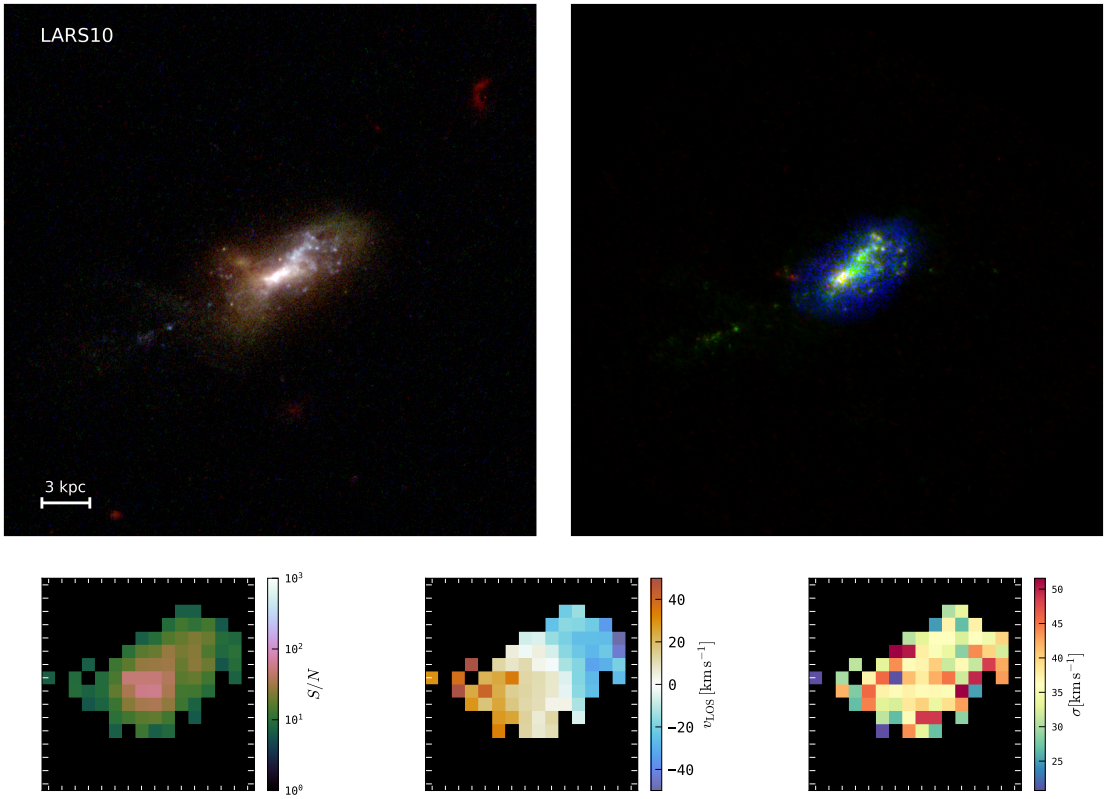

Figure A.1 continued for LARS10.

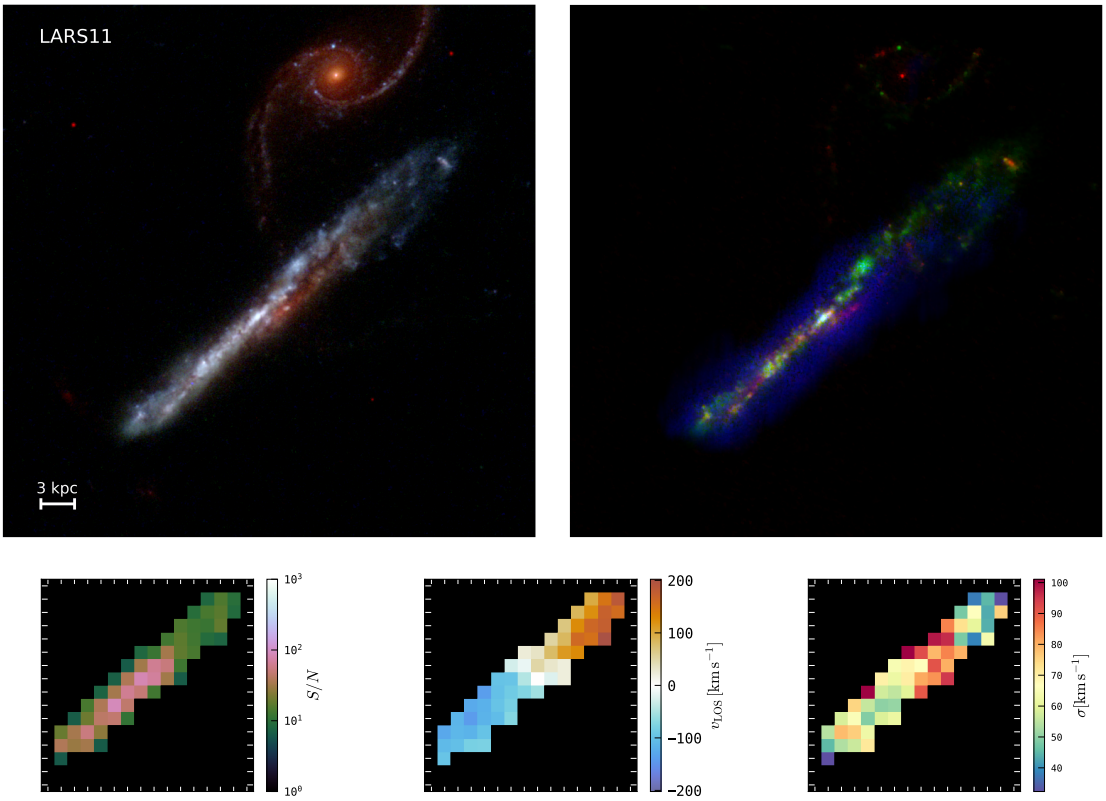

Figure A.1 continued for LARS11.

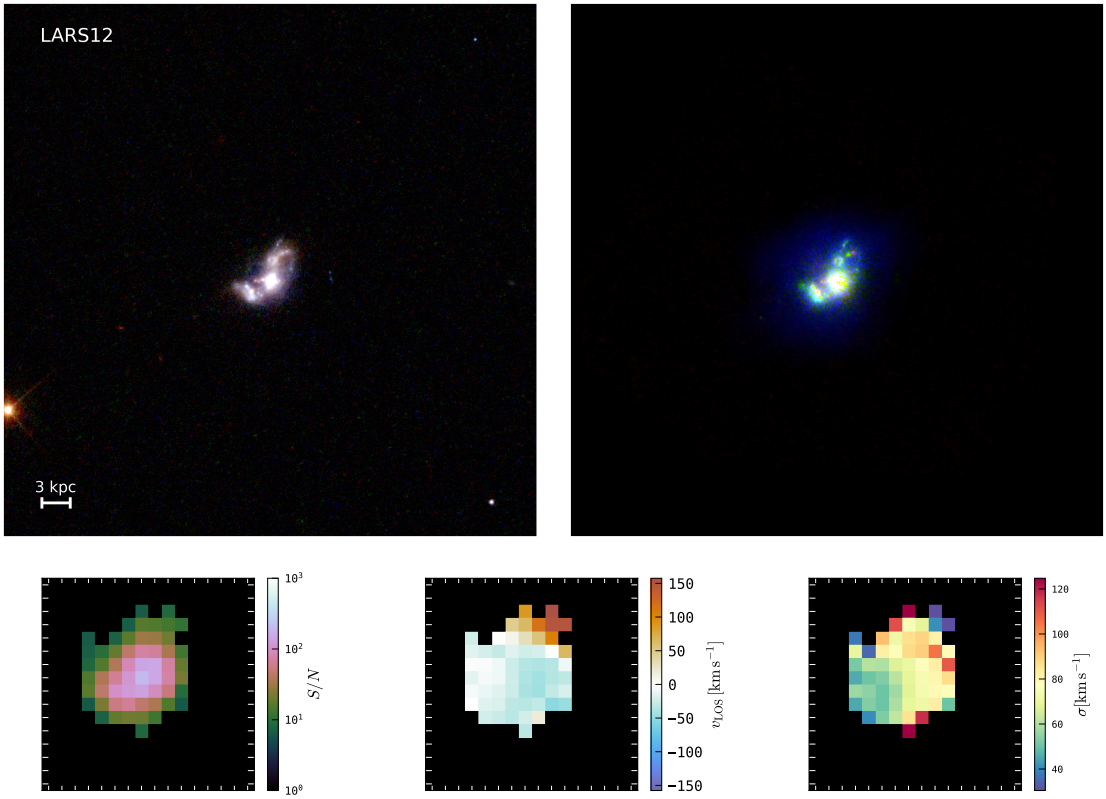

Figure A.1 continued for LARS12.

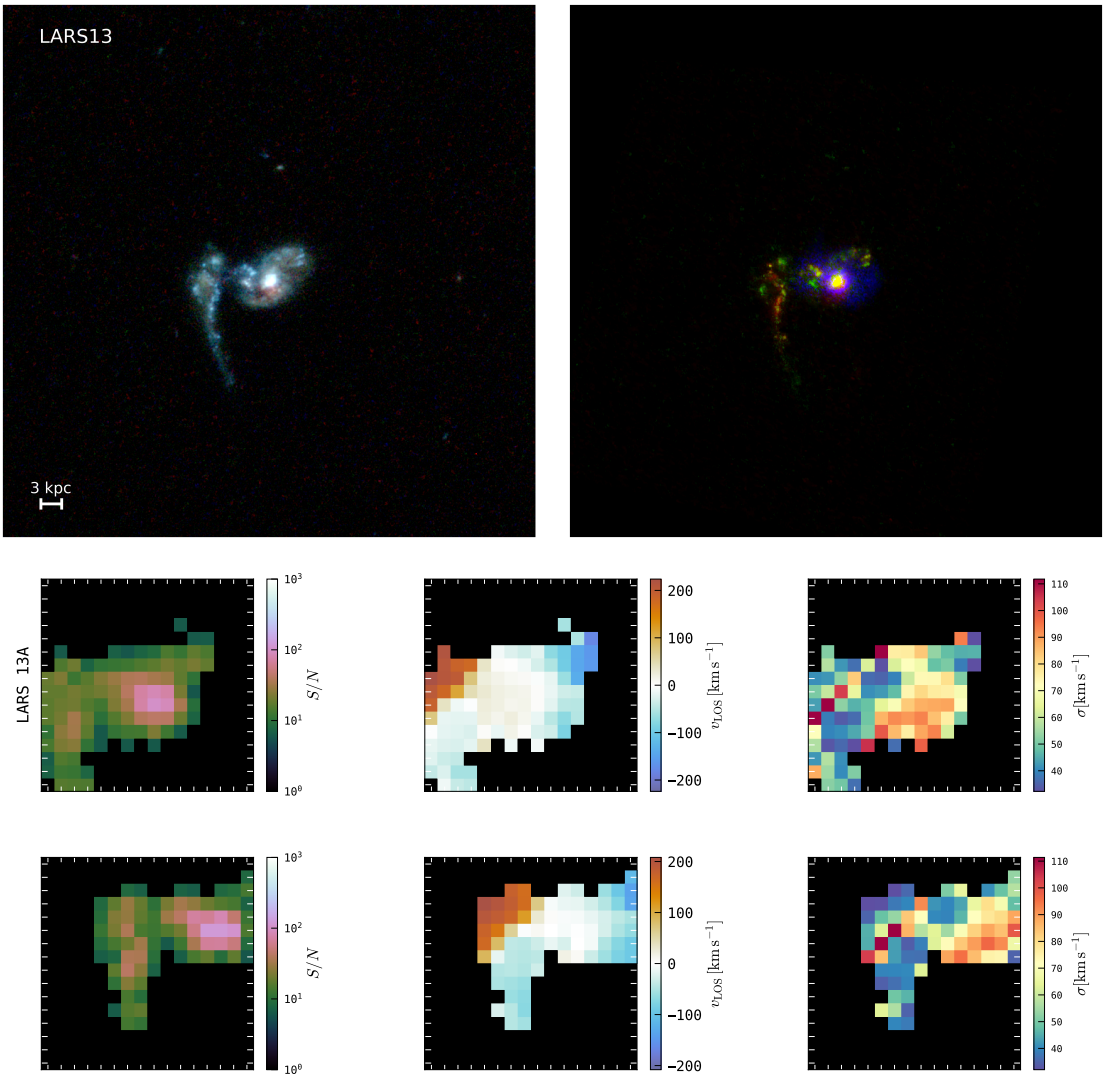

Figure A.1 continued for LARS13.

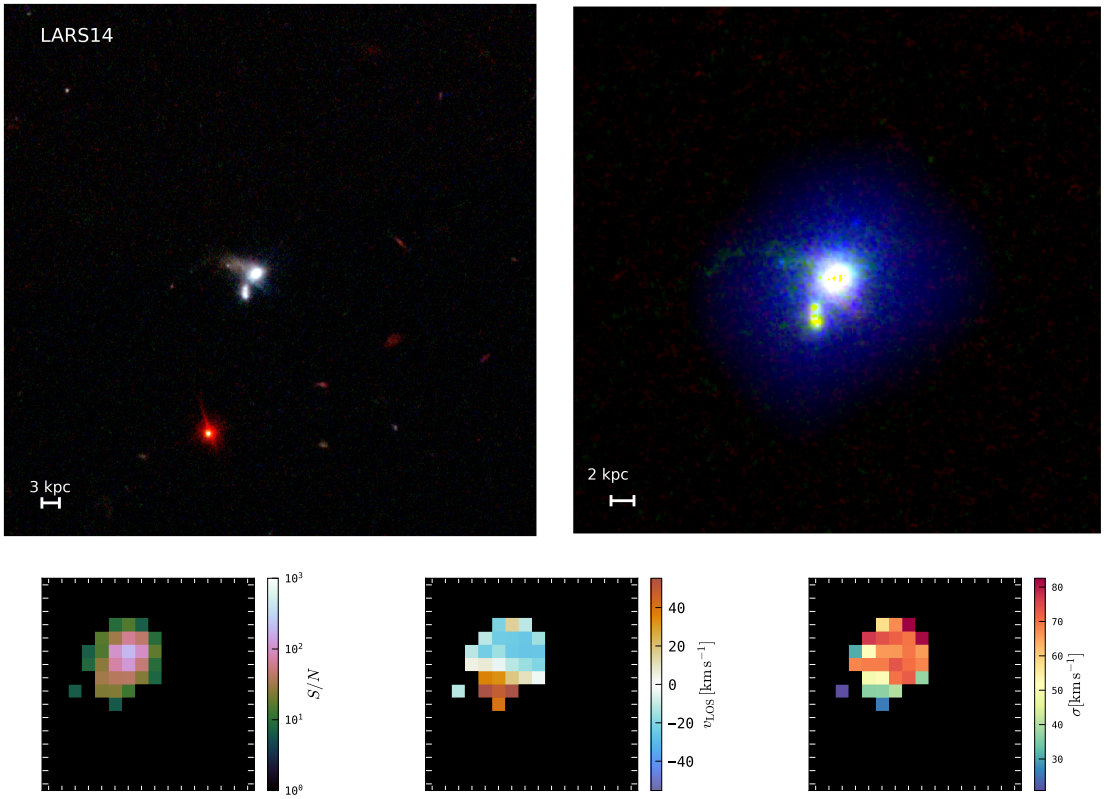

Figure A.1 continued for LARS14.

A.2 Effect of flux weighting on the velocity dispersion

We calculate the weighted average of the observed velocity dispersion by weighting with the S/N as the eLARS galaxies are not flux-calibrated. The LARS galaxies are flux-calibrated. Therefore, we compare the velocity dispersion values with flux weighting and with S/N weighting for all LARS single pointings. The values are listed in Table A.1. The differences are more or less within the error bars, which proofs that we can use S/N weighting to calculate the weighted average of the observed velocity dispersion for our sample.

Table A.1: Empiric velocity dispersion for the LARS galaxies weighted by flux and weighted by S/N.

	$\sigma_{\mathrm{m}}^{\mathrm{flux}}$ $[\mathrm{km\,s^{-1}}]$	$\Delta\sigma_{\mathrm{m}}^{\mathrm{flux}}$ $[\mathrm{km\,s^{-1}}]$	$\sigma_{\mathrm{m}}^{(\mathrm{S/N})}$ $[\mathrm{km\,s^{-1}}]$	$\Delta\sigma_{\mathrm{m}}^{(\mathrm{S/N})}$ $[\mathrm{km\,s^{-1}}]$	$\sigma_{\mathrm{m}}^{\mathrm{flux}} - \sigma_{\mathrm{m}}^{(\mathrm{S/N})}$ $[\mathrm{km\,s^{-1}}]$
LARS01	47.1	0.1	46.7	0.1	0.4
LARS02	38.1	0.2	37.9	0.2	0.2
LARS03	87.1	0.2	88.9	0.2	-1.8
LARS04	44.2	0.1	43.6	0.1	0.6
LARS05	46.0	0.1	45.6	0.1	0.4
LARS06	28.0	0.3	27.2	0.2	0.8
LARS07	57.6	0.1	58.3	0.2	-0.7
LARS08	48.3	0.1	47.1	0.1	1.2
LARS10	37.0	0.4	36.6	0.4	0.4
LARS11	66.7	0.5	65.3	0.5	1.4
LARS12	70.9	0.3	70.0	0.3	0.9
LARS14	66.1	0.4	65.2	0.4	0.9

A.3 Difference in our LARS values compared to E. C. Herenz et al. (2016)

Our values and the E. C. Herenz et al. (2016) values for the LARS galaxies differ as shown in Table A.2. The new shearing velocity and velocity dispersion values are smaller than in E. C. Herenz et al. (2016).

Table A.2: Comparison between our kinematic values for the LARS galaxies and the values in E. C. Herenz et al. (2016).

ID	σ_{m} [km s^{-1}]	$\Delta\sigma_{\mathrm{m}}$ [km s^{-1}]	σ_{H16} [km s^{-1}]	$\Delta\sigma_{\mathrm{H16}}$ [km s^{-1}]	$\sigma_{\mathrm{m}} - \sigma_{\mathrm{H16}}$ [km s^{-1}]	v_{shear} [km s^{-1}]	$\Delta v^{+}_{\mathrm{shear}}$ [km s^{-1}]	$\Delta v^{-}_{\mathrm{shear}}$ [km s^{-1}]	v_{H16} [km s^{-1}]	Δv_{H16} [km s^{-1}]	$v_{\mathrm{shear}} - v_{\mathrm{H16}}$ [km s^{-1}]
LARS01	46.7	0.1	47.5	0.1	- 0.8	52.4	1.6	2.8	56	2	- 3.6
LARS02	37.9	0.2	38.6	0.9	- 0.7	15.4	8.0	2.9	23	3	- 7.6
LARS03	88.9	0.2	99.5	3.7	- 10.6	130.2	5.4	6.7	138	3	- 7.8
LARS04	43.6	0.1	44.1	0.1	- 0.5	68.2	2.9	5.7	74	9	- 5.8
LARS05	45.6	0.1	46.8	0.3	- 1.2	30.6	5.8	1.2	37	4	- 6.4
LARS06	27.2	0.2	27.2	0.3	0.0	50.6	1.9	1.0	52	7	- 1.4
LARS07	58.3	0.1	58.7	0.3	- 0.4	26.0	4.9	2.7	31	3	- 5.0
LARS08	47.1	0.1	49.0	0.1	- 1.9	148.9	4.4	3.2	155	3	- 6.1
LARS09	56.5	0.1	58.6	0.1	- 2.1	159.6	3.0	8.5	182	3	- 22.4
LARS10	36.6	0.4	38.2	1.0	- 1.6	32.4	5.5	6.0	36	3	- 3.6
LARS11	65.3	0.5	69.3	3.8	- 4.0	149.1	11.2	6.1	149	4	0.1
LARS12	70.0	0.3	72.7	1.0	- 2.7	81.3	18.7	3.3	96	3	- 14.7
LARS13	65.5	0.4	69.2	0.7	- 3.7	168.5	18.7	3.3	183	4	- 14.5
LARS14	65.2	0.4	67.3	1.3	- 2.1	38.8	2.3	0.1	40	1	- 1.2

Table A.3: Comparison between the PSF corrected velocity dispersions and the E. C. Herenz et al. (2016) velocity dispersions.

ID	$\sigma_{\text{m, uniform, corr}}$ [km s^{-1}]	$\Delta\sigma_{\text{m, uniform, corr}}$ [km s^{-1}]	σ_{H16} [km s^{-1}]	$\Delta\sigma_{\text{H16}}$ [km s^{-1}]	$\sigma_{\text{m, uniform corr}} - \sigma_{\text{H16}}$ [km s^{-1}]
LARS01	47.2	0.6	47.5	0.1	-0.3
LARS02	38.2	0.7	38.6	0.9	-0.4
LARS03	77.4	2.9	99.5	3.7	-22,1
LARS04	43.0	0.3	44.1	0.1	-1.1
LARS05	51.2	0.5	46.8	0.3	4,4
LARS06	26.2	0.5	27.2	0.3	-1.0
LARS07	60.6	0.8	58.7	0.3	1.9
LARS08	41.2	0.4	49.0	0.1	-7.8
LARS09	56.1	0.4	58.6	0.1	-2.5
LARS10	36.5	0.6	38.2	1.0	-1.7
LARS11	60.9	1.4	69.3	3.8	-8.4
LARS12	64.8	1.1	72.7	1.0	-7.9
LARS13	61.0	0.9	69.2	0.7	-8.2
LARS14	59.0	1.2	67.3	1.3	-8.3

E. C. Herenz et al. (2016) bins spaxels with low S/N. However, in our analysis, we chose not to bin spaxels with low S/N. As a result, the number of spaxels used in our calculations differs from theirs and leads to different calculated values.

By comparing the maps obtained with the two approaches, it becomes apparent that not binning the low S/N spaxels leads to clearer maps and could provide more accurate values.

For our analysis we use the velocity dispersion corrected for PSF smearing by a gradient. Therefore, we use different velocity dispersion values than E. C. Herenz et al. (2016). We list our used velocity dispersion for the LARS galaxies, the E. C. Herenz et al. (2016) and the difference in Table A.3. 12 of 14 galaxies have lower σ_{H16} than $\sigma_{\text{m, uniform, corr}}$. The differences range from 0.3 km s^{-1} up to 22.1 km s^{-1} with a mean difference of 5.4 km s^{-1}.

A.4 Effect of different methods for calculating σ on the correlation statistics

We now study the effect of the different methods, which we use for calculating the velocity dispersion, on the rank correlation test results. Towards this aim we compute τ and p_0 for the parameter combinations studied in Chapter 4.

We compare $\sigma_{\mathrm{m,\ uniform,\ corr}}$ (Equation 3.17), $\sigma_{\mathrm{m,\ corr}}$ (Equation 3.18), $\sigma_{\mathrm{m,\ uniform}}$ (Equation 3.3) and σ_{m} (Equation 3.4). We list the correlation test results in Table A.4.

Except for the relation $L_{\mathrm{Ly}\alpha}/L_{\mathrm{H}\alpha} - v_{\mathrm{shear}}/\sigma$, the different methods for calculating the velocity dispersion do not change the statistical statement, whether we assume that there is a correlation or not. Taking the 5 % mark, $L_{\mathrm{Ly}\alpha}/L_{\mathrm{H}\alpha} - v_{\mathrm{shear}}/\sigma_{\mathrm{m,\ uniform}}$ is above and all other three relations are below the 5 % mark. However, it has to be kept in mind that a strict p_0-value cutoff is not a good idea and even for the $L_{\mathrm{Ly}\alpha}/L_{\mathrm{H}\alpha} - v_{\mathrm{shear}}/\sigma$ relation all four different calculations show very low p_0-values with a maximum value of 0.053, which is slightly above our cutoff. Our σ_{m} is the analog to the parameter used in E. C. Herenz et al. (2016). Using the PSF smearing correction by our gradient method does not change the statistical statement of the sample. One aspect of why the correlation analysis for the weighted and simple mean does not arrive at drastically different results, is that less than half of our sample are actually affected by the gradient masking.

Table A.4: Kendall τ and the p_0-value for the relation between Lyα observables and the kinematic parameters, derived by different methods.

	τ $[\sigma_{\mathrm{m,\ uniform,\ corr}}]$	p_0 $[\sigma_{\mathrm{m,\ uniform,\ corr}}]$	τ $[\sigma_{\mathrm{m,\ corr}}]$	p_0 $[\sigma_{\mathrm{m,\ corr}}]$	τ $[\sigma_{\mathrm{m,\ uniform}}]$	p_0 $[\sigma_{\mathrm{m,\ uniform}}]$	τ $[\sigma_{\mathrm{m}}]$	p_0 $[\sigma_{\mathrm{m}}]$
$EW_{\mathrm{Ly}\alpha} - \sigma$	0.337	0.003	0.366	0.001	0.349	0.002	0.363	0.001
$EW_{\mathrm{Ly}\alpha} - v_{\mathrm{shear}}/\sigma$	-0.149	0.191	-0.155	0.174	-0.172	0.131	-0.195	0.087
$f_{\mathrm{esc}}^{\mathrm{Ly}\alpha} - \sigma$	0.156	0.170	0.196	0.085	0.139	0.222	0.154	0.178
$f_{\mathrm{esc}}^{\mathrm{Ly}\alpha} - v_{\mathrm{shear}}/\sigma$	-0.256	0.024	-0.290	0.011	-0.236	0.038	-0.282	0.013
$L_{\mathrm{Ly}\alpha}/L_{\mathrm{H}\alpha} - \sigma$	0.238	0.037	0.272	0.017	0.232	0.041	0.240	0.034
$L_{\mathrm{Ly}\alpha}/L_{\mathrm{H}\alpha} - v_{\mathrm{shear}}/\sigma$	-0.186	0.102	-0.220	0.053	-0.169	0.137	-0.226	0.047

A.5 MCMC chains from the GalPaK3D modeling

Figure A.43 shows the MCMC chains for the 10 free parameters and the χ^2 evolution for each galaxy, which is modeled with GalPaK. Each of the small panels correspond to one parameter. The bottom panel shows the χ^2 evolution relative to the minimum. χ^2 is a statistical quantity commonly used to assess the goodness of the fit between observed data and model. The smaller the χ^2 value, the better the model fits the data. We can see that the burn in phase is in the around first 1000 iterations.

For the 10 free parameters, the estimated parameters are shown with the red line and are calculated from the last 60 % of the chain. The gray lines show the 1σ standard deviations, and the dotted lines show the 95 % confidence interval (Bouché et al. 2015).

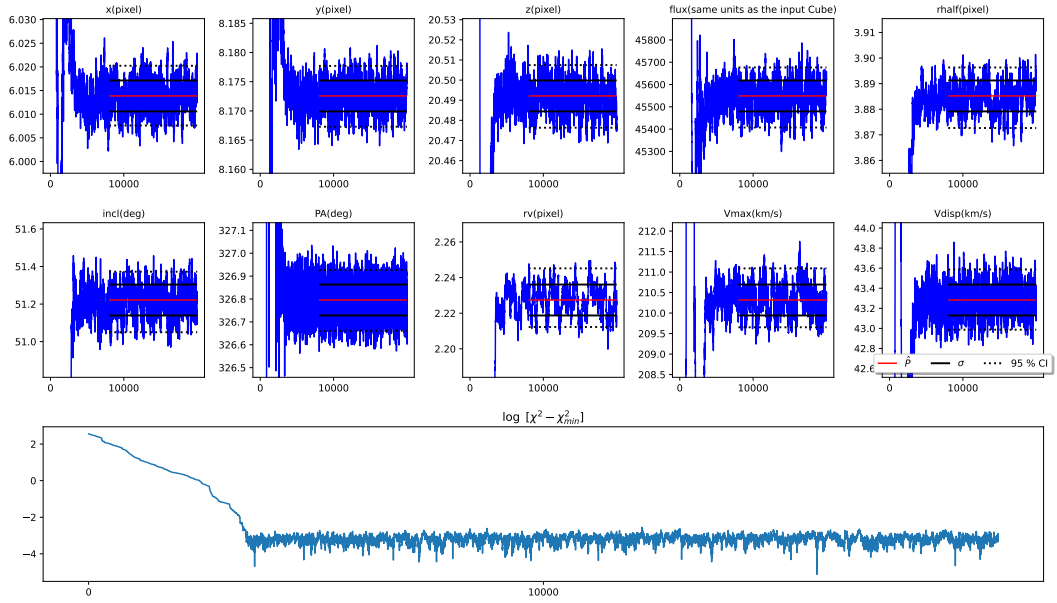

Figure A.43: MCMC for LARS08.

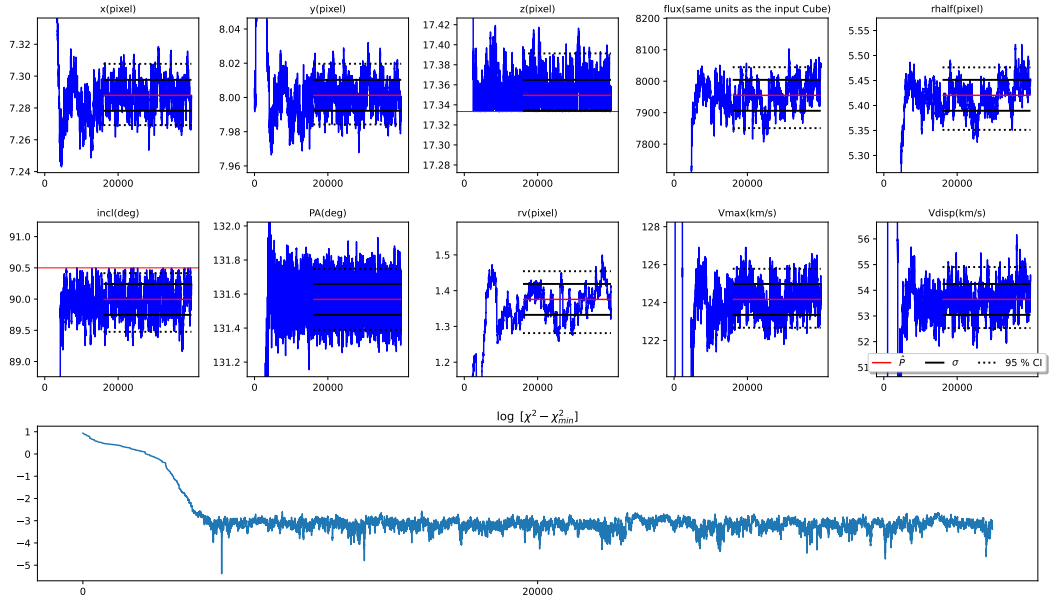

MCMC for LARS11.

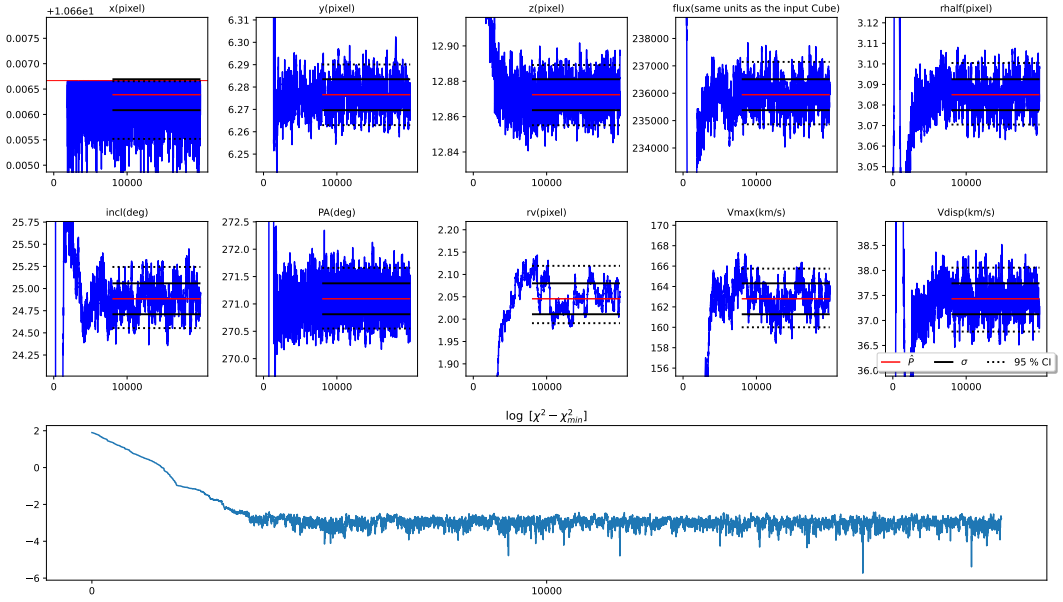

MCMC for eLARS04.

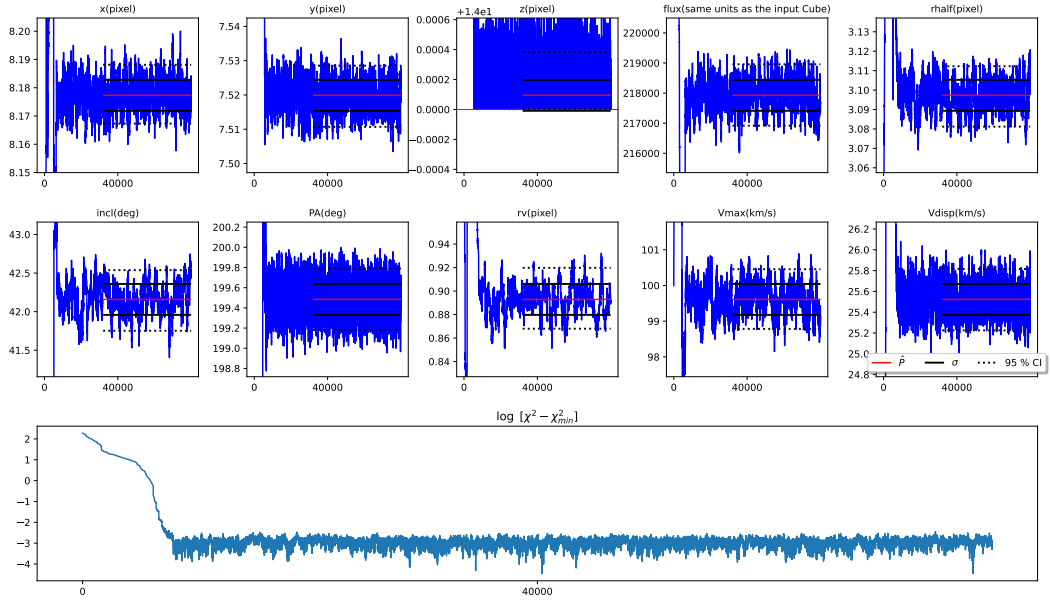

MCMC for eLARS06.

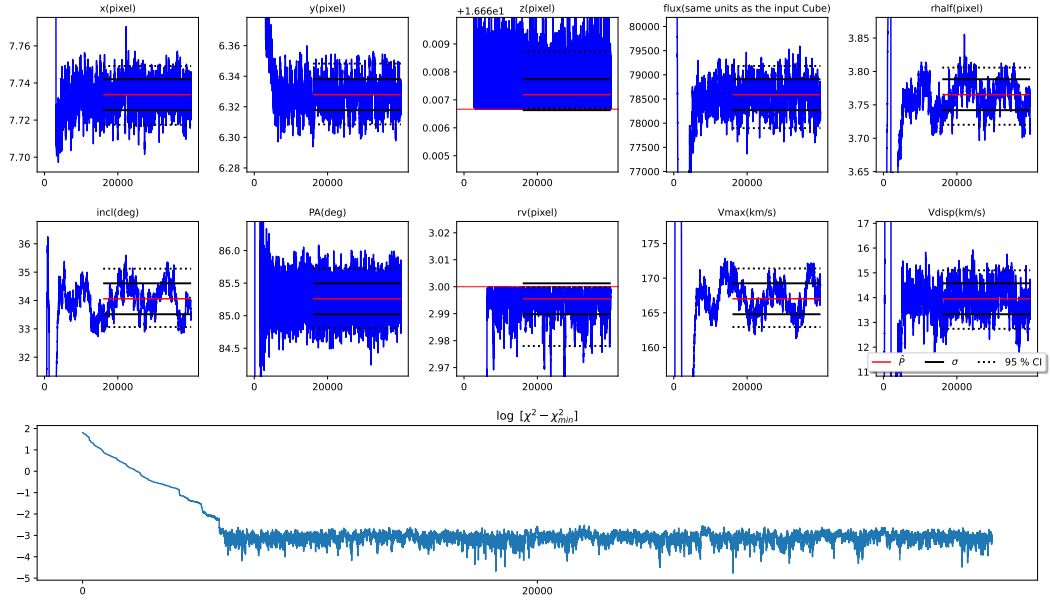

MCMC for eLARS08.

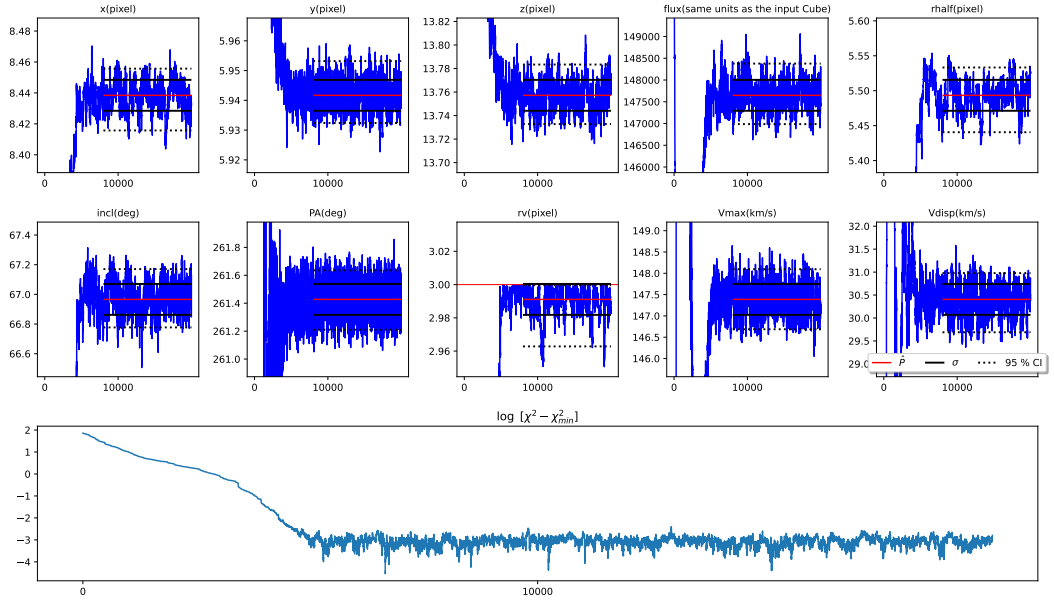

MCMC for eLARS10.

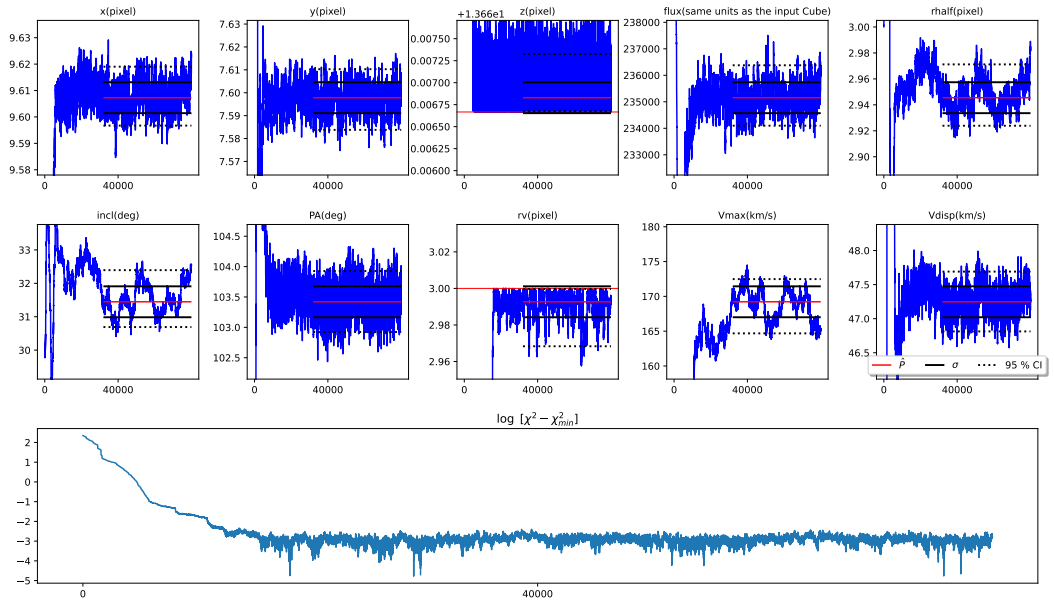

MCMC for eLARS11.

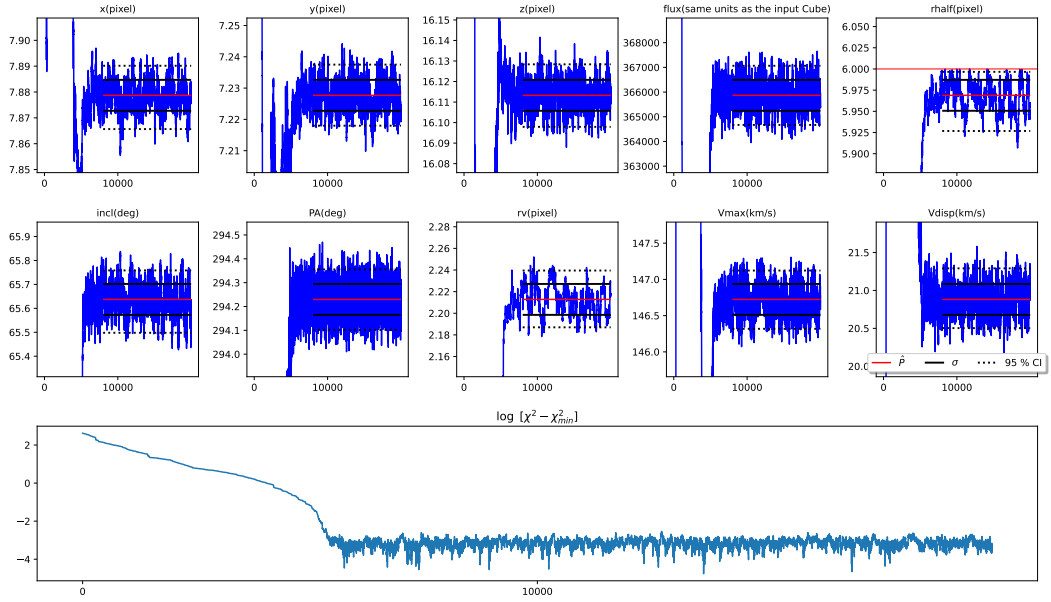

MCMC for eLARS12.

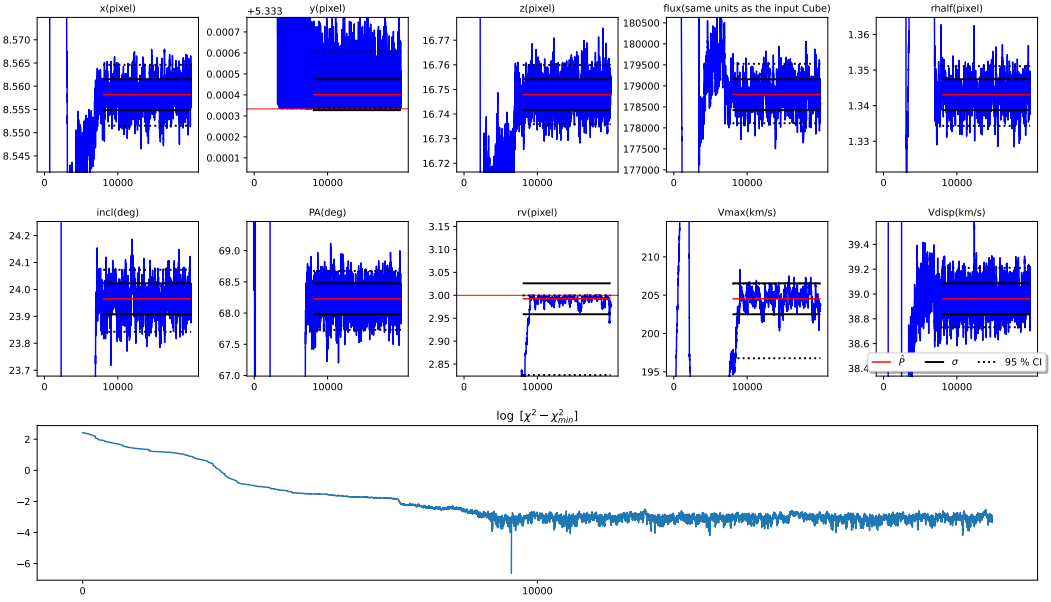

MCMC for eLARS14.

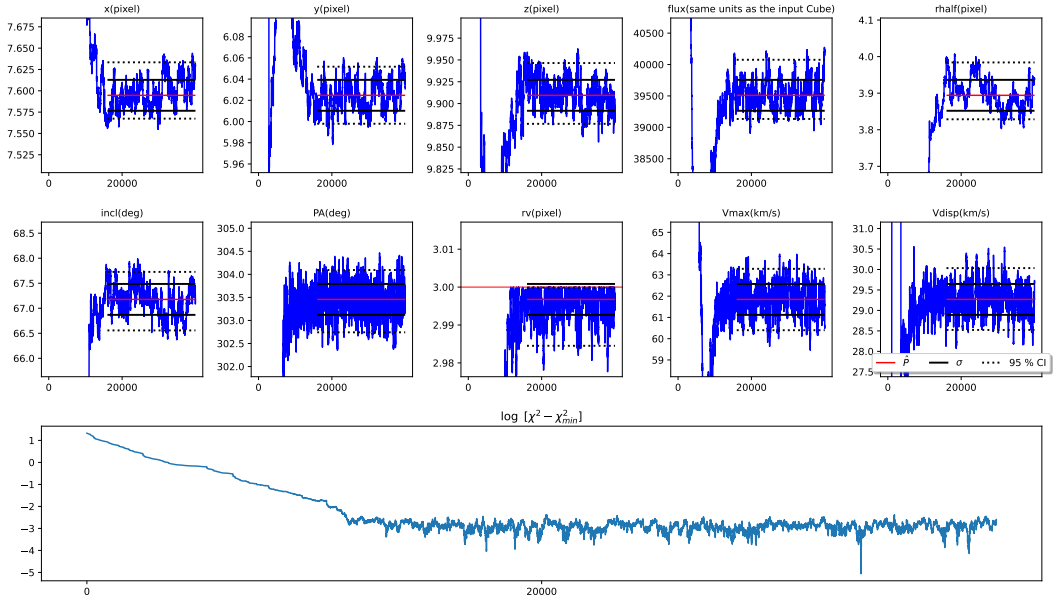

MCMC for eLARS16.

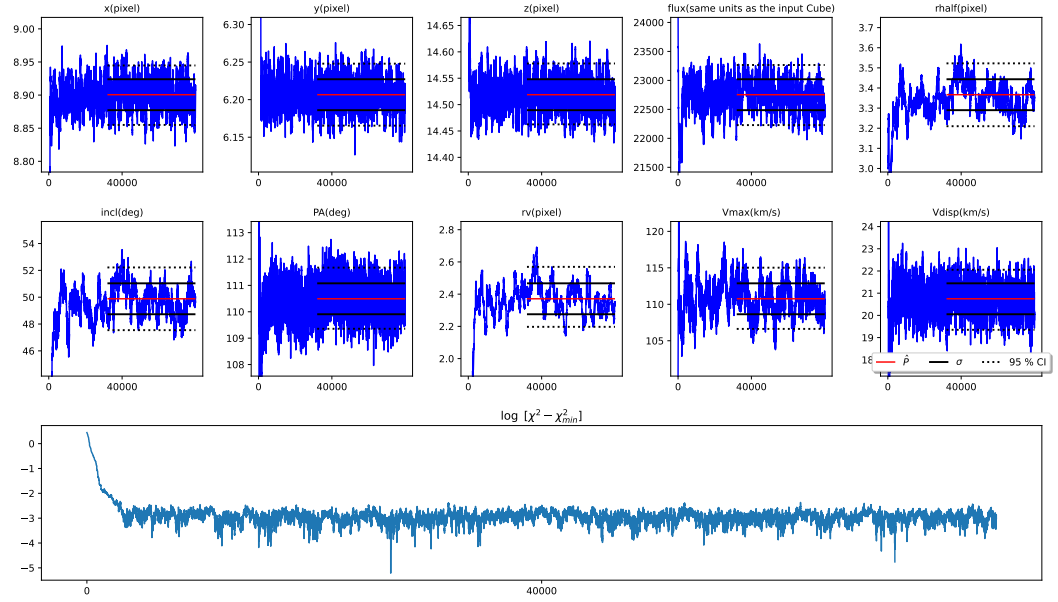

MCMC for eLARS17.

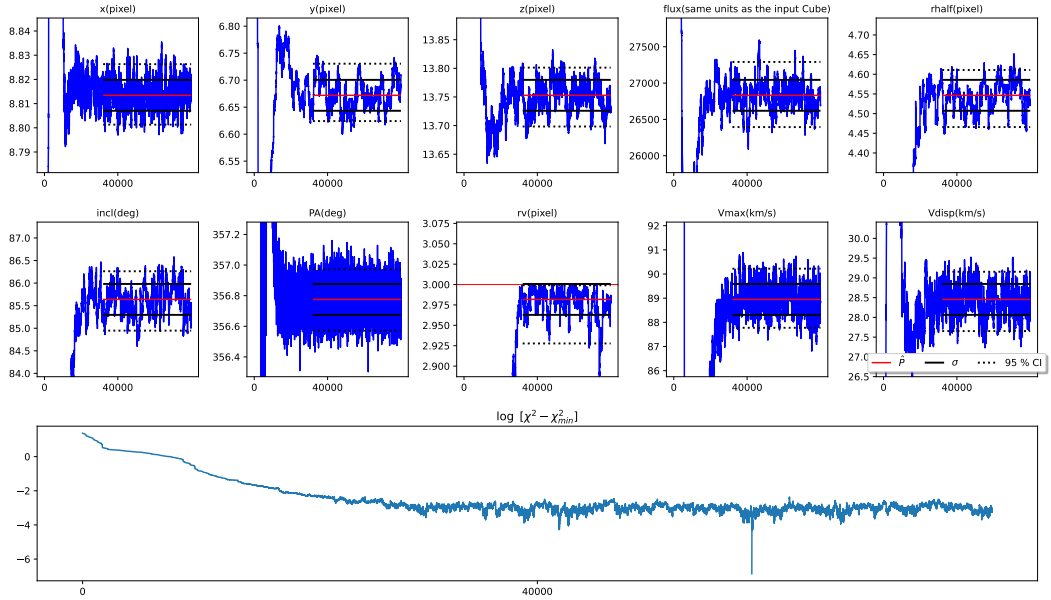

MCMC for eLARS18.

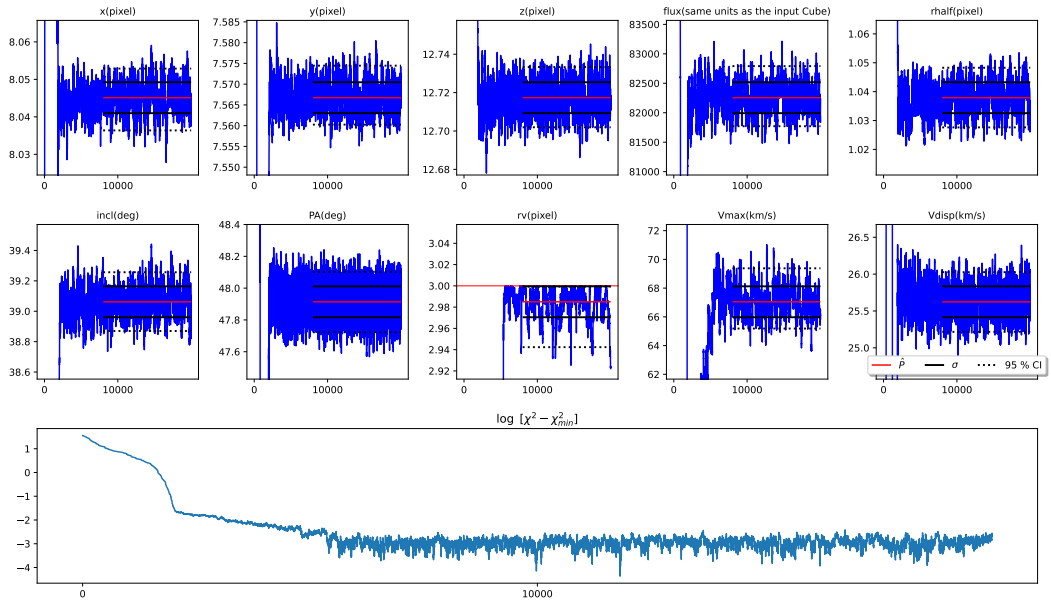

MCMC for eLARS19.

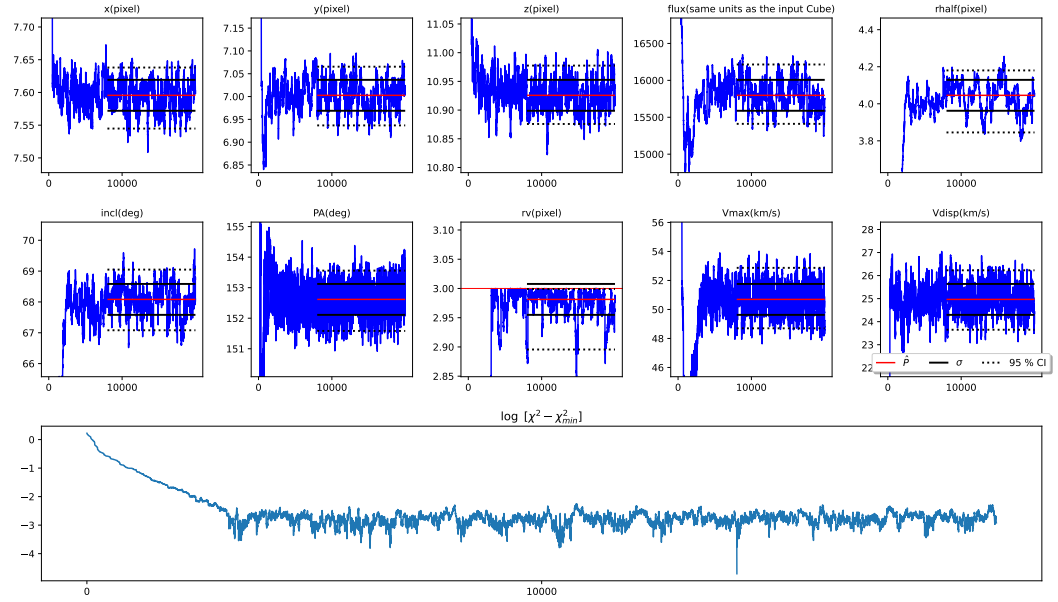

MCMC for eLARS21.

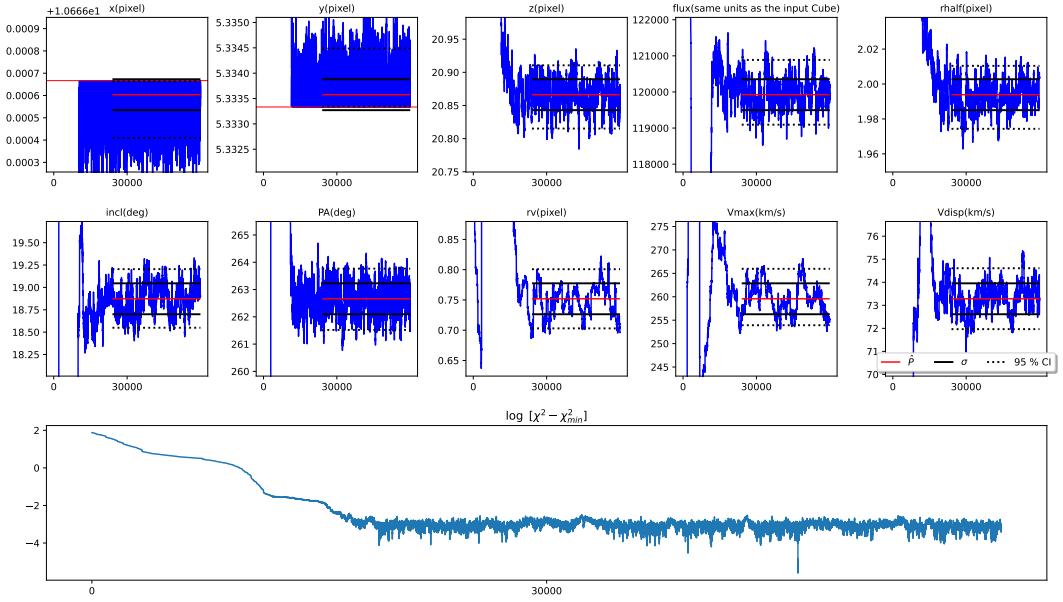

MCMC for eLARS24.

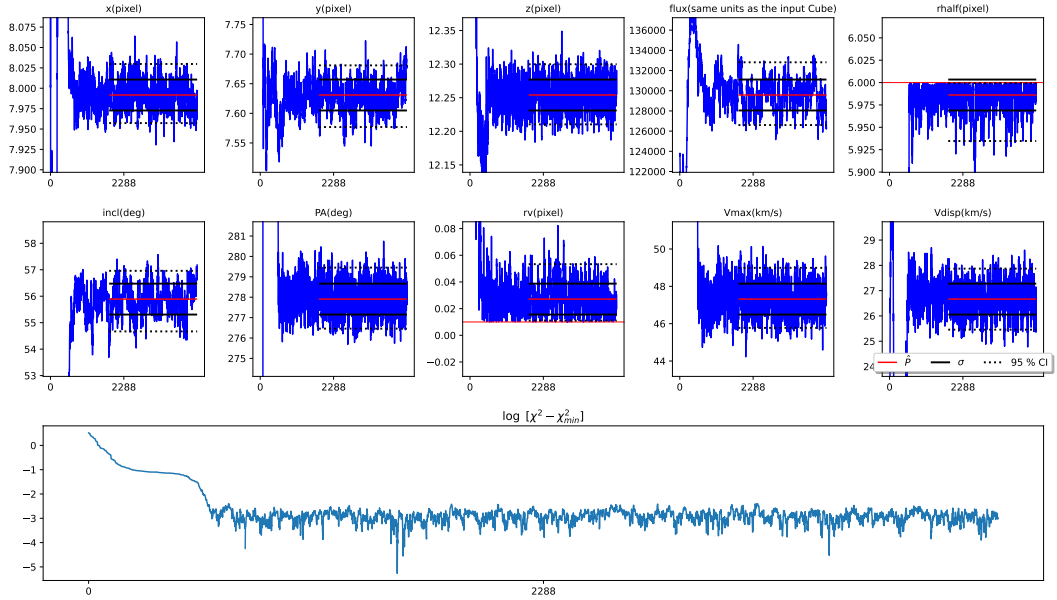

MCMC for eLARS27.

Bibliography

Akritas, Michael G., Susan A. Murphy, and Michael P. Lavalley (Mar. 1995). "The Theil-Sen Estimator with Doubly Censored Data and Applications to Astronomy". In: *Journal of the American Statistical Association* 90.429, pp. 170–177. DOI: 10.1080/01621459.1995.10476499.

Andersen, David R. and Matthew A. Bershady (May 2013). "The Photometric and Kinematic Structure of Face-on Disk Galaxies. III. Kinematic Inclinations from Hα Velocity Fields". In: *Astrophysical Journal* 768.1, 41, p. 41. DOI: 10.1088/0004-637X/768/1/41.

Bacon, Roland and Guy Monnet (Mar. 2017). *Optical 3D-Spectroscopy for Astronomy*. Wiley. DOI: 10.1002/9783527674824.

Barat, Dilyar et al. (Sept. 2020). "SHDE: survey description and mass–kinematics scaling relations for dwarf galaxies". In: *Monthly Notices of the Royal Astronomical Society* 498.4, pp. 5885–5903. DOI: 10.1093/mnras/staa2716.

Behrens, C. and H. Braun (Dec. 2014). "Inclination dependence of Lyman-α properties in a turbulent disk galaxy". In: *Astronomy and Astrophysics* 572, A74, A74. DOI: 10.1051/0004-6361/201424755. arXiv: 1410.3733 [astro-ph.GA].

Bellocchi, Enrica et al. (Sept. 2013). "VLT/VIMOS integral field spectroscopy of luminous and ultraluminous infrared galaxies: 2D kinematic properties". In: *Astronomy and Astrophysics* 557, A59, A59. DOI: 10.1051/0004-6361/201221019. arXiv: 1307.1659 [astro-ph.CO].

Blaizot, Jérémy et al. (Aug. 2023). "Simulating the diversity of shapes of the Lyman-α line". In: *Monthly Notices of the RAS* 523.3, pp. 3749–3772. DOI: 10.1093/mnras/stad1523. arXiv: 2305.10047 [astro-ph.GA].

Bouché, N. et al. (Jan. 2015). *GalPaK 3D: Galaxy parameters and kinematics extraction from 3D data*. Astrophysics Source Code Library, record ascl:1501.014. ascl: 1501.014.

Brinchmann, J. et al. (July 2004). "The physical properties of star-forming galaxies in the low-redshift Universe". In: *Monthly Notices of the RAS* 351.4, pp. 1151–1179. DOI: 10.1111/j.1365-2966.2004.07881.x. arXiv: astro-ph/0311060 [astro-ph].

Cardelli, Jason A., Geoffrey C. Clayton, and John S. Mathis (Oct. 1989). "The Relationship between Infrared, Optical, and Ultraviolet Extinction". In: *Astrophysical Journal* 345, p. 245. DOI: 10.1086/167900.

Chabrier, Gilles (July 2003). "Galactic Stellar and Substellar Initial Mass Function". In: *Publications of the ASP* 115.809, pp. 763–795. DOI: 10.1086/376392. arXiv: astro-ph/0304382 [astro-ph].

Courteau, Stéphane et al. (Jan. 2014). "Galaxy masses". In: *Reviews of Modern Physics* 86.1, pp. 47–119. DOI: 10.1103/RevModPhys.86.47. arXiv: 1309.3276 [astro-ph.CO].

Davies, R. et al. (Oct. 2011). "HOW WELL CAN WE MEASURE THE INTRINSIC VELOCITY DISPERSION OF DISTANT DISK GALAXIES?" In: *The Astrophysical Journal* 741.2, p. 69. DOI: 10.1088/0004-637x/741/2/69.

Dijkstra, Mark (2019). *Lyman-alpha as an Astrophysical and Cosmological Tool - chapter 1*. Ed. by Anne Verhamme et al. Springer Berlin Heidelberg. DOI: 10.1007/978-3-662-59623-4.

Eddington, A. S. (Mar. 1924). "On the Relation between the Masses and Luminosities of the Stars.: (Plate 8.)" In: *Monthly Notices of the Royal Astronomical Society* 84.5, pp. 308–333. DOI: 10.1093/mnras/84.5.308.

Epinat, B. et al. (Feb. 2010). "Evidence for strong dynamical evolution in disc galaxies through the last 11 Gyr. GHASP VIII - a local reference sample of rotating disc galaxies for high-redshift studies". In: *Monthly Notices of the RAS* 401.4, pp. 2113–2147. DOI: 10.1111/j.1365-2966.2009.15688.x. arXiv: 0904.3891 [astro-ph.CO].

Feng, James Q. and C. F. Gallo (Dec. 2011). "Modeling the Newtonian dynamics for rotation curve analysis of thin-disk galaxies". In: *Research in Astronomy and Astrophysics* 11.12, pp. 1429–1448. DOI: 10.1088/1674-4527/11/12/005. arXiv: 1104.3236 [astro-ph.GA].

Flores, H. et al. (Aug. 2006). "3D spectroscopy with VLT/GIRAFFE. I. The true Tully Fisher relationship at z $\sim$ 0.6". In: *Astronomy and Astrophysics* 455.1, pp. 107–118. DOI: 10.1051/0004-6361:20054217. arXiv: astro-ph/0603563 [astro-ph].

Glazebrook, Karl (Nov. 2013). "The Dawes Review 1: Kinematic Studies of Star-Forming Galaxies Across Cosmic Time". In: *Publications of the Astron. Soc. of Australia* 30, e056, e056. DOI: 10.1017/pasa.2013.34. arXiv: 1305.2469 [astro-ph.CO].

Gonçalves, Thiago S. et al. (Dec. 2010). "The Kinematics of Ionized Gas in Lyman-break Analogs at z $\sim$0.2". In: *Astrophysical Journal* 724.2, pp. 1373–1388. DOI: 10.1088/0004-637X/724/2/1373. arXiv: 1009.4934 [astro-ph.CO].

Graham, Alister W. and Simon P. Driver (Jan. 2005). "A Concise Reference to (Projected) Sérsic $R^{1/n}$ Quantities, Including Concentration, Profile Slopes, Petrosian Indices, and Kron Magnitudes". In: *Publications of the Astron. Soc. of Australia* 22.2, pp. 118–127. DOI: 10.1071/AS05001. arXiv: astro-ph/0503176 [astro-ph].

Green, Andrew W., Karl Glazebrook, Peter J. McGregor, Roberto G. Abraham, et al. (Oct. 2010). "High star formation rates as the origin of turbulence in early and modern disk galaxies". In: *Nature* 467.7316, pp. 684–686. DOI: 10.1038/nature09452. arXiv: 1010.1262 [astro-ph.GA].

Green, Andrew W., Karl Glazebrook, Peter J. McGregor, Ivana Damjanov, et al. (Jan. 2014). "DYNAMO - I. A sample of Hα-luminous galaxies with resolved kinematics". In: *Monthly Notices of the RAS* 437.2, pp. 1070–1095. DOI: 10.1093/mnras/stt1882. arXiv: 1310.6082 [astro-ph.GA].

Hayes, Matthew (2019). *Lyman-alpha as an Astrophysical and Cosmological Tool - chapter 4*. Ed. by Anne Verhamme et al. Springer Berlin Heidelberg. DOI: 10.1007/978-3-662-59623-4.

Herenz, E. C. et al. (Mar. 2016). "The Lyman alpha reference sample. VII. Spatially resolved Hα kinematics". In: *Astronomy and Astrophysics* 587, A78, A78. DOI: 10.1051/0004-6361/201527373. arXiv: 1511.05406.

Herenz, Edmund Christian (2016). "Detecting and Understanding Extragalactic Lyman alpha EmissionUsing 3D Spectroscopy". In: PhD thesis, Universität Potsdam.

Herenz, Edmund Christian et al. (Jan. 2019). "The MUSE-Wide Survey: A determination of the Lyman α emitter luminosity function at $3 < z < 6$". In: *Astronomy and Astrophysics* 621, A107, A107. DOI: 10.1051/0004-6361/201834164. arXiv: 1810.05037 [astro-ph.GA].

Hickson, Paul (Oct. 2014). "Atmospheric and adaptive optics". In: *The Astronomy and Astrophysics Review* 22.1. DOI: 10.1007/s00159-014-0076-9.

Holmberg, E. (Jan. 1958). "A photographic photometry of extragalactic nebulae." In: *Meddelanden fran Lunds Astronomiska Observatorium Serie II* 136, p. 1.

Hsieh, Jin-Jian (June 2010). "Estimation of Kendall's tau from censored data". In: *Computational Statistics &amp Data Analysis* 54.6, pp. 1613–1621. DOI: 10.1016/j.csda.2010.01.015.

Hu, E. M. et al. (Dec. 2010). "An Atlas of $z = 5.7$ and $z = 6.5$ Lyα Emitters". In: *Astrophysical Journal* 725.1, pp. 394–423. DOI: 10.1088/0004-637X/725/1/394. arXiv: 1009.1144 [astro-ph.CO].

Hummer, D. G. and P. J. Storey (Feb. 1987). "Recombination-line intensities for hydrogenic ions - I. Case B calculations for H I and He II." In: *Monthly Notices of the RAS* 224, pp. 801–820. DOI: 10.1093/mnras/224.3.801.

Isobe, Yuki et al. (July 2023). "EMPRESS. IX. Extremely Metal-poor Galaxies are Very Gas-rich Dispersion-dominated Systems: Will the James Webb Space Telescope Witness Gaseous Turbulent High-z Primordial Galaxies?" In: *Astrophysical Journal* 951.2, 102, p. 102. DOI: 10.3847/1538-4357/accc87. arXiv: 2206.04709 [astro-ph.GA].

Ivezić, Željko et al. (2014). *Statistics, Data Mining, and Machine Learning in Astronomy: A Practical Python Guide for the Analysis of Survey Data*. DOI: 10.1515/9781400848911.

James, Gareth et al. (2013). *An Introduction to Statistical Learning with Applications in R*. Springer; 1st ed. 2013, Corr. 7th printing 2017 Edition (25. Juni 2013).

Jiménez-Vicente, J. et al. (Feb. 1999). "Fabry-Perot observations of the ionized gas in NGC 3938". In: *Astronomy and Astrophysics* 342, pp. 417–425. arXiv: astro-ph/9811391 [astro-ph].

Kashikawa, Nobunari et al. (Sept. 2006). "The End of the Reionization Epoch Probed by Lyα Emitters at z = 6.5 in the Subaru Deep Field". In: *Astrophysical Journal* 648.1, pp. 7–22. DOI: 10.1086/504966. arXiv: astro-ph/0604149 [astro-ph].

Kendall, Maurice G. (1990). *Rank correlation methods*. New York, NY : Oxford University Press.

Kennicutt, Robert C. (Jan. 1998a). "Star Formation in Galaxies Along the Hubble Sequence". In: *Annual Review of Astron and Astrophys* 36, pp. 189–232. DOI: 10.1146/annurev.astro.36.1.189. arXiv: astro-ph/9807187 [astro-ph].

— (May 1998b). "The Global Schmidt Law in Star-forming Galaxies". In: *Astrophysical Journal* 498.2, pp. 541–552. DOI: 10.1086/305588. arXiv: astro-ph/9712213 [astro-ph].

Kennicutt, Robert C. and Neal J. Evans (Sept. 2012). "Star Formation in the Milky Way and Nearby Galaxies". In: *Annual Review of Astronomy and Astrophysics* 50.1, pp. 531–608. DOI: 10.1146/annurev-astro-081811-125610.

Kerutt, J. et al. (Mar. 2022). "Equivalent widths of Lyman α emitters in MUSE-Wide and MUSE-Deep". In: *Astronomy and Astrophysics* 659, A183, A183. DOI: 10.1051/0004-6361/202141900. arXiv: 2202.06642 [astro-ph.GA].

Krajnovic, Davor et al. (Mar. 2006). "Kinemetry: a generalization of photometry to the higher moments of the line-of-sight velocity distribution". In: *Monthly Notices of the Royal Astronomical Society* 366.3, pp. 787–802. DOI: 10.1111/j.1365-2966.2005.09902.x.

Kroupa, Pavel, Christopher A. Tout, and Gerard Gilmore (June 1993). "The Distribution of Low-Mass Stars in the Galactic Disc". In: *Monthly Notices of the RAS* 262, pp. 545–587. DOI: 10.1093/mnras/262.3.545.

Krumholz, Mark R. et al. (June 2018). "A unified model for galactic discs: star formation, turbulence driving, and mass transport". In: *Monthly Notices of the RAS* 477.2, pp. 2716–2740. DOI: 10.1093/mnras/sty852. arXiv: 1706.00106 [astro-ph.GA].

Kusakabe, Haruka et al. (Jan. 2018). "The stellar mass, star formation rate and dark matter halo properties of LAEs at z $\sim$ 2". In: *Publications of the ASJ* 70.1, 4, p. 4. DOI: 10.1093/pasj/psx148. arXiv: 1707.09373 [astro-ph.GA].

Landman, D. A., R. Roussel-Dupre, and G. Tanigawa (Oct. 1982). "On the statistical uncertainties associated with line profile fitting". In: *Astrophysical Journal* 261, pp. 732–735. DOI: 10.1086/160383.

Laursen, Peter (2010). "Interpreting Lyman radiationfrom young, dusty galaxies". In: *Dark Cosmology Centre, Niels Bohr InstituteFaculty of Science, University of Copenhagen*.

Laursen, Peter et al. (July 2019). "Lyman α-emitting galaxies in the epoch of reionization". In: *Astronomy and Astrophysics* 627, A84, A84. DOI: 10.1051/0004-6361/201833645. arXiv: 1806.07392 [astro-ph.GA].

Law, David R., Francesco Belfiore, et al. (Mar. 2022). "SDSS-IV MaNGA: Understanding Ionized Gas Turbulence Using Integral Field Spectroscopy of 4500 Star-forming Disk Galaxies". In: *Astrophysical Journal* 928.1, 58, p. 58. DOI: 10.3847/1538-4357/ac5620. arXiv: 2112.11281 [astro-ph.GA].

Law, David R., Charles C. Steidel, et al. (Nov. 2007). "Integral Field Spectroscopy of High-Redshift Star-forming Galaxies with Laser-guided Adaptive Optics: Evidence for Dispersion-dominated Kinematics". In: *Astrophysical Journal* 669.2, pp. 929–946. DOI: 10.1086/521786. arXiv: 0707.3634 [astro-ph].

Leitherer, Claus et al. (July 1999). "Starburst99: Synthesis Models for Galaxies with Active Star Formation". In: *Astrophysical Journal, Supplement* 123.1, pp. 3–40. DOI: 10.1086/313233. arXiv: astro-ph/9902334 [astro-ph].

Lenz, Dawn D. and Thomas R. Ayres (Nov. 1992). "Errors Associated with Fitting Gaussian Profiles to Noisy Emission-Line Spectra". In: *Publications of the ASP* 104, p. 1104. DOI: 10.1086/133096.

Licquia, Timothy C. and Jeffrey A. Newman (June 2015). "Improved Estimates of the Milky Way's Stellar Mass and Star Formation Rate from Hierarchical Bayesian Meta-Analysis". In: *Astrophysical Journal* 806.1, 96, p. 96. DOI: 10.1088/0004-637X/806/1/96. arXiv: 1407.1078 [astro-ph.GA].

Lintott, Chris et al. (Jan. 2011). "Galaxy Zoo 1: data release of morphological classifications for nearly 900 000 galaxies". In: *Monthly Notices of the RAS* 410.1, pp. 166–178. DOI: 10.1111/j.1365-2966.2010.17432.x. arXiv: 1007.3265 [astro-ph.GA].

Malhotra, Sangeeta and James E. Rhoads (Feb. 2002). "Large Equivalent Width Lyα line Emission at z=4.5: Young Galaxies in a Young Universe?" In: *Astrophysical Journal, Letters* 565.2, pp. L71–L74. DOI: 10.1086/338980. arXiv: astro-ph/0111126 [astro-ph].

Matthee, Jorryt and Joop Schaye (Mar. 2019). "The origin of scatter in the star formation rate-stellar mass relation". In: *Monthly Notices of the RAS* 484.1, pp. 915–932. DOI: 10.1093/mnras/stz030. arXiv: 1805.05956 [astro-ph.GA].

Melinder, Jens et al. (Feb. 2023). "The Lyman α Reference Sample XIV: Lyman α imaging of 45 low redshift star-forming galaxies and inferences on global emission". In: *arXiv e-prints*, arXiv:2302.14077, arXiv:2302.14077. DOI: 10.48550/arXiv.2302.14077. arXiv: 2302.14077 [astro-ph.GA].

Mo, Houjun, Frank van den Bosch, and Simon White (May 2010). *Galaxy Formation and Evolution*. Cambridge University Press. DOI: 10.1017/cbo9780511807244.

Moffat, A. F. J. (Dec. 1969). "A Theoretical Investigation of Focal Stellar Images in the Photographic Emulsion and Application to Photographic Photometry". In: *Astronomy and Astrophysics* 3, p. 455.

Moiseev, A. V., S. A. Pustilnik, and A. Y. Kniazev (July 2010). "Very metal-poor galaxies: ionized gas kinematics in nine objects". In: *Monthly Notices of the RAS* 405.4, pp. 2453–2470. DOI: 10.1111/j.1365-2966.2010.16621.x. arXiv: 1003.0771 [astro-ph.CO].

Moiseev, Alexei V., Anton V. Tikhonov, and Anatoly Klypin (June 2015). "What controls the ionized gas turbulent motions in dwarf galaxies?" In: *Monthly Notices of the RAS* 449.4, pp. 3568–3580. DOI: 10.1093/mnras/stv489. arXiv: 1405.5731 [astro-ph.GA].

Negus, James et al. (Oct. 2021). "The Physics of the Coronal-line Region for Galaxies in Mapping Galaxies at Apache Point Observatory". In: *Astrophysical Journal* 920.1, 62, p. 62. DOI: 10.3847/1538-4357/ac1343.

Ning, Yuanhang et al. (Feb. 2022). "The Magellan M2FS Spectroscopic Survey of High-z Galaxies: Lyα Emitters at z $\approx$ 6.6 and the Evolution of Lyα Luminosity Function over z $\approx$ 5.7-6.6". In: *Astrophysical Journal* 926.2, 230, p. 230. DOI: 10.3847/1538-4357/ac4268. arXiv: 2112.07800 [astro-ph.GA].

Oliva-Altamirano, P. et al. (Feb. 2018). "The connection between the peaks in velocity dispersion and star-forming clumps of turbulent galaxies". In: *Monthly Notices of the RAS* 474.1, pp. 522–535. DOI: 10.1093/mnras/stx2797. arXiv: 1710.09457 [astro-ph.GA].

Osterbrock, Donald E. and Gary J. Ferland (2006). *Astrophysics of gaseous nebulae and active galactic nuclei*.

Östlin, Göran et al. (Dec. 2014). "The Lyα Reference Sample. I. Survey Outline and First Results for Markarian 259". In: *Astrophysical Journal* 797.1, 11, p. 11. DOI: 10.1088/0004-637X/797/1/11. arXiv: 1409.8347 [astro-ph.GA].

Ouchi, Masami (2019). *Lyman-alpha as an Astrophysical and Cosmological Tool - chapter 3*. Ed. by Anne Verhamme et al. Springer Berlin Heidelberg. DOI: 10.1007/978-3-662-59623-4.

Oyarzún, Grecco A. et al. (July 2017). "A Comprehensive Study of Lyα Emission in the High-redshift Galaxy Population". In: *Astrophysical Journal* 843.2, 133, p. 133. DOI: 10.3847/1538-4357/aa7552. arXiv: 1706.01886 [astro-ph.GA].

Padilla, Nelson D. and Michael A. Strauss (Aug. 2008). "The shapes of galaxies in the Sloan Digital Sky Survey". In: *Monthly Notices of the RAS* 388.3, pp. 1321–1334. DOI: 10.1111/j.1365-2966.2008.13480.x. arXiv: 0802.0877 [astro-ph].

Partridge, R. B. and P. J. E. Peebles (Mar. 1967). "Are Young Galaxies Visible?" In: *Astrophysical Journal* 147, p. 868. DOI: 10.1086/149079.

Press, William H (1986). *Numerical recipes : the art of scientific computing*. Cambridge [Cambridgeshire] ; New York : Cambridge University Press.

Pucha, Ragadeepika et al. (Oct. 2022). "Lyα Escape from Low-mass, Compact, High-redshift Galaxies". In: *Astronomical Journal* 164.4, 159, p. 159. DOI: 10.3847/1538-3881/ac83a9. arXiv: 2207.14303 [astro-ph.GA].

Puech, M. et al. (June 2008). "IMAGES. III. The evolution of the near-infrared Tully-Fisher relation over the last 6 Gyr". In: *Astronomy and Astrophysics* 484.1, pp. 173–187. DOI: 10.1051/0004-6361:20079313. arXiv: 0803.3002 [astro-ph].

Rasekh, A. et al. (June 2022). "The Lyman Alpha Reference Sample. XII. Morphology of extended Lyman alpha emission in star-forming galaxies". In: *Astronomy and Astrophysics* 662, A64, A64. DOI: 10.1051/0004-6361/202140734. arXiv: 2110.01626 [astro-ph.GA].

Rhoads, James E., Pascale Hibon, et al. (June 2012). "A Lyα Galaxy at Redshift z = 6.944 in the COSMOS Field". In: *Astrophysical Journal, Letters* 752.2, L28, p. L28. DOI: 10.1088/2041-8205/752/2/L28. arXiv: 1205.3161 [astro-ph.CO].

Rhoads, James E. and Sangeeta Malhotra (Dec. 2001). "Lyα Emitters at Redshift z = 5.7". In: *Astrophysical Journal, Letters* 563.1, pp. L5–L9. DOI: 10.1086/338477. arXiv: astro-ph/0110280 [astro-ph].

Rhoads, James E., Sangeeta Malhotra, et al. (Jan. 2014). "The Dynamical Masses, Densities, and Star Formation Scaling Relations of Lyα Galaxies". In: *Astrophysical Journal* 780.1, 20, p. 20. DOI: 10.1088/0004-637X/780/1/20. arXiv: 1301.3140 [astro-ph.CO].

Rhoads, James E., Chun Xu, et al. (Aug. 2004). "A Luminous Lyα-emitting Galaxy at Redshift z = 6.535: Discovery and Spectroscopic Confirmation". In: *Astrophysical Journal* 611.1, pp. 59–67. DOI: 10.1086/422094. arXiv: astro-ph/0403161 [astro-ph].

Rodríguez, Silvio and Nelson D. Padilla (Sept. 2013). "The intrinsic shape of galaxies in SDSS/Galaxy Zoo". In: *Monthly Notices of the RAS* 434.3, pp. 2153–2166. DOI: 10.1093/mnras/stt1168. arXiv: 1306.3264 [astro-ph.CO].

Roth, Martin M. et al. (June 2005). "PMAS: The Potsdam Multi-Aperture Spectrophotometer. I. Design, Manufacture, and Performance". In: *Publications of the ASP* 117.832, pp. 620–642. DOI: 10.1086/429877. arXiv: astro-ph/0502581 [astro-ph].

Runnholm, Axel et al. (Mar. 2020). "The Lyman Alpha Reference Sample. X. Predicting Lyα Output from Star-forming Galaxies Using Multivariate Regression". In: *Astrophysical Journal* 892.1, 48, p. 48. DOI: 10.3847/1538-4357/ab7a91. arXiv: 2002.12378 [astro-ph.GA].

Sandin, C. et al. (June 2010). "P3D: a general data-reduction tool for fiber-fed integral-field spectrographs". In: *Astronomy and Astrophysics* 515, A35, A35. DOI: 10.1051/0004-6361/201014022. arXiv: 1002.4406 [astro-ph.IM].

Sandin, Christer et al. (Sept. 2012). "Automated and generalized integral-field spectroscopy data reduction using p3d". In: *Software and Cyberinfrastructure for Astronomy II*. Ed. by Nicole M. Radziwill and Gianluca Chiozzi. Vol. 8451. Society of Photo-Optical Instrumentation Engineers (SPIE) Conference Series, 84510F, 84510F. DOI: 10.1117/12.926092.

Scarlata, C. et al. (Oct. 2009). "The Effect of Dust Geometry on the Lyα Output of Galaxies". In: *Astrophysical Journal, Letters* 704.2, pp. L98–L102. DOI: 10.1088/0004-637X/704/2/L98. arXiv: 0909.3847 [astro-ph.CO].

Schneider, Peter (2006). *Einführung in die Extragalaktische Astronomie und Kosmologie*. Springer Berlin Heidelberg. DOI: 10.1007/3-540-30589-0.

Smith, Aaron et al. (Nov. 2022). "The physics of Lyman-α escape from disc-like galaxies". In: *Monthly Notices of the RAS* 517.1, pp. 1–27. DOI: 10.1093/mnras/stac2641. arXiv: 2111.13721 [astro-ph.GA].

Sobral, David and Jorryt Matthee (Mar. 2019). "Predicting Lyα escape fractions with a simple observable. Lyα in emission as an empirically calibrated star formation rate indicator". In: *Astronomy and Astrophysics* 623, A157, A157. DOI: 10.1051/0004-6361/201833075. arXiv: 1803.08923 [astro-ph.GA].

Terlevich, R. and J. Melnick (June 1981). "The dynamics and chemical composition of giant extragalactic H II regions". In: *Monthly Notices of the RAS* 195, pp. 839–851. DOI: 10.1093/mnras/195.4.839.

Übler, H. et al. (July 2019). "The Evolution and Origin of Ionized Gas Velocity Dispersion from z $\sim$ 2.6 to z $\sim$ 0.6 with KMOS^{3D}". In: *Astrophysical Journal* 880.1, 48, p. 48. DOI: 10.3847/1538-4357/ab27cc. arXiv: 1906.02737 [astro-ph.GA].

Unsöld, Albrecht and Bodo Baschek (1981). *Der neue Kosmos*. Springer Berlin Heidelberg. DOI: 10.1007/978-3-662-06533-4.

Unterborn, Cayman T. and Barbara S. Ryden (Nov. 2008). "Inclination-Dependent Extinction Effects in Disk Galaxies in the Sloan Digital Sky Survey". In: *Astrophysical Journal* 687.2, pp. 976–985. DOI: 10.1086/591898. arXiv: 0801.2400 [astro-ph].

Varidel, Mathew et al. (Mar. 2016). "Resolved Gas Kinematics in a Sample of Low-Redshift High Star-Formation Rate Galaxies". In: *Publications of the Astron. Soc. of Australia* 33, e006, e006. DOI: 10.1017/pasa.2016.3. arXiv: 1602.00737 [astro-ph.GA].

Varidel, Mathew R., Scott M. Croom, Geraint F. Lewis, Brendon J. Brewer, et al. (May 2019). "The SAMI Galaxy Survey: Bayesian inference for gas disc kinematics using a hierarchical Gaussian mixture model". In: *Monthly Notices of the RAS* 485.3, pp. 4024–4044. DOI: 10.1093/mnras/stz670. arXiv: 1903.03121 [astro-ph.GA].

Varidel, Mathew R., Scott M. Croom, Geraint F. Lewis, Deanne B. Fisher, et al. (June 2020). "The SAMI galaxy survey: gas velocity dispersions in low-z star-forming galaxies and the drivers of turbulence". In: *Monthly Notices of the RAS* 495.2, pp. 2265–2284. DOI: 10.1093/mnras/staa1272. arXiv: 2005.04874 [astro-ph.GA].

Verhamme, A. et al. (Oct. 2012). "Lyman-α emission properties of simulated galaxies: interstellar medium structure and inclination effects". In: *Astronomy and Astrophysics* 546, A111, A111. DOI: 10.1051/0004-6361/201218783. arXiv: 1208.4781 [astro-ph.CO].

Verolaĭnen, Ya F and A Ya Nikolaich (June 1982). "Radiative lifetimes of excited states of atoms". In: *Soviet Physics Uspekhi* 25.6, pp. 431–447. DOI: 10.1070/pu1982v025n06abeh004565.

Wall, J. V. (Dec. 1996). "Practical Statistics for Astronomers - II. Correlation, Data-modelling and Sample Comparison". In: *Quarterly Journal of the RAS* 37, p. 519.

Wang, J. X. et al. (June 2004). "X-Ray Nondetection of the Lyα Emitters at z$\backsim$4.5". In: *Astrophysical Journal, Letters* 608.1, pp. L21–L24. DOI: 10.1086/422311. arXiv: astro-ph/0404611 [astro-ph].

Wang, Weichen et al. (Dec. 2018). "Galaxy Inclination and the IRX-β Relation: Effects on UV Star Formation Rate Measurements at Intermediate to High

Redshifts". In: *Astrophysical Journal* 869.2, 161, p. 161. DOI: 10.3847/1538-4357/aaef79. arXiv: 1811.03671 [astro-ph.GA].

Weigert, A., H.J. Wendker, and L. Wisotzki (2012). *Astronomie und Astrophysik: Ein Grundkurs*. Wiley. ISBN: 9783527670956. URL: https://books.google.de/books?id=X6aif39qZ7wC.

Willett, Kyle W. et al. (Nov. 2013). "Galaxy Zoo 2: detailed morphological classifications for 304 122 galaxies from the Sloan Digital Sky Survey". In: *Monthly Notices of the RAS* 435.4, pp. 2835–2860. DOI: 10.1093/mnras/stt1458. arXiv: 1308.3496 [astro-ph.CO].

Wisnioski, E. et al. (Feb. 2015). "The KMOS^{3D} Survey: Design, First Results, and the Evolution of Galaxy Kinematics from 0.7 <= z <= 2.7". In: *Astrophysical Journal* 799.2, 209, p. 209. DOI: 10.1088/0004-637X/799/2/209. arXiv: 1409.6791 [astro-ph.GA].

Yu, Xiaoling et al. (Aug. 2021). "The major mechanism to drive turbulence in star-forming galaxies". In: *Monthly Notices of the RAS* 505.4, pp. 5075–5083. DOI: 10.1093/mnras/stab1681. arXiv: 2106.05474 [astro-ph.GA].

Zhou, Luwenjia et al. (Oct. 2017). "The SAMI Galaxy Survey: energy sources of the turbulent velocity dispersion in spatially resolved local star-forming galaxies". In: *Monthly Notices of the RAS* 470.4, pp. 4573–4582. DOI: 10.1093/mnras/stx1504. arXiv: 1706.04754 [astro-ph.GA].

Acknowledgments

Without persons involved in and around my master thesis project, I would not have been able to do this research project. I want to thank:

- **Christian**, my supervisor, the person to ask any question and the best mentor for my Master thesis.
- **Professor Jörg Main** for supervising me at the University of Stuttgart and for supporting me.
- **Professor Speck** for co-examined this thesis.
- **Peter** for aligning the PMAS observations with the HST observations and the insightful discussions contributing to this research and the paper.
- **Axel and Matthew** for discussions on the multivariate linear regression.
- **Jens** for answering numerous questions concerning the HST data.
- **Nicolas** for answering numerous questions concerning GalPaK3D.
- **LARS Collaboration** for the discussions and for answering a lot of questions.
- **Daniel Kunth** for organizing the LARS collaboration workshop and the Institute of Astrophysics of Paris (IAP) for funding my attendance.
- **The 2023 Saas-Fee Advanced Course Organizing Team** for organizing the winter school and **professor Daghofer** and the school support grant for funding my attendance.
- **Polychronis** for organizing the Lyman labyrinths conference and the Institute of Theoretical Physics 1 (ITP1) for sponsoring my participation.
- **Monika Bund** for the administrative support at the University of Stuttgart.
- **DAAD RISE program** for funding an internship, which was the starting point of this project.
- **My mother and Silas** for supporting me during my study.
- **Marco, Simon, Joshua, and Chris** for being amazing fellow students and friends.

Each of you contributed a lot to the project and supported me. You made the time of my Master thesis unique.

Erklärung

Ich versichere,

- dass ich diese Masterarbeit selbstständig verfasst habe,
- dass ich keine anderen als die angegebenen Quellen benutzt und alle wörtlich oder sinngemäß aus anderen Werken übernommenen Aussagen als solche gekennzeichnet habe,
- dass die eingereichte Arbeit weder vollständig noch in wesentlichen Teilen Gegenstand eines anderen Prüfungsverfahrens gewesen ist,
- und dass das elektronische Exemplar mit den anderen Exemplaren übereinstimmt.

Stuttgart, den 12. Oktober 2023 *Anna Lena Schaible*